**School of Science and Engineering**

**Department of Chemistry**

# Design, Synthesis and Application of Luminescent Metal Tetrazolato Complexes in Optical Imaging

**Melissa V. Werrett**

**This thesis is presented for the Degree of**

**Doctor of Philosophy**

**of**

**Curtin University**

**November, 2014**

# Contents

# Symbols and Abbreviations

| | |
|---|---|
| Å | angstroms |
| $\delta$ | nuclear magnetic resonance chemical shift in ppm |
| $\varepsilon$ | molar extinction coefficient |
| $\lambda$ | wavelength |
| $\lambda_{ex}$ | excitation wavelength |
| $\lambda_{em}$ | emission wavelength |
| $\mu$m | micrometer |
| $\tau$ | lifetime |
| $\phi$ | quantum yield |
| $^{o}$ | degrees |
| | |
| 1D-NOESY | one dimensional Nuclear Overhauser Effect Spectroscopy |
| $^{1}$ | singlet spin multiplicity |
| 2D-HMBC | two dimensional Heteronuclear Multiple Bond Correlation |
| 2D-HSQC | two dimensional Heteronuclear Single Quantum Coherence |
| $^{3}$ | triplet spin multiplicity |
| app. | apparent |
| **bipy** | 2,2'-bipyridine |
| br | broad |
| d | doublet (NMR signal splitting) |
| DAPI | 4',6-diamidino-2-phenylindole |
| DCM | dichloromethane |
| dec. | decomposition |
| **diim** | diimine |
| DCC | N,N'-dicyclohexylcarbodiimide |
| DMAP | 4-dimethylaminopyridine |
| DMF | dimethylformamide |
| DMSO | dimethylsulfoxide |
| EDCI | 1-ethyl-3-(3-dimethylaminopropyl) carbodiimide |
| eq | equivalents |

| | |
|---|---|
| EWG | electron withdrawing group |
| ES | excited state |
| FT | Fourier Transform |
| GS | ground state |
| GF-AAS | raphite furnace-atomic absorption spectrometry |
| $H_m$ | hydrogen, *meta* |
| $H_o$ | hydrogen, *ortho* |
| $H_p$ | hydrogen, *para* |
| HOMO | highest occupied molecular orbital |
| IC | internal converison |
| ICP-MS | inductively coupled plasma-mass spectrometry |
| IR | infrared |
| ISC | intersystem crossing |
| IL | intraligand |
| *J* | coupling constant |
| K | Kelvin |
| LLCT | ligand-to-ligand charge transfer |
| LUMO | lowest unoccupied molecular orbital |
| m | multiplet (NMR), medium (IR) |
| MC | metal centred |
| MLCT | metal-to-ligand charge transfer |
| MLLCT | metal-to-ligand-to-ligand charge transfer |
| mmol | millimole |
| m/z | mass per unit charge |
| NIR | near infrared |
| NMR | Nuclear Magnetic Resonance |
| O.D. | optical density |
| PET | positron emission tomography |
| **phen** | 1,10-phenanthroline |
| ROI | region of interest |
| s | singlet (NMR signal splitting), strong (IR) |
| S | total spin angular momentum |

| | |
|---|---|
| sh | shoulder |
| SPECT | single-photon emission computed tomography |
| t | triplet (NMR signal splitting) |
| THF | tetrahydrofuran |
| UV | ultraviolet |
| w | weak (IR) |

# Compound Numbering and Codes

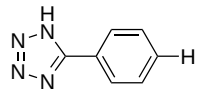

**1**

5-phenyl-1H-tetrazole (**Tph**H)

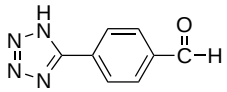

**2**

4-(1H-tetrazol-5-yl)-benzaldehyde (**Tbz**H)

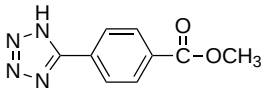

**3**

methyl 4-(1H-tetrazol-5-yl)-benzoate (**Tmeb**H)

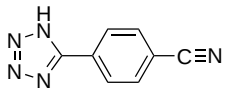

**4**

4-(1H-tetrazol-5-yl)cyanobenzene ( **Tcya**H)

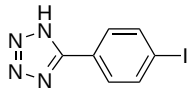

**5**

5-(4-iodophenyl)-1H-tetrazole (**TIod**H)

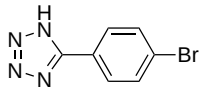

**6**

5-(4-bromophenyl)-1H-tetrazole (**TBr**H)

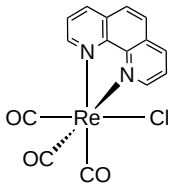

**7**

*fac*-[Re(**phen**)$(CO)_3$(Cl)]

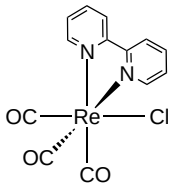

**8**

*fac*-[Re(**bipy**)$(CO)_3$(Cl)]

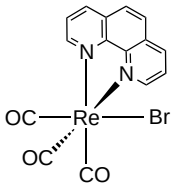

**9** *fac*-[Re(**phen**)$(CO)_3$(Br)]

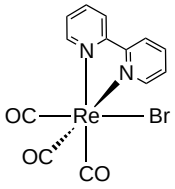

**10** *fac*-[Re(**bipy**)$(CO)_3$(Br)]

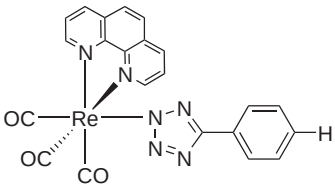

**11** *fac*-[Re(**phen**)$(CO)_3$(**Tph**)]

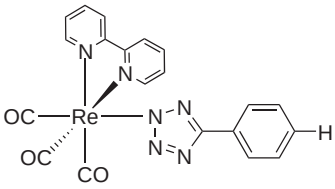

**12** *fac*-[Re(**bipy**)$(CO)_3$(**Tph**)]

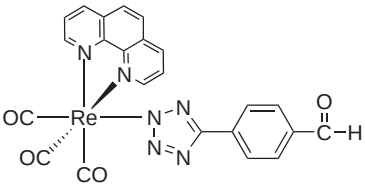

**13** *fac*-[Re(**phen**)$(CO)_3$(**Tbz**)]

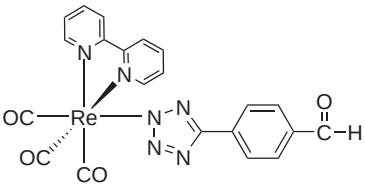

**14** *fac*-[Re(**bipy**)$(CO)_3$(**Tbz**)]

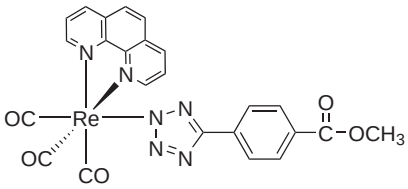

**15** *fac*-[Re(**phen**)$(CO)_3$(**Tme**)]

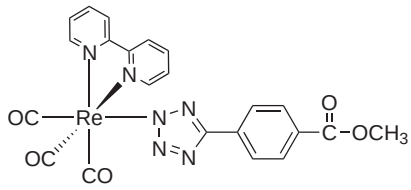

**16** *fac*-[Re(**bipy**)$(CO)_3$(**Tme**)]

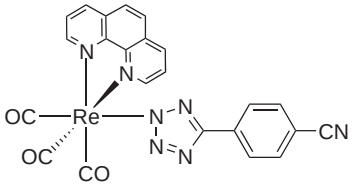

**17** *fac*-[Re(**phen**)$(CO)_3$(**Tcya**)]

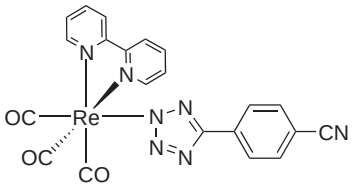

**18** *fac*-[Re(**bipy**)$(CO)_3$(**Tcya**)]

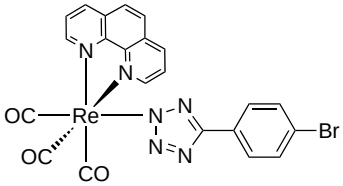

**19** *fac*-[Re(**phen**)$(CO)_3$(**TBr**)]

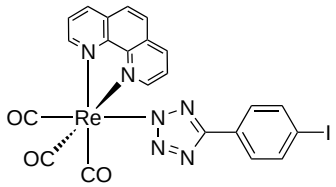

**20** *fac*-[Re(**phen**)$(CO)_3$(**TIod**)]

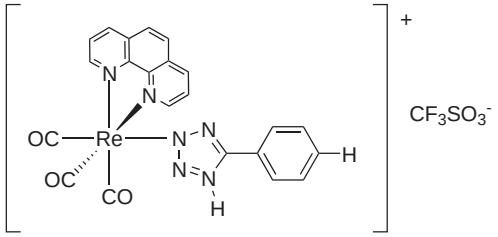

**21** *fac*-[Re(**phen**)$(CO)_3$(**Tph**H)]$^+$

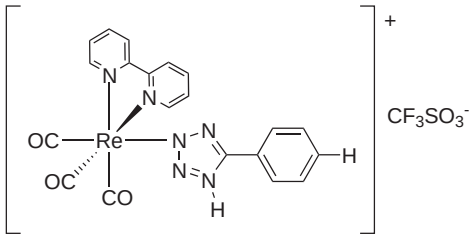

**22** *fac*-[Re(**bipy**)$(CO)_3$(**Tph**H)]$^+$

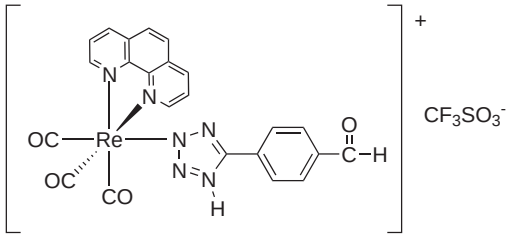

**23** *fac*-[Re(**phen**)$(CO)_3$(**Tbz**H)]$^+$

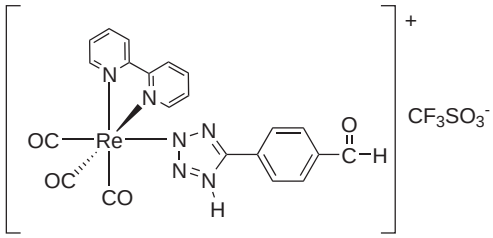

**24** *fac*-[Re(**bipy**)$(CO)_3$(**Tbz**H)]$^+$

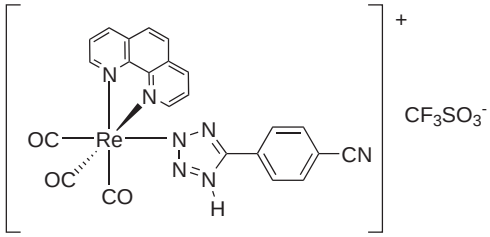

**25** *fac*-[Re(**phen**)$(CO)_3$(**Tcya**H)]$^+$

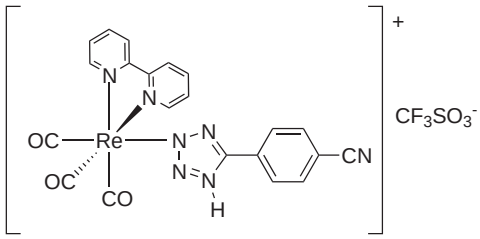

**26** *fac*-[Re(**bipy**)$(CO)_3$(**Tcya**H)]$^+$

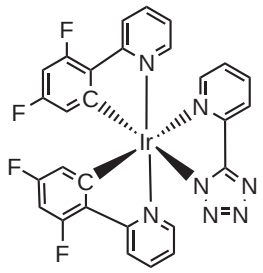

**27** [Ir(PyrTzF)]

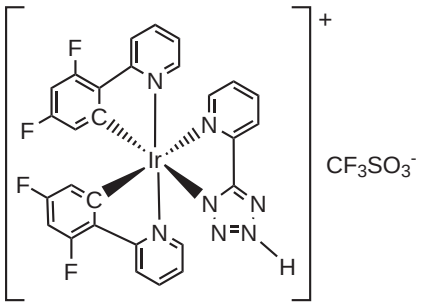

**28** $[Ir(PyrTzFH)]^{+}$

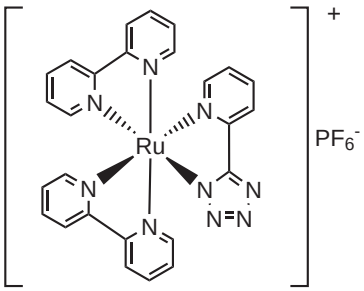

**29** $[Ru(PyrTz)]^{+}$

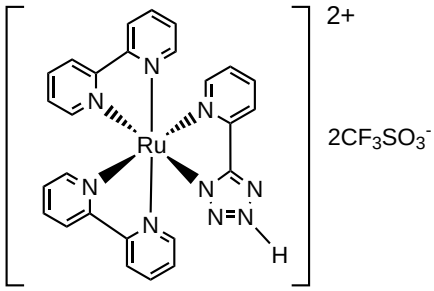

**30** $[Ru(PyrTzH)]^{2+}$

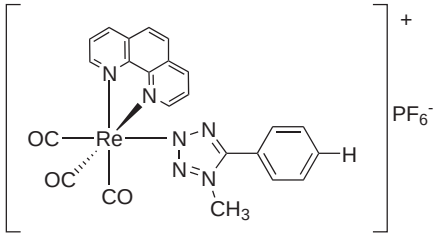

**31**

*fac*-[Re(**phen**)(CO)$_3$(**Tph**CH$_3$)]$^+$

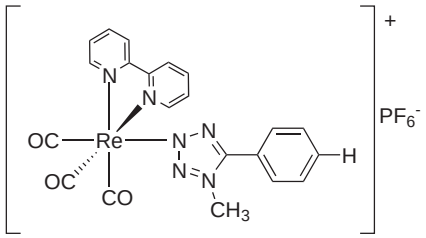

**32**

*fac*-[Re(**bipy**)(CO)$_3$(**Tph**CH$_3$)]$^+$

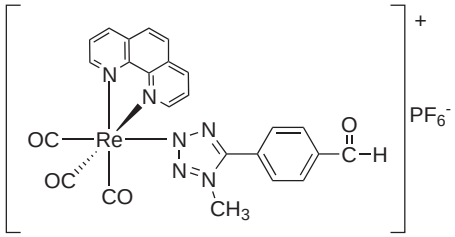

**33**

*fac*-[Re(**phen**)(CO)$_3$(**Tbz**CH$_3$)]$^+$

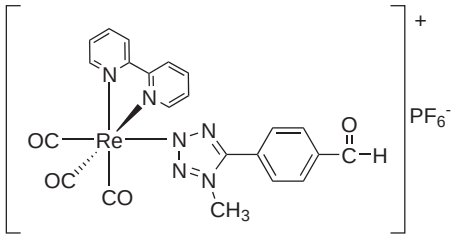

**34**

*fac*-[Re(**bipy**)(CO)$_3$(**Tbz**CH$_3$)]$^+$

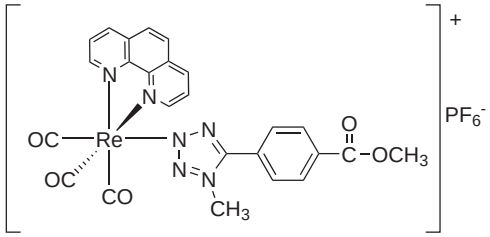

**35**

*fac*-[Re(**phen**)(CO)$_3$(**Tme**CH$_3$)]$^+$

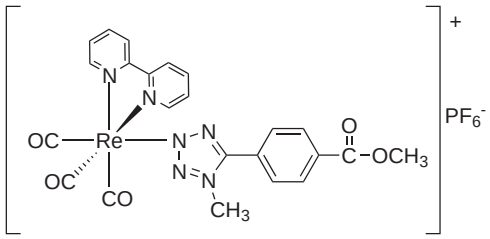

**36**

*fac*-[Re(**bipy**)(CO)$_3$(**Tme**CH$_3$)]$^+$

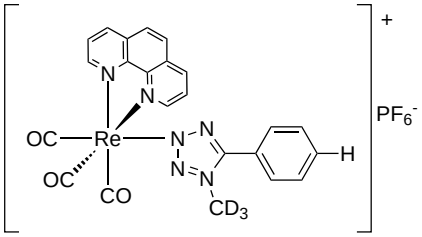

**37** *fac*-[Re(**phen**)$(CO)_3$(**Tph**$CD_3$)]$^+$

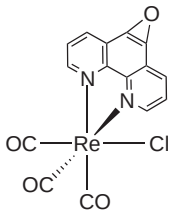

**38** *fac*-[Re(**ephen**)$(CO)_3$(Cl)]

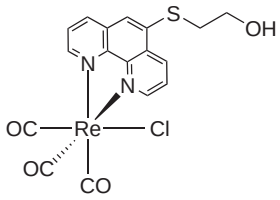

**39** *fac*-[Re(**phen-RS**)$(CO)_3$(Cl)]

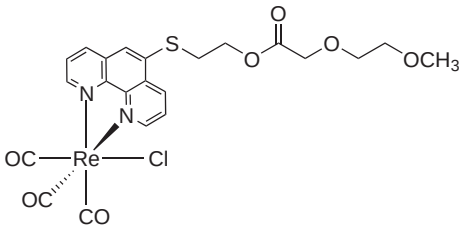

**40** *fac*-[Re(**phen-S-PEG**)$(CO)_3$(Cl)]

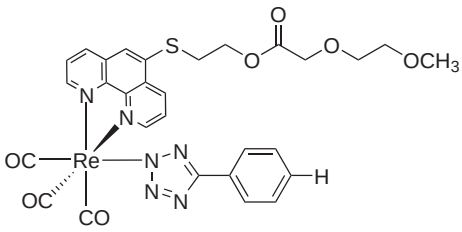

**41** *fac*-[Re(**phen-S-PEG**)$(CO)_3$(**Tph**)]

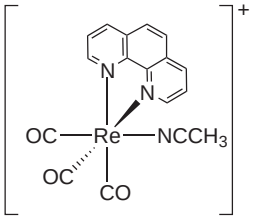


**42**

*fac*-[Re(**phen**)$(CO)_3(NCCH_3)]^+$

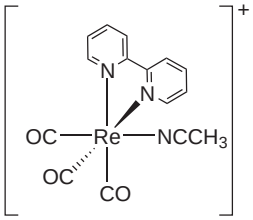


**43**

*fac*-[Re(**bipy**)$(CO)_3(NCCH_3)]^+$

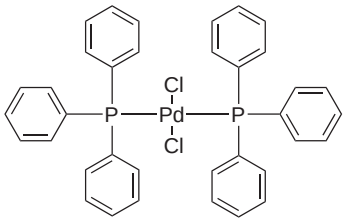


**44**

**Bis(tri-phenylphosphine)palladium(II) dichloride**

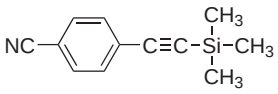


**45**

**4-trimethylsilylethynylbenzonitrile**

# Acknowledgments

I owe endless thanks to Dr. Max Massi for his support, knowledge and enthusiasm. Every chat with Max gave me new found motivation. I am grateful for the opportunity to have worked on such an interesting project. Max also encouraged me to spend time working at the University of Bologna, an invaluable experience. This leads me to thank Assoc/Prof. Stefano Stagni and Dr. Sara Muzzioli for welcoming me into their lab and also to Bologna. Italy would not have been the amazing experience it was without you both. I really enjoyed all of the work that we did together...but maybe I am most grateful for the introduction to “aperitivo.” Grazie mille!

The multidisciplinary nature of this research was made possible by Assoc/Prof. Paul Rigby and Ms Alysia Buckley. Thank you for the knowledge and training that made the live cell imaging experiments possible. I have learnt so much from you both. Paul, thank you for your honesty and encouragement. Alysia, thank you for teaching me to carry out tissue culture to a high standard.

Ching, Curtin chemistry would fall apart without you. Thank you for everything.

Chappy, thank you for your help setting up and maintaining the spectrofluorometer.

Robert Herman, thank you for running the elemental samples.

To Dr. Brian Skelton from UWA and Assoc/Prof. Stefano Zacchini from the University of Bologna for all of the crystallography.

Thanks Phil Wright, Dr. Paolo Raiteri and Prof. Julian Gale for all of the computational calculations.

To all of my friends at Curtin who made the completion of my PhD possible, you know who you are and I am very grateful to each and every one of you. Special thanks to members of The Empire, past and present.

Guy Travers, I owe you many beers and thanks. You have helped me so much and it has been such an experience (and pleasure) sitting next to you for all of these years. I don’t think I will ever meet anyone quite like you again. Another special mention is to Jamila. Since the day I introduced myself to you in undergrad - so many good times have been shared. Thanks for being awesome and a huge support to me throughout

these PhD years. To Karen and Anusha, who made up the rest of the “normal four,” thank you for your friendship, support and also many good times!

I also owe a huge thank you to my family for their endless support. To all of my friends for their understanding, especially during the write-up phase.

Finally, to Branden; you were there from the beginning and have always been so supportive of me. Thank you for sticking by me, no matter where I was.

# Abstract

A series of Re(I) complexes was synthesised and investigated as optical imaging agents. Fundamental studies provided insight into how structural modifications influenced their chemical, photophysical and biological properties.

The synthesis, structural and photophysical properties of a series of *fac*-[Re(**diim**)$(CO)_3$(**L**)] complexes has been reported, where **diim** is either 1,10-phenanthroline (**phen**) or 2,2'-bipyridine (**bipy**) and **L** is one of a series of 5-substituted aryl tetrazoles. NMR and X-ray crystallography indicated that all of the complexes coordinate to the tetrazolato ligand through the N2 atom. Phosphorescent emission was characterised as originating from a $^3$MLLCT state. Structural changes to the diimine ligand from **bipy** to **phen** led to an improvement in the photoluminescence quantum yield ($\phi$) and an elongation of lifetime ($\tau$). Changes to the electron withdrawing *para* substituents on the aryl tetrazolato ligand allowed fine tuning of the complexes $\tau$ , $\phi$ and, to a lesser extent, the maximum emission wavelengths.

The photophysical properties of the prepared neutral Re(I) complexes were reversibly modulated upon protonation of the tetrazolato ligand. The cationic complexes of the form *fac*-[Re(**diim**)$(CO)_3$(**L**H)]$^+$ exhibited increased emission intensity, a blue shifted emission maxima and increased $\tau$ and $\phi$, compared to their neutral analogues. Different photophysical modulation was observed upon protonation of Ir(III) and Ru(II) tetrazolato complexes. The iridium emission was red shifted whilst the ruthenium emission was significantly quenched. These changes were reversible upon addition of triethylamine. To harness the enhanced photophysical output of the protonated Re(I) complexes in an irreversible way, methylation reactions were carried out to yield complexes of the form *fac*-[Re(**diim**)$(CO)_3$(**L**$CH_3$)]$^+$. The photophysical output was again increased with longer $\tau$ and improved $\phi$, with respect to the neutral species. Crystal structures revealed the formation of both Re-N2 and Re-N1 linkage isomers. The stability of the Re(I) complexes was lost upon methylation as evidenced by the detachment of the tetrazolato ligand in coordinating solvents.

In an attempt to improve the water solubility of the *fac*-[Re(**phen**)$(CO)_3$(**L**)] complexes, a small polyethylene glycol chain was functionalised onto the **phen** ligand. Analysis of the *n*-octanol/water distribution coefficient revealed that the PEG chain was of insufficient length to modify the lipophilicity of the complexes. However, upon structural change to the **phen** ligand, photophysical output was not appreciably altered.

To extend applications of the Re(I) complexes, *fac*-[Re(**phen**)$(CO)_3$(**Talk**)] was synthesised. The terminal alkyne group on the tetrazolato ligand can be functionalised utilising "click" chemistry. Studies revealed that the *para* substituent is not significantly involved in the HOMO and so further modification here should not considerably alter photophysical output.

Live HeLa cell imaging revealed that the neutral complexes *fac*-[Re(**phen**)$(CO)_3$(**Tph**)], *fac*-[Re(**phen**)$(CO)_3$(**Tbz**)] and *fac*-[Re(**phen-S-PEG**)$(CO)_3$(**Tph**)] showed good cellular uptake with perinuclear localisation. This was confirmed through spectral imaging and analysis. *fac*-[Re(**phen**)$(CO)_3$(**Tph**)] and *fac*-[Re(**phen**)$(CO)_3$(**Tbz**)] were non toxic during incubation and imaging. Upon continual illumination (for approximately three minutes, as in a z-stack experiment) these complexes became cytotoxic as evidenced by the rounding up of cells and formation of membrane blebs. *fac*-[Re(**phen-S-PEG**)$(CO)_3$(**Tph**)] had a strong emission within HeLa cells but was the most phototoxic complex imaged. The phototoxic nature of the Re(I) complexes was rationalised by their ability to produce singlet oxygen upon excitation to their triplet excited state.

Supporting publications include:

Bader, C.A.; Brooks, R. D.; Ng, Y.S.; Sorvina, A.; Werrett, M.V.; Wright, P.J.; Anwer, A.G.; Brooks, D.A.; *et al*. *R. Soc. Chem. Adv.* **2014**, 4, 16345–16351.

Werrett, M. V.; Muzzioli, S.; Wright, P. J.; Palazzi, A.; Raiteri, P.; Zacchini, S.; Massi, M.; Stagni, S. *Inorg. Chem.* **2014**, 53, 229–43.

Werrett, M.V.; Chartrand, D.; Gale, J.D.; Hanan, G.S.; MacLellan, J.G.; Massi, M.; Muzzioli, S.; Raiteri, P.; Skelton, B.W.; Silberstein, M.; Stagni, S. *Inorg. Chem.* **2011**, 4, 50, 1229–1241.

# Chapter 1

# Introduction

## 1.1 Medical Imaging Modalities

Medical imaging techniques have greatly advanced since the 19$^{th}$ century. Improvements in technology have allowed for the whole body, including anatomical structures and/or physiological function, to be imaged for medicinal purposes.[1] These developments translate to a more rapid response to disease detection and therefore early and more efficient treatment of patients. The progression of the medical imaging field has seen the reduction of potentially risky and invasive diagnostic techniques, such as exploratory surgery.[1,2] A number of imaging procedures are established in medicine including X-ray imaging (including computed tomography [CT] scans), magnetic resonance imaging (MRI) and ultrasound, as shown in Figure 1.1.[3–5]


Figure 1.1: Medical images (left to right); MRI, ultrasound and X-ray.[3–5]

More recent developments include positron emission tomography (PET) and single photon emission computed tomography (SPECT) imaging techniques.

### 1.1.1 Radiography

Radiography uses X-rays to image internal structures of the patient, producing an overall 2D image. Patients are placed in front of a detector as X-rays are pulsed through the body or area of interest. Bones are efficient at absorbing X-rays, whereas tissue and muscle allow more X-rays to pass through to the detector. This difference makes bones appear white while soft tissue shows up in shades of grey on a developed X-ray image. Radiography can be used to image the whole body and is commonly used to image anatomical structures, for example teeth and the skeletal system.[6] It is one of the most widespread technologies used in medical imaging but has fairly poor resolution and only produces 2D images.[7] To increase the information gained from radiography, contrast agents (particularly iodine based) have been employed. Contrast agents improve image quality and allow further functional information to be gained.[6] X-rays are a form of ionising radiation and therefore exposure must be monitored as excessive levels can be harmful.[8]

### 1.1.2 X-ray Computed Tomography (CT)

CT scans use X-rays to produce multiple 2D images which are then digitally reconstructed to give a 3D view of the area. This technique revolutionised medical imaging[9] and is now the most commonly used technique for evaluating cancer patients.[10] Contrast agents are also used in X-ray CT imaging to help improve the level of information gained from each image.[6] Unlike the whole body capability of simple X-ray imaging, CT scans can only image a limited area and are not used to image the whole body at one time.[7]

### 1.1.3 Magnetic Resonance Imaging (MRI)

During an MRI scan the subject is placed inside a strong magnetic field which aligns the protons in the body (most commonly found in water) in a predominantly low energy state. A radio frequency pulse will excite the protons to a higher energy state. Once the pulse is switched off, protons relax and the energy released upon relaxation is used to produce the final MR image.[11] Contrast in tissues is achieved by the dif-

ferent relaxation times of protons, depending on their location. $T_1$ and $T_2$ describe the relaxation time constants along the z axis and in the x-y planes respectively.[12,13] Whole body imaging can be achieved using MRI and it is commonly used in diagnostic medicine. As with CT scans, MRIs have the potential to produce 3D images to increase the amount of information gained from the process. Exogenous contrast agents (paramagnetic substances such as $Gd^{3+}$ complexes) are commonly used to improve image output.[14]

### 1.1.4 Ultrasound

Ultrasound can not be detected by the human ear. This imaging technique is most commonly associated with the imaging of foetuses in pregnant women but it can also be used as a diagnostic tool. Generally, ultrasound imaging uses a transducer which produces small pulses of ultrasound waves (echoes) into the body. Some of these will penetrate deeper while others are reflected back to the transducer, eventually producing an image.[15] Ultrasound does not use ionising radiation, can image in real time and is generally portable. These factors are some of the advantages of ultrasound over other imaging modalities. Similar to other techniques, technology has allowed the production of 3D ultrasound images.[9]

### 1.1.5 Radioimaging

Radioimaging involves the use of radioactive tracers, for example $^{18}$F and $^{99m}$Tc labeled compounds. These are introduced into the body to assist in the visualisation of structures (eg: organs) at more of a molecular and functional level than the techniques discussed above. The tracer is usually attached to a biologically relevant molecule that has specificity for an organ/region of interest. The radiotracer emits gamma rays, detected by a camera to produce a 2D or 3D image of the organ inside the patient.[16] The most common forms of radioimaging are PET and SPECT. They are similar techniques however PET is more sensitive, whereas SPECT is cheaper and more widely available. The radionuclides commonly used in PET include $^{18}$F, $^{11}$C, $^{13}$N and $^{15}$O whereas $^{99m}$Tc is predominantly used for SPECT imaging.[17] SPECT can give information about blood flow and metabolism. The radiotracers used in SPECT generally

have a longer half-life compared to those used in PET. Therefore SPECT is commonly used in cardiology cases where scans can take hours.[16]

### 1.1.6 Multimodal Imaging

Multimodal imaging can be used to describe the acquisition of images with multiple techniques and digitally combining them or, the simultaneous acquisition of different image types. The combination of different imaging techniques can give rise to improved diagnostic outputs which has seen their employment in medicine increase over the last two decades.[10,18,19] The first type of multimodal imaging was the combination of CT and SPECT in 1966. In 1998 both SPECT-CT and PET-CT became commercially available and are commonly used today.[20]

The techniques discussed above in sections 1.1.1-1.1.5, are all non-invasive however, they do not have the power of subcellular resolution achievable through optical imaging. Optical imaging can be used as a stand alone technique or as a complementary procedure to those mentioned above, leading to an increase in the power of diagnostic medicine.

### 1.1.7 Optical Imaging

Optical imaging, often referred to as fluorescence imaging, is a technique utilising ultraviolet to near infrared (NIR) wavelengths of light to visualise chemical and biological moieties. It is a rapidly developing area in the medical imaging field as it is non-invasive, utilises non-ionising radiation and can produce high resolution images at a sub-cellular level.[21] There are various ways optical imaging is employed in medicine however fluorescence microscopy is one of the most common techniques utilised. It can be used to image cell cultures *in vitro* or to analyse tissue samples *ex vivo*. The high resolution achieved through fluorescence microscopy is illustrated in Figure 1.2, where subcellular co-staining of the DNA (blue) and microtubules (red) is shown.[22] Different fluorescent labels have been used in the HeLa cells (Figure 1.2) to target different organelles. Fluorescence microscopy is well established in research and is also employed in diagnostic clinical applications.[23]

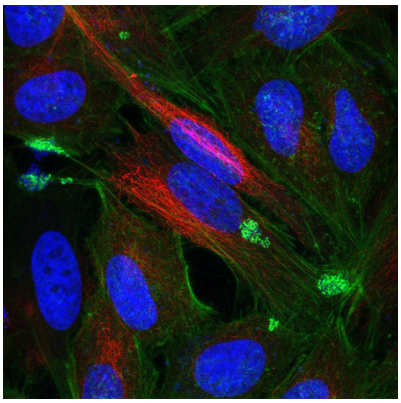

Figure 1.2: Fluorescence staining of cancerous cells.[22]

Fluorescence imaging *in vivo* (on animal models) has become one of the most commonly used tools in pre-clinical research. Whole body *in vivo* imaging is still not routinely used and research is still in its infancy.[21,24,25] Fluorescence image-guided surgery is another technique emerging in the area of optical imaging.[26] Current limitations of fluorescence imaging include the interference of small structures within tissue, the level of light penetration achievable and the overall contrast produced. Despite these limitations, the progress of optical imaging (including whole body and surgical imaging) is rapid and will soon be commonly employed in a range of research, diagnostic and even therapeutic applications. For this advancement, continued development of specialised instrumentation is required. However, just as important is the development of suitable probes, commonly required for optical imaging. These probes are luminescent and are used to target and therefore image particular components of the body and/or tissues.

It is possible to carry out label-free imaging on certain samples and it is always desirable to avoid the introduction of exogenous chemicals to the body and biological samples. Some optical imaging techniques make this possible. For example, confocal Raman spectroscopy has been used to analyse samples at a cellular level.[27] A recent example has demonstrated the ability to image brain activity patterns in animal models, label free, by harnessing the endogenous fluorescence from flavins.[28] It would be ideal to conduct all optical imaging without the introduction of labels however, to achieve high specificity and high contrast imaging, probes are often necessary.

## 1.2 Probes for Optical Imaging and the Principles of Fluorescence

In order to carry out the optical imaging techniques discussed above, there is a need for optimised probes to ensure maximum image contrast and specificity. This will lead to improved diagnosis and patient outcomes as well as advances in pre-clinical research. A range of dyes are commercially available and are routinely used in optical imaging to assist in the visualisation of cellular structure and function.[29,30] These probes can be used alone or can be conjugated to specific biomolecules (such as antibodies, proteins etc). The structure of the probe or the conjugated biomolecule is used to control uptake and specificity or to selectively sense chemical species in a biological environment. The most commonly available commercial probes are small organic fluorescent molecules, for example the Alexa Fluor dyes, Fluorescein and DAPI (**46** and **47**, Figure 1.3). Over the past three decades research into their development has progressed rapidly.[25] The use of fluorescent proteins, for example the commonly known green fluorescent protein, in conjunction with genetic engineering has also been exploited in both imaging and sensing applications.[31–33]

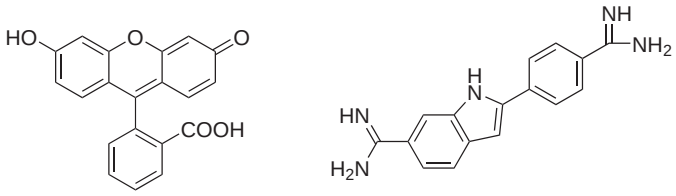


**46** **47**

Figure 1.3: Fluorescent labels Fluorescein and 4',6-diamidino-2-phenylindole (DAPI) used in optical imaging.

### 1.2.1 Fluorescence

Fluorescence is a form of luminescence that is characterised by the emission of light from an electronically excited state to a ground state of the same spin multiplicity. The Jablonski diagram,[34] illustrated in Figure 1.4, is used to represent the processes that occur when a molecule interacts with light (*hv*).

Light is required to excite an electron from the highest occupied molecular orbital

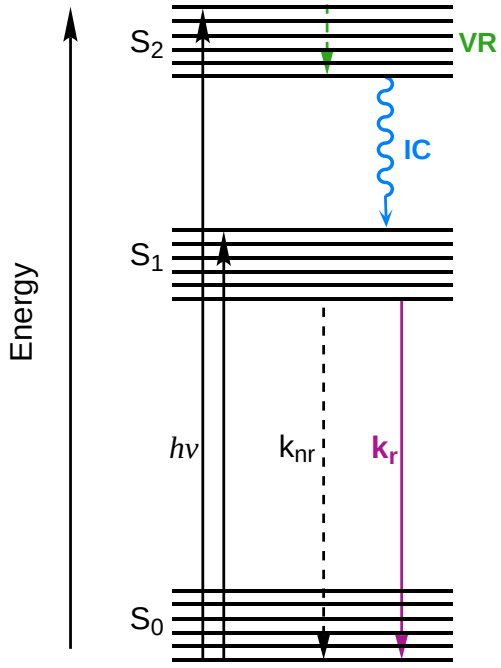


Figure 1.4: Simplified Jablonski diagram, illustrating fluorescence.

(HOMO) to the lowest unoccupied molecular orbital (LUMO) of a compound, when the transition is $S_0 \rightarrow S_1$. The absorbance of light promotes the compound from its ground state (eg: $S_0$) into an electronically excited state (eg: $S_1$, $S_2$), considering the ground state as a singlet. The excited electron will be in the opposite spin to its partner in the ground state. Therefore the multiplicity of this excited state is termed a singlet, based on the equation: 2S+1. S is the is the total spin angular momentum for all electrons and in this case will equal zero, therefore 2S + 1 = 1. Upon excitation of a molecule, many vibrational excited states will be populated. Vibrational relaxation (VR) occurs between vibrational levels of the same excited state whereas internal conversion (IC) occurs between different electronic levels. Both VR and IC are rapid radiationless processes that occur in the order of $10^{-14}$-$10^{-13}$ seconds.[35,36]

The population of many vibronic levels upon excitation is directly related to the Franck-Condon principle, an important concept in relation to all luminescent molecules. The Franck-Condon principle is based around the Born-Oppenheimer approximation which states that electronic transitions are very fast compared to nuclear motions, due to the relative light weight of electrons compared to nuclei. Therefore, vertical electronic transitions will be favoured when there is a minimal change in the position of the nuclei.[37] This concept is illustrated in Figure 1.5. Kasha's rule states that emission occurs

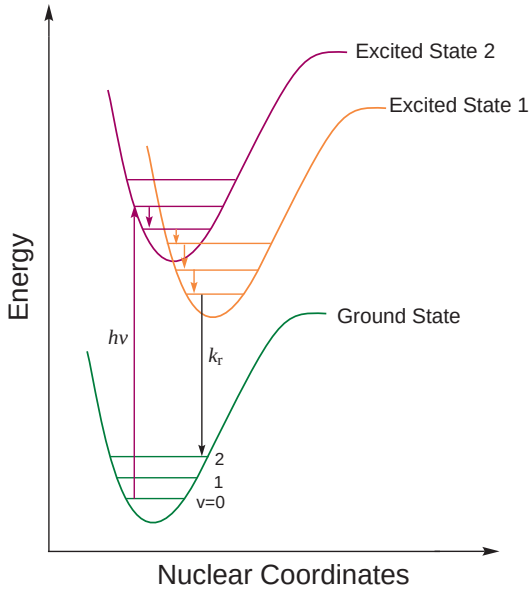


Figure 1.5: Franck-Condon principle for electronic transitions.

from the lowest lying excited state.[35] This emission will then occur to various vibrational levels of the ground state, some which are more likely than others, according to Franck-Condon considerations (Figure 1.5). It can be thought that the emission band is the sum of all emission from v = 0 in the excited state, to each vibronic level in the ground state. Emission to a vibrational level is preferred when it corresponds to a minimal change in the position of the nuclear coordinates.[37] From any vibrational level, the molecule will relax to the lowest energy ground state. Kasha's rule also provides an explanation as to why the excitation energy is higher than the emission energy. The Jablonski diagram also shows that the energy of emission is less than that of excitation. This difference is known as the Stokes shift,[38] commonly represented as $\lambda_{em}$ - $\lambda_{ex}$.[39]

The probability of a transition is governed by a set of selection rules which relate to the multiplicity and symmetry of the ground and excited states. The spin conservation selection rule states that transitions are only allowed between states of the same spin multiplicity. For example, a singlet to singlet transition is allowed whereas a triplet to singlet transition is forbidden.[40] An electronic transition must also involve a change in parity, which is the basis of the Laporte selection rule. This selection rule applies to centrosymmetric molecules or ions where parity is either symmetric (gerade, *g*) or antisymmetric (ungerade, *u*), with respect to the inversion centre. Therefore $g \rightarrow g$ and $u \rightarrow u$ transitions are forbidden.[41]

In the Jablonski diagram (Figure 1.4) emission from $S_1$ to the ground state is spin allowed as the excited and ground state posses the same multiplicity.[35] As the transition is spin allowed, the emission of light is usually fast, in the order of $10^{-8}$ seconds. The average time a molecules spends in the excited state, before returning to its ground state, is known as the lifetime ($\tau$). The radiative lifetime ($\tau_r$) is the time it takes for the excited state to depopulate, assuming non-radiative decay pathways are not possible. The radiative decay constant can be defined by; $k_r = \frac{1}{\tau_r}$, and assumes no contribution from non-radiative decay. However, relaxation from the lowest energy state to the ground state can occur either radiatively, by the emission of a photon or non-radiatively, such as vibrational relaxation. Therefore lifetime ($\tau$) is usually measured, which takes into account the radiative and non-radiative decay constants; $\tau = \frac{1}{k_{nr}+k_r}$ .

Quantum yield ($\phi$) is another parameter used to characterise luminescent materials and is described as the ratio of photons the molecule emits versus the number of photons absorbed.[35,39] The equations below outline the relationships between $\phi$, $k_{nr}$, $k_r$ and $\tau$.

$$k_r = \frac{\phi}{\tau} \qquad k_{nr} = \frac{1-\phi}{\tau}$$

$$\phi = \frac{k_r}{k_{nr}+k_r}$$

### 1.2.2 Drawbacks of Fluorescent Probes

Certain organic fluorophores are known to be able to possess high molar extinction coefficients ($\varepsilon$) and $\phi$ meaning that they are efficient at absorbing and emitting light.[42] However, in certain situations they can suffer from a range of issues reducing image quality and resolution hence limiting the imaging potential of the label. Due to their relatively short lived fluorescence lifetimes and small Stokes shifts, they can suffer interference from autofluorescence. Autofluorescence originates from endogenous fluorophores such as aromatic amino acids, including tryptophan, tyrosine (**48**, Figure 1.6) and phenylalanine.[43,44] Enzyme cofactors, such as nicotinamide adenine dinucleotide (NADH), pyridoxal phosphate (**49**, Figure 1.6) and flavin adenine dinucleotide (FAD)

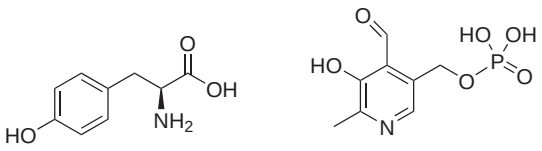


**48** **49**

Figure 1.6: Examples of autofluorescent compounds, tyrosine and pyridoxal phosphate.

are also endogenous fluorophores.[44] Typically, endogenous species involved in autofluorescence also exhibit small Stokes shifts (tens of nm) and relatively short lived lifetimes (<<10 ns). Interference occurs because signals from both the applied label and endogenous biological species are detected. Overlapping of emission and absorption profiles (small Stokes shift), can also cause self-quenching of molecules in close proximity to each other due to reabsorption of emitted photons.[43] This is a major issue when the dye is used to image a specific organelle or protein. The molecules accumulate, increasing the chance of self-quenching which can reduce the signal intensity of the probe dramatically. Finally, many of these organic labels can undergo photobleaching. Photobleaching is the loss of fluorescence intensity caused by continual imaging.[45] The excited state of the organic probe is unstable and might undergo chemical transformations, causing photochemical destruction of the fluorophore into a species that no longer possess luminescent properties.[46]

In order for optical imaging techniques to be successfully exploited in diagnostic medicine there is a crucial need for the development of superior labels. Currently, as fluorescent probes have been used for so many years, much of the instrumentation employed in optical imaging is customised to their particular photophysical properties (short $\tau$, small Stokes shift etc). Despite this, investigation into luminescent heavy metal complexes for optical imaging has recently increased. In conjunction with these studies has been the development of specialised instrumentation and techniques to accommodate and take advantage of the unique photophysical properties exhibited by metal complexes.

## 1.3 Metal Complexes in Optical Imaging

Phosphorescent heavy metal complexes have been gaining increased attention as alternative probes for optical imaging. They often exhibit the desired properties needed to overcome the issues associated with organic fluorophores.

### 1.3.1 Photophysics of $d^6$ Metal Complexes

The photophysical processes of heavy metal complexes with a low spin $d^6$ configuration are different to those exhibited by organic fluorescent molecules. Metal complexes are often characterised by emission from a triplet excited state (2S + 1 = 3) down to the ground singlet state.

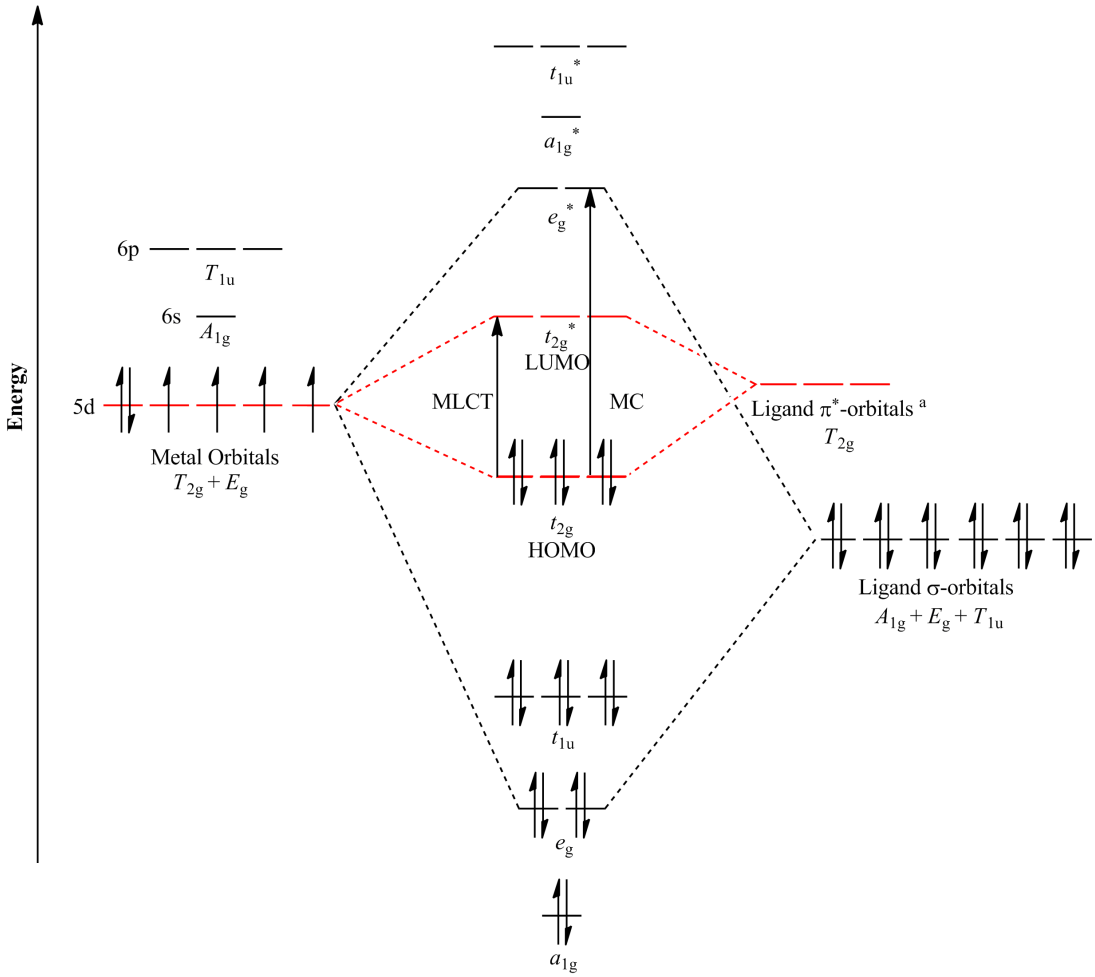


Figure 1.7: Generalised partial molecular orbital diagram for $d^6$ transition metals, coordinated to equivalent π-accepting ligands. This case represents a situation where the metal centre is a second or third row transition metal and the surrounding ligands have low energy $\pi^*$ orbitals. [a]Only the $T_{2g}$ combination is considered for simplicity.

The molecular orbital diagram, Figure 1.7, is a representation of a $d^6$ heavy metal complex (as the focus of this research), showing some of the possible electronic transitions. For simplicity, in the construction of the diagram all of the ligands around the metal are assumed to be equivalent and only the $\pi^*$ ligand orbitals of $T_{2g}$ symmetry are shown forming molecular orbitals with the metal. Figure 1.7 illustrates the stability of low spin $d^6$ metal complexes as they have completely filled bonding orbitals and empty anti-bonding orbitals. The frontier orbitals (HOMO-LUMO) correspond to $t_{2g}$, and $t_{2g}{}^*$ respectively, while the $e_g{}^*$ orbital is positioned at a higher energy than the $t_{2g}{}^*$. Many of the $d^6$ heavy metals belong to the second and third transition rows and therefore experience a stronger crystalline field from the surrounding ligands, from increased metal-ligand interaction, raising the energy of $e_g{}^*$ . The relative position of the $t_{2g}$ is determined by the presence and specific energies of the $\pi^*$ orbitals of the ligands. The higher energy of the $e_g{}^*$ is an important requirement for the metal complexes to be luminescent, as decay from metal centred states is usually non-radiative. The $t_{2g}$ and $e_g{}^*$ orbitals are mainly metal in character and therefore transitions between them are known as d-d, metal-centred (MC) transitions.

One possible transition for $d^6$ metal complexes, shown in Figure 1.7, is the metal-to-ligand charge transfer (MLCT). It is generally the transition between the HOMO and LUMO, to form the $^1$MLCT state ($t_{2g}{}^5 t_{2g}{}^{*1}$). It is important to know that in order to maximise the emission of light, the MLCT state must be sufficiently distanced from the MC state, to avoid thermal population of the latter. At the same time, a wide HOMO-LUMO gap is necessary to avoid high values of $k_{nr}$ according to the energy gap law.[47–49] In metal complexes, an increase in the energy gap between the $t_{2g}$ and $t_{2g}{}^*$ orbitals will lead to a decrease in the non-radiative decay constant, $k_{nr}$ which in turn leads to an increase in $\tau$ and $\phi$.

Intraligand (IL) transitions are not shown in Figure 1.7 but are possible within the ligand and are known as $\pi - \pi^*$ transitions. If the surrounding ligands are not all equivalent and have $\pi$-accepting abilities, then there is also the possibility of having ligand-to-ligand charge transfers (LLCTs). These however are not shown in Figure 1.7 but again involve a transition from the filled $\pi$ system of one ligand to the empty $\pi^*$ system of another.

Figure 1.8 is a Jablonski diagram, illustrating both fluorescent and phosphorescence.

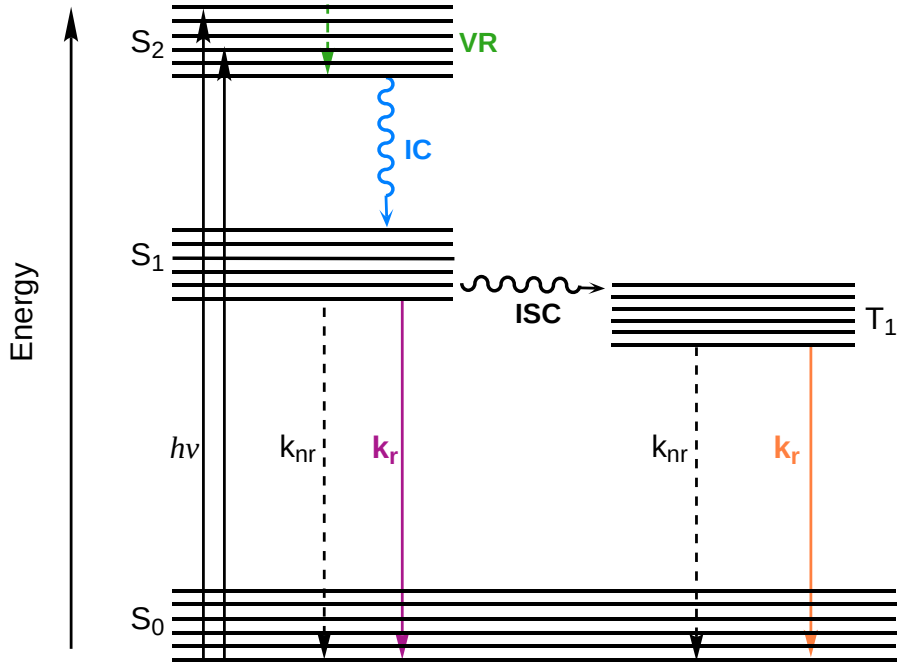


Figure 1.8: Simplified Jablonski diagram, illustrating fluorescence and phosphorescence.

The radiative emission from a triplet to singlet state is known as phosphorescence. The main difference for the Jablonski diagram of a phosphorescent molecule is a process known as intersystem crossing (ISC). ISC is a radiationless transition from the singlet excited state to the more stable triplet state ($T_1$ in Figure 1.8). Spin orbit coupling, which is more efficient in molecules containing a heavy atom, allows the ISC transition due to the mixing of the singlet and triplet states.[50,51] As relaxation from the $^3$MLCT to the ground singlet state requires a change of spin, the transition is spin forbidden and hence the $\tau$ of metal complexes are generally longer than observed in (fluorescent) organic molecules.

#### 1.3.1.1 Singlet Oxygen

It is well known that molecular oxygen can quench the emission from the triplet excited states of metal complexes.[52] Molecular oxygen has a triplet ground state configuration. As the emission from the triplet states of metal complexes is spin forbidden, it is generally long lived. This allows oxygen, which can diffuse fast through solution due to its small size, to quench this excited state through intermolecular interactions.[53,54] Figure 1.9 shows a simplified view of how the ground state of molecular oxygen is

excited to its triplet state, through triplet-triplet energy transfer. The energy transfer is spin allowed and can therefore occur more rapidly than radiative decay from the complex. Emission from the lowest lying excited state of oxygen ($^1\Delta_g$) has a characteristic emission band around 1270 nm which can be directly detected[54,55], using an NIR detector.

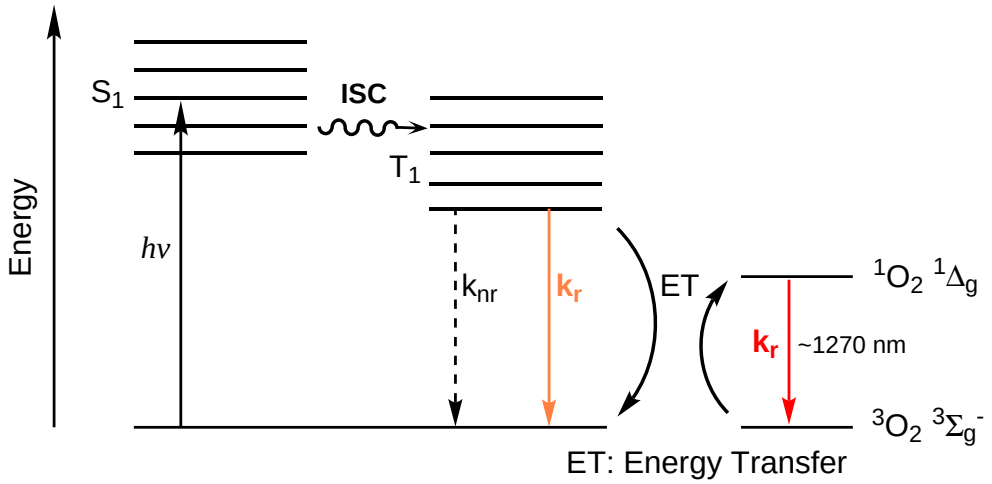


Figure 1.9: Simplified Jablonski diagram demonstrating how molecular oxygen can quench the emission from the triplet states of metal complexes.

It is important to be aware of the production of singlet oxygen, especially in biological systems. Singlet oxygen can be cytotoxic as it undergoes redox reactions which can oxidise important cellular species including proteins, DNA and lipids. It can also lead to apoptosis (programmed cell death) of cells which is the basis of cancer treatment using photodynamic therapy.[56]

#### 1.3.1.2 Multiphoton Excitation

Many heavy metal complexes have demonstrated the ability to be able to undergo multiphoton excitation (MPE).[41,57–59] MPE is a non-linear process which occurs when a molecule simultaneously absorbs two or more photons.[57,60] These two photons of lower energy will combine and have the energy required for the molecule to undergo one photon excitation, see Figure 1.10.[57,60] This means that longer wavelengths of light (commonly in the NIR region) are used to facilitate the process of excitation from the ground to excited state.[57,60]

To achieve two or multiphoton excitation of a molecule, high intensity pulsed lasers are

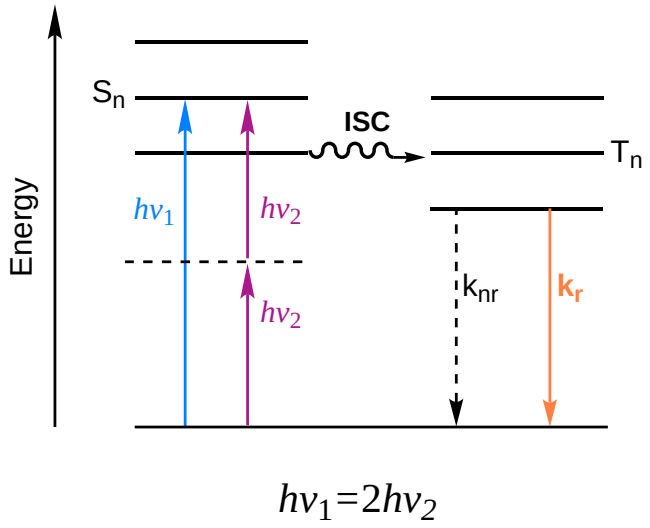


Figure 1.10: Simplified Jablonski diagram showing two-photon excitation.

used so that the molecule can simultaneously absorb two (longer wavelength) photons, to be excited to a singlet excited state. The emission profile of the complex in general, will be the same as if it had undergone single photon excitation at a lower wavelength, see Figure 1.10. The advantage of complexes that can undergo multiphoton excitation is described in section 1.3.2.2.

## 1.3.2 General Requirements for the Application of Metal Complexes in Bioimaging

There are a range of desirable properties that optical imaging probes must exhibit to be successful. It is important that heavy metal complexes exhibit most, if not all of these properties in order to be applicable in biological imaging applications.

### 1.3.2.1 Physical and Chemical Properties

Probes must exhibit good solubility in aqueous environments, specifically cellular media, to be useful for optical imaging. For the probe to easily cross the cellular membrane, lipophilicity is required.[61,62] Therefore, it is important to have a balance between aqueous solubility and lipophilicity. Depending on the precise application of the probe, they must exhibit specific localisation within a cell or have the ability to be conjugated to a biological molecule that can induce this specificity.[61] If the probe is

also to be used for sensing, then it must have a preferential repose to a specific change in the environment (eg: pH or concentration of $Ca^{2+}$) that can be easily monitored and measured.[62] The biodistribution of the probe must also be considered if eventually applied *in vivo*.

High stability and kinetic inertness are required to reduce photobleaching and potential toxic effects the probe might exhibit. The probe cannot exhibit toxicity to the biological environment at any time during an imaging experiment.[6,62] This includes the generation of singlet oxygen ($^1O_2$) to a toxic concentration upon irradiation (discussed below). Generation of $^1O_2$ is often difficult to avoid and therefore careful planning is required to ensure that the concentration of $^1O_2$ is kept to a minimum, so that the cell is not impacted.

#### 1.3.2.2 Photophysical Properties: Tissue Penetration

For biological imaging *(ex vivo/in vivo*), it is vital that the light used to excite the applied dye penetrates the tissue easily. Svoboda *et al.* describe a "window of transparency" for biological materials where certain wavelengths of light can easily penetrate the tissue. This translates to more efficient excitation and detection of the dye, into deeper tissues.[63]

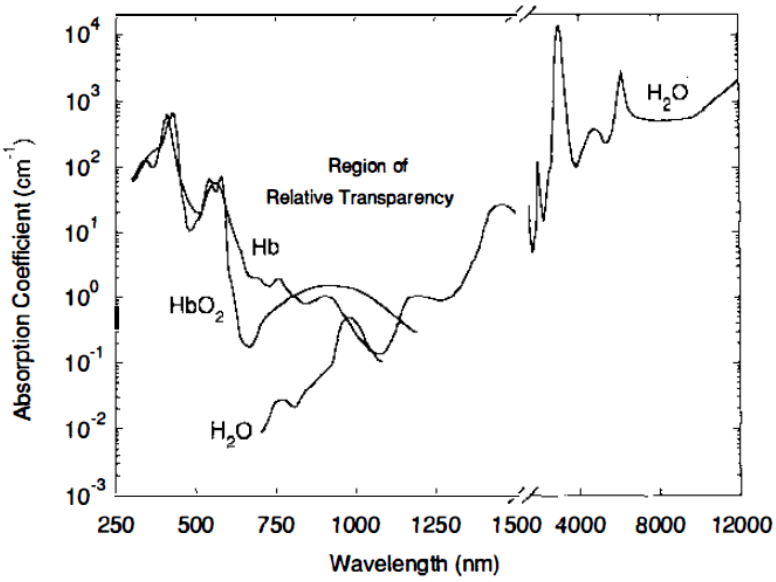


Figure 1.11: Graph illustrating the relative transparency of biological material.[63]

Biological chromophores such as haemoglobin and other abundant cytochromes ab-

sorb increasingly less light towards the NIR region of the spectrum.[64] On the other hand, water becomes less transparent to light further into the IR and so these opposing patterns of light absorption form a window of transparency: ~ 600-1250 nm as seen in Figure 1.11.[63] Therefore the probe should be optimised in order to absorb and emit radiation within this region, for maximum tissue penetration. UV radiation can cause damage to live tissue and so excitation in this region should be avoided.[65,66] Probes with the potential for two photon absorption can overcome this issue as longer wavelengths of light (close to the red/NIR region of the spectrum) are used for excitation.[67]

#### 1.3.2.3 Photophysical Properties: Stokes Shift and Lifetime

Large Stokes shifts are required to overcome the problems associated with self-quenching and interference from autofluorescence.[61] Endogenous cellular species typically have Stokes shifts in the order of tens of nm. If the applied dye has an appreciably different excitation and emission wavelength to the endogenous species, autofluorescence can be minimised through specific excitation of the dye and/or the use of various filters to block out autofluorescence. Figure 1.12 shows a basic schematic of a fluorescence microscope, including the location of excitation and emission filters.[68] If the applied dye has an appreciably longer lifetime compared to the endogenous species (lifetimes of typically <10 ns), then time gated imaging techniques can be employed to reduce/remove the autofluorescent signal. Time gating components can be placed before the detecor (Figure 1.12), to ensure significant time delay, before detection. The endogenous species will only fluoresce for a short time and once the excitation source is removed, the probe should continue to luminescence for a longer period[61,68] as illustrated in Figure 1.13.

Many conventional epifluorescence microscopes have filter cubes (Figure 1.12) from the UV to visible spectrum where the excitation and emission bands allowable for each filter is fairly narrow. This can be an issue in regards to the large Stokes shifts of many metal complexes as the excitation may require a filter cube in the UV region but emission will be far away in the green. Specialised filter cube systems can be employed to avoid this issue however they are not common and usually require specific manufacture or purchase.

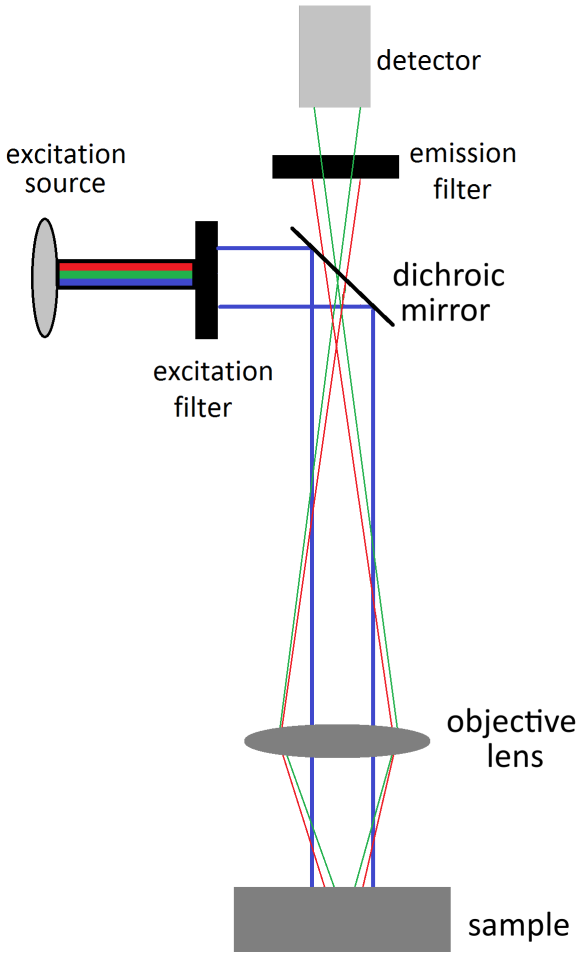


Figure 1.12: Basic schematic of a fluorescence microscope.

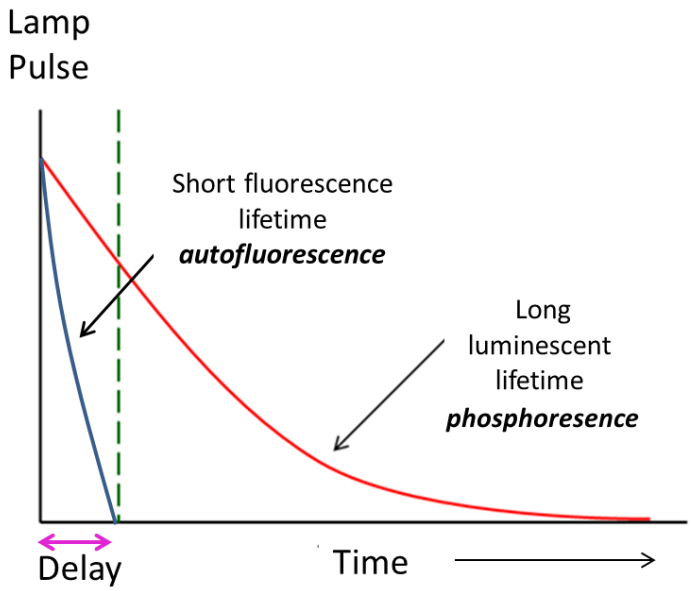


Figure 1.13: Schematic showing the advantage of time gated techniques in conjunction with phosphorescent probes.

Another option is to use laser excitation in confocal microscopy where emission can be detected across multiple channels at once allowing for the use of probes with large Stokes shifts.

It is not trivial to design a probe optimised in all of the areas listed above. Therefore it is important to consider all of these aspects in their design to ensure a reasonable balance between the physical, chemical and photophysical properties.

### 1.3.3 Advantages of Heavy Metal Complexes in Optical Imaging

Heavy metal complexes have the potential to exhibit the desirable photophysical and chemical properties discussed above, making them attractive candidates for biological imaging.[25] The $d^6$ metal complexes have become widely studied in this field but also $d^8$ platinum(II) and $d^{10}$ gold(I) complexes. Lanthanide complexes have also been studied in bioimaging applications.[69–73] The emergence of the application of $d^6$ metal complexes in optical imaging has occurred due to their highly favourable photophysical properties and coordination chemistry.[74] Heavy metal complexes generally exhibit large Stokes shifts, (up to hundreds of nm) and long luminescence lifetimes (hundreds of ns to ms) which can open up the opportunity to carry out time gated imaging techniques which are not possible with many commercially available organics.[25,68] In their low spin $d^6$ state, they are kinetically inert, which helps prevent photobleaching. This stability can also translate to a reduced toxicity. A problem associated with phosphorescent metal complexes (emission from the triplet state) is that they are prone to quenching by $^3O_2$. This reduces the luminescence intensity from the sample and also produces $^1O_2$ which can be harmful to the biological sample.[68,75] Another advantage of heavy metal complexes is that their synthesis can be more straight forward compared to organic molecules; it can be easier to change and modify ligands. There is also the opportunity for a range of ancillary ligands to be used with these metals which can be a way to alter their physical, chemical and photophysical properties.[25,68] There has been a surge in the number of publications and reviews surrounding the use of $d^6$ metal complexes as luminescent optical imaging agents, with a strong emphasis on tuning their chemical and photophysical properties.

## 1.4 Brief Review of Metal Complexes in Optical Imaging

Metal complexes are already routinely used in clinical applications of MRI, PET and SPECT, however, the use of luminescent $d^6$ metal complexes in optical imaging is still not well established. Research into their use as alternative optical imaging probes is expanding. A short overview covering the development of Ir(III), Ru(II) and Re(I) metal complexes in optical imaging is presented below. Evidence of the expanding field is noted in the wide variety of optical imaging applications investigated. Some studies focus on the metal complexes alone, relying on the properties of the molecule to exhibit localisation, whereas other research has looked at complexes conjugated to a biomolecule to confer uptake or specificity.[25] Confocal microscopy is the main technique used to evaluate the biological behaviour of these complexes. Some studies also employ two-photon absorption microscopy or time gated imaging.

### 1.4.1 Iridium

Ir(III) complexes of the form $Ir[(C\hat{}N)_2Ir(L\hat{}L)]$ are the most commonly studied type of iridium complexes in luminescent imaging applications; where C^N is a monoanionic cyclometallating ligand and L^L is a chelating neutral ligand, which combine to give an overall cationic complex.[61,62,68] The first report on the use of iridium complexes in luminescent cell imaging was in 2008[76] where two fluorinated Ir complexes were shown to stain the cytoplasm of HeLa cells. The complexes were also found to be non toxic to these cells. Yu's complexes, **50** and **51** (Figure 1.14) exhibited green and red

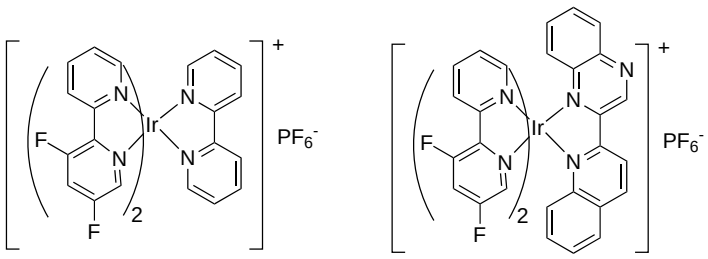


**50** **51**

Figure 1.14: Iridium complexes reported in 2008.

emission respectively.[76]

Although mostly cationic iridium species have been investigated, a recent study by Zhou *et al.*[77] has demonstrated that a series of neutral iridium carbene complexes stain the cytoplasm of cells without the need for extra functionalisation.

The first report using time-resolved emission imaging with iridium complexes in cells was in 2010 by Murphy *et al.*[78] The investigation showed the potential of Ir(III) complexes to be imaged without interference from autofluorescence. Time gated imaging was also used to discriminate emission of the Ir(III) from other dyes with shorter lifetimes. The complex studied is in the typical form for an Ir(III) probe, as seen in Figure 1.15.[78]

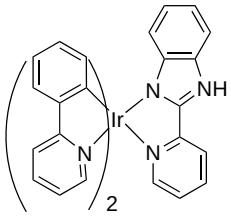


**52**

Figure 1.15: Iridium complex used in time gated cellular imaging.

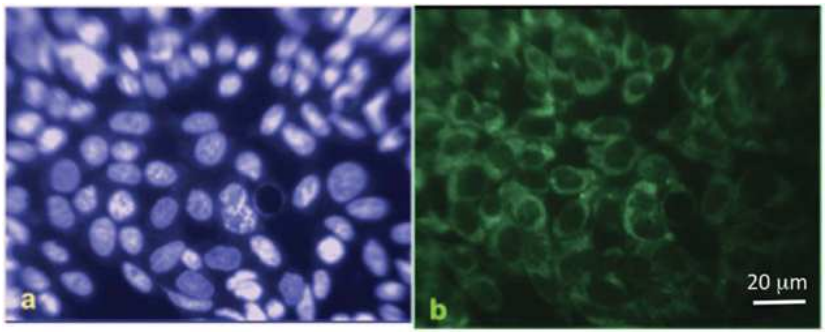


Figure 1.16: Fluorescence microscopy of CHO cells stained with Ir complex (**52**) and Hoechst using time gated imaging. (a) no delay between laser pulse and aquisition and (b) image recorded after 10 ns delay.

Figure 1.16 shows the incubation of CHO cells with **52** and Hoechst (an organic nuclear stain), from the study of Murphy *et al.*[78] Image *a* is flooded with the blue emission from the Hoechst, whereas image *b* taken 10 ns after the laser pulse, shows predominantly the green emission from **52**.

The extreme colour tunability of Ir(III) complexes was demonstrated in a recent publication by Zhang and co-workers who developed a cationic, NIR-emitting complex

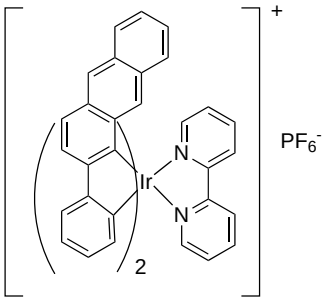


**53**

Figure 1.17: NIR emitting Iridium complex.

which stains the cytoplasm of living cells (Figure 1.17).[79] By modifying both the cyclometallating and diimine ligand from their basic formations, Zhang *et al.* was able to tune the emission properties of the complex, with **53** exhibiting a structured emission (typical of Ir complexes) at 698, 760 nm.[79] This emission wavelength is desirable as it is in the red/NIR region of the spectrum.

Iridium complexes have also been explored as phosphorescent sensors for biological ions. A report from You *et al.*[80] investigated the detection of a range of metal ions by introducing metal-chelating receptors onto the Ir(III) complexes. Figure 1.18 shows an example of a complex synthesised, demonstrating the ability to sense $Zn^{2+}$.

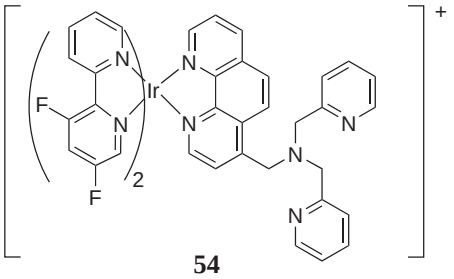


**54**

Figure 1.18: Iridium complex exhibiting increasesd emission intensity upon coordinatoin to Zinc ions.

The study was also extended to sense $Zn^{2+}$ in mammalian cells. Despite the success of their probes, You *et al.* raise the issue of $^1O_2$ generation in biological samples, leading to high cytotoxicity of the complex.

### 1.4.2 Ruthenium

The most common form that Ru(II) imaging agents take is based around the $[Ru(\mathbf{bpy})_n]^{2+}$ core with a total of three diimine ligands coordinated to the metal centre.[68] Two of these three ligands may be a simpler diimine unit such as bipyridine or phenanthroline and the third is often a substituted version conferring specific properties to the complex.[62] Ruthenium has been studied for applications as both imaging and sensing agents.[62] One of the most commonly known uses in biology, for these types of ruthenium complexes is the sensing of molecular oxygen.[81,82] This is done through monitoring the lifetime of the Ru complex as the luminescence notably decreases due to quenching from oxygen.[83–85] DNA detection is also well studied using Ru complexes containing extended diimine ligands such as dipyridophenazine and in these cases, the emission of the Ru complex increases upon binding to DNA.[86–89]

Biotinylation of complexes has been exploited as a common strategy to aid in cellular uptake[68] or for developing sensitive luminescent probes for detecting avidin (as biotin-avidin binding is known to be strong).[90] Lo *et al.*[91,92] have synthesised a series of Ru(II) amidodipyridoquinoxaline biotin complexes which show strong binding to avidin, for example **55** (Figure 1.19). Interestingly the emission intensity and lifetime of this complex (and others similar) is fairly weak under ambient conditions however upon binding to avidin, the photophysical output of the complex is enhanced. This study, along with others similar, show the potential for metal complexes to be used as sensing probes for avidin.[93,94]

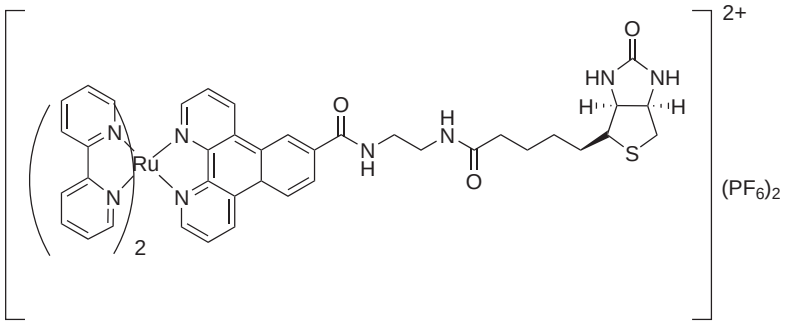


**55**

Figure 1.19: Luminescent ruthenium(II) amidodipyridoquinoxaline biotin complex.

### 1.4.3 Rhenium

Phosphorescent Rhenium(I) complexes for imaging are most commonly based around the *fac*-[Re(**diim**)$(CO)_3]^+$ core, where **diim** is usually a diimine ligand such as 1,10-phenathroline or 2,2'-bipyridine however, other ligands such as quinolines and *N*-heterocyclic carbenes have also been studied. The ancillary ligand can exist in its simplest form as a halogen (Cl, Br) but is commonly a pyridyl based ligand. A review of $d^6$ metal complexes in biological imaging was published in 2010 by Fernández-Moreira *et al.*[68] and at the time, there had only been six publications of luminescent Re(I) complexes in cellular imaging. The first report of rhenium complexes with an optical imaging focus was from Zubieta *et al.* in 2004. They looked at designing a pair of isostructural probes based around Re(I) and $^{99m}$Tc, to be used in radio- and luminescent imaging, to "bridge the gap" between *in vivo* and *in vitro* imaging.[95] These complexes were based around the Re(I) tricarbonyl core, utilising the quinoline ligands.

In 2007, a series of Re(I) complexes were synthesised and incubated with parasitic flagellate (*Spironucleus vortens).* This study was the fist report of Re(I) phosphorescent complexes incubated with a biological sample and imaged using microscopy.[96] The Re(I) complexes consisted of bipyridine and substituted phenanthroline ligands with a range of pyridyl ancillary ligands, for example **56** (Figure 1.20).[96] Confocal microscopy studies revealed that the complexes retained their fluorescence in biological systems. The conclusions of the study indicated that [Re(**diim**)$(CO)_3$(**L**)$]^+$ complexes may be viable probes for luminescent imaging. Interestingly, a follow up publication from the same group showed that derivatives of **56** exhibited mitochondrial accumulation in MCF-7 cells.[97]

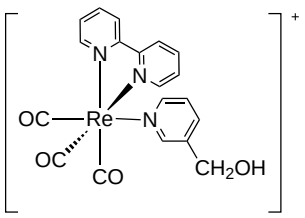


**56**

Figure 1.20: One of the first Re(I) bipyridine complexes used in luminescent cellular imaging studies.

Lo and co-workers[98] were the next group to publish studies of Re(I) complexes as luminescent cellular imaging agents. The complexes synthesised were chemically more elaborate than in the report of Amoroso *et al.* in 2007,[96] as they were conjugated to biotin and contained an isothiocyanate group, which was shown to react with amines to give the corresponding thiourea. An example of this product is complex **57** (Figure 1.21)[98], which was applied to a HeLa cell line and showed passive uptake into the cytoplasm of the cells (no co-localisation experiments were undertaken).

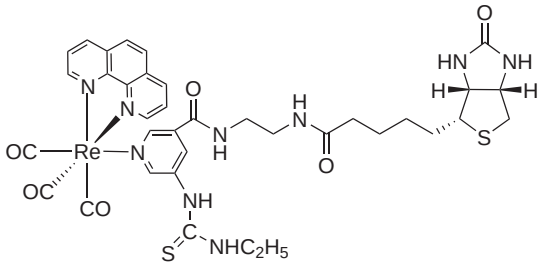


**57**

Figure 1.21: A Re(I) biotin isothiocyanate complex used in luminescent cellular imaging studies.

In 2009 Louie and co-workers published the synthesis of a rhenium complex with a functionalised ancillary pyridine ligand which demonstrated sensitivity to the environment.[99] For example, increased pH generally quenched the emission however in the presence of $Zn^{2+}$ and $Cd^{2+}$ ions, $\tau$ increased and emission was enhanced. Cellular imaging experiments with these complexes revealed cytoplasmic localisation. These were the first examples of rhenium metal complexes showing a photophysical response toward $Zn^{2+}$ and $Cd^{2+}$ ions (also *in vitro*). Despite this, the probe is not optimised and exhibits fairly poor sensitivity to the particular cations. The probe also exhibits toxicity greater than cisplatin. Nonetheless, the fundamental study showed the potential for further development of Re(I) complexes as biological sensors.

### 1.4.4 Summary

Ruthenium $d^6$ metal complexes have been more heavily investigated as specific $O_2$ sensors or for DNA intercalators in the context of biological imaging. There does not appear to be the same focus on Ru(II) complexes as stand alone optical probes, as there is with Ir(III) and Re(I). Many studies surrounding ruthenium complexes are

aimed towards applications as therapeutic anti-cancer agents.[100–102] Iridium $d^6$ metal complexes are photophysically desirable for imaging applications as their emission is highly tunable. Their cationic and relatively lipophilic nature makes their uptake into cells efficient. Localisation of Ir(III) complexes has generally been observed in the cytoplasm of cells with many reports observing non-specific uptake. The majority of rhenium complexes reported for applications in optical imaging have demonstrated the to be easily substituted, altering photophysical output but also cellular uptake. There have been examples of rhenium complexes localising in various cellular organelles, including membranes,[103] mitochondria[97,104] and also the nucleoli.[103] Despite the rise in publications, the field of metal complexes for optical imaging is still in its infancy and there is a lot to understand in relation to their behaviour in biological environments; including localisation, responsiveness and toxicity. Optical imaging is a technique with both clinical diagnostic and research applications and therefore the development of improved probes is vital for the advancement of the field

## 1.5 Rationale and Overview of the Project

Many complexes, specifically utilising Ir(III), Ru(II) and Re(I) have been developed with the intent for being used as optical imaging and/or sensing probes. Several of these complexes do in fact show many of the desired properties required for these applications. However, it is still not a trivial task to optimise all aspects of optical probes, including the chemical structure (for solubility and stability) and photophysical properties. Even more of a challenge is understanding how to control the uptake and localisation of the complexes in cells. Many of the attempts discussed above have been serendipitous, without complete knowledge of what particular structural properties govern uptake and specific localisation. Even minor changes to the chemical structure, charge or lipophilicity can greatly influence the localisation of the complexes in cells.[105]

To further expand the knowledge in this field, the study herein investigates a series of rhenium complexes, of the type *fac*-[Re(**diim**)$(CO)_3$(**L**)], where **diim** is either 1,10-phenanthroline (**phen**) or 2,2'-bipyridine (**bipy**) and **L** is one of a series of 5-substituted aryl tetrazoles, as shown in Figure 1.22.

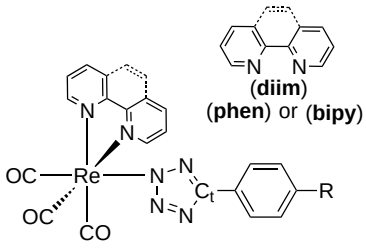


Figure 1.22: Re(I) tetrazolato complexes of the type; *fac*-[Re(**diim**)$(CO)_3$(**L**)].

### 1.5.1 Tetrazoles

Tetrazoles are a class of aromatic heterocyclic compounds, consisting of a five membered ring with four nitrogen atoms and one carbon atom. They are carboxylic acid isosteres[106] exhibiting a similar p$K_a$.[107] Tetrazoles are used in medicinal chemistry as a metabolically stable analogue of the carboxylic acid moiety.[108,109] They also demonstrate enhanced biological stability. Tetrazoles exist in two tautomeric forms, as illustrated in Scheme 1.1.

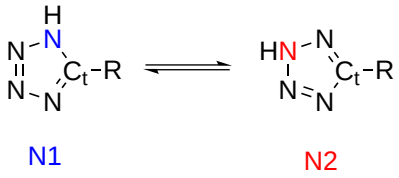


Scheme 1.1: The N1 and N2 tautomers of tetrazoles.

The first known study of the coordination of a tetrazolate anion to a rhenium metal centre was by Szczepura *et al.* in 2007 where 5-methyl-tetrazolate was coordinated to a hexanuclear $Re_6Se_8^{2+}$ cluster core.[110] The synthesis involved the addition of $N_3^-$ to a coordinated molecule of acetonitrile to produce the first example of a tetrazolato rhenium complex.

Studies have also shown the sensitivity of tetrazolate ligands coordinated to various metal centres including, iron[111,112] iridium[113] and ruthenium.[114] When these complexes undergo reactions with electrophiles structural and/or photophysical changes are observed. Despite the use of tetrazolato ligands in a range of coordination complexes, up until 2014, there had been no reports of rhenium tetrazolato complexes in biological imaging.[115] The sensitivity of tetrazoles is exploited herein, as part of the fundamental research into the *fac*-[Re(**diim**)$(CO)_3$(**L**)], to not only be applied in optical imaging but also as responsive probes (sensing agents).

### 1.5.2 Structure Property Relationship

Up until 2010 the number of reports of Re(I) complexes in optical imaging were minimal and it is still the least investigated out of the metal $d^6$ complexes mentioned above. Rhenium complexes have also shown the ability to respond to their environment to produce a detectable photophysical repose.[99,116–120] The aim of this multidisciplinary research is to increase the understanding of how small changes to the structure of *fac*-[Re(**diim**)$(CO)_3$(**L**)] complexes affect their chemical and photophysical properties as well as uptake and localisation in a biological environment. By making small structural modifications to the core *fac*-[Re(**diim**)$(CO)_3$(**L**)] complex, a structure-property relationship can be established. As part of this, the sensing potential of these complexes is explored in a fundamental manner. Figure 1.23 provides an overview of the types of structural modifications made to the Re(I) tetrazolato complexes throughout this study.

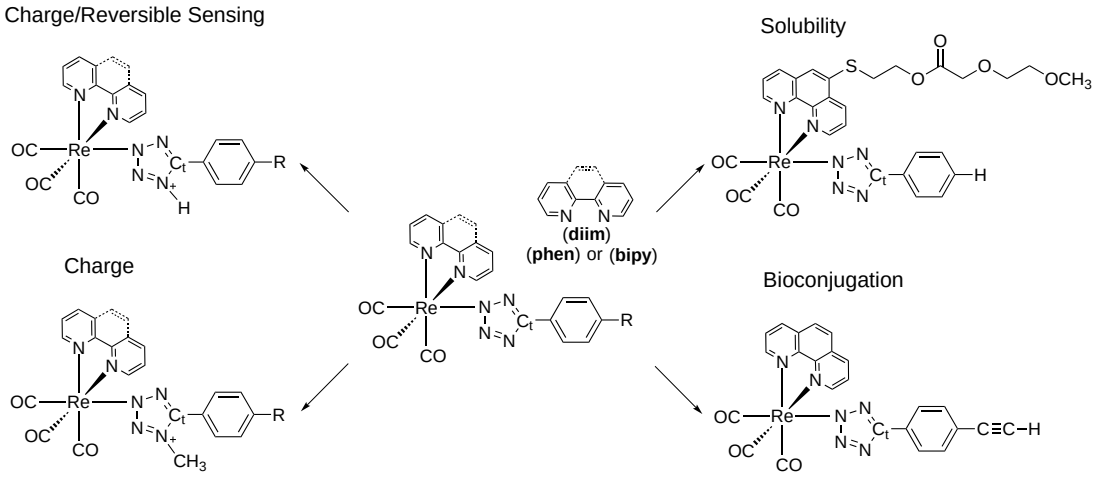


Figure 1.23: Structural modifications to Re(I) complexes.

#### 1.5.2.1 Analysis

Various techniques are employed to gain an insight into the structure-property relationship of the *fac*-[Re(**diim**)$(CO)_3$(**L**)] complexes. Infrared spectroscopy and NMR are used to gain a basic understanding of structure. These techniques will also be used to indirectly determine the change/movement of electron density on the complexes upon structural modification. This also assists the interpretation of photophysical measurements. X-ray crystallography is also used in the structural identification of the Re(I)

complexes in the solid state. X-ray crystal analyses were done in collaboration with Dr. Brian Skelton from the University of Western Australia and Associate Professor Stefano Zacchini from the University of Bologna. Photophysical characterisation was carried out to determine how the excitation and emission energies, as well as $\phi$ and $\tau$ of the complexes are altered through changes to structure and overall charge.

To further interpret the photophysical measurements of the Re(I) complexes, time-dependent density functional theory (TD-DFT) was employed. DFT is a theory which represent electrons as a density "cloud" and is based on optimisation of this electron density. Earlier molecular orbital theories (such as the Hartree-Fock method) are based on the optimisation of wavefunctions.[121,122] TD-DFT is an extension of DFT and is necessary to use when external, time dependent potentials are taken into consideration.[123] This is of particular relevance when looking at the excitation of molecules with light. TD-DFT was used to simulate the absorption spectra whereas DFT was used to determine the minimised geometry for the complexes in the ground state and to produce the orbital diagrams. The calculations were all done in collaboration with Mr. Philip Wright and Dr. Paolo Raiteri from Curtin University.

Confocal imaging experiments were conducted to assess the uptake, localisation and toxicity of a range of the synthesised rhenium complexes.

The combination of each technique described above was used to recognise how structural changes to the complexes affect the chemical and photophysical properties, as well as their behaviour in a biological environment.

# Chapter 2

# Synthesis, Structural and Photophysical Investigation of Neutral Rhenium Tetrazolato Complexes

## 2.1 Abstract

The synthesis, structural and photophysical properties of a series of *fac*-[Re(**diim**)$(CO)_3$(**L**)] complexes are reported, where **diim** is either 1,10-phenanthroline (**phen**) or 2,2'-bipyridine (**bipy**) and **L** is one of a series of 5-substituted aryl tetrazolates. NMR and X-ray crystallography revealed that all of the tetrazolato ligands coordinated to the Re centre through the N2 atom. The absorption profiles indicated the presence of high energy $\pi - \pi^*$ transitions and lower energy transitions which were assigned to admixtures of metal-to-ligand charge transfer (MLCT) and ligand-to-ligand charge transfer (LLCT) bands. The mixed nature of these bands lends their assignment to a metal-ligand-to-ligand charge transfer (MLLCT), which was also supported by TD-DFT. The photophysical output of the **phen** complexes were superior to that of the **bipy** analogues in terms of $\tau$ and $\phi$. The electron withdrawing *para* substituents on the phenyltetrazolato ligand allowed fine tuning of the complexes photophysical properties, including their $\tau$ and $\phi$, and to a lesser extent the maximum emission wavelengths.

## 2.2 Introduction

Wrighton and Morse first studied the luminescent properties of *fac*-[Re(**phen**)$(CO)_3$(Cl)] in 1974 and identified that the observed emission was from a $^3$MLCT state and was therefore classified as phosphorescence.[124] Since then, a number of studies have been published investigating the interesting photophysical and photochemical properties demonstrated by complexes based around the *fac*-[Re(**diim**)$(CO)_3]^+$ core.[49,125–147] In recent years the applications of rhenium complexes have expanded to organic light emitting devices (OLEDs)[148–150] and photocatalysis.[151–153] More recently, their investigation as optical imaging and/or sensing agents has increased,[68,95,103,105,154–158] due to their highly favourable photophysical properties in comparison to the commonly used fluorescent probes. Many studies on rhenium complexes as optical imaging agents have investigated them as a simple molecules[68,95,103,154] or as extended systems conjugated to biologically relevant compounds[157,159–161] (to confer uptake and specificity).

Important to the development of metal complexes as optical imaging agents is the fundamental understanding of how small structural changes to the molecule will effect the chemical, photophysical and biological properties. The specific properties include stability and solubility, $\lambda_{ex}$, $\lambda_{em}$, $\phi$ and $\tau$ as well uptake, localisation and toxicity of the complexes in a biological environment. Development of optical imaging probes/sensors is a multidisciplinary area of research requiring extensive fundamental studies to completely understand each aspect of the potential probe. Optimisation of the chemical, photophysical and biological properties is not a trivial task. Therefore, an increased understanding of what structural changes govern different properties, is vital for progression of the field.

Previous research has shown the great potential for rhenium complexes to be developed either as stand alone imaging probes or sensors as well as the ability to be bioconjugated to confer specificity. The work described in this chapter is based on the design, synthesis and photophysical investigation of a series of neutral *fac*-[Re(**diim**)$(CO)_3$(**L**)] complexes where the diimine ligand is either 1,10-phenanthroline (**phen**) or 2,2'-bipyridine (**bipy**) and **L** is one of a series of *para* functionalised 5-aryltetrazolates. These ancillary ligands (**L**) are 5-phenyl-1H-tetrazole (**Tph**H), 4-(1H-tetrazol-5-yl)-

benzaldehyde (**Tbz**H), Methyl-4-(1H-tetrazol-5-yl)-benzoate (**Tmeb**H), 4-(1H-tetrazol-5-yl)cyanobenzene (**Tcya**H), 5-(4-iodophenyl)-1H-tetrazole (**TIod**H) and 5-(4-bromophenyl)-1H-tetrazole (**TBr**H). Scheme 2.1 shows the Re(I) complexes described in this chapter and their associated abbreviations.

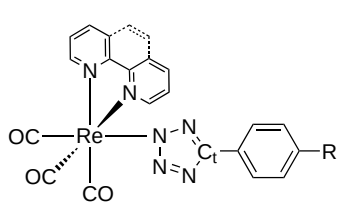


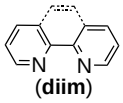


(**diim**)

(**phen**) or (**bipy**)

| R = | Complex = |
|---|---|
| H | *fac*-[Re(**diim**)(CO)$_3$(**Tph**)] |
| CHO | *fac*-[Re(**diim**)(CO)$_3$(**Tbz**)] |
| $COOCH_3$ | *fac*-[Re(**diim**)(CO)$_3$(**Tme**)] |
| CN | *fac*-[Re(**diim**)(CO)$_3$(**Tcya**)] |
| I | *fac*-[Re(**diim**)(CO)$_3$(**TIod**)] |
| Br | *fac*-[Re(**diim**)(CO)$_3$(**TBr**)] |

Scheme 2.1: The neutral Re(I) complexes reported in Chapter Two and their abbreviations.

Positively charged rhenium analogues typically exhibit blue shifted emissions and superior photophysical properties ($\tau$ and $\phi$), according to the energy gap law.[47,48,162] The tetrazole ancillary ligand will form an overall neutral complex once coordinated to rhenium but is used here for its biological compatibility.[107] Moreover, tetrazole ligands are generally strong $\sigma$ donors but also $\pi$ acceptors,[111] which should aid in increasing the HOMO-LUMO energy gap of these Re(I) complexes and therefore their luminescent output compared to those where the ancillary ligand is a halogen or other $\pi$ donor ligand. Complexes containing a proton as the *para* substituent (Scheme 2.1) will act as the fundamental probes in establishing a structure-property relationship between the complexes. It is necessary to understand how changing to the nature of the ancillary ligand (various *para* functional groups) or diimine ligand (**phen** versus **bipy**) will affect the properties of the Re(I) complexes. The *para* substituent on the tetrazole ligands will not only aid in determining a structure-property relationship but can act as a point of conjugation to biomolecules.

## 2.3 Results and Discussion

### 2.3.1 Synthesis and Spectroscopic Characterisation of the 5-aryl-1H-tetrazoles

The synthesis of the 5-aryl-1H-tetrazoles was carried out using a relatively safe, high yielding and straightforward procedure developed by Koguro *et al.*[109] as outlined in Scheme 2.2.

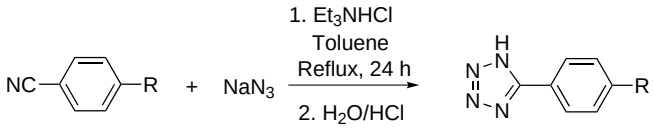


Scheme 2.2: Synthesis of the 5-aryl-1H-tetrazoles.

Triethylammoniumchloride is formed *in situ* and once the azide is added, the intermediate [$Et_3N$•$HN_3$], is formed. This is only approximately 1% soluble in toluene but is polarised as $[Et_3NH]^{\delta+}[N_3]^{\delta-}$, which is not solvated in toluene. It therefore has increased reactivity towards the nitrile, compared to using solvents which can solvate this intermediate (for example dimethylformamide).[109] $[Et_3NH]^{\delta+}[N_3]^{\delta-}$ reacts with the triple bond of the nitrile to produce the triethylammonium salt of the final product via a 1,3-dipolar cycloaddition. There is still debate in regards to the exact mechanistic pathway for these types of reactions. One is the concerted cycloaddition pathway and the other is a two-step mechanism where the azide first acts as a nucleophile and reacts with the nitrile, followed by ring closure.[163] A study by Himo *et al.* indicates that these two mechanistic pathways are essentially the same. The transition state for the concerted 1,3-dipolar cycloaddition is the same as the ring closing state for the two step pathway.[164]

The final tetrazole product was isolated as a white to off-white solid through the addition of acid, precipitating out the neutral tetrazole ligand. Melting points were attempted however in all cases decomposition was observed instead due to the high percentage of nitrogen atoms. The decomposition points for the tetrazoles synthesised vary from literature values, up to 16 °C, however difficulties in obtaining consistent data have been previously reported.[163] The spectroscopic characterisation of the

products agrees with the proposed structures. The yields of the various tetrazoles are reported in Table 2.3.1.

Table 2.3.1: Yields obtained for each of the prepared aryl tetrazoles.

| Tetrazole | R | Yield (%) |
|---|---|---|
| 5-phenyl-1H-tetrazole (**Tph**H, **1**) | H | 50 |
| 4-(1H-tetrazol-5-yl)-benzaldehyde (**Tbz**H, **2**) | CHO | 89 |
| methyl 4-(1H-tetrazol-5-yl)-benzoate (**Tme**H, **3**) | $COOCH_3$ | 59 |
| 4-(1H-tetrazol-5-yl)cyanobenzene ( **Tcya**H, **4**) | CN | ~ 43 |
| 5-(4-bromophenyl)-1H-tetrazole (**TBr**H, **6**) | Br | 63 |
| 5-(4-iodophenyl)-1H-tetrazole (**TIod**H, **5**) | I | 57 |

The spread in the yields can be attributed to the different *para* functional groups on the organonitrile. The reactivity of the nitrile is increased when the -R group is electron withdrawing, as it polarises the nitrile making the carbon atom more susceptible to nucleophilic addition. The prepared tetrazole species were further characterised using IR and NMR.

The main IR bands indicative of tetrazole formation are the aromatic C=N and NH stretches, observed at approximately 1600 and 3400 $cm^{-1}$ respectively. These peaks are not observed in the organonitrile starting material and their presence in the products supports formation of the tetrazole ring. The disappearance of the sharp nitrile band (C≡N) around 2260-2240 $cm^{-1}$ also supports consumption of the starting material.

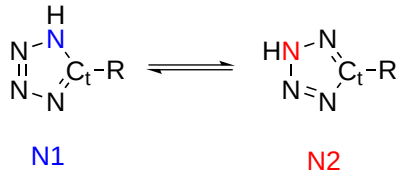


Scheme 2.3: The N1 and N2 tautomers of tetrazoles.

Tetrazoles exist in two tautomeric forms, with the tetrazolic proton residing on either the N1 or N2 atom (Scheme 2.3). NMR studies by Butler *et al*. on analogous N1 and N2 methylated 5-aryl tetrazoles has determined that chemical shifts for the tetrazolic carbon ($C_t$) ranging from 156-152 ppm indicate the predominant presence of the N1 tautomer; whereas values in the range of 165-162 ppm correspond to the N2

tautomer.[165–167] In studies looking at 5-substituted phenyl tetrazoles, Butler also proposed that the $C_t$ can be used to probe the extent of interannular conjugation between the tetrazole and phenyl rings. The tetrazole ring can exhibit an inductive withdrawal effect (-I) on the phenyl ring as shown in Scheme 2.4 a. There is also the possibility for the tetrazole ring to mesomerically withdraw (-M) or donate (+M) electron density, as shown in Scheme 2.4. The effect that the tetrazole ring exhibits greatly depends on the substituents on the phenyl ring. The higher resonances observed for the $C_t$ in the N2 tautomer supports an increase in the interannular conjugation between the aryl and tetrazole rings as there is an increase in +M from the tetrazole to the phenyl ring (Scheme 2.4 b-c). This requires the 2p orbitals of the tetrazole and phenyl rings to be parallel (ie: the two rings must be coplanar).

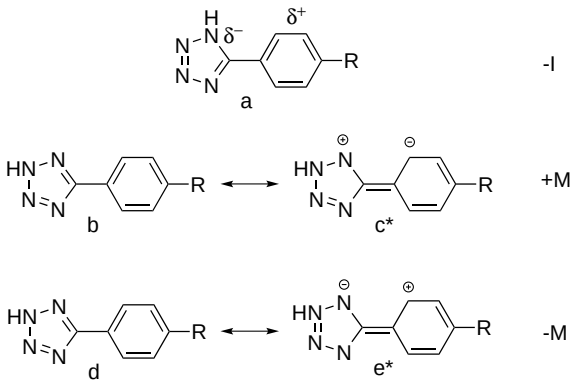


Scheme 2.4: Inductive withdrawal (-I), mesomeric donation (+M) and mesomeric withdrawal (-M) effects of the tetrazole ring. *c and e are not the only resonance formulae that are possible for +M and -M respectively.

Resonance formulae of the c and e type in Scheme 2.4 suggest that the two rings are coplanar in the N2 tautomer, whereas the shielded $C_t$ of the N1 tautomer indicates a more twisted ring system.[165–167] The steric hindrance present in the N1 tautomer causes out of plane rotation of the rings (Scheme 2.5).[166] The twisted ring configuration reduces interannular conjugation and the intensity of possible +M donation, resulting in the predominance of -I (Scheme 2.4).

In DMSO-$d_6$, all of the prepared aryl tetrazoles (**1**, **2**, **3**, **4**, **5** and **6**) exhibit $C_t$ signals around 155 ppm. The NMR values of the tetrazole compounds are further discussed in section 2.3.2.2 and shown in Table 2.3.3. According to the studies of Butler, the $C_t$ value of 155 ppm observed here, indicates the presence of the N1 tautomer. In fact, the N1 tautomer is more polar and is therefore favoured in polar DMSO.[167]

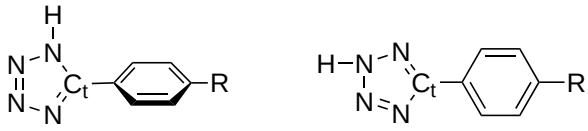


N1: Twisted N2: Planar

Scheme 2.5: Twisted and planar structures of the N1 and N2 substituted tetrazoles.

### 2.3.2 Synthesis and Spectroscopic Characterisation of the Neutral Re(I) complexes

The neutral Re(I) complexes of the form *fac*-[Re(**diim**)$(CO)_3$(**L**)] were synthesised using a range of methods, outlined below. Commercially available [Re$(CO)_5$(X)] (where X is Cl or Br) was heated at reflux with **phen** or **bipy** in toluene producing *fac*-[Re(**diim**)$(CO)_3$(X)] in high yields, according to previously published methods.[168,169] Complexes *fac*-[Re(**phen**)$(CO)_3$(**Tph**)](**11**), *fac*-[Re(**bipy**)$(CO)_3$(**Tph**)] (**12**), *fac*-[Re(**phen**)$(CO)_3$(**Tbz**)] (**13**), *fac*-[Re(**bipy**)$(CO)_3$(**Tbz**)] (**14**), *fac*-[Re(**phen**)$(CO)_3$(**Tcya**)] (**17**), *fac*-[Re(**bipy**)$(CO)_3$(**Tcya**)] (**18**), *fac*-[Re(**phen**)$(CO)_3$(**TBr**)] (**19**) and *fac*-[Re(**phen**)$(CO)_3$(**TIod**)] (**20**) were synthesised according to the method outlined in Scheme 2.6. To a suspension of *fac*-[Re(**diim**)$(CO)_3$(X)] in ethanol/water (3:1 v/v), the corresponding tetrazole ligand with triethylamine was added. After heating at reflux for 20 hours, the final complex was filtered off and did not require further purification. The exception was **17**, purified by column chromatography.

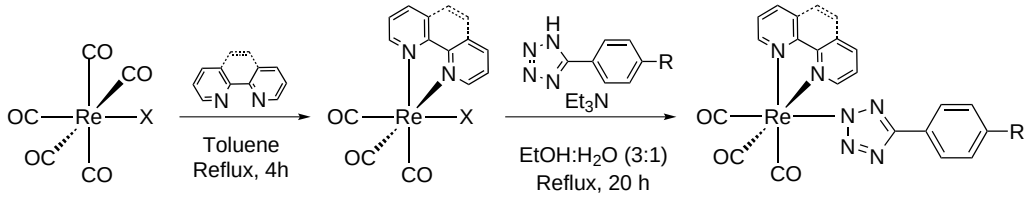


Scheme 2.6: Synthesis of the neutral rhenium tetrazolato complexes using an ethanol/water solvent system, where X is Cl or Br.

This method does not rely on first forming a solvato[170] or triflato[171–173] rhenium complex and subsequently the halogen ligand is directly substituted by the deprotonated tetrazole alone. Any unreacted starting material, *fac*-[Re(**diim**)$(CO)_3$(X)], remains dissolved in the ethanol/water (3:1 v/v) solvent system and the product forming precipitates out for a convenient isolation. In some cases, if there was no solid present in the reaction upon cooling, some of the ethanol was evaporated off until the first

presence of solid was observed. At this point, no more solvent was removed and the reaction was placed in an ice bath to encourage precipitation.

The synthesis of *fac*-[Re(**bipy**)$(CO)_3$(**Tme**)] (**16**) was carried out using a previously published method, as outlined in Scheme 2.7.[154,170] $AgBF_4$ and *fac*-[Re(**bipy**)$(CO)_3$(Cl)] (**8**) were heated at reflux in acetonitrile to form the acetonitrile solvate, *fac*-[Re(**bipy**)$(CO)_3(NCCH_3)]^+$ (**43**). **43** was not isolated but filtered off from a white precipitate (AgCl) and immediately used. Methyl-4-(1H-tetrazol-5-yl)-benzoate (**3**) was deprotonated using triethylamine, added to the yellow solution of **43** and heated at reflux for 60 hours. The complex was purified by reprecipitation with acetonitrile/dichloromethane (1:4) and excess diethyl ether.

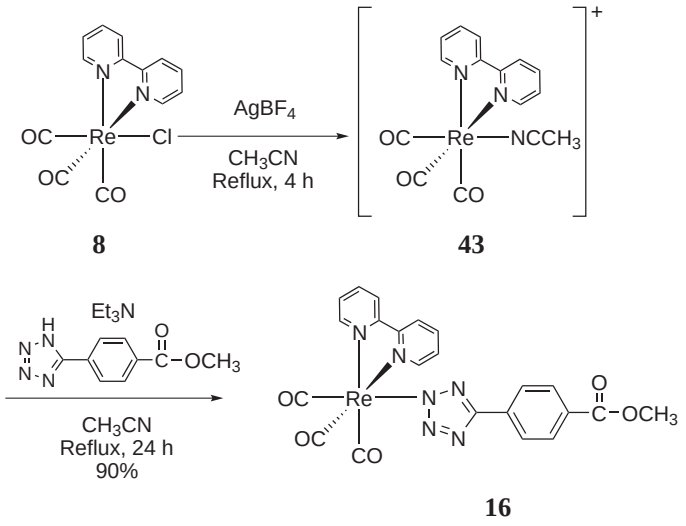


Scheme 2.7: Synthesis of **16** via halogen abstraction.

The synthesis of *fac*-[Re(**phen**)$(CO)_3$(**Tme**)] (**15**) was carried out according to a previously published method.[174] *fac*-[Re(**phen**)$(CO)_3$(Cl)] (**7**) and the methyl-4-(1H-tetrazol-5-yl)-benzoate (**3**) (deprotonated using triethylamine) were heated at reflux in acetonitrile for 60 hours. The final complex was purified via column chromatography on neutral alumina using ethyl acetate (100%) as the eluent (second product, yellow).

Out of all the methods used, the one employing ethanol/water as the solvent system was the most straightforward. Generally no further purification was required and good yields were achieved in a 24 hour period, which is shorter than the time required for the other methods (48 h).[174] The starting material was not recovered however the high overall yields (63-82 %) were satisfactory. This method was trialled with both *fac*-[Re(**phen**)$(CO)_3$(Cl)] (**7**) and *fac*-[Re(**phen**)$(CO)_3$(Br)] (**9**) however the reaction

seemed to proceed better with the bromo analogue. This could be ascribed to the more labile nature of Br over Cl, making it easier to be displaced by the tetrazolate anion.

The silver abstraction method, employing acetonitrile as the solvent generally produced a mixture of starting and final complexes.[174] Column chromatography was used to purify the product and recover the starting material. The silver abstraction method produced high yields, unless a column was employed for purification. The yield of *fac*-[Re(**bipy**)$(CO)_3$(**Tme**)] (**16**) was 90 % and purification was achieved through a simple reprecipitation. In general, whenever a column was used for purification, overall yields were significantly lower. However, the advantage of purification via column chromatography was the recovery of the starting material, *fac*-[Re(**diim**)$(CO)_3$(X)].

#### 2.3.2.1 Infrared Spectroscopy Analysis

The Re(I) diimine complexes were all isolated as the *facial* isomers (*fac*-[Re(**diim**)$(CO)_3$(X)]), confirmed by IR (and X-ray crystallography). The *meridional* isomer is not formed due to the *trans* effect of the CO ligands.[175] Once the diimine has been coordinated, no further substitution of carbonyl ligands will occur. This is based on the stability of the complex formed and the increased electron density on the rhenium centre strengthening the remaining rhenium-carbonyl bonds via backbonding (Figure 2.1). The CO ligands in the tetrazolato complexes were also confirmed to be in a *facial* arrangement.

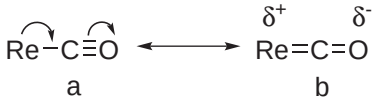


Figure 2.1: $\pi$ backbonding of rhenium to a carbonyl ligand.

IR was used to probe the progress of reactions from the halogen precursors, *fac*-[Re(**diim**)$(CO)_3$(X)], to the formation of the rhenium tetrazolato complexes. Table 2.3.2 shows the changes to the stretching frequencies of the intense carbonyl bands in the complexes. Free carbon monoxide has a bond order of three and a stretching frequency of approximately 2143 $cm^{-1}$.[176] Conversely, when coordinated to a metal centre, the stretching frequency is reduced by an amount that depends on the extent to which the metal donates electron density into the anti-bonding orbitals of the carbonyl ligand.[177] The CO ligand is a weak $\sigma$ donor and good $\pi$ acceptor ligand. The $\sigma$ donation occurs

through the $\sigma$ orbital on the carbon of carbon monoxide (HOMO) which contains an electron pair. This weakly donates electron density to the rhenium metal centre forming the sigma bond. Carbon monoxide also has two empty $\pi^*$ orbitals, predominantly localised on the carbon which will accept electron density from the rhenium metal centre (LUMO). The combined effect is illustrated in Figure 2.2.

Table 2.3.2: CO stretching frequency values ($cm^{-1}$) of the prepared neutral rhenium complexes.

| CO stretching frequency ($cm^{-1}$)[a] | A´(1) | A´(2) | A´´ |
|---|---|---|---|
| *fac*-[Re(**phen**)$(CO)_3$(Cl)] (**7**) | 2014 | 1923 | 1885 |
| *fac*-[Re(**bipy**)$(CO)_3$(Cl)] (**8**) | 2013 | 1891 | 1872 |
| *fac*-[Re(**phen**)$(CO)_3$(Br)] (**9**) | 2015 | 1925 | 1882 |
| *fac*-[Re(**bipy**)$(CO)_3$(Br)] (**10**) | 2011 | 1901 | 1865 |
| *fac*-[Re(**phen**)$(CO)_3(NCCH_3)][BF_4]$ | 2040 | 1938 | |
| *fac*-[Re(**bipy**)$(CO)_3(NCCH_3)][BF_4]$[b] | 2031 | 1909 | |
| *fac*-[Re(**phen**)$(CO)_3$(**Tph**)] (**11**) | 2019 | 1909 | 1881 |
| *fac*-[Re(**bipy**)$(CO)_3$(**Tph**)] (**12**) | 2018 | 1893 | |
| *fac*-[Re(**phen**)$(CO)_3$(**Tbz**)] (**13**) | 2020 | 1916 | 1892 |
| *fac*-[Re(**bipy**)$(CO)_3$(**Tbz**)] (**14**) | 2021 | 1885 | |
| *fac*-[Re(**phen**)$(CO)_3$(**Tme**)] (**15**) | 2020 | 1912 | 1887 |
| *fac*-[Re(**bipy**)$(CO)_3$(**Tme**)] (**16**) | 2020 | 1902 | |
| *fac*-[Re(**phen**)$(CO)_3$(**Tcya**)] (**17**) | 2017 | 1912 | 1896 |
| *fac*-[Re(**bipy**)$(CO)_3$(**Tcya**)] (**18**) | 2018 | 1923 | 1899 |
| *fac*-[Re(**phen**)$(CO)_3$(**TIod**)] (**20**) | 2023 | 1908 | |
| *fac*-[Re(**phen**)$(CO)_3$(**TBr**)] (**19**) | 2025 | 1913 | |

[a]; solid state FT-IR measurements, [b]; Previously published data obtained from an acetonitrile solution.[178]

Rhenium complexes of the formula *fac*-[Re(**diim**)$(CO)_3$(**L**)] exhibit a $C_s$ symmetry and therefore three separate CO bands are expected: i) A´(1), totally symmetric in phase stretching, ii) A´(2), totally symmetric out of phase stretching and iii) A´´, asymmetric stretching of the equatorial carbonyl ligands. The relative energies of these bands were assigned based on previous reports.[179] In the starting halogen complexes

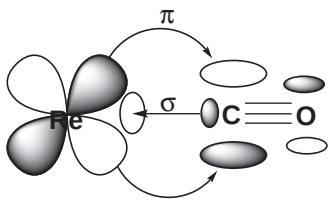


Figure 2.2: $\sigma$ and $\pi$ interactions of the CO ligand with rhenium.

*fac*-[Re(**diim**)$(CO)_3$(X)] (**7**, **8**, **9**, **10**) the A´(1) stretch is found between 2011-2015 $cm^{-1}$. In some instances, the A´(2) and the A´´ CO bands can collapse to form one broader peak, which has been previously reported.[178] Upon coordination of the tetrazolato ligand, the A´(1) stretching frequency increases by approximately 10 $cm^{-1}$. This can be ascribed to the increase in $\pi$ accepting abilities of the tetrazolato ligands, compared to the chloro or bromo. Strong $\pi$ donation of the ancillary ligand favours resonance structure "b" in Figure 2.1. This explains why the Re(I) complex exhibits lower CO stretching frequencies when the ancillary ligand is the halogen (ie: the bond order of the CO has been reduced, lowering the force constant). In the tetrazolato complexes, the reduction of electron density on the rhenium centre translates to a decreased backbonding from the rhenium to the CO ligands, ie: "b" in Figure 2.1 is less favoured. The intermediate products (*fac*-[Re(**diim**)$(CO)_3(NCCH_3)]^+$) formed *in situ* as part of the silver abstraction method, have the highest CO stretching frequencies of all complexes synthesised, Table 2.3.2. This is due to the even greater reduction in electron density on the rhenium centre as the complex has an overall positive charge, reducing the amount of backbonding to the CO ligands. A higher stretching frequency is therefore observed as the bond order remains closer to that of a triple bond.

Studies by Palazzi *et al*. indicate that aryl tetrazolato ligands coordinated to $[FeCp(CO)_2]^+$ fragments show fairly strong $\pi$ accepting character.[108,111] In contrast, the strength of the rhenium back bonding onto the tetrazole seems to be much weaker in the prepared rhenium complexes. This is noted in the IR by the relatively small increase in the CO stretching frequencies upon coordination of the tetrazole ligand. One possible explanation to this could be that there is a less favourable overlap between the diffuse 5d rhenium orbitals and the 2p orbitals from the tetrazolic nitrogen. This is in comparison to the more favourable overlap between the 3d and 2p orbitals of the iron and nitrogen, respectively.

### 2.3.2.2 NMR Characterisation

$^{1}H$ and $^{13}C$ NMR studies have been carried out on all of the rhenium tetrazolato complexes and the spectra match with the proposed structures. 2D HMBC experiments were used to determine the assignment of the $H_{ortho}$ and $H_{meta}$ protons on the aryl tetrazolato ligand (see Scheme 2.8 for the NMR referencing).

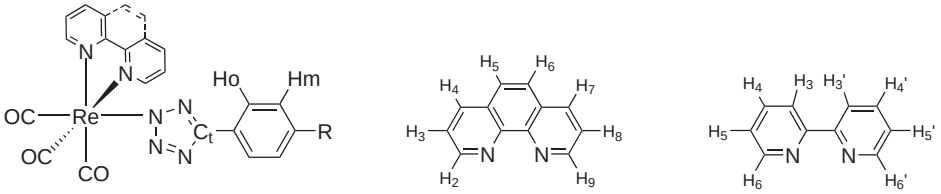


Scheme 2.8: NMR referencing layout.

HMBC shows cross peaks between protons and carbons that are two or three bonds away (in some cases, up to five bonds away). One bond cross peaks are not shown and this is what HSQC experiments are utilised for. HSQC shows the cross peak of a carbon and directly bonded hydrogen. HMBC experiments were used herein to identify the $H_{ortho}$, which forms a cross signal with the $C_t$ resonance (in both the ligand and Re(I) complexes). Where the *para* substituent on the tetrazolato ligand contains a carbon, HMBC was used to identify the $H_{meta}$. The HMBC spectra of *fac*-[Re(**phen**)$(CO)_3$(**Tbz**)] (**13**) in DMSO-$d_6$ is shown in Figure 2.3. This representative example illustrates the cross sections of the signals used to verify the relative positions of the $H_{ortho}$ and $H_{meta}$ resonances.

NMR was not only useful for structure determination but was also used to assess the structure property relationships of these complexes. The relative positions of the $C_t$, $H_{ortho}$ and $H_{meta}$ significantly change once the tetrazole ligand is coordinated to the rhenium centre (Table 2.3.3).

In all of the 5-substituted aryl tetrazole ligands alone, the signal of the $H_{ortho}$ is always more downfield with respect to the $H_{meta}$, except in 5-(4-iodophenyl)-1H-tetrazole (**5**) where the situation is reversed. Upon coordination to the rhenium metal centre, the $H_{ortho}$ and $H_{meta}$ resonances become more shielded.

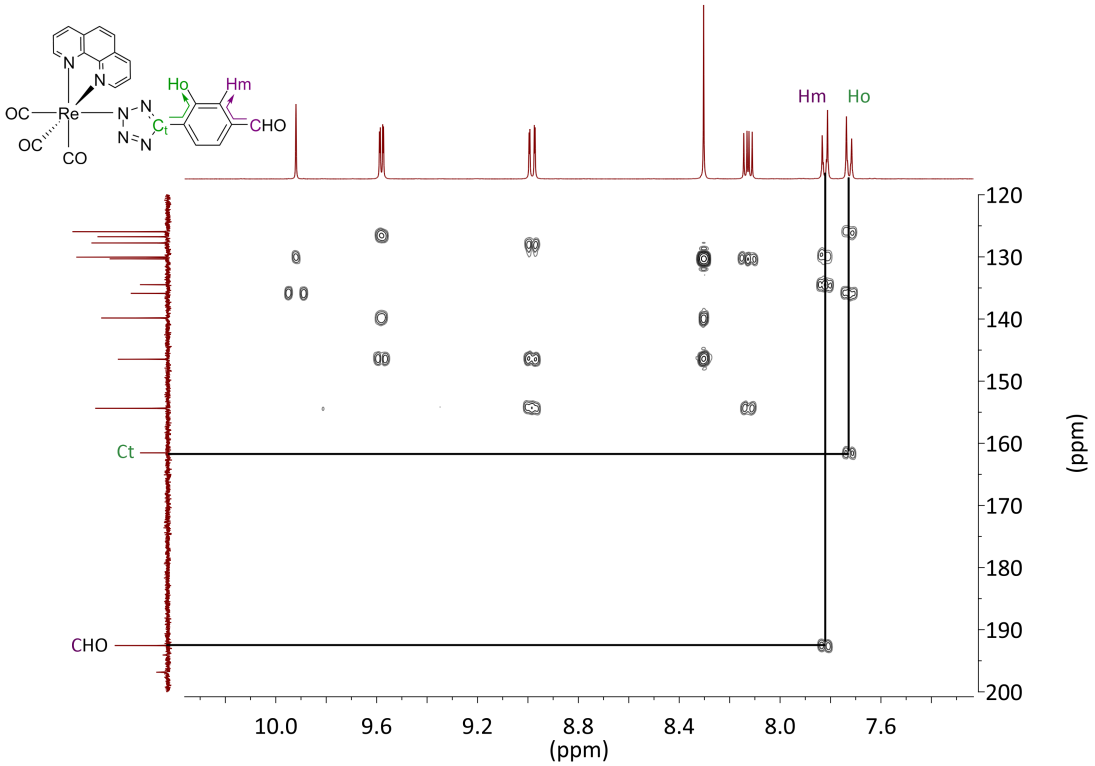


Figure 2.3: HMBC spectrum of *fac*-[Re(**phen**)$(CO)_3$(**Tbz**)] (**13**) in DMSO-$d_6$.

Table 2.3.3: NMR chemical shift data of the $H_o$, $H_m$ and $C_t$ for the tetrazole ligand before and after complexation.

| Rhenium complex (δ, ppm, Acetone-$d_6$) | | | | Corresponding aryl tetrazole (δ, ppm, DMSO-$d_6$) | | |
|---|---|---|---|---|---|---|
| R | $H_o$ | $H_m$ | $C_t$ | $H_o$ | $H_m$ | $C_t$ |
| -H (**11**) | 7.63 | 7.22−7.20[a,b] | 163.4 | 8.05-8.03[a] | 7.61-7.58[a,b] | 155.2 |
| -H (**12**) | 7.82−7.79[a] | 7.32−7.24[a,b] | 163.7 | | | |
| -CHO (**13**) | 7.80 | 7.84 | 162.8 | 8.25 | 8.11 | 155.5 |
| -CHO (**14**) | 7.87 | 8.01 | 163.0 | | | |
| -COOH (**15**) | 7.45 | 7.88 | 162.9 | 8.17 | 8.13 | 155.3 |
| -COOH (**16**) | 7.91 | 7.95 | 163.0 | | | |
| -CN (**17**) | 7.65 | 7.81 | 162.4 | 8.21 | 8.08 | 155.4 |
| -CN (**18**) | 7.72 | 7.96 | 162.5 | | | |
| -Br (**19**) | 7.57 | 7.42 | 162.8 | 7.98 | 7.83 | 155.1 |
| -I (**20**) | 7.43 | 7.62 | 162.9 | 7.81 | 7.98 | 155.2 |

R: see Scheme 2.8,[a]; multiplet range, [b]; the peak includes the resonances of the $H_m$ and $H_p$.

In all of the rhenium complexes where the tetrazolato ligand contains an EWG in the *para* position, the relative signals of the $H_{ortho}$ and $H_{meta}$ are reversed with respect to the starting tetrazole ligand (ie: the $H_{ortho}$ is now more upfield). This can be rationalised by the fact that coordination to the Re centre triggers an increased mesomeric donation (+M) from the tetrazole compared to the predominant inductive withdrawal (-I) effect it was having in the free ligands. The only exception to this is the *fac*-[Re(**phen**)$(CO)_3$(**TBr**)] (**19**) where the relative position of the signals ($H_o$ and $H_m$) remains the same. The inconsistent behaviour of the halogen containing compounds could be explained by their competing -I and +M effects. Their electronegative nature leads to -I whereas lone pairs of electrons facilitate +M.

The chemical shift of the $C_t$ in the rhenium complexes has been deshielded by approximately 7-8 ppm with respect to the uncoordinated tetrazole ligands. The free tetrazole ligands have $C_t$ values at 155 ppm and upon coordination the $C_t$ resonance is observed between 165-162 ppm (Table 2.3.3). This shift can again be rationalised in the same way used to describe the change in the $H_{ortho}$ and $H_{meta}$ signals. The observed +M effect of the tetrazole ring upon coordination is suggestive of extended interannular conjugation and coplanarity between the phenyl and tetrazole rings.[166,167] The $C_t$ resonances between 162-165 ppm also suggest that coordination of the tetrazolato ligand to the rhenium centre is regioselective for the N2 position[108,111,112,165] (ie: Re-N2 linkage isomer). This assignment is also supported in the solid state by X-ray crystallography (section 2.3.3).

Two signals around 198-194 ppm are observed in the $^{13}C$ NMR of the complexes which correspond to the CO ligands of the *fac*-[Re(**diim**)$(CO)_3$(**L**)] complexes. According to the $C_s$ symmetry of the rhenium tetrazolato complexes, two of the three carbonyl ligands are equivalent as they are *trans* to the diimine ligand and the other carbonyl group is *trans* to the tetrazolato ligand. These signals are fairly weak and not well resolved in the NMR of all complexes.

### 2.3.3 X-ray Crystallography of the Neutral Re(I) Complexes

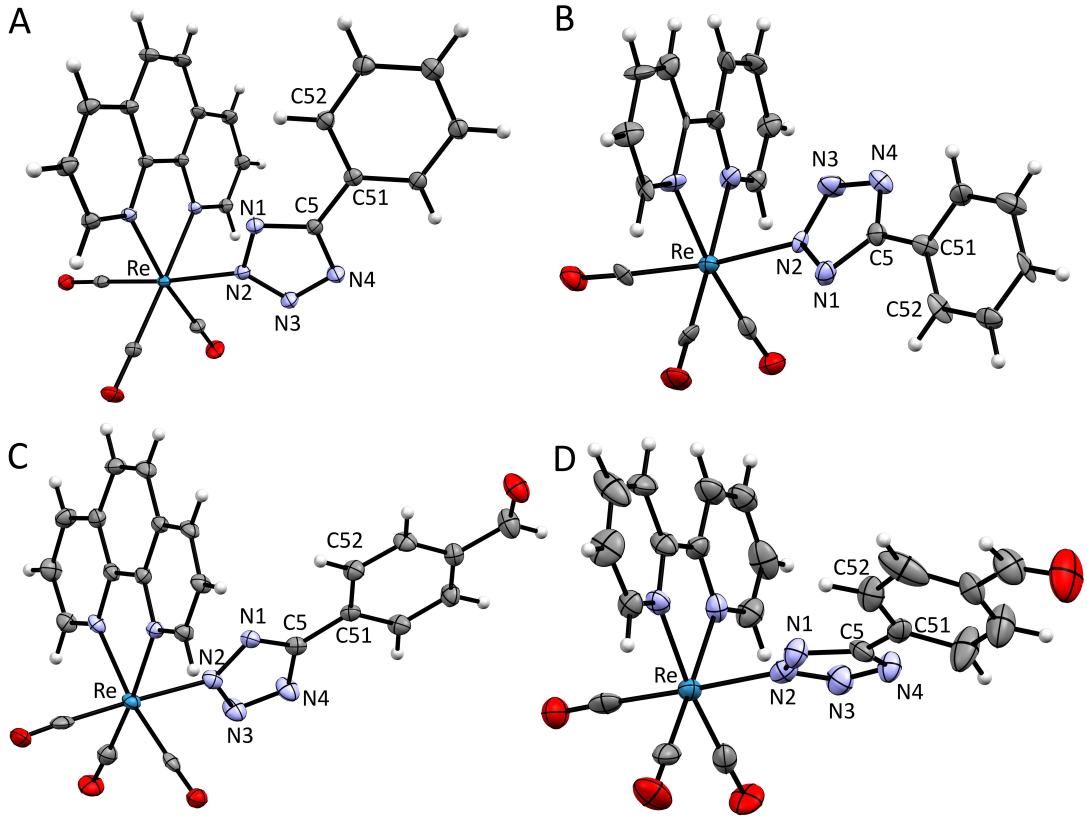


Figure 2.4: X-ray crystal structures of *fac*-[Re(**phen**)$(CO)_3$(**Tph**)] (**11**, A), *fac*-[Re(**bipy**)$(CO)_3$(**Tph**)] (**12**, B), *fac*-[Re(**phen**)$(CO)_3$(**Tbz**)] (**13**, C) and *fac*-[Re(**bipy**)$(CO)_3$(**Tbz**)] (**14**, D) where thermal ellipsoids have been drawn at 50% probability.

Single crystals were obtained for all of the neutral Re(I) tetrazolato complexes. X-ray crystallographic analysis illustrates formation of the Re-N2 linkage isomer in the solid state, as shown in Figure 2.4, Figure 2.5 and Figure 2.6. The solid state data supports the conclusions drawn from analysis of the $^{13}C$ NMR. Formation of the N1 linkage isomer was not observed in solution nor in the solid state. This is not surprising given the steric bulk of the *fac*-[Re(**diim**)$(CO)_3]^+$ fragment, favouring coordination of the (also bulky) aryl tetrazolato ring at the N2 position. The three carbonyl ligands are observed to be in a *facial* arrangement, consistent with the IR data.

$\pi$-$\pi$ interactions are a relatively weak non-covalent intermolecular force however their existence can contribute to the way a molecule packs in the solid state. $\pi$ interactions usually occur at distances between 3.3 and 3.5 Å.

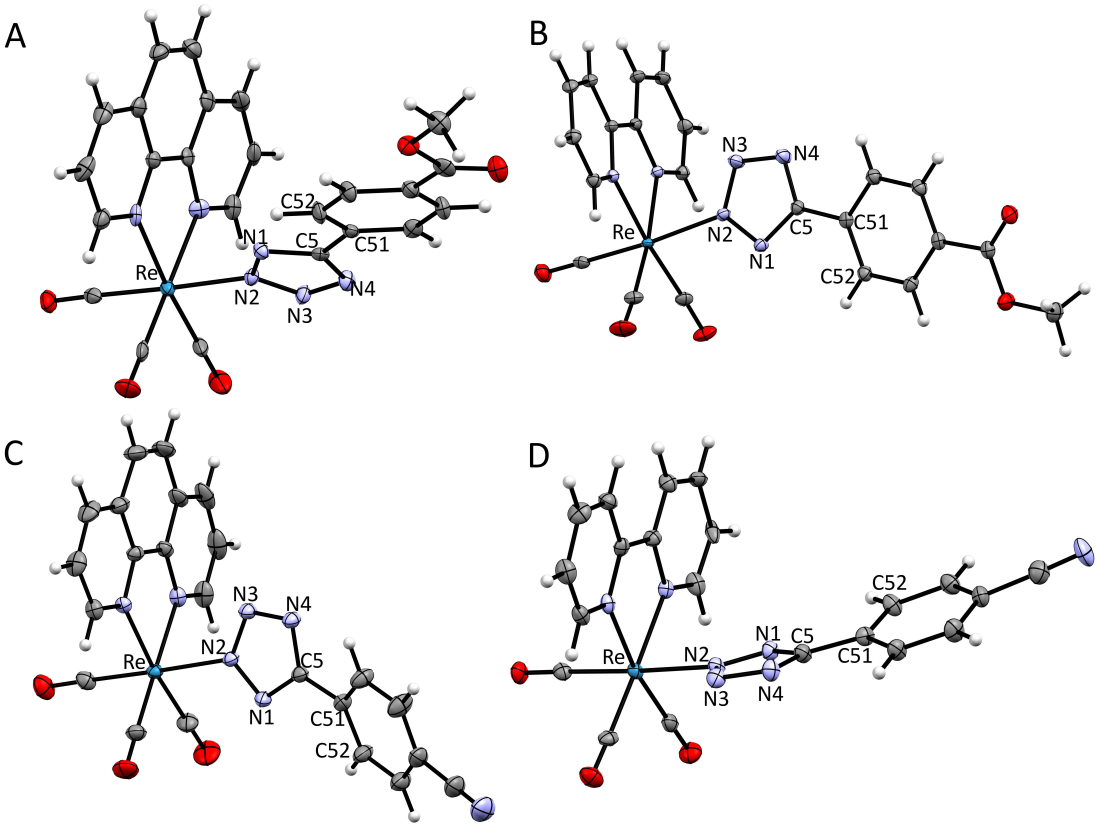


Figure 2.5: X-ray crystal structures of *fac*-[Re(**phen**)$(CO)_3$(**Tme**)] (**15**, A), *fac*-[Re(**bipy**)$(CO)_3$(**Tme**)] (**16**, B), *fac*-[Re(**phen**)$(CO)_3$(**Tcya**)] (**17**, C) and *fac*-[Re(**bipy**)$(CO)_3$(**Tcya**)] (**18**, D) where thermal ellipsoids have been drawn at 50% probability.

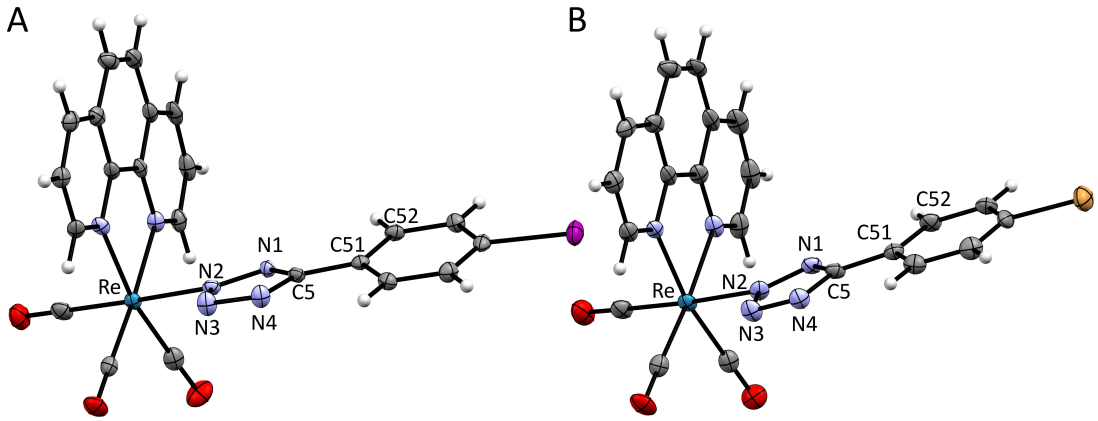


Figure 2.6: X-ray crystal structures of *fac*-[Re(**phen**)$(CO)_3$(**TIod**)] (**20**, A) and *fac*-[Re(**phen**)$(CO)_3$(**TBr**)] (**19**, B) where thermal ellipsoids have been drawn at 50% probability.

Distances between aromatic molecules more than 3.8 Å are generally not considered.[180] The level of intermolecular interactions throughout the lattices varies significantly between the complexes. *fac*-[Re(**phen**)$(CO)_3$(**Tph**)] (**11**) is arranged in the lattice to favour $\pi$ stacking of the **phen** units, with an average distance of 3.7 Å. *fac*-[Re(**phen**)$(CO)_3$(**Tme**)] (**15**), *fac*-[Re(**phen**)$(CO)_3$(**TBr**)] (**19**) and *fac*-[Re(**phen**)$(CO)_3$(**TIod**)] (**20**) show evidence of moderate $\pi$ intermolecular interactions between the **phen** units and the tetrazolato ligands, with an average distance of 3.6 Å calculated. The rest of the complexes (**12**, **14**, **16**, **17** and **18**) do not exhibit any evidence of $\pi$ stacking.

Table 2.3.4: Deviation from coplanarity between the aryl and tetrazole rings in the neutral Re(I) tetrazolato complexes.

| Rhenium Complex | Deviation from Coplanarity (˚) |
|---|---|
| *fac*-[Re(**phen**)$(CO)_3$(**Tph**)] (**11**) | 2.03 |
| *fac*-[Re(**bipy**)$(CO)_3$(**Tph**)] (**12**) | 3.26 |
| *fac*-[Re(**phen**)$(CO)_3$(**Tbz**)] (**13**) | 6.83 |
| *fac*-[Re(**bipy**)$(CO)_3$(**Tbz**)] (**14**) | 20.53 |
| *fac*-[Re(**phen**)$(CO)_3$(**Tme**)] (**15**) | 10.62 |
| *fac*-[Re(**bipy**)$(CO)_3$(**Tme**)] (**16**) | 13.17 |
| *fac*-[Re(**phen**)$(CO)_3$(**Tcya**)] (**17**) | 26.47 |
| *fac*-[Re(**bipy**)$(CO)_3$(**Tcya**)] (**18**) | 12.16 |
| *fac*-[Re(**phen**)$(CO)_3$(**TIod**)] (**20**) | 11.06 |
| *fac*-[Re(**phen**)$(CO)_3$(**TBr**)] (**19**) | 2.39 |

As discussed in relation to the NMR studies, Re-N2 coordination relates to extended interannular conjugation and therefore an extended coplanar arrangement of the aryl and tetrazole rings.[111,112] The torsion angle between these rings can indicate the extent of coplanarity observed in the solid state. An absolute value for the torsion angle close to 0° or 180° indicates coplanarity, whereas significant deviation indicates twist-

ing. Table 2.3.4 lists the deviation from coplanarity for the complexes. Unexpectedly, there is some deviation from coplanarity observed in the solid state, as indicated by torsion angles between 2.03 and 26.47 º. This disagreement with the NMR data can be rationalised by the twisted arrangement of the rings relaxing to coplanarity in solution. Also, the observed torsion angle in the crystal structures may be caused by crystal packing interactions.[170] Previously reported computational studies indicate that as intermolecular interactions are reduced (as in a relatively dilute solution), the torsion angles tend to values close to zero.[170]

### 2.3.4 Photophysical Investigation

Table 2.3.5: Absorption data for the rhenium tetrazolato complexes at $10^{-5}$ M in DCM.

| Rhenium Complex | Absorption $\lambda_{max}$/nm ($\varepsilon$ /$10^4$M$^{-1}$cm$^{-1}$) |
|---|---|
| *fac*-[Re(**phen**)(CO)$_3$(**Tph**)] (**11**) | 259 (4.90), 363 (0.455) |
| *fac*-[Re(**bipy**)(CO)$_3$(**Tph**)] (**12**) | 251 (3.45), 285 (1.91), 373 (0.329) |
| *fac*-[Re(**phen**)(CO)$_3$(**Tbz**)] (**13**) | 272 (3.25). 366 (0.411) |
| *fac*-[Re(**bipy**)(CO)$_3$(**Tbz**)] (**14**) | 296 (3.75), 372 (0.407) |
| *fac*-[Re(**phen**)(CO)$_3$(**Tme**)] (**15**) | 275 (3.83), 370 (0.428) |
| *fac*-[Re(**bipy**)(CO)$_3$(**Tme**)] (**16**) | 252 (2.30), 288 (2.82), 370 (0.294) |
| *fac*-[Re(**phen**)(CO)$_3$(**Tcya**)] (**17**) | 274 (4.36), 360 (0.549) |
| *fac*-[Re(**bipy**)(CO)$_3$(**Tcya**)] (**18**) | 251 (2.91), 285 (3.51), 373 (0.331) |
| *fac*-[Re(**phen**)(CO)$_3$(**TBr**)] (**19**) | 263 (4.62), 367 (0.422) |
| *fac*-[Re(**phen**)(CO)$_3$(**TIod**)] (**20**) | 267 (5.15), 365 (0.500) |

The absorption spectra of the neutral rhenium complexes were measured in dilute DCM solutions at approximately $10^{-5}$ M and the absorption data is shown in Table 2.3.5. All of the profiles (Figure 2.7 to Figure 2.9) exhibit high intensity transitions in the UV region between 250-300 nm and a broad, lower intensity transition between 340-400 nm. Computational calculations were used to further interpret the photophysical results. The energetics and absorption spectra of (some) complexes were simulated through TD-DFT, using GAUSSIAN09.[181] The computational calculations indicate that the high energy transitions can be assigned to $\pi - \pi^*$ IL transitions, which is in agreement with reports of similar rhenium complexes.[182,183] DFT indicated that for the prepared complexes in the singlet state, the HOMO-type orbitals are mainly localised on the rhenium metal centre but also delocalised over the entire tetrazole component of the ancillary ligand. The LUMO type orbitals are clearly localised only on the diimine ligand (**phen** or **bipy**). Figure 2.10 and Figure 2.11 show the localisation of the HOMO and LUMO, for a selection of the synthesised Re(I) complexes.

Table 2.3.6: Photophysical data for the rhenium tetrazolato complexes at $10^{-5}$ M in DCM. $\phi$ measured against rhodamine 101, unless otherwise stated.

| Rhenium Complex | Emission 298 K $\lambda_{max}$(nm) | $\tau$ ($\mu$s)$^a$ | $\tau$ ($\mu$s)$^b$ | $\phi^a$ | $\phi^b$ |
|---|---|---|---|---|---|
| *fac*-[Re(**phen**)(CO)$_3$(**Cl**)] (**7**)$^d$ | 602 | 0.173 | 0.288 | - | 0.036 |
| *fac*-[Re(**bipy**)(CO)$_3$(**Cl**)] (**8**)$^d$ | 615 | - | 0.050 | | 0.005 |
| *fac*-[Re(**phen**)(CO)$_3$(**Tph**)] (**11**) | 592 | 0.268 | 0.517 | 0.045 | 0.072 |
| *fac*-[Re(**bipy**)(CO)$_3$(**Tph**)] (**12**) | 606 | 0.085 | 0.092 | 0.028 | 0.085 |
| *fac*-[Re(**phen**)(CO)$_3$(**Tbz**)] (**13**) | 584 | 0.343 | 0.775 | 0.043 | 0.070 |
| *fac*-[Re(**bipy**)(CO)$_3$(**Tbz**)] (**14**) | 596 | 0.105 | 0.124 | 0.015 | 0.025 |
| *fac*-[Re(**phen**)(CO)$_3$(**Tme**)] (**15**)$^c$ | 586 | 0.285 | 0.552 | 0.027 | 0.109 |
| *fac*-[Re(**bipy**)(CO)$_3$(**Tme**)] (**16**)$^c$ | 600 | 0.092 | 0.118 | 0.011 | 0.015 |
| *fac*-[Re(**phen**)(CO)$_3$(**Tcya**)] (**17**) | 584 | 0.382 | 0.518 | 0.060 | 0.053 |
| *fac*-[Re(**bipy**)(CO)$_3$(**Tcya**)] (**18**) | 598 | 0.107 | 0.139 | 0.021 | 0.021 |
| *fac*-[Re(**phen**)(CO)$_3$(**TBr**)] (**19**)$^c$ | 586 | 0.258 | 0.708 | 0.031 | 0.113 |
| *fac*-[Re(**phen**)(CO)$_3$(**TIod**)] (**20**)$^c$ | 590 | 0.262 | 0.591 | 0.028 | 0.083 |

$^a$; air-equilibrated samples, $^b$; degassed ($O_2$ free) samples, $^c$; $\phi$ measured against quinine sulfate, $^d$; previously published data.[48,124,169]

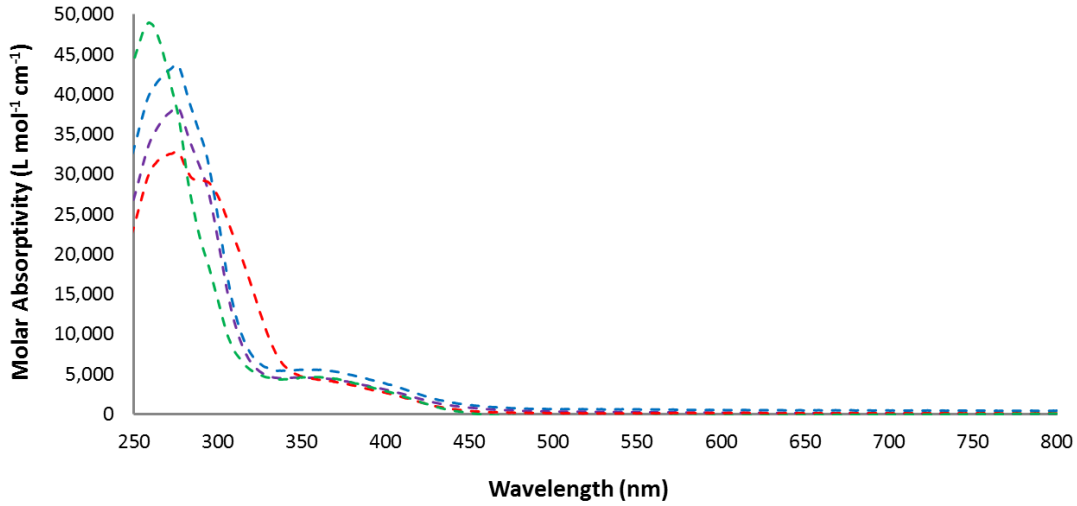


Figure 2.7: Absorption of *fac*-[Re(**phen**)(CO)$_3$(**Tph**)] (**11**, green), *fac*-[Re(**phen**)(CO)$_3$(**Tbz**)] (**13**, red), *fac*-[Re(**phen**)(CO)$_3$(**Tme**)] (**15**, purple) and *fac*-[Re(**phen**)(CO)$_3$(**Tcya**)] (**17**, blue) in DCM.

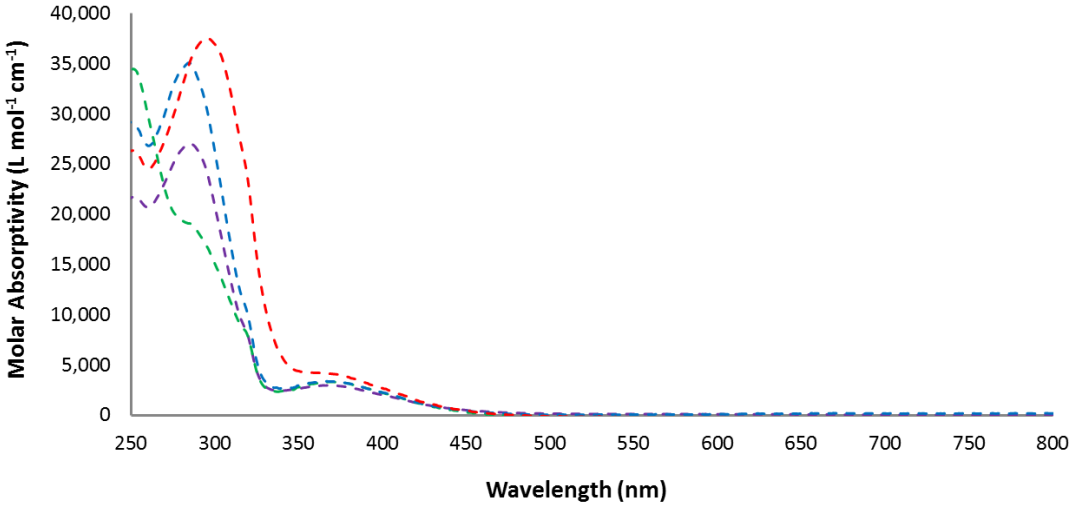


Figure 2.8: Absorption of *fac*-[Re(**bipy**)$(CO)_3$(**Tph**)] (**12**, green), *fac*-[Re(**bipy**)$(CO)_3$(**Tbz**)] (**14**, red), *fac*-[Re(**bipy**)$(CO)_3$(**Tme**)] (**16**, purple) and *fac*-[Re(**bipy**)$(CO)_3$(**Tcya**)] (**18**, blue) in DCM.

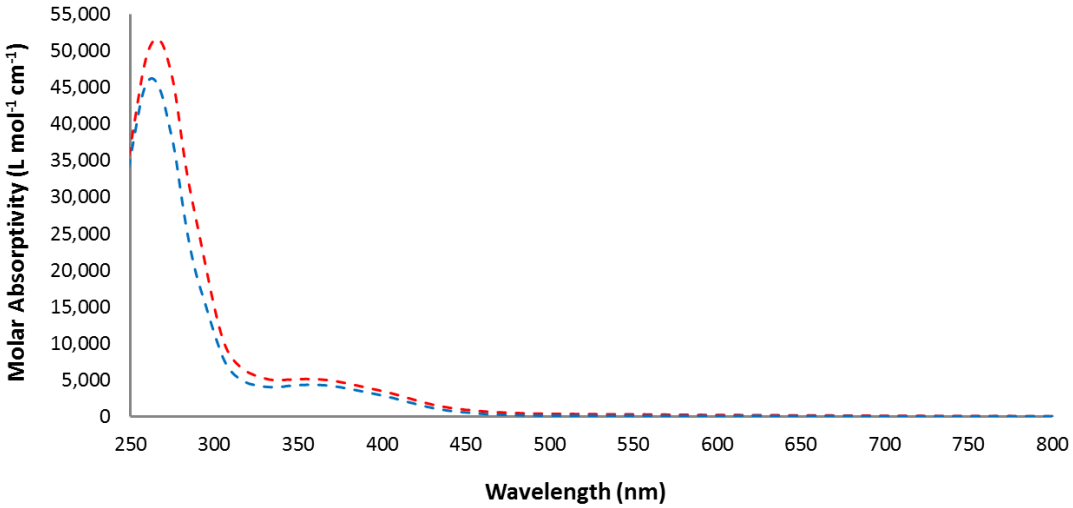


Figure 2.9: Absorption of *fac*-[Re(**phen**)$(CO)_3$(**TIod**)] (**20**, red) and *fac*-[Re(**phen**)$(CO)_3$(**TBr**)] (**19**, blue) in DCM.

Based on the localisation of the HOMO and LUMO type orbitals, the broad absorption band can be assigned to a mixture of MLCT (Re→diimine) and LLCT (tetrazole→diimine) transitions.

The close proximity of these bands has been previously described as a metal-ligand-to-ligand charge transfer (MLLCT).[145,182,184–186] For *fac*-[Re(**phen**)$(CO)_3$(**Tph**)] (**11**) and *fac*-[Re(**bipy**)$(CO)_3$(**Tph**)] (**12**) the HOMO is delocalised over the complete aryl tetrazolato ligand. For those complexes containing an EWG in the *para* position of the ligand, the contribution of the aryl ring to the HOMO is reduced. By adding an EWG to the phenyl ring, the contribution of LLCT to the MLLCT state is reduced. The broad nature of the MLLCT band in the absorption spectra can make the identification of the maximum difficult to assign, as has been previously reported by Villegas *et al.*[182] The **phen** complexes exhibit higher molar absorptivities ($\varepsilon$) compared to their **bipy** analogues (Table 2.3.5), which is expected due to their increased conjugation.

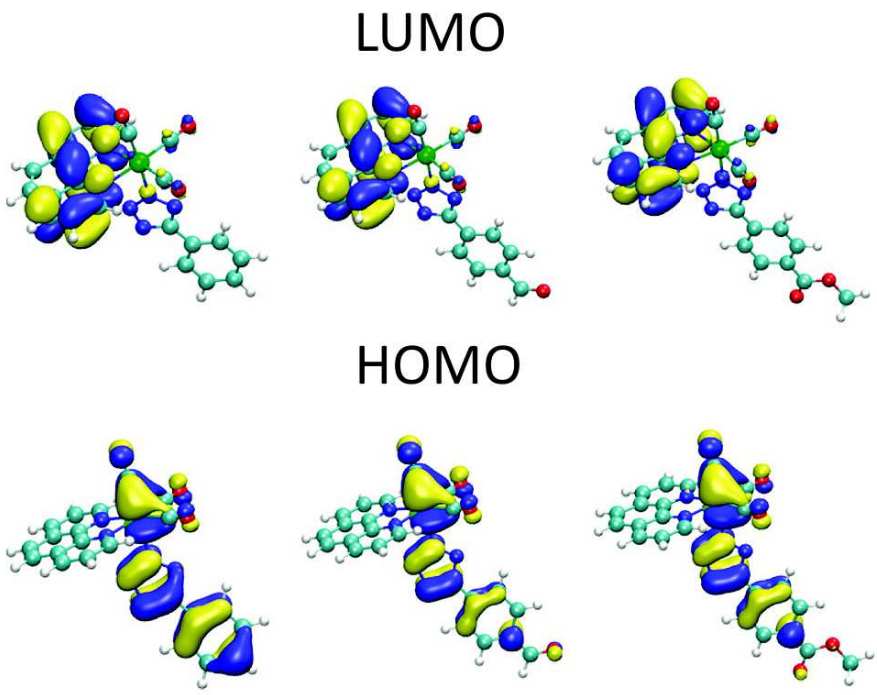


Figure 2.10: Localisation of the HOMO and LUMO for the neutral **phen** complexes (left to right); *fac*-[Re(**phen**)$(CO)_3$(**Tph**)] (**11**), *fac*-[Re(**phen**)$(CO)_3$(**Tbz**)] (**13**) and (*fac*-[Re(**phen**)$(CO)_3$(**Tme**)] (**15**).

The MLLCT absorption band for the complexes containing **bipy** are at lower energies compared to those containing the **phen** ligand. According to theoretical calculations the LUMO type orbitals are localised on the diimine ligand for all of the complexes.

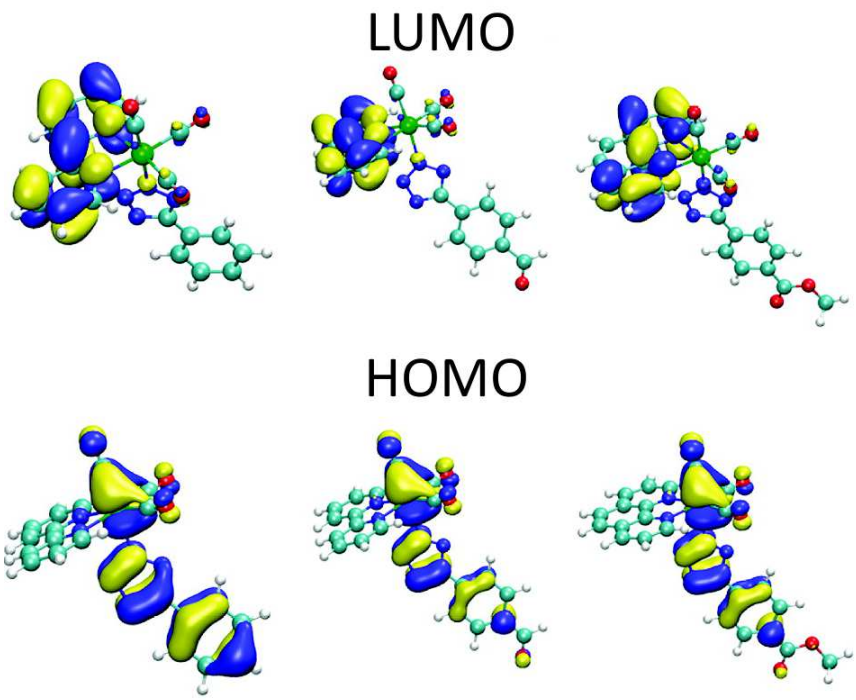


Figure 2.11: Localisation of the HOMO and LUMO for the neutral **bipy** complexes (left to right); *fac*-[Re(**bipy**)$(CO)_3$(**Tph**)] (**12**), *fac*-[Re(**bipy**)$(CO)_3$(**Tbz**)] (**14**) and (*fac*-[Re(**bipy**)$(CO)_3$(**Tme**)] (**16**).

Therefore the blue shifted MLLCT observed for the **phen** complexes is counterintuitive, considering the increased conjugation of this ligand. Extended conjugation in a LUMO system usually translates to stabilisation of the empty $\pi^*$ orbitals and therefore a red shift is expected. However, according to the DFT, the LUMO on the 1,10-phenanthroline ligand is not fully conjugated over the three rings as seen in Figure 2.10. This diimine ligand actually mimics a bipyridine system with two methyl groups attached (ie: 2,2'-bipyridine-3,3'-dimethyl). The additional "methyl" groups are inductively electron donating and therefore destabilise the LUMO even more than the simple 2,2'-bipyridine ligand. This destabilisation causes an increase in the HOMO-LUMO gap for the **phen** complexes which translates to a blue shift in the absorption, excitation and emission spectra.

Assignment of the $\pi - \pi^*$ and MLLCT absorption bands was further confirmed through the solvatochromic nature of the latter. Solvatochromism describes the stabilisation of the excited state dipole upon change of solvent. Solvatochromism is observed when there is a significant shift in electron density, resulting from a transition in the molecule.[187] The transition causes a change in the dipole, which is more commonly

observed in charge transfer transitions (eg: LLCT, MLCT), rather than $\pi - \pi^*$ (IL) or metal centred (MC) transitions. If the solvent has a permanent dipole then it will orient itself with the molecule (being excited) and cause stabilisation effects.[188] In particular a bathochromic shift describes a red shift in the absorption band upon increasing the solvent polarity and a hypsochromic shift (negative solvatochromism) corresponds to a blue shifted transition.[189] A hypsochromic shift of the MLCT band has been previously reported for the **phen** and **bipy** parent halogen complexes.[169] Upon measurement of the absorption spectra in DCM and DMSO, a hypsochromic shift[190] of approximately 14-16 nm was observed for the MLLCT bands of the prepared rhenium complexes. The assigned IL bands were essentially unaffected by this change in solvent. The blue shift in DMSO (a more polar solvent than DCM) suggests that the ground state of the complexes is more polar than the excited states.

Table 2.3.7: Emission data for the rhenium tetrazolato complexes at 77 K in DCM.

| Rhenium Complex | Emission 77K | |
|---|---|---|
| | $\lambda$(nm) | $\tau$ ($\mu$s) |
| *fac*-[Re(**phen**)$(CO)_3$(**Tph**)] (**11**) | 534 | 6.75 |
| *fac*-[Re(**bipy**)$(CO)_3$(**Tph**)] (**12**) | 528 | 2.97 |
| *fac*-[Re(**phen**)$(CO)_3$(**Tbz**)] (**13**) | 516 | 8.0 |
| *fac*-[Re(**bipy**)$(CO)_3$(**Tbz**)] (**14**) | 528 | 3.55 |
| *fac*-[Re(**phen**)$(CO)_3$(**Tme**)] (**15**) | 530 | 3.08 (21%), 8.29 (79%) |
| *fac*-[Re(**bipy**)$(CO)_3$(**Tme**)] (**16**) | 530 | 2.27 (44%), 5.59 (56%) |
| *fac*-[Re(**phen**)$(CO)_3$(**Tcya**)] (**17**) | 528 | 6.75 |
| *fac*-[Re(**bipy**)$(CO)_3$(**Tcya**)] (**18**) | 526 | 3.64 |
| *fac*-[Re(**phen**)$(CO)_3$(**TBr**)] (**19**) | 530 | 3.94 (30%), 9.70 (70%) |
| *fac*-[Re(**phen**)$(CO)_3$(**TIod**)] (**20**) | 526 | 3.58 (28%), 9.07 (72%) |

The emission profiles of the Re(I) complexes were obtained from DCM solutions and each complex can be characterised by a broad structureless emission band around 584-606 nm. This profile is characteristic of emission from an MLLCT state.[145,186,191] Emission from the neutral rhenium complexes originates from a $^3$MLLCT excited state, accounting for their phosphorescent nature.[182,190] Evidence supporting emission from a triplet state can be found in Table 2.3.6, as the synthesised complexes exhibit

sensitivity to molecular oxygen. It is known that molecular oxygen can quench the triplet excited states of complexes.[52] This occurs due to energy transfer from the triplet excited state of the complex to the triplet ground state of oxygen[52,54] (as outlined in section 1.3.1.1). Upon removal of oxygen, this quenching no longer occurs, explaining the observed increase in $\tau$ and $\phi$ upon de-oxygenating the Re(I) solutions before measurement. There is also luminescence rigidochromism observed passing from room temperature to 77 K (Table 2.3.7). The rigidochromic effect is usually indicative of emission from a charge transfer state.[127,192,193] As mentioned above, (in a fluid environment) solvent molecules can cause stabilisation of the complex by orienting to accommodate the change in dipole occurring upon excitation. In a more rigid environment, such as a frozen matrix, the solvent can no longer rearrange to stabilise the complex, resulting in destabilisation of the triplet charge transfer state. This explains the blue shifted emission observed.[127] $\pi - \pi^*$ transitions are usually insensitive to the medium rigidity as the transition does not involve a large change in dipole moment.[193]

All of the lifetime measurements at 298 K are mono-exponential (Table 2.3.6) however, as shown in Table 2.3.7, some of the complexes exhibit a bi-exponential decay at 77 K. The bi-exponetial lifetime decay observed at 77 K could be attributed to the co-existence of chemically identical species with different structural arrangements/packing in the frozen matrix. Similar effects have been observed in other studies of metal complexes,[194] however further strucutral analysis would be required to confirm this hypothesis.

All of the complexes display large Stokes shifts, illustrated in the excitation and emission plots; Figure 2.12, Figure 2.13 and Figure 2.14.

The Stokes shifts are within the range of 212-234 nm which is slightly higher than some previously reported *fac*-[Re(**diim**)$(CO)_3$(**L**)]$^+$ complexes.[97,154]

A slight blue shift in the absorption and emission maxima is observed when the tetrazolato ligand bears an electron withdrawing group (EWG). It can be rationalised that EWGs increase the HOMO-LUMO gap by stabilising HOMO type orbitals. The HOMO, as demonstrated through DFT (Figure 2.10 and Figure 2.11) is delocalised over the Re 5d orbitals and also the tetrazolato ligand. Excitation of an electron from HOMO to LUMO type orbitals therefore requires increased energy.

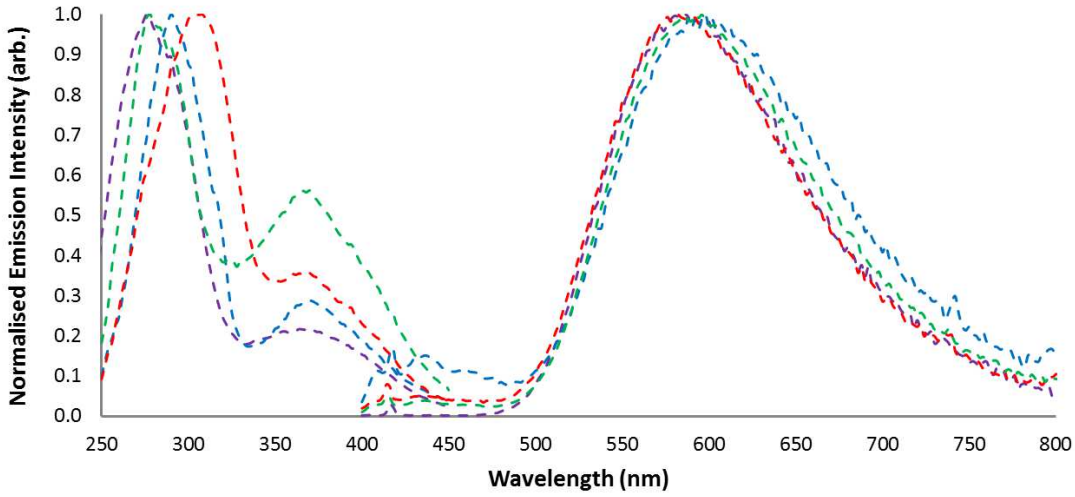


Figure 2.12: Excitation and emission profiles of *fac*-[Re(**phen**)$(CO)_3$(**Tph**)] (**11**, green), *fac*-[Re(**phen**)$(CO)_3$(**Tbz**)] (**13**, red), *fac*-[Re(**phen**)$(CO)_3$(**Tme**)] (**15**, purple) and *fac*-[Re(**phen**)$(CO)_3$(**Tcya**)] (**17**, blue) in DCM.

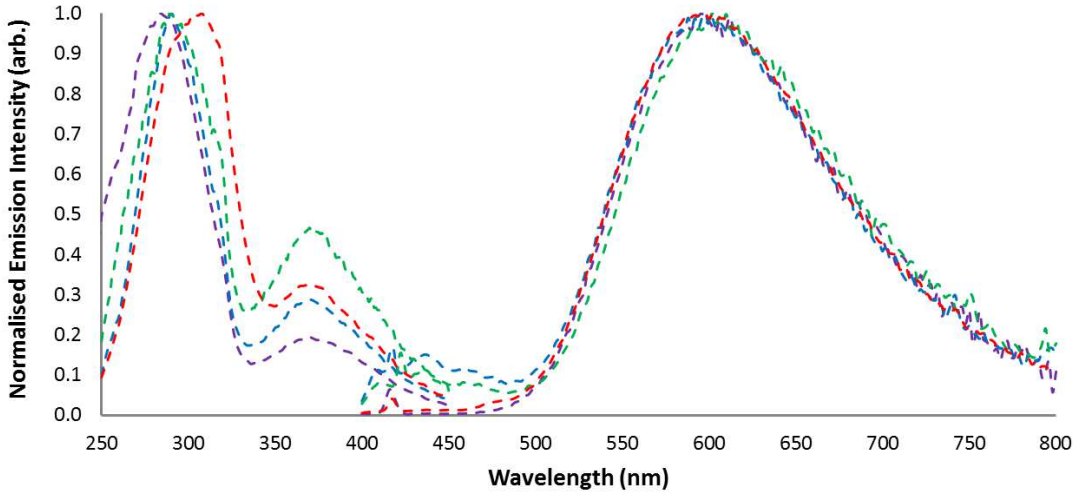


Figure 2.13: Excitation and emission profiles of *fac*-[Re(**bipy**)$(CO)_3$(**Tph**)] (**12**, green), *fac*-[Re(**bipy**)$(CO)_3$(**Tbz**)] (**14**, red), *fac*-[Re(**bipy**)$(CO)_3$(**Tme**)] (**16**, purple) and *fac*-[Re(**bipy**)$(CO)_3$(**Tcya**)] (**18**, blue) in DCM.

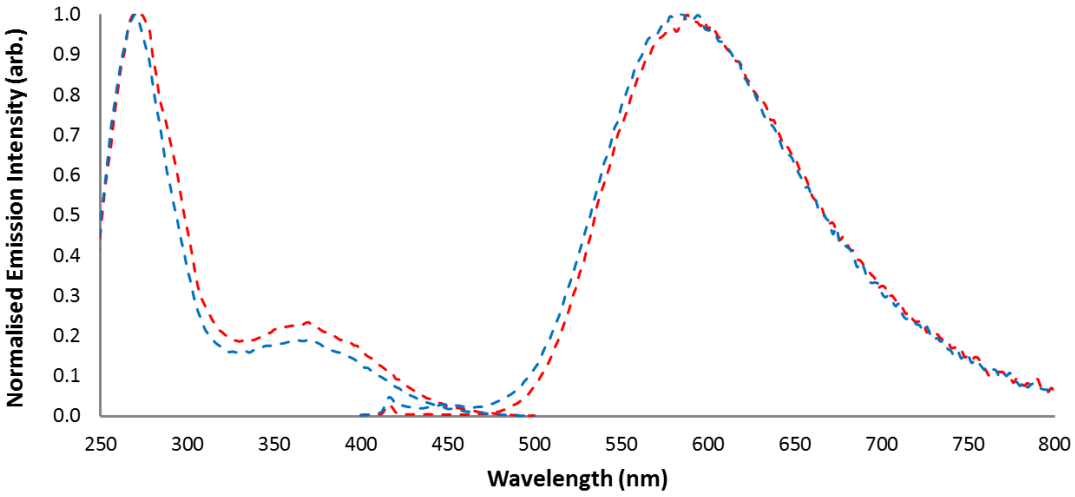


Figure 2.14: Excitation and emission profiles of *fac*-[Re(**phen**)$(CO)_3$(**TIod**)] (**20**, red) and *fac*-[Re(**phen**)$(CO)_3$(**TBr**)] (**19**, blue) in DCM.

The relatively small change observed between different EWGs can be rationalised by the fact that they are only having an indirect effect as the HOMO is not delocalised over the entire aryl ring of the aryltetrazolato ligand.

When comparing the lifetimes of the complexes (Table 2.3.6) it is clear that the *fac*-[Re(**phen**)$(CO)_3$(**L**)] complexes exhibit significantly longer $\tau$ than the corresponding *fac*-[Re(**bipy**)$(CO)_3$(**L**)] complexes. The **phen** complexes have $\tau$ in the range of 0.262-0.382 $\mu$s whereas the **bipy** are in the range of 0.085-0.107$\mu$s (air-equilibrated). This difference can be rationalised by the rigidity of **phen** compared to **bipy**, which is known to induce vibrational quenching.[195] The quantum yields for the neutral Re(I) complexes are between 1.5-6%. When comparing complexes with the same EWG on the tetrazolato ligand, those containing the **phen** always exhibit higher quantum yields. Table 2.3.8 shows the radiative and non-radiative decay constants of the prepared neutral Re(I) complexes; refer to page 9 for the equations used to calculate these constants. The values obtained for the synthesised Re(I) complexes are within the range observed for similar complexes.[145] The **phen** complexes have a significantly lower $k_{nr}$ (four to six times) compared to their **bipy** analogues. A lower $k_{nr}$ is directly related to higher $\phi$ and elongated $\tau$.[47] Refer to 9 for the equations used to calculate the involving the calculations

The photophysical output ($\phi$ and $\tau$ ) of the synthesised *fac*-[Re(**diim**)$(CO)_3$(**L**)] complexes are greatly improved compared to their parent halogen complexes[48,124,169] (Ta-

ble 2.3.6). The absorption and emission energies of the synthesised Re(I) tetrazolato complexes are blue shifted with respect to the halogen analogues.[136,151] This blue shift along with the increased $\phi$ and $\tau$ can be accounted for by the $\pi$ accepting nature of the tetrazolato ligands (although fairly weak as confirmed by IR) compared to the strong $\pi$ donating nature of the halogen ligands. The $\pi$ donating nature of the halogen ligands will destabilise the metal orbitals (HOMO), reducing the HOMO-LUMO gap and increasing the $k_{nr}$, according to the energy gap law.[47–49]

Table 2.3.8: Radiative and non-radiative decay constants ($k_r$ and $k_{nr}$) for the neutral rhenium complexes calculated for the degassed ($O_2$ free) solutions.

| **Rhenium Complex** | $k_r(10^6\ s^{-1})$ | $k_{nr}(10^6\ s^{-1})$ |
|---|---|---|
| *fac*-[Re(**phen**)$(CO)_3$(**Tph**)] (**11**) | 0.139 | 1.79 |
| *fac*-[Re(**bipy**)$(CO)_3$(**Tph**)] (**12**) | 0.924 | 9.95 |
| *fac*-[Re(**phen**)$(CO)_3$(**Tbz**)] (**13**) | 0.090 | 1.20 |
| *fac*-[Re(**bipy**)$(CO)_3$(**Tbz**)] (**14**) | 0.202 | 7.86 |
| *fac*-[Re(**phen**)$(CO)_3$(**Tme**)] (**15**) | 0.197 | 1.61 |
| *fac*-[Re(**bipy**)$(CO)_3$(**Tme**)] (**16**) | 0.127 | 8.35 |
| *fac*-[Re(**phen**)$(CO)_3$(**Tcya**)] (**17**) | 0.102 | 1.83 |
| *fac*-[Re(**bipy**)$(CO)_3$(**Tcya**)] (**18**) | 0.151 | 7.04 |
| *fac*-[Re(**phen**)$(CO)_3$(**TBr**)] (**19**) | 0.160 | 1.25 |
| *fac*-[Re(**phen**)$(CO)_3$(**TIod**)] (**20**) | 0.140 | 1.55 |

## 2.4 Conclusion

A series of neutral rhenium *fac*-[Re(**diim**)$(CO)_3$(**L**)] complexes, where **diim** is either 1,10-phenanthroline or 2,2'-bipyridine and **L** is a 5-aryltetrazolato ligand, have been synthesised and characterised structurally and photophysically. NMR and X-ray crystallography studies confirm that all of the prepared complexes exist exclusively as the Re-N2 linkage isomer. This allows the two rings of the ancillary ligand to have maximum interannular conjugation, even though some ring distortion was observed in the solid state.

The tetrazolato ligand is a good $\sigma$ donor and a partial $\pi$ acceptor (as indicated by IR), which results in a slight reduction in electron density on the rhenium metal centre, compared to the parent *fac*-[Re(**diim**)$(CO)_3$(X)] complexes (where X is Cl or Br). The lowest energy absorption transition for the Re(I) tetrazolato complexes has been assigned to a mixed MLLCT state, as supported by theoretical calculations.

This study has given insight into how simple modifications to the diimine and ancillary ligands effect the overall photophysical output. Those complexes where structural modification has been made to the diimine, ie: from **bipy** to **phen**, has seen an increase in the photophysical performance of the complex. Changing the *para* substituent on the aryltetrazolato ligand does not greatly alter the photophysical properties of the complex but can offer a way to fine tune $\phi$ and $\tau$ and, to a lesser extent the excitation and emission energies.

## 2.5 Experimental

### 2.5.1 General Procedures

All reagents were purchased from Sigma Aldrich or Alfa Aesar and used as received, without further purification. All procedures involving rhenium complexes were carried out under nitrogen using standard Schlenk techniques, although not necessarily required.

Nuclear magnetic resonance spectra (consisting of $^{1}H$, $^{13}C$, 1D NOE, 2D HMBC and HSQC experiments) were recorded using a Bruker Avance 400 spectrometer (400.1 MHz for $^{1}H$, 100 MHz for $^{13}C$) at room temperature. $^{1}H$ and $^{13}C$ chemical shifts were referenced to residual solvent resonances. The assignment of peaks for the tetrazole compounds, and their derivatives, is based on the referencing outlined in Scheme 2.8.

Infrared spectra were recorded either in the solid or solution state, as specified. Solid state measurements were carried out using an attenuated total reflectance Perkin Elmer Spectrum 100 FT-IR with a diamond stage. Compounds were scanned from 650 to 4000 $cm^{-1}$. The intensities of the IR bands were reported as strong (s), medium (m) or weak (w), with broad (br) bands and shoulders (sh) also indicated. IR spectra recorded as DCM solutions were done using a NaCl (5 mm) disc on a Perkin-Elmer Spectrum 2000 FT-IR spectrometer.

Elemental analyses were performed by Chemical and MicroAnalytical Services Pty Ltd. Victoria, Melbourne, or by Dr Thomas Rodemann at the Central Science Laboratory, University of Tasmania or by Robert Herman at the Department of Chemistry, Curtin University. All analysis were run on the desolvated bulk samples.

Melting points were determined using a BI Barnsted Electrothermal 9100 apparatus and are uncorrected.

### Photophysics

Absorption spectra were recorded at room temperature using a Perkin Elmer Lambda 35 UV/Vis spectrometer. Uncorrected steady state emission and excitation spectra were recorded on an Edinburgh FLSP980-S2S2-stm spectrometer equipped with: i)

a temperature-monitored cuvette holder; ii) 450 W Xenon arc lamp; iii) double excitation and emission monochromators; iv) a Peltier cooled Hamamatsu R928P photomultiplier tube (spectral range 200-870 nm). Emission and excitation spectra were corrected for source intensity (lamp and grating) and emission spectral response (detector and grating) by a calibration curve supplied with the instrument. According to the approach described by Demas and Crosby,[196] luminescence quantum yields ($\phi$) were measured in optically dilute solutions (O.D. < 0.1) at the excitation wavelength (nm) obtained from absorption spectra and compared to the reference emitter by the following equation:

$$\phi_x = \phi_r \left[\frac{A_r(\lambda_r)}{A_x(\lambda_x)}\right]\left[\frac{I_r(\lambda_r)}{I_x(\lambda_x)}\right]\left[\frac{n_x^2}{n_r^2}\right]\left[\frac{D_x}{D_r}\right]$$

where $A$ is the absorbance at the excitation wavelength ($\lambda$), $I$ is the intensity of the excitation light at the excitation wavelength ($\lambda$), $n$ is the refractive index of the solvent, $D$ is the integrated intensity of the luminescence and $\phi$ is the quantum yield. The subscripts $r$ and $x$ refer to the reference and the sample, respectively. The quantum yield determinations were performed at identical excitation wavelengths, for the sample and the reference, therefore canceling out the $I_r(\lambda_r)/I_x(\lambda_x)$ term in the above equation.[40] The quantum yields of the complexes were either measured against an air-equilibrated 0.1 M $H_2SO_4$ solution of quinine sulfate ($\phi_r = 0.53$) or an air-equilibrated solution of rhodamine 101 in ethanol ($\phi_r = 1$),[40] as specified.

Emission lifetimes ($\tau$) were determined with the time correlated single photon counting technique (TCSPC) with the same Edinburgh FLSP980-S2S2-stm spectrometer using pulsed picosecond LEDs (EPLED/EPL 377 nm, FHWM < 800 ps) as the excitation source and the above-mentioned photomultiplier tube as the detector. The goodness of fit was assessed by minimising the reduced $\chi^2$ function and by visual inspection of the weighted residuals.

To record the 77 K luminescence spectra, the samples were placed in quartz tubes (2 mm diameter) and inserted in a special quartz dewar filled with liquid nitrogen.

Degassed solutions were prepared by gently bubbling nitrogen gas into the prepared sample for 15 min before measurement.

Experimental uncertainties are estimated to be ±8% for lifetime determinations, ±20% for quantum yields, ±2 nm and ±5 nm for absorption and emission peaks, respectively.

## 2.5.2 Synthesis

### 2.5.2.1 General methodology for the synthesis of 5-aryl-1H-tetrazoles.

The synthesis of 5-aryl-1H-tetrazoles was adapted from a previously reported procedure by Koguro *et al*.[109] Unless otherwise stated, the following conditions were used. Triethylamine (1.2 eq) was added to toluene (~ 40 mL) and the solution was cooled to 0 ºC. 32% HCl (1.2 eq) was added to the reaction and the flask was immediately stoppered. After 15 minutes, the corresponding nitrile (1 eq) and sodium azide (1.2 eq) were added to the reaction and heated at reflux for 24 hours. After cooling to room temperature, water (~ 25 mL) was added to the reaction mixture. The aqueous phase was then collected and acidified to ~ pH 3 with HCl (32%), to produce a white solid which was filtered to yield the corresponding tetrazole.

**5-phenyl-1H-tetrazole**

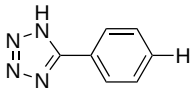

**1**

Yield of **1**: 0.706 g, 50%. M.p. 217-218 ºC (dec.) (literature value 215-216 ºC).[163] $\nu_{max}$ (ATR)/cm$^{-1}$: 3130 w, 3055 w, 2981 m, 2907 m, 2835 m, 2686 s, 2539 s, 2480 s, 1860 m br, 1609 m (tetrazole CN), 1564 s, 1486 m , 1465 m, 1410 m, 1289 w, 1257 w, 1163 w, 1085 m, 1056 m, 1034 m, 1016 m, 989 m, 790 m, 725 m, 703 m, 686 m. $^1$H NMR (δ, ppm, DMSO-d$_6$): 8.05-8.03 (m, 2H, $CN_4$-$C_6H_5$ $H_{ortho}$), 7.61-7.58 (m, 3H, $CN_4$-$C_6H_5H_{meta, para}$). $^{13}$C NMR (δ, ppm, DMSO-d$_6$): 155.2 ($CN_4$-$C_6H_5$), 131.2, 129.4, 126.9, 124.2.

**4-(1H-tetrazol-5-yl)-benzaldehyde**

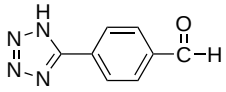

**2**

Yield of **2**: 1.19 g, 89%. M.p. 186.8-187.5ºC (dec.) (literature value 182-184 ºC).[197] $\nu_{max}$ (ATR)/cm$^{-1}$: 3403 s (NH), 3275 m, 3080 m, 3019 m, 2675 m, 2611 m, 1940 w, 1687 m, 1667 s (aldehyde CO), 1617 w, 1580 s (tetrazole CN), 1505 w, 1445 w, 1405 w, 1357 w, 1305 m, 1289 w, 1239 w, 1214 s, 1167 w, 1148 w, 1124 w, 1088 w, 1015 w, 993 m, 934 w br, 842 m, 833 m, 744 m, 697 w. $^1$H NMR (δ, ppm, DMSO-d$_6$): 10.09 (s, 1H, C*H*O), 8.25 (d, 2H, *J* = 8.0 Hz, $CN_4$-$C_6H_4$-CHO $H_{ortho}$), 8.11 (d, 2H, *J* = 8.8 Hz, $CN_4$-$C_6H_4$ -CHO $H_{meta}$). $^{13}$C NMR (δ, ppm, DMSO-d$_6$): 192.7 (aldehyde *C*O), 155.5 (*C*$N_4$-$C_6H_4$CHO), 137.6, 130.4, 129.6, 127.64.

**Methyl-4-(1H-tetrazol-5-yl)-benzoate**

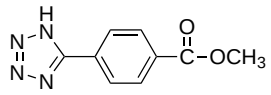

**3**

Yield of **3**: 0.748 g, 59%. M.p. 237.9-238.4ºC (dec.) (literature value 225.7 ºC).[198] $\nu_{max}$ (ATR)/cm$^{-1}$: 3503 s (NH), 3312 m br, 3227 m br, 2650 m br, 1704 s (ester CO), 1654 w, 1570 m (tetrazole CN), 1504 w, 1470 w, 1442 m, 1427 m, 1310 m, 1281 s, 1191 m, 1180 m, 1151 w, 1111 m, 1068 m, 1010 w, 997 m, 955 m, 860 m, 831 w, 778 w, 732 m, 709 m, 689 w. $^1$H NMR (δ, ppm, DMSO-d$_6$): 8.17 (d, 2H, *J* = 8.4 Hz, $CN_4$-$C_6H_4$ -$COOCH_3$ $H_{ortho}$), 8.13 (d, 2H, *J* = 8.8 Hz, $CN_4$-$C_6H_4$ -$COOCH_3$ $H_{meta}$), 3.88 (s, 3H, COO*C*$H_3$). $^{13}$C NMR (δ, ppm, DMSO-d$_6$): 165.5 (ester *C*O), 155.3 (*C*$N_4$-$C_6H_4$$COOCH_3$), 131.6, 130.1, 128.6, 127.2, 52.4.

**5-(4-iodophenyl)-1H-tetrazole**

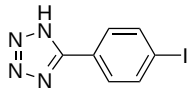

**5**

The synthesis of **5** employed a slight excess of reagents compared to the general methodology reported. In particular 1.5 eq of triethylamine, 32% HCl and sodium azide were used with 1 eq of iodobenzonitrile .

Yield of **5**: 0.506 g, 57%. M.p. 268-269 ºC (dec.) (literature value 269-271ºC (dec.))[199] $\nu_{max}$ (ATR)/cm$^{-1}$: 2964 w, 2816 w, 2668 w, 2514 m, 2445 m, 1906 m, 1602 s, 1557 m, 1492 w, 1478 m, 1431 s, 1405 w, 1364 w, 1272 w, 1252 w, 1165 m, 1117 w, 1088 w, 1055 m, 1025 w, 1005 w, 981 s, 826 s, 742 m, 711 w, 693 w. $^1$H

NMR (δ, ppm, DMSO-$d_6$): 7.98 (2H, d, $J$ = 8.4 Hz, $CN_4$-$C_6H_4$ -I $H_{meta}$), 7.81 (2H, d, $J$ = 8.4 Hz, $CN_4$-$C_6H_4$ -I $H_{ortho}$). $^{13}$C NMR (δ, ppm, DMSO-$d_6$): 155.2 ($C$$N_4$-$C_6H_4$-I ), 138.3, 128.7, 123.8, 98.4.

**5-(4-bromophenyl)-1H-tetrazole**

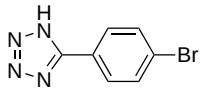


**6**

The synthesis of **6** employed a slight excess of reagents compared to the general methodology reported. In particular 1.5 eq of triethylamine, 32% HCl and sodium azide were used with 1 eq of bromobenzonitrile.

Yield of **6**: 0.367 g, 63%. M.p. 267-270 ºC (dec.) (literature value 278-279 ºC (dec.)).[200] $\nu_{max}$ (ATR)/$cm^{-1}$: 3092 w, 2973 w, 2902 w, 2848 w, 2728 w, 2638 w, 1605 s, 1562 w, 1483 s, 1431 s, 1279 w, 1255 w, 1158 m, 1077 m, 1054 m, 1019 m, 990 m, 869 m, 876 s, 742 s, 709 w, 692 w. $^1$H NMR (δ, ppm, DMSO-$d_6$): 7.98 (2H,d, $J$ = 6.8 Hz, $CN_4$-$C_6H_4$ -Br $H_{ortho}$), 7.83 (2H, d, $J$ = 6.6 Hz, $CN_4$-$C_6H_4$ -Br $H_{meta}$). $^{13}$C NMR (δ, ppm, DMSO-$d_6$): 155.1 ($C$$N_4$-$C_6H_4$ -Br), 132.5, 128.9, 124.7, 123.6.

**4-(1H-tetrazol-5-yl)cyanobenzene**

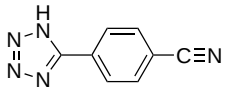


**4**

The synthesis of **4** used no excess of the reagents, compared to the general methodology reported. In particular 1 eq of triethylamine, 32% HCl, 1,4-dicyanobenzene and sodium azide (1 eq) were used. The pure form of the compound was not isolated. A small amount (less than 8%) of bis-tetrazole compound, 5-[4-(1H-tetrazol-5-yl-phenyl]-1H-tetrazole, was present in the NMR (singlet at 8.26 ppm) but the compound was used in further reactions without purification.

Yield of **4**: 0.253 g, ~ 43 %. M.p. 181-183 ºC (dec.) (literature value 188-189 ºC)[167] $\nu_{max}$ (ATR)/$cm^{-1}$: 3433 s, 3357 s, 3246 m, 3095 m, 2537 m, 2241 and 2232 s (nitrile), 1644 w, 1619 w (C=N), 1577 m, 1564 m, 1499 m, 1437 m, 1371 w, 1281 w, 1255 w, 1245 w, 1153 w, 1124 w, 1072 w, 1060 w, 990 (947 sh) s, 848 s, 751 s, 703 w. $^1$H NMR (δ, ppm, DMSO-$d_6$): 8.21 (2H, d, $J$ = 8.4 Hz, $CN_4$-$C_6H_4$ -CN $H_{ortho}$), 8.08 (2H, d, $J$

= 8.8 Hz, $CN_4$-$C_6H_4$ -CN $H_{meta}$). $^{13}$C NMR (δ, ppm, DMSO-$d_6$): 155.4 ($CN_4$-$C_6H_4$ -CN ), 133.4, 128.8, 127.7, 118.2, 113.5.

### 2.5.2.2 General methodology for the synthesis of *fac*-[Re(diim)(CO)$_3$(X)]

The preparation of *fac*-[Re(**diim**)(CO)$_3$(X)] (**diim** = 1,10-phenanthroline or 2,2'- bipyridine) was carried out following procedures adapted from previously published work.[168,169] Rhenium pentacarbonyl chloride or bromide (1 eq) and the corresponding diimine (**bipy** or **phen**) (1.1 eq) were added to toluene and heated at reflux for 4 hours. A yellow solid was filtered off and washed with cold toluene to yield the final complex.

*fac*-[Re(**phen**)(CO)$_3$(Cl)]

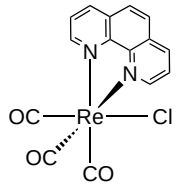


**7**

Yield of **7**: 0.651 g, 90%. M.p. 300 °C (dec.). $\nu_{max}$ (ATR)/cm$^{-1}$: 3897 w, 3749 w, 3088 w, 2014 s (CO, A´(1)), 1923 s (CO, A´(2)), 1885 s br (CO, A´´), 1629 w, 1602 w, 1584 w, 1518 w, 1492 w, 1425 m, 1409 m, 1340 w, 1315 w, 1302 w, 1210 w, 1196 w, 1143 w, 1108 w, 1098 w,1063 w, 961 w, 850 m, 782 w, 722 m.

*fac*-[Re(**bipy**)(CO)$_3$(Cl)]

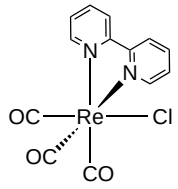


**8**

Yield of **8**: 0.643 g (98%). M.p. 330 °C (dec.). $\nu_{max}$ (ATR)/cm$^{-1}$: 3749 w, 3085 w, 2013 s (CO, A´(1)), 1891 s (CO, A´(2)), 1872 s br (CO, A´´), 1601 m, 1571 w, 1491 w, 1470 m, 1443 m, 1314 w, 1246 w, 1162 w, 1122 w, 1105 w, 1070 w, 967 w, 764 m, 732 m.

*fac*-[Re(**phen**)$(CO)_3$(Br)]

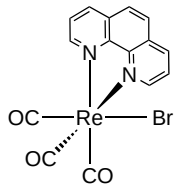


**9**

Yield of **9**: 0.598, 92 %. M.p. 336 °C (dec.). $\nu_{max}$ (ATR)/$cm^{-1}$: 3084 w, 2015 s (CO, A´(1)), 1925 s (CO, A´(2)), 1882 (1863 sh) s (CO, A´´), 1629 w, 1584 w, 1517 w, 1424 m, 1407 w, 1342 w, 1314 w, 1300 w, 1259 w, 1210 w, 1142 w, 1096 w, 957 w, 850 m, 782 w, 722 w.

*fac*-[Re(**bipy**)$(CO)_3$(Br)]

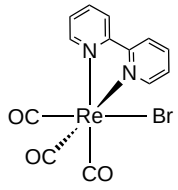


**10**

Yield of **10**: 0.239 g, 92 %. M.p. 331-332 °C (dec.). $\nu_{max}$ (ATR)/$cm^{-1}$: 3067 w, 2516 w, 2397 w, 2011 s (CO, A´(1)), 1901 m (CO, A´(2)), 1865 (1851 sh) s (CO, A´´), 1603 m, 1573 w, 1493 w, 1471 m, 1442 m, 1442 (1429 sh) m, 1314 w , 1245 w, 1223 w, 1155 w, 1120 w, 1072 w, 1047 w, 959 w, 768 m, 731 w.

#### 2.5.2.3 General methodology for the synthesis of *fac*-[Re(diim)$(CO)_3$(L)]

*fac*-[Re(**diim**)$(CO)_3$(**L**)] : Where (**diim** = 1,10-phenanthroline or 2,2'-bipyridine) and **L** is a 5-aryl-1H-tetrazole.

To a 20 mL ethanol/water solvent system (3:1 v/v) under an argon atmosphere **7**, **8**, **9** or **10** (1 eq) was added. The corresponding tetrazole ligand (1.6 eq) with triethylamine (1.6 eq) in a 5.0 mL portion of ethanol/water (3:1 v/v) was added. The resulting suspension was heated at reflux for 20 h. After this time, the mixture was cooled to room temperture and filtered over a glass frit, affording the desired complexes as yellow microcrystalline powders. The product complexes did not require any further purification

process, except for *fac*-[Re(**phen**)$(CO)_3$(**Tcya**)] (**17**). All of complexes of the form; *fac*-[Re(**diim**)$(CO)_3$(**L**)] were synthesised according to this method, unless otherwise stated.

Elemental analysis was carried out for all new complexes (not previously published), otherwise characterisation was in agreement with previously published data.[170,174]

*fac*-[Re(**phen**)$(CO)_3$(**Tph**)]

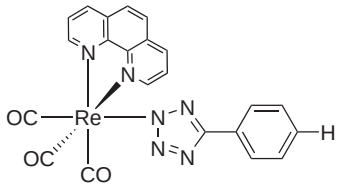

**11**

Yield of **11**: 0.085 g, 75%. M.p. 284 °C (dec.). ESI-MS (m/z) = 619 $[M + Na]^+$. $\nu_{max}$ (IR)/$cm^{-1}$, DCM, rt: 2029 s (CO, A´(1)), 1922 s br (CO, A´(2)/A´´), 1606 w (tetrazole C=N). $^1$H NMR (δ, ppm, Acetone-$d_6$): 9.65 (2H, d, $J$ = 4.8 Hz, phen $H_{2,9}$), 8.96 (2H, d, $J$ = 8.2 Hz, phen $H_{4,7}$), 8.30 (2H, s, phen $H_{5,6}$), 8.19−8.15 (2H, m, phen $H_{3,8}$), 7.63 (2H, d, $J$ = 7.2 Hz, $CN_4$-$C_6H_5$ $H_{ortho}$), 7.22−7.20 (3H, m, $CN_4$-$C_6H_5$ $H_{meta, para}$). $^{13}$C NMR (δ, ppm, Acetone-$d_6$): 163.4 ($CN_4$-$C_6H_5$), 155.1, 148.3, 140.3, 131.7, 131.3, 129.1, 128.9, 128.7, 127.4, 126.6.

*fac*-[Re(**bipy**)$(CO)_3$(**Tph**)]

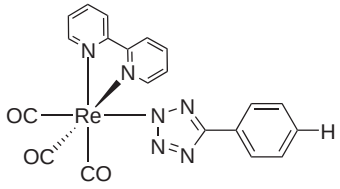

**12**

Yield of **12**: 0.072 g, 63%. M.p. 253 °C (dec.). ESI-MS (m/z) = 595 $[M + Na]^+$. $\nu_{max}$ (IR)/$cm^{-1}$, DCM, rt: 2029 s (CO, A´(1)), 1924 s br (CO, A´(2)/A´´), 1606 w (tetrazole C=N). $^1$H NMR (δ, ppm, Acetone-$d_6$): 9.25 (2H, d, $J$ = 5.2 Hz, bipy $H_{6,6'}$), 8.69 (2H, d, $J$ = 8.0 Hz, bipy $H_{3,3'}$), 8.35 (2H, t, $J$ = 7.2 Hz, bipy $H_{4,4'}$), 7.82−7.79 (4H, m, bipy $H_{5,5'}$ and $CN_4$-$C_6H_5$ $H_{ortho}$), 7.32−7.24 (3H, m, $CN_4$-$C_6H_5$ $H_{meta, para}$). $^{13}$C NMR (δ, ppm, Acetone-$d_6$): 163.7 ($CN_4$-$C_6H_5$), 157.5, 154.7, 141.2, 131.5, 129.2, 128.9, 128.7, 126.8, 124.7.

*fac*-[Re(**phen**)$(CO)_3$(**Tbz**)]

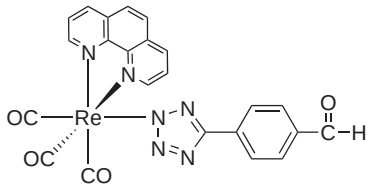

**13**

Yield of **13**: 0.097 g, 82%. M.p. 268 °C (dec.). ESI-MS (m/z) = 647 $[M + Na]^+$. $\nu_{max}$ (IR)/$cm^{-1}$, DCM, rt: 2029 s (CO, A´(1)), 1923 br (CO, A´(2)/A´´), 1699 s (aldehyde CO), 1610 w (tetrazole C=N). $^1$H NMR (δ, ppm, Acetone-$d_6$): 9.96 (1H, s,$CN_4$-$C_6H_4$-C*H*O), 9.67 (2H, d, *J* = 5.2 Hz, phen $H_{2,9}$), 8.98 (2H, d, *J* = 8.4 Hz, phen $H_{4,7}$), 8.32 (2H, s, phen $H_{5,6}$), 8.20− 8.17 (2H, m, phen $H_{3,8}$), 7.84 (2H, d, *J* = 8.8 Hz, $CN_4$-$C_6H_4$ -CHO $H_{meta}$), 7.80 (2H, d, J = 8.4 Hz, $CN_4$-$C_6H_4$ -CHO $H_{ortho}$). $^{13}$C NMR (δ, ppm, Acetone-$d_6$): 192.4, 162.8 (*C*$N_4$-$C_6H_4$-CHO), 155.2, 148.2, 140.4, 137.1, 136.6, 131.7, 130.5, 128.7, 127.4, 127.0.

*fac*-[Re(**bipy**)$(CO)_3$(**Tbz**)]

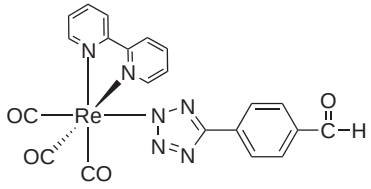

**14**

Yield of **14**: 0.102 g, 83%. M.p. 265 °C (dec.). ESI- MS (m/z) = 623 $[M + Na]^+$. $\nu_{max}$ (IR)/$cm^{-1}$, DCM, rt: 2029 s (CO, A´(1)), 1922 br (CO, A´(2)/A´´), 1699 s (aldehyde CO), 1607 w (tetrazole C=N). $^1$H NMR (δ, ppm, Acetone-$d_6$): 10.01 (1H, s, $CN_4$-$C_6H_4$-C*H*O), 9.27 (2H, d, *J* = 5.5 Hz, bipy $H_{6,6'}$), 8.71 (2H, d, *J* = 8.4 Hz, bipy $H_{3,3'}$), 8.37 (2H, t, *J* = 7.8 Hz, bipy $H_{4,4'}$), 8.01 (2H, d, *J* = 8.0 Hz, $CN_4$-$C_6H_4$ -CHO $H_{meta}$), 7.87 (2H, d, J = 8.4 Hz, $CN_4$-$C_6H_4$ -CHO $H_{ortho}$), 7.83 (2H, t, *J* = 5.6 Hz, bipy $H_{5,5'}$). $^{13}$C NMR (δ, ppm, Acetone-$d_6$): 192.4, 163.0 (*C*$N_4$-$C_6H_4$-CHO), 157.5, 154.7, 141.3, 137.2, 136.7, 130.6, 128.7, 127.1, 124.7.

*fac*-[Re(**phen**)$(CO)_3$(**Tme**)]

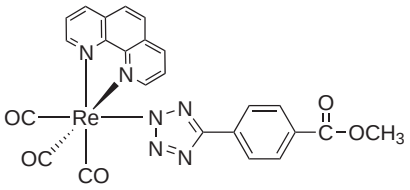

**15**

The synthesis of **15** was carried out using previously published methods by Wright *et al.*[174] *fac*-[Re(**phen**)$(CO)_3$(Cl)] **7** (1 eq, 0.21 mmol) was added to acetonitrile (10 mL) under a nitrogen atmosphere. To this suspension, methyl-4-(1H-tetrazol-5-yl)-benzoate **3** (1.6 eq, 0.34 mmol) with triethylamine (1.6 eq, 0.34 mmol) in acetonitrile (3 mL) was added. The reaction was heated at reflux for 4 nights. The complex was purified via neutral alumina-filled column chromatography using ethyl acetate (100%) as the eluent (second product, yellow).

Yield of **15**: 0.085 g, 63%. M.p. 243 °C (dec.). $\nu_{max}$ (ATR)/$cm^{-1}$: 3049 w, 2957 w, 2020 s (CO, A´(1)), 1912 s (CO, A´(2)), 1887 (CO, A´´), 1722 s (ester CO), 1678 w, 1615 m (tetrazole CN), 1584 w, 1534 w, 1519 w, 1449 w, 1427 m, 1307 w, 1277 m, 1226 w, 1212 w, 1190 w, 1174 w, 1150 w, 1141 w, 1108 w, 1098 w, 1037 w, 1005 w, 975 w, 864 w, 851 m, 829 w, 777 w, 737 m, 721 m, 698 m. $^1$H NMR (δ, ppm, Acetone-$d_6$): 9.66 (2H, d, $J$ = 5.0 Hz, phen $H_{2,9}$), 8.97 (2H, d, $J$ = 10.2 Hz, phen $H_{4,7}$), 8.30 (2H, s, phen $H_{5,6}$), 8.19-8.16 (2H, m, phen $H_{3,8}$), 7.88 (2H, d, $J$ = 7.4 Hz, $CN_4$-$C_6H_4$-$COOCH_3$ $H_{meta}$), 7.75 (2H, d, $J$ = 7.4 Hz, $CN_4$-$C_6H_4$-$COOCH_3$ $H_{ortho}$), 3.84 (3H, s, -OC$H_3$). $^{13}$C NMR (δ, ppm, Acetone-$d_6$): 197.9 (*C*O), 166.9 (*C*$OCH_3$), 162.9 (*C*$N_4$-$C_6H_4$-$COOCH_3$), 155.2, 148.3, 140.4, 135.5, 131.7, 130.5, 130.4, 128.7, 127.4, 126.5, 52.3 (-O*C*$H_3$).

*fac*-[Re(**bipy**)$(CO)_3$(**Tme**)]

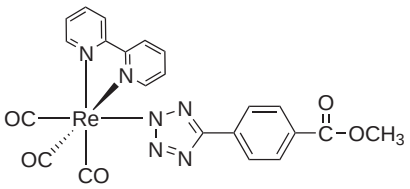

**16**

The synthesis of **16** was carried out using previously published methods by Werrett *et al.*[170] *fac*-[Re(**bipy**)$(CO)_3$(Cl)], **8** (1 eq, 0.50 mmol) and $AgBF_4$ (1.2 eq, 0.60 mmol) were combined in dry acetonitrile (15 mL) and heated at reflux, in the dark for 4 hours

under a nitrogen atmosphere. The white solid was filtered off through Celite, to yield a yellow solution, containing, *fac*-[Re(**bipy**)$(CO)_3(NCCH_3)][BF_4]$ which was used immediately. To this yellow solution, methyl-4-(1H-tetrazol-5-yl)-benzoate **3**, (1.2 eq, 0.60 mmol) with triethylamine (1.2 eq, 0.60 mmol) in acetonitrile (3 mL), was added and heated under reflux for 24 hours. The complex was purified via reprecipitation from acetonitrile/dichloromethane and diethylether.

Yield of **16**: 0.287 g, 90 %. M.p. 275 °C (dec.). $\nu_{max}$ (ATR)/$cm^{-1}$: 3075 w, 3035 w, 2949 w, 2020 s (CO, A´(1)), 1902 s br (CO, A´(2)/A´´), 1721 s (ester CO), 1603 m (tetrazole CN), 1573 w, 1496 m, 1474 m, 1447 m, 1433 m, 1379 m, 1306 w, 1271 m, 1175 m, 1123 m, 1094 m, 1036 w, 1005 w, 863 w, 779 m, 740 m, 732 m, 694 w. $^1$H NMR (δ, ppm, Acetone-$d_6$): 9.26 (2H, d, $J$ = 5.5 Hz, bipy $H_{6,6'}$), 8.71 (2H, d, $J$ = 8.0 Hz, bipy $H_{3,3'}$), 8.37 (2H, t, $J$ = 8.0 Hz, bipy $H_{4,4'}$), 7.95 (2H, d, $J$ = 7.4 Hz, $CN_4$-$C_6H_4$-$COOCH_3$ $H_{meta}$), 7.91 (2H, d, $J$ = 7.4 Hz, $CN_4$-$C_6H_4$-$COOCH_3$ $H_{ortho}$), 7.84-7.80 (2H, m, bipy $H_{5,5'}$), 3.86 (3H, s, -OC$H_3$). $^{13}$C NMR (δ, ppm, Acetone-$d_6$): 167.0 ($C$O$CH_3$), 163.0 ($C$$N_4$-$C_6H_4$-$COOCH_3$), 157.5, 154.7, 141.3, 135.6, 130.6, 130.4, 128.7, 126.7, 124.7, 52.3 (-O$C$$H_3$).

*fac*-[Re(**phen**)$(CO)_3$(**Tcya**)]

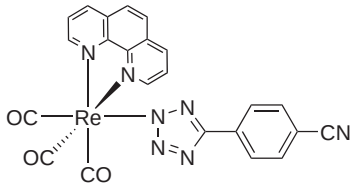


**17**

The complex was purified via neutral alumina-filled column chromatography using acetonitrile (100%) as the eluent (second fraction, yellow).

Yield of **17**: 0.050 g, 42%. M.p. 242-243 °C (dec.). ESI-MS (m/z) = 644 $[M + Na]^+$. $\nu_{max}$ (IR)/$cm^{-1}$, DCM, rt: 2229 w (CN), 2030 s (CO, A´(1)), 1923 br (CO, A´(2)/A´´), 1606 w (tetrazole C=N). $^1$H NMR (δ, ppm, Acetone-$d_6$): 9.67 (2H, d, $J$ = 4.0 Hz, phen $H_{2,9}$), 8.97 (2H, d, J = 7.2 Hz, phen $H_{4,7}$), 8.31 (2H, s, phen $H_{5,6}$), 8.20−8.16 (2H, m, phen $H_{3,8}$), 7.81 (2H, d, $J$ = 6.4 Hz, $CN_4$-$C_6H_4$ -CN $H_{meta}$), 7.65 (2H, d, $J$ = 4.0 Hz, $CN_4$-$C_6H_4$ -CN $H_{ortho}$). $^{13}$C NMR (δ, ppm, Acetone-$d_6$): 162.4 ($C$$N_4$-$C_6H_4$-CN), 155.2, 148.2, 140.4, 135.3, 133.2, 131.7, 128.7, 127.4, 127.1, 119.3, 112.2.

*fac*-[Re(**bipy**)$(CO)_3$(**Tcya**)]

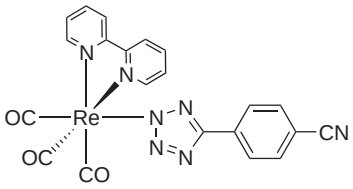

**18**

Yield of **18**: 0.090 g, 75%. M.p. 283-284 °C (dec.) Elemental analysis for $C_{21}H_{12}N_7O_3Re$: calculated: C 42.28, H 2.03, N 16.43; found: C 42.25, H 1.88, N 16.26. ESI-MS (m/z) = 620 $[M + Na]^+$. $\nu_{max}$ (IR)/$cm^{-1}$, DCM, rt: 2229 w (CN), 2029 s (CO, A´(1)), 1923 br (CO, A´(2)/A´´), 1606 w (tetrazole C=N). $^1H$ NMR (δ, ppm, Acetone-$d_6$): 9.27 (2H, d, $J$ = 5.5 Hz, bipy $H_{6,6'}$), 8.71 (2H, d, $J$ = 8.40 Hz, bipy $H_{3,3'}$), 8.37 (2H, t, $J$ = 8.0 Hz, bipy $H_{4,4'}$), 7.96 (2H, d, $J$ = 9.2 Hz, $CN_4$-$C_6H_4$ -CN $H_{meta}$), 7.83−7.79 (2H, m, bipy $H_{5,5'}$), 7.72 (2H, d, $J$ = 7.5 Hz, $CN_4$-$C_6H_4$ -CN $H_{ortho}$). $^{13}C$ NMR (δ, ppm, Acetone-$d_6$): 162.5 ($CN_4$-$C_6H_4$-CN), 157.4, 154.7, 141.3, 135.5, 133.3, 128.7, 127.3, 124.7, 119.3, 112.3. Crystals suitable for X-ray analysis (identified as **18**, $C_{21}H_{12}N_7O_3Re$) were obtained by slow diffusion of diethyl ether into a DCM solution of the complex in dichloromethane.

*fac*-[Re(**phen**)$(CO)_3$(**TBr**)]

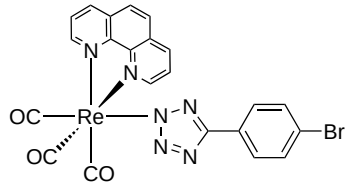

**19**

Yield of **19**: 0.150 g, 83 %. M.p.282-283 ºC (dec.). Elemental analysis for $C_{22}H_{12}BrN_6O_3Re$: calculated: C 39.18, H 1.79, N 12.46; found: C 38.99 , H 1.84 , N 12.60. $\nu_{max}$ (ATR)/$cm^{-1}$: 3062 w, 2996 w, 2025 s (CO, A´(1)), 1913 s, (CO, A´(2)/A´´), 1632 w, 1602 w, 1584 w, 1517 w, 1427 m, 1414 m, 1340 w, 1270 w, 1229 w, 1178 w, 1140 w, 1120 w, 1096 w, 1068 w, 1038 w, 1003 w, 849 m, 827 m, 780 w, 750 w, 722 m.$^1H$ NMR (δ, ppm, Acetone-$d_6$): 9.65 (2H, d, $J$ = 5.2 Hz, phen $H_{2,9}$), 8.97 (2H, d, $J$ = 8.2 Hz, phen $H_{4,7}$), 8.30 (2H, s, phen $H_{5,6}$), 8.19-8.16 (2H, m, phen $H_{3,8}$), 7.57 (2H, d, $J$ = 8.8 Hz, $CN_4$-$C_6H_4$ -Br $H_{ortho}$), 7.42 (2H, d, $J$ = 8.8 Hz, $CN_4$-$C_6H_4$ -Br $H_{meta}$). $^{13}C$

NMR (δ, ppm, Acetone-$d_6$): 162.8 (*C*$N_4$-$C_6H_4$-Br), 155.2, 148.2, 140.4, 132.3, 131.7, 130.5, 128.7, 128.5, 127.4, 122.3. Crystals suitable for X-ray analysis (identified as **19**, $C_{22}H_{12}Br\ N_6O_3Re$) were obtained by liquid liquid diffusion of petroluem spirits into a DCM solution of the complex.

*fac*-[Re(**phen**)$(CO)_3$(**TIod**)]

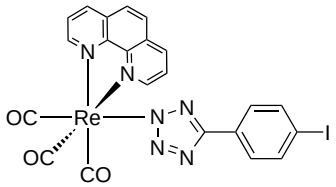


**20**

Yield of **20**: 0.139 g, 95 %. M.p. 291.3-291.9 °C (dec.). Elemental analysis for $C_{22}H_{12}I\ N_6O_3Re$: calculated: C 36.62, H 1.68, N 11.65; found: C 36.43 , H 1.44 , N 11.46. $\nu_{max}$ (ATR)/$cm^{-1}$: 3798 w, 3060 w, 2023 s (CO, A´(1)), 1908 br s (CO, A´(2)/A´´), 1631 w, 1600 w, 1584 w, 1425 m, 1411 m, 1338 w, 1269 w, 1226 w, 1177 w, 1146 w, 1117 w, 1038 w, 1000 w, 965 w, 848 w, 825 w, 779 w, 748 w, 721 w. $^1$H NMR (δ, ppm, Acetone-$d_6$): 9.65 (2H, d, *J* = 5.2 Hz, phen $H_{2,9}$), 8.96 (2H, d, *J* = 8.2 Hz, phen $H_{4,7}$), 8.30 (2H, s, phen $H_{5,6}$), 8.19-8.15 (2H, m, phen $H_{3,8}$), 7.62 (2H, d, *J* = 8.4 Hz, $CN_4$-$C_6H_4$ -I $H_{meta}$), 7.43 (2H, d, *J* = 8.8 Hz, $CN_4$-$C_6H_4$ -I $H_{ortho}$). $^{13}$C NMR (δ, ppm, Acetone-$d_6$): 162.9 (*C*$N_4$-$C_6H_4$-I), 155.2, 148.3, 140.4, 138.4, 131.7, 130.9, 128.7, 128.6, 127.4, 93.9. Crystals suitable for X-ray analysis (identified as **20**, $C_{22}H_{12}I\ N_6O_3Re$) were obtained by liquid liquid diffusion of petroluem spirits into a DCM solution of the complex.

### 2.5.3 X-ray Crystallography

Diffraction data for the complexes discussed in Chapter Two were collected by Dr. Brian Skelton at the University of Western Australia and can be found in previously published work; **11**, **12**, **13**, **14**, **15**,**16**,[170] **17**[174] and **18**.[201]

Diffraction data for *fac*-[Re(**phen**)$(CO)_3$(**TBr**)] (**19**) and *fac*-[Re(**phen**)$(CO)_3$(**TIod**)] (**20**) were collected by Dr. Brian Skelton at the University of Western Australia, at 100(2) K on an Xcalibur diffractometer (**20**) or on an Oxford Diffraction Gemini

diffractometer (**19**) both fitted with Mo K$\alpha$ radiation. Following analytical absorption corrections and solution by direct methods, the structure was refined against $F^2$ with full-matrix least-squares using the program SHELXL-97.[202] All hydrogen atoms were added at calculated positions and refined by use of a riding model with isotropic displacement parameters based on those of the parent atom. The crystallographic data can be found in Table A1.1, Appendix A1.1.

### 2.5.4 Computational Calculations

The TD-DFT and DFT calculations were performed by Dr. Paolo Raiteri. Computational details on the complexes presented in this Chapter can be found in previously published work.[170]

# Chapter 3

# Reversible Protonation of Metal Tetrazolato Complexes and their Change in Luminescence

## 3.1 Abstract

The reactivity of Re(I) complexes toward electrophiles was investigated to understand their potential to be utilised as responsive probes/sensing agents. If a metal complex is to be applied in this context, it must have a preferential and measurable response to a specific change in the environment.[62] The tetrazole ring in the Re(I) complexes appears to act as a Brønsted-type base and was protonated by triflic acid. Upon protonation, a detectable elongation of the $\tau$ and increase in the $\phi$ was observed, as well as a blue shift in the emission wavelength. The modulation caused by protonation of the Re(I) complexes was completely reversible by treatment with triethylamine. The study was extended to isoelectronic Ir(III) and Ru(II) tetrazolato complexes. Protonation of [Ir(PyrTzF)] caused a red shift of the emission maxima whereas protonation of $[Ru(PyrTz)]^+$caused significant quenching of the emission.

## 3.2 Introduction

The coordinated ligands in Ru(II), Re(I) and Ir(III) complexes play a significant role in their photophysical output. The ligands are directly involved in the metal-to-ligand charge transfer (MLCT) excited states and can therefore influence the emission of the complex. If a ligand is changed or modified to become more reducible a red-shifted emission is favoured, by stabilisation of the LUMO. Likewise, if an ancillary ligand is altered to indirectly make the metal centre more oxidisable, then a red-shifted emission is favoured by destabilisation of the HOMO type orbitals.

The right combination of ligands (with modified functional groups) and metal centres has led to the development of a range of $d^6$ metal complexes with emission spanning from the visible to near infrared spectrum. This tunability has led to the applications of $d^6$ metal complexes in light emitting devices,[203–205] dye sensitised solar cells,[206–209] as optical imaging probes[62,67,210] and as general luminescent sensors.[211,212] Here, luminescent sensors refer to the capacity of a compound to detect or sense changes to the surrounding environment by exhibiting a detectable change in luminescent the output.

A range of ions and molecules are present within a cell, responsible for life processes.[213] Recently $d^6$ metal complexes have emerged as potential *in vivo* and *in vitro* sensing agents. Examples include the ability to sense species including $O_2$,[81,82] divalent cations (eg: $Zn^{2+}$, $Ca^{2+}$and $Hg^{2+}$),[118] water,[214] hypochlorous acid[215] and also pH changes.[89,119] Many of these sensing agents are still being optimised for applications specific for biology but show potential for development within this field. The complexes exhibit a preferential response to external stimuli that can be monitored by a significant change in their photophysical output. Often, a modification of the ligand is responsible for this photophysical modulation. Modification of the ligands often occurs through the binding of, or reactions with, specific analytes.

As discussed in Chapter Two, the tetrazolato ligands on the Re(I) diimine complexes directly contribute to the emissive state (eg: $^3$MLLCT) and can therefore be used to fine tune emission. This chapter investigates the potential for the *fac*-[Re(**diim**)$(CO)_3$(**L**)] complexes to have applications in sensing different pH environments. The rhenium complexes described herein are outlined in Scheme 3.1.

A series of reversible protonation and deprotonation reactions have been carried out on

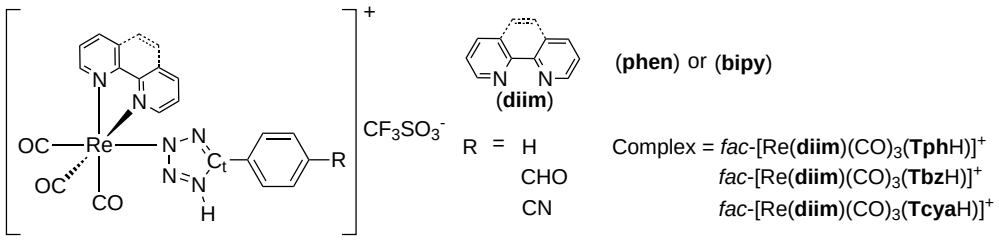


Scheme 3.1: Codes and abbreviations for the protonated Re(I) complexes reported in Chapter Three.

the Re(I) complexes and the change in luminescent output monitored. The study is a proof of concept approach and the conditions used for protonation are extreme (triflic acid). The study has also been extended to isoelectronic Ir(III) and Ru(II) tetrazolato complexes.

## 3.3 Results and Discussion: Rhenium

### 3.3.1 Synthesis and Spectroscopic Characterisation

A slight excess (*ca.* 1.2 eq) of triflic acid was added to a dichloromethane solution of the neutral Re(I) tetrazolato complex maintained at -50 °C for 30 minutes, as shown in Scheme 3.2. The tetrazole ring contains three free nitrogen atoms which are all potential sites for protonation. Scheme 3.2 shows the three possible protonation products. Low temperatures were employed to favour protonation at N4 (Scheme 3.2 C).

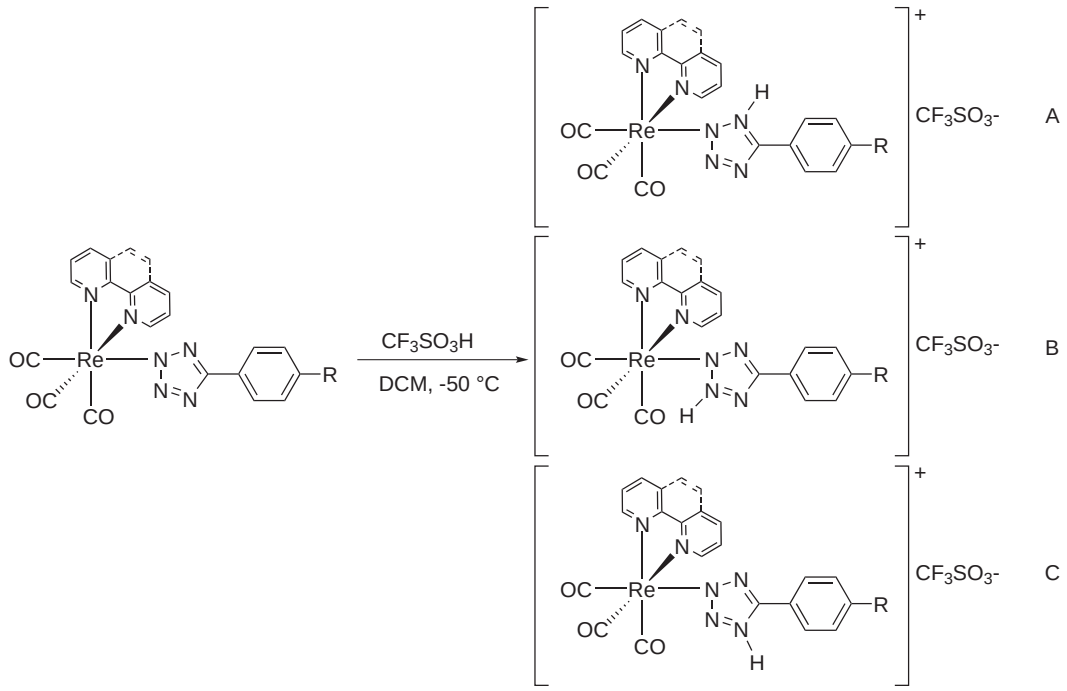


Scheme 3.2: Synthesis of the protonated rhenium tetrazolato complexes showing potential protonation at N1 (A), N3 (B) or N4 (C).

Szczepura and co-workers[216] carried out protonation of a hexanuclear rhenium tetrazolate cluster complex using $HBF_4$. For protonation to occur, temperatures of 100 ºC were required, unlike the reactions reported herein which occurred without heating.

The intense carbonyl bands of the complexes were monitored through solution state IR spectroscopy. The stretching frequency of the CO bands shifted to higher wavenumbers upon formation of the protonated species as shown in Table 3.3.1. Protonation causes a significant reduction in the electron density on the tetrazolato ligand and it therefore becomes less $\sigma$ donating and more $\pi$ accepting.[108] This in turn reduces the amount of electron density on the rhenium centre causing a reduction in backbonding

to the CO ligands. These CO ligands now exhibit a higher bond order which explains the increase in stretching frequency observed. As discussed in Chapter 2 and shown in Figure 2.1 on page 39, the situation represented in "b" (Re→CO backbonding) is disfavoured (even more for these cationic complexes). In all cases the *facial* configuration of the Re complexes was maintained: one band was observed at 2039-2040 $cm^{-1}$ consistent with A´(1) and a broader band seen at 1936-1938 $cm^{-1}$, which is the superimposition of A´(2) and A´´.[178]

Table 3.3.1: Solution state IR measurements carried out in DCM at room temperature.

| Stretching frequency ($cm^{-1}$) | CO A´(1) | CO A´(2)/A´´ |
|---|---|---|
| *fac*-[Re(**phen**)$(CO)_3$(**Tph**)] (**11**) | 2029 | 1922 |
| *fac*-[Re(**phen**)$(CO)_3$(**Tph**H)]$^+$ (**21**) | 2039 | 1936 |
| *fac*-[Re(**bipy**)$(CO)_3$(**Tph**)] (**12**) | 2029 | 1924 |
| *fac*-[Re(**bipy**)$(CO)_3$(**Tph**H)] $^+$(**22**) | 2039 | 1936 |
| *fac*-[Re(**phen**)$(CO)_3$(**Tbz**)] (**13**) | 2029 | 1923 |
| *fac*-[Re(**phen**)$(CO)_3$(**Tbz**H)] $^+$(**23**) | 2040 | 1938 |
| *fac*-[Re(**bipy**)$(CO)_3$(**Tbz**)] (**14**) | 2029 | 1922 |
| *fac*-[Re(**bipy**)$(CO)_3$(**Tbz**H)] $^+$(**24**) | 2040 | 1937 |
| *fac*-[Re(**phen**)$(CO)_3$(**Tcya**)] (**17**) | 2030 | 1923 |
| *fac*-[Re(**phen**)$(CO)_3$(**Tcya**H)]$^+$ (**25**) | 2040 | 1937 |
| *fac*-[Re(**bipy**)$(CO)_3$(**Tcya**)] (**18**) | 2029 | 1923 |
| *fac*-[Re(**bipy**)$(CO)_3$(**Tcya**H)]$^+$ (**26**) | 2040 | 1938 |

The protonated Re complexes were characterised by $^1H$ and $^{13}C$ NMR spectroscopy. The number of peaks, chemical shifts, and integration values for each spectrum are consistent with the proposed structure of the complexes. The addition of the $H^+$ is directed towards the tetrazole ligand, which behaves as a Brønsted-type base. The N-H proton was not identified in the $^1H$ NMR spectra of the protonated species, however, an overall downfield shift of the resonances was observed. The signals from the phenyl

protons of the aryl tetrazolato ligand were the most significantly shifted, as outlined in Table 3.3.2. This shift is expected due to the reduction in electron density on the tetrazolato ligand, upon protonation.

Table 3.3.2: Comparison of NMR chemical shift data in acetone-$d_6$ relative to the *ortho*, *meta* and *para* protons before and after protonation.

| **Rhenium Complex** | $\delta H_o$ | $\delta H_m$ |
|---|---|---|
| *fac*-[Re(**phen**)$(CO)_3$(**Tph**)] (**11**) | 7.63 | 7.22-7.20[a] |
| *fac*-[Re(**phen**)$(CO)_3$(**Tph**H)]$^+$ (**21**) | 7.69 | 7.56-7.36[a] |
| *fac*-[Re(**bipy**)$(CO)_3$(**Tph**)] (**12**) | 7.82−7.79[c] | 7.32-7.24 |
| *fac*-[Re(**bipy**)$(CO)_3$(**Tph**H)] $^+$(**22**) | 7.90-7.83[b] | 7.54-7.49[a] |
| *fac*-[Re(**phen**)$(CO)_3$(**Tbz**)] (**13**) | 7.80 | 7.84 |
| *fac*-[Re(**phen**)$(CO)_3$(**Tbz**H)] $^+$(**23**) | 7.90 | 7.95 |
| *fac*-[Re(**bipy**)$(CO)_3$(**Tbz**)] (**14**) | 7.87 | 8.01 |
| *fac*-[Re(**bipy**)$(CO)_3$(**Tbz**H)] $^+$(**24**) | 8.07 | |
| *fac*-[Re(**phen**)$(CO)_3$(**Tcya**)] (**17**) | 7.65 | 7.81 |
| *fac*-[Re(**phen**)$(CO)_3$(**Tcya**H)]$^+$ (**25**) | 7.91 | |
| *fac*-[Re(**bipy**)$(CO)_3$(**Tcya**)] (**18**) | 7.72 | 7.96 |
| *fac*-[Re(**bipy**)$(CO)_3$(**Tcya**H)]$^+$ (**26**) | 7.94-7.88[b] | 8.04 |

[a]; Peak range includes the resonances for $H_m$ and $H_p$,[b]; Peak range includes the resonance for bipy $H_{5,5'}$, [c];Peak range includes the resonance for bipy $H_{4,4'}$.

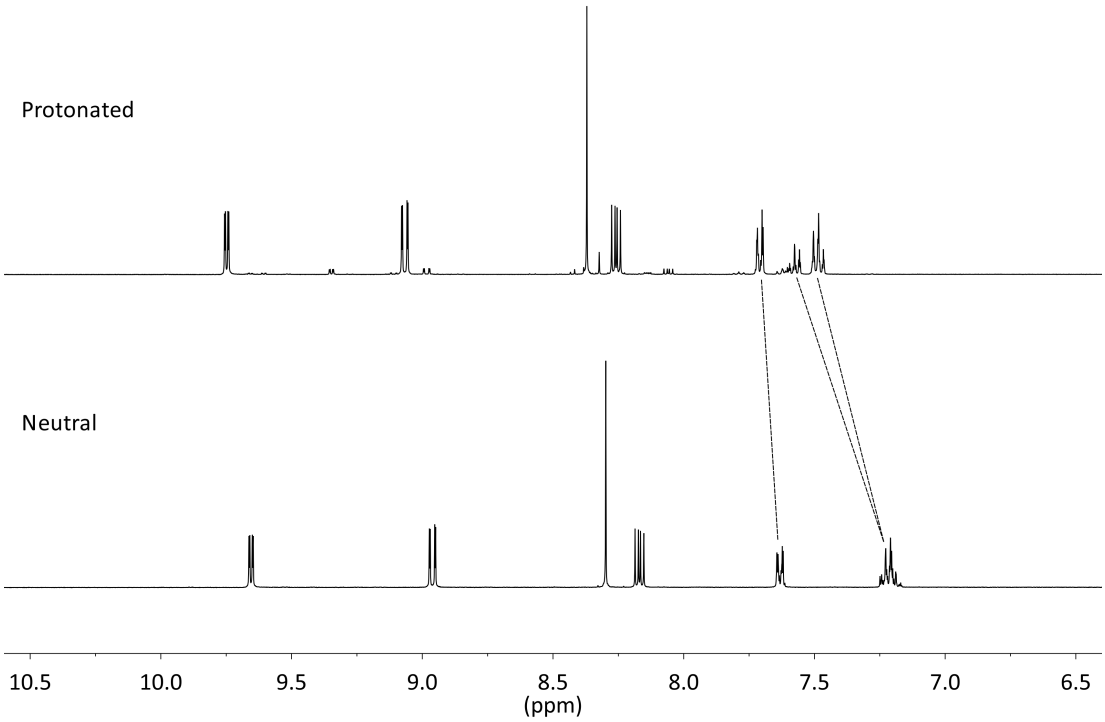


Figure 3.1: $^{1}$H NMR spectra of the neutral complex *fac*-[Re(**phen**)$(CO)_3$(**Tph**)], **11** (bottom) compared to the protonated species, *fac*-[Re(**phen**)$(CO)_3$(**Tph**H)]$^{+}$, **21** (top).

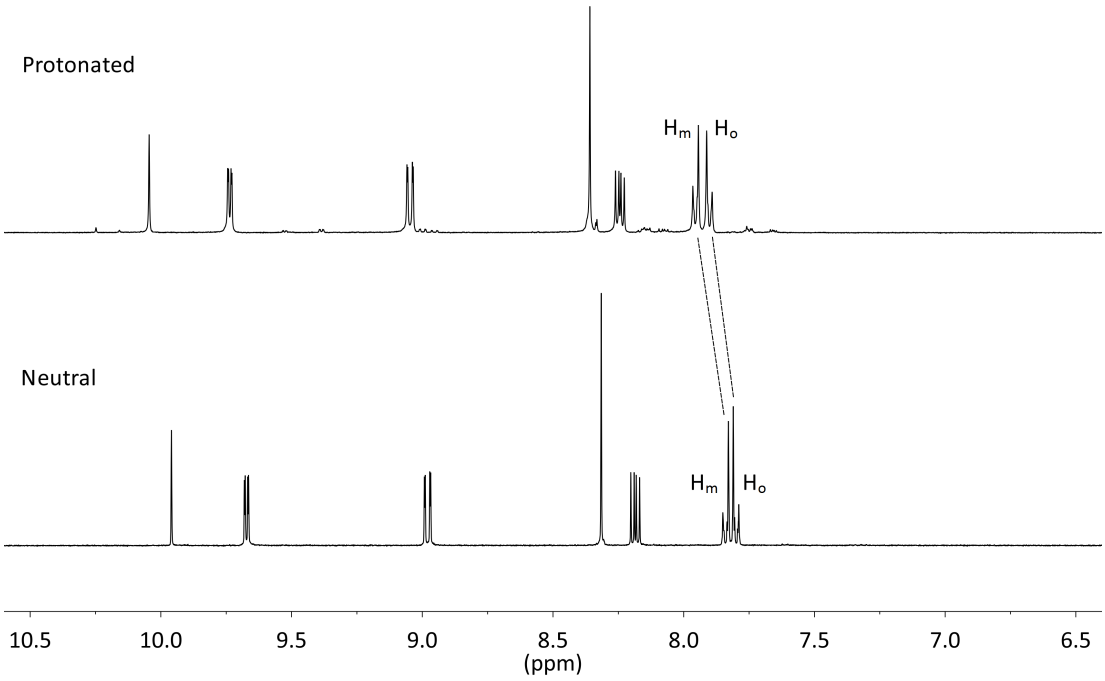


Figure 3.2: $^{1}$H NMR spectra of the neutral complex *fac*-[Re(**phen**)$(CO)_3$(**Tbz**)], **13** (bottom) compared to the protonated species, *fac*-[Re(**bipy**)$(CO)_3$(**Tbz**H)]$^{+}$, **23** (top).

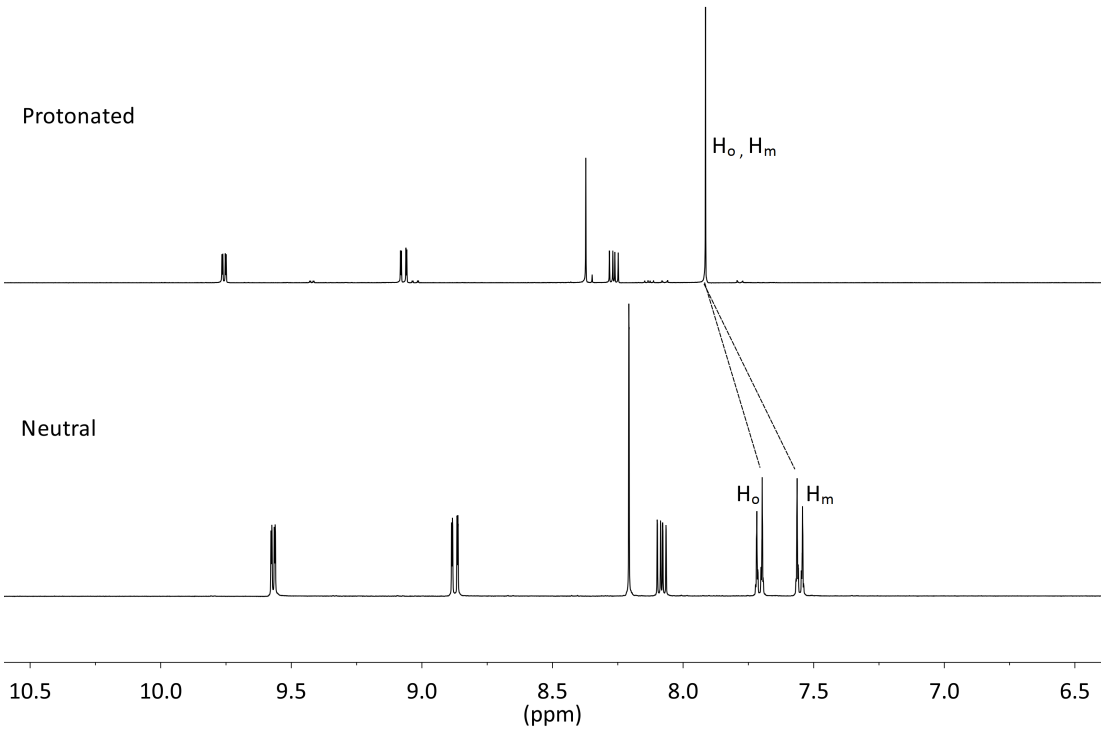


Figure 3.3: $^{1}$H NMR spectra of the neutral complex *fac*-[Re(**phen**)$(CO)_3$(**Tcya**)], **17** (bottom) compared to the protonated species, *fac*-[Re(**phen**)$(CO)_3$(**Tcya**H)]$^{+}$ , **25** (top).

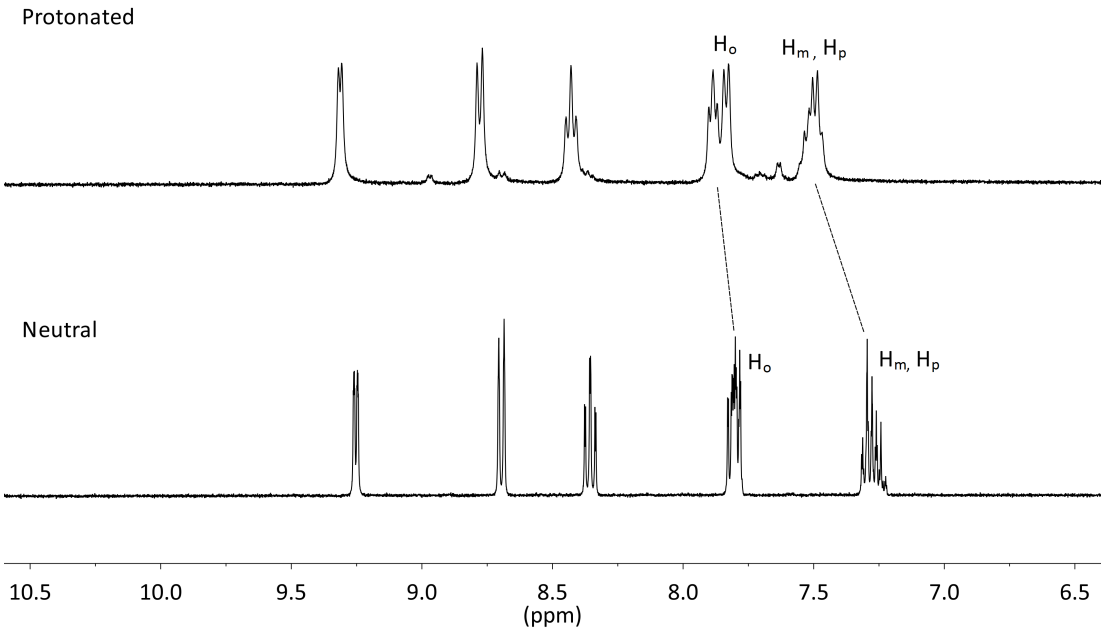


Figure 3.4: $^{1}$H NMR spectra of the neutral complex *fac*-[Re(**bipy**)$(CO)_3$(**Tph**)], **12** (bottom) compared to the protonated species, *fac*-[Re(**bipy**)$(CO)_3$(**Tph**H)]$^{+}$ , **22** (top).

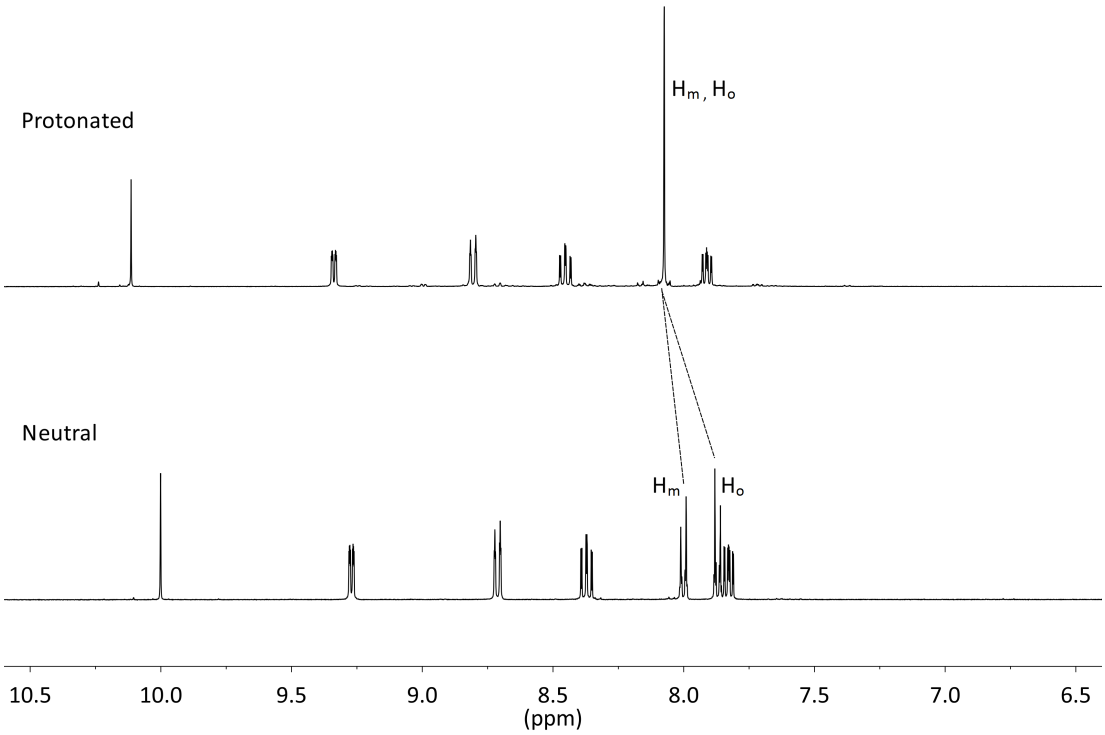


Figure 3.5: $^{1}$H NMR spectra of the neutral complex *fac*-[Re(**bipy**)$(CO)_3$(**Tbz**)], **14** (bottom) compared to the protonated species, *fac*-[Re(**bipy**)$(CO)_3$(**Tbz**H)]$^{+}$, **24** (top).

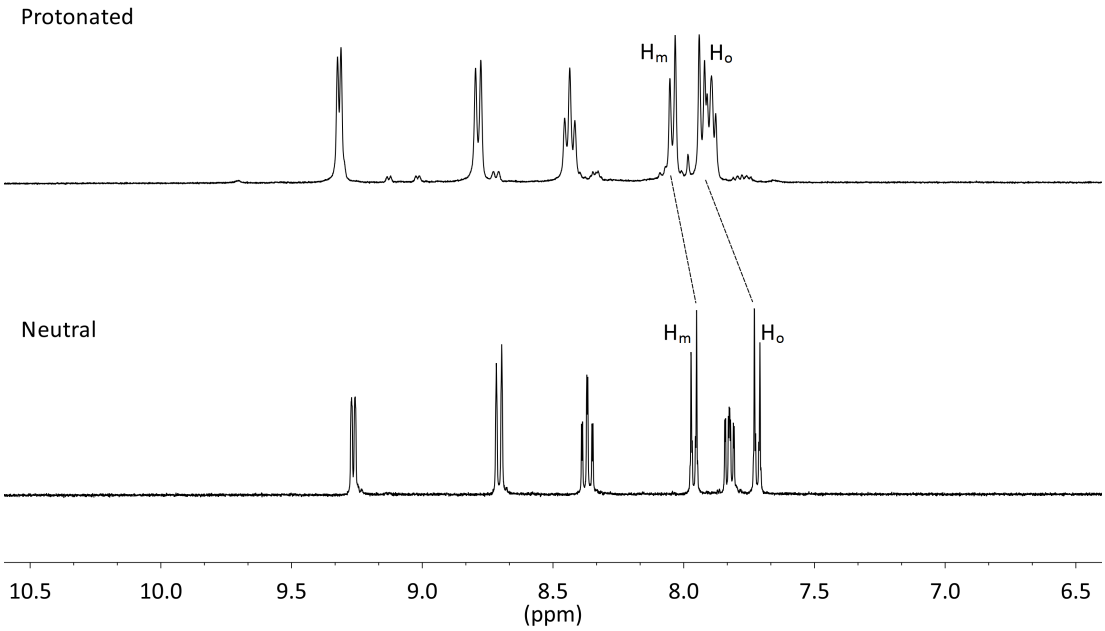


Figure 3.6: Comparison of the $^{1}$H NMR spectra of the neutral *fac*-[Re(**bipy**)$(CO)_3$(**Tcya**)], **18** (bottom) with that of the protonated species, *fac*-[Re(**bipy**)$(CO)_3$(**Tcya**H)]$^{+}$, **26** (top).

NMR measurements were carried out in acetone-$d_6$ and Figure 3.1 to Figure 3.6 illustrate the shift in the $^1$H NMR signals upon protonation. In particular, upon the protonation of *fac*-[Re(**bipy**)$(CO)_3$(**Tbz**)] (**14**) and *fac*-[Re(**phen**)$(CO)_3$(**Tcya**)] (**17**) the $H_{ortho}$ and $H_{meta}$ peaks in the corresponding protonated species (**24** and **25** respectively) collapse, forming a singlet (as seen in Figure 3.5 and Figure 3.3). The collapse of $H_{ortho}$ and $H_{meta}$ suggests that the electron withdrawing substituent on the phenyl ring (ie: -CHO or -CN) has equal electron withdrawing power to that of the tetrazole ring. In the neutral complexes the -R substituent was the stronger electron withdrawing group as the $H_{meta}$ signals were more deshielded with respect to $H_{ortho}$ (Table 3.3.2). Upon protonation the $H_{ortho}$ becomes deshielded and collapses with the $H_{meta}$. The $^1$H NMR data supports a chemoselective protonation at the tetrazole ring, making the downfield shift of the diimine protons the result of indirect shielding. In the cases where the $H_{ortho}$ and $H_{meta}$ are still resolved after protonation, a downfield shift is observed. Deshielding of these peaks also suggests that the tetrazole ring has a stronger -I effect compared to the neutral complexes (where +M from the tetrazole was dominant, see section 2.3.2.2 on page 42). This is not unexpected as the tetrazolato ligand is now neutral, with reduced electron density and therefore a reduced in +M effect. Interestingly, reduction in +M could also be associated with a twisting of the phenyl and tetrazole rings.

An investigation of Ru tetrazolato complexes by Stagni *et al.*[114] observed protonation at the N4 atom of the monocoordinated tetrazole ligand. Based on that study it is assumed that the same occurs for the Re(I) complexes. Usually when there is coordination at the N4 position on a tetrazole, there is a reduction of interannular conjugation due to the twisted nature acquired by the aryl and tetrazole rings (as discussed in Chapter Two).[166,167] Scheme 2.5 shows the difference in the planarity of the phenyl and tetrazole rings when there is coordination at either the N1 or N2 site (or in this case N4, not N1).[166,167] As discussed in Chapter Two, the aryl and tetrazolato rings are planar in the neutral Re(I) complexes, as the ligand is coordinated to the rhenium via the N2 atom,[170] (Scheme 2.5). Protonation at N4 could be causing steric interactions, leading to out of plane rotation of the rings and therefore a reduction in interannular conjugation. There are two competing coordination sites that are both occupied and so the studies of Butler[165–167] may not be completely applicable to this case. Analysis of

the tetrazolic carbon ($C_t$) can provide insight into the coordination of the tetrazolato ligand. Unfortunately the $C_t$ resonance was not observed in the protonated samples. Nonetheless, protonation at N4 was observed in the solid state by analysis of the structures by X-ray diffraction, see section 3.3.2.

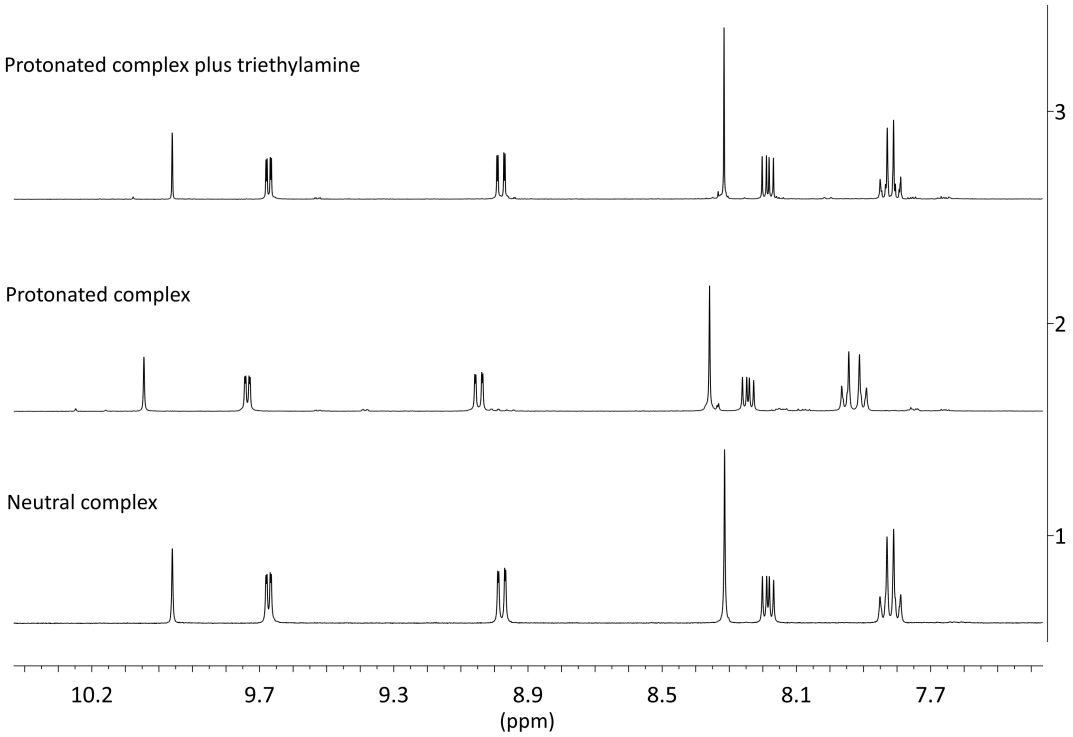


Figure 3.7: $^1$H NMR spectra of *fac*-[Re(**phen**)$(CO)_3$(**Tbz**)], **13** (1), compared to the protonated species, *fac*-[Re(**phen**)$(CO)_3$(**Tbz**H)]$^+$, **23** (2) and the product from the addition of triethylamine to a solution of *fac*-[Re(**phen**)$(CO)_3$(**Tbz**H)]$^+$, **23** (3).

When triethylamine was added to an NMR solution of the protonated complex there was an upfield shift of the $^1$H NMR resonances, which matched with those values of the neutral starting complex. Figure 3.7 compares the $^1$H NMR spectra of *fac*-[Re(**phen**)$(CO)_3$(**Tbz**)] (**13**), *fac*-[Re(**phen**)$(CO)_3$(**Tbz**H)]$^+$ (**23**) and the result of **23** + $Et_3N$. It is clear that the reaction is reversible as the signals in the spectrum of *fac*-[Re(**phen**)$(CO)_3$(**Tbz**)] (**13**) match well with those of the spectrum produced from the addition of triethylamine to the protonated species, **23**.

During NMR experiments of the protonated species (in acetone-$d_6$) small but detectable peaks were observed in the baseline over time. Some of these peaks could be assigned to the corresponding neutral starting material, as illustrated in Figure 3.8. No such observations were noticed for the neutral complexes, which were stable in

solution over extended time periods. Figure 3.8 (top) also shows the presence of other peaks in the baseline. These peaks were minor and therefore not characterised but could be ascribed to the formation of a solvato-complex or degradation of the cationic Re(I). For one of the cationic Re(I) complexes, a dimeric rhenium species was isolated. It is discussed in section 3.3.2 but shows two Re(I) centres coordinated to one tetrazole ligand. This suggests that the tetrazole ligand, once protonated, can become labile and therefore degradation or solvato-complexes in solution are not unexpected. The unstable nature of these types of complexes is also known from the methylation experiments, discussed in Chapter Four.

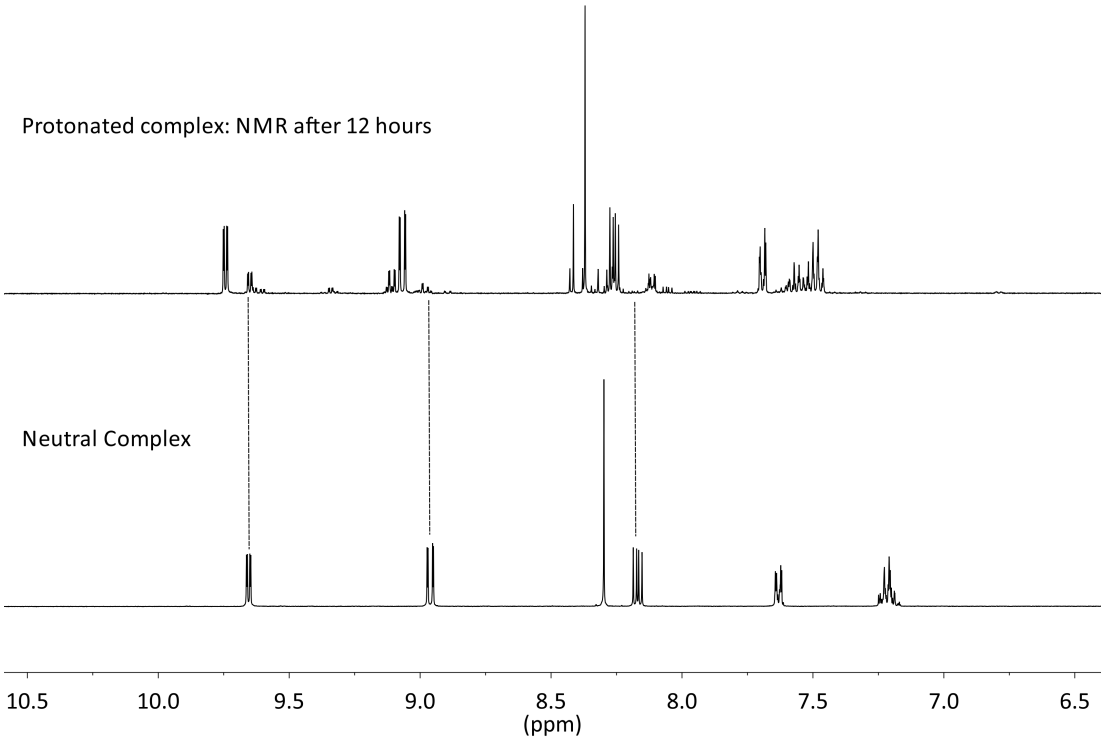


Figure 3.8: $^{1}$H NMR spectra of *fac*-[Re(**phen**)$(CO)_3$(**Tph**)], **11** (bottom), compared to the spectra of the protonated species, *fac*-[Re(**phen**)$(CO)_3$(**Tph**H)]$^{+}$, **21** (top) taken 12 hours after the sample was prepared.

### 3.3.2 X-Ray Crystallography

Table 3.3.3: Torsion angles between the aryl and tetrazole rings in the protonated Re(I) complexes.

| Rhenium Complex | Deviation from Coplanarity (°) |
|---|---|
| *fac*-[Re(**phen**)$(CO)_3$(**Tph**H)]$^+$ (**21**) | 7.65 |
| *fac*-[Re(**phen**)$(CO)_3$(**Tph**H)]$^+$ (**21**$\cdot$ 0.25$Et_2O$) | 26.23 |
| *fac*-[Re(**bipy**)$(CO)_3$(**Tph**H)]$^+$ (**22**) | 58.12 |
| *fac*-[Re(**phen**)$(CO)_3$(**Tbz**H)]$^+$(**23**) | 5.31 |
| *fac*-[Re(**bipy**)$(CO)_3$(**Tbz**H)]$^+$(**24**) | 20.97 |
| *fac*-[Re(**phen**)$(CO)_3$(**Tcya**H)]$^+$ (**25**) | 5.95 |
| *fac*-[Re(**bipy**)$(CO)_3$(**Tcya**H)]$^+$(**26**) | 24.18 |

Single crystals of the protonated rhenium complexes were obtained by slow diffusion of diethyl ether into a DCM solution of the complex, with a few drops of dilute triflic acid. For all of the protonated species the tetrazole ligand is coordinated to Re via the N2 atom and protonation occurs at N4. The only exception was *fac*-[Re(**bipy**)$(CO)_3$(**Tph**H)]$^+$(**24**), where crystallographic analysis revealed isolation of a dimeric rhenium species. All of the crystal structures are shown in Figure 3.9 and Figure 3.10. Interestingly, crystallisation of *fac*-[Re(**phen**)$(CO)_3$(**Tph**H)]$^+$ (**21**) produced two different looking crystals when visualised under a UV lamp. One set appeared yellow under the light and were small and flat while the other set looked more blue/green and had a prism shape. Analysis revealed that they were both the protonated complex however one set had crystallised with diethyl ether in the lattice.

The deviation from coplanarity observed in the solid state can aid in understanding the degree of twisting between the aryl and tetrazole rings caused by protonation at N4. Table 3.3.3 shows the deviation from coplanarity between the rings, calculated by analysis of their torsion angle. The complexes vary in the level of twisting between the

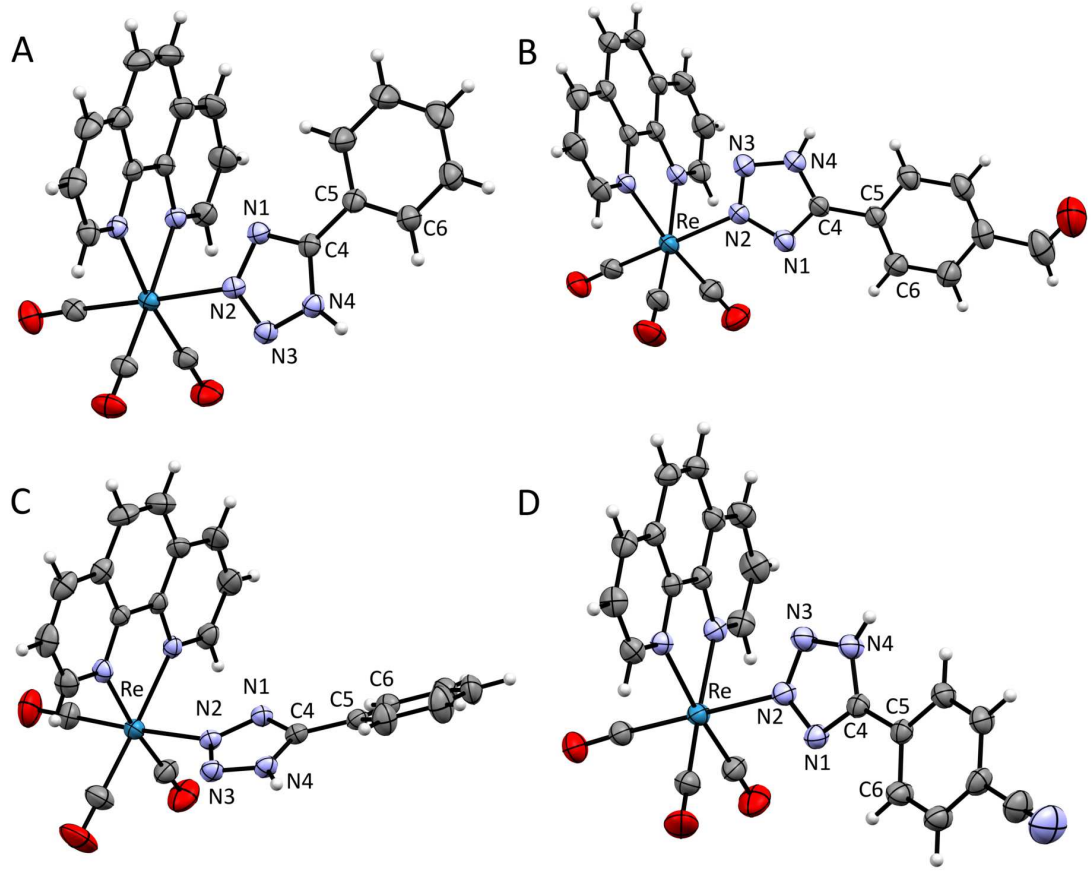


Figure 3.9: X-ray crystal structures of *fac*-[Re(**phen**)$(CO)_3$(**Tph**H)]$^+$ (**21**, A), *fac*-[Re(**phen**)$(CO)_3$(**Tbz**H)]$^+$ (**23**, B), *fac*-[Re(**phen**)$(CO)_3$(**Tph**H)]·0.25$Et_2O$ (**21**, C), and *fac*-[Re(**phen**)$(CO)_3$(**Tcya**H)]$^+$ (**25**, D) where thermal ellipsoids have been drawn at 30% probability. The triflate counter ion and $Et_2O$ has been omitted for clarity.

aryl and tetrazole rings however, generally the complexes do not greatly deviate from coplanarity. The two crystals of **21** have different torsion angles which could indicate that the relative orientations of the aryl and tetrazole rings of the protonated complexes in the solid state are mainly determined by crystal packing effects rather than electronic conjugation. This makes it difficult to conclude the effect protonation has on the degree of twisting between the two rings. Nonetheless, when comparing to the deviation from colplanarity of the protonated complexes to the neutral species, there does not appear to be a significant difference (see section 2.3.3). The main crystal structure that clearly has a significant level of twisting is that of the dimeric rhenium complex formed from crystallisation of the protonated species; *fac*-[Re(**bipy**)$(CO)_3$(**Tph**H)]$^+$ (**12**). Figure 3.10 A, shows that there is significant twisting of the rings, especially compared to the other protonated complexes. This is expected as the bulky rhenium fragment is coordinated to both the N2 and the N4 atoms of the tetrazole ligand.

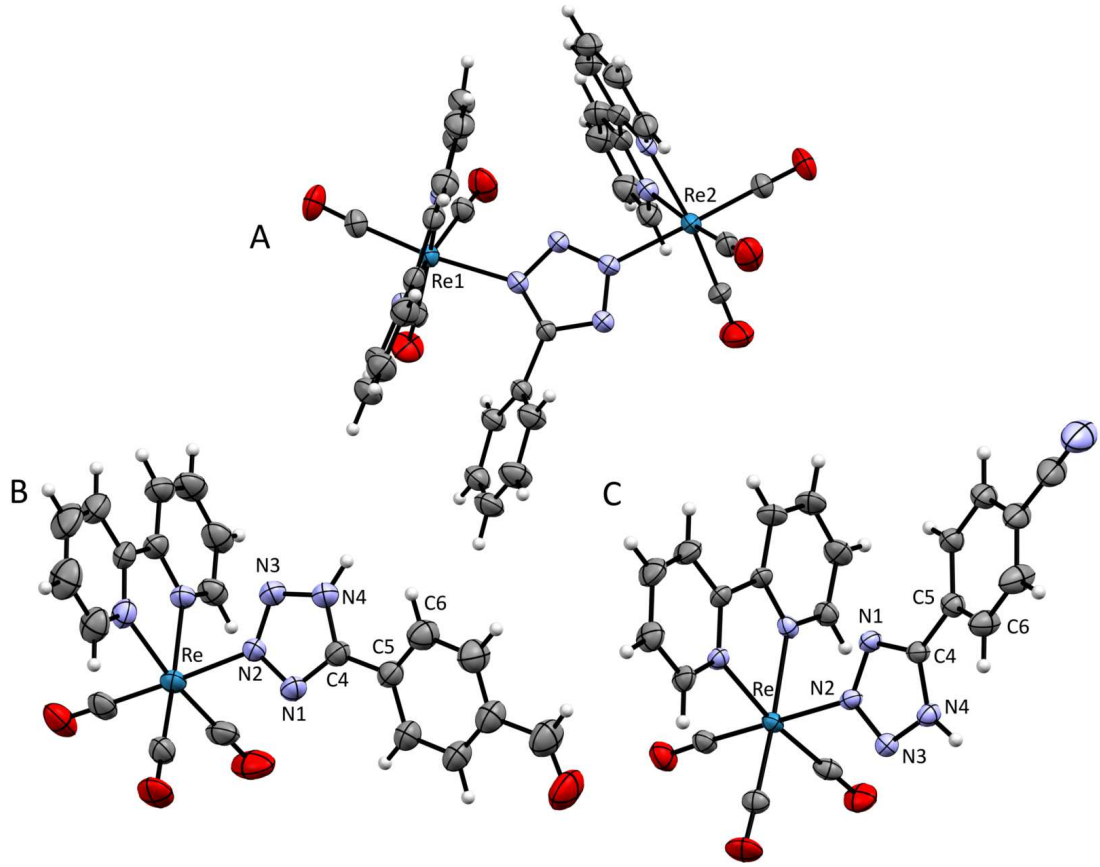


Figure 3.10: X-ray crystal structures of *fac*-[Re(**bipy**)$(CO)_3$(**Tph**H)]$^+$ (dimeric form, **22**, A), *fac*-[Re(**bipy**)$(CO)_3$(**Tbz**H)]$^+$ (**24**, B) and *fac*-[Re(**bipy**)$(CO)_3$(**Tcya**H)]$^+$ (**26**, D) where thermal ellipsoids have been drawn at 30% probability. The triflate counter ion has been omitted for clarity.

In all of the crystal structures, there is hydrogen bonding present between the proton on the tetrazole ring, N4-H (which acts as a donor) and on the oxygen atoms of the triflate anion (which acts as the acceptor). The crystal structure of complex **25** shows weak $\pi$ stacking between the aryl rings of tetrazole ligands, with a distance of 3.8 Å between the centroid of the two rings. The only other protonated complex exhibiting $\pi$-$\pi$ interactions is **25**. There is moderate interaction between the centre rings of the phenanthroline ligands with a distance of 3.5 Å.

### 3.3.3 Photophysical Investigation

Table 3.3.4: Absorption data for the protonated rhenium tetrazolato complexes at $10^{-5}$ M in DCM.

| Rhenium Complex | Absorption $\lambda_{max}$/nm ($\varepsilon/10^4 M^{-1}cm^{-1}$) |
|---|---|
| *fac*-[Re(**phen**)$(CO)_3$(**Tph**H)]$^+$ (**21**) | 254 (1.325), 335 (0.240) |
| *fac*-[Re(**bipy**)$(CO)_3$(**Tph**H)]$^+$(**22**) | 245 (1.556), 319 (0.520), 352 (0.185) |
| *fac*-[Re(**phen**)$(CO)_3$(**Tbz**H)]$^+$(**23**) | 272 (1.262), 351 (0.940) |
| *fac*-[Re(**bipy**)$(CO)_3$(**Tbz**H)]$^+$(**24**) | 266 (1.291), 319 (0.410), 356 (0.508) |
| *fac*-[Re(**phen**)$(CO)_3$(**Tcya**H)]$^+$ (**25**) | 257 (1.650), 342 (0.180) |
| *fac*-[Re(**bipy**)$(CO)_3$(**Tcya**H)]$^+$(**26**) | 254 (1.010), 319 (0.310), 350 (0.120) |

Table 3.3.5: Emission data for the protonated rhenium tetrazolato complexes.

| Rhenium | Emission 298 K | | | | |
|---|---|---|---|---|---|
| Complex[a] | $\lambda_{max}$(nm) | $\tau$ ($\mu$s)[b] | $\tau$ ($\mu$s)[c] | $\phi^b$ | $\phi^c$ |
| *fac*-[Re(**phen**)$(CO)_3$(**Tph**H)]$^+$ (**21**) | 538 | 1.293 | 2.505 | 0.328 | 0.470 |
| *fac*-[Re(**bipy**)$(CO)_3$(**Tph**H)]$^+$(**22**) | 548 | 0.596 | 0.660 | 0.120 | 0.135 |
| *fac*-[Re(**phen**)$(CO)_3$(**Tbz**H)]$^+$(**23**) | 534 | 1.333 | 2.186 | 0.105 | 0.206 |
| *fac*-[Re(**bipy**)$(CO)_3$(**Tbz**H)]$^+$(**24**) | 546 | 0.612 | 0.825 | 0.145 | 0.276 |
| *fac*-[Re(**phen**)$(CO)_3$(**Tcya**H)]$^+$ (**25**) | 534 | 1.819 | 2.948 | 0.296 | 0.540 |
| *fac*-[Re(**bipy**)$(CO)_3$(**Tcya**H)]$^+$(**26**) | 546 | 0.655 | 0.874 | 0.103 | 0.204 |

[a]; All data for complexes in $10^{-5}$ M DCM solutions and all quantum yields measured against rhodamine 101, [b]; air-equilibrated samples, [c]; degassed ($O_2$ free) samples.

The absorption profiles for the protonated rhenium complexes are relatively similar and generally exhibit intense transitions in the high energy UV region, between 245-272 nm and lower intensity bands between 319-352 nm. To further interpret the photophysical results, the energetics and absorption spectra of the complexes were simulated with time-dependent density functional theory using GAUSSIAN09.[181] The crystal isolated for *fac*-[Re(**bipy**)$(CO)_3$(**Tph**H)]$^+$ (**22**) was a dimeric complex and as there was no evidence of the dimer in solution, DFT calculations were carried out assuming protonation was the same as the other Re(I) complexes (monomer, with protonation on the N4). As

discussed in Chapter Two, the lowest energy excited state for the neutral rhenium complexes was characterised as an MLLCT. For the protonated rhenium species, the lowest energy excited state seems to originate predominantly from HOMO-$n$→LUMO transitions, where $n$ = 0-2. Further computational detail including listed transitions can be found in previously published work.[201] Figure 3.11 and Figure 3.12 show the localisation of the HOMO and LUMO calculated for the protonated complexes. Localisation of the HOMO-1 and HOMO-2 for all protonated rhenium complexes are included in A2.2 and have similar localisation to the HOMO. The HOMO type orbitals are mainly localised over the 5d orbitals of the Re center (with a small contribution from the CO ligands) however there is no significant contribution from the tetrazole $\pi$ system. The LUMO type orbitals are exclusively localised on the diimine ligand. Therefore, the lowest energy transition observed in the absorption profiles is assigned to an MLCT (Re → diimine). The high energy transitions seen in the absorption spectra around 245-272 nm can be assigned to $\pi - \pi^*$ IL transitions.

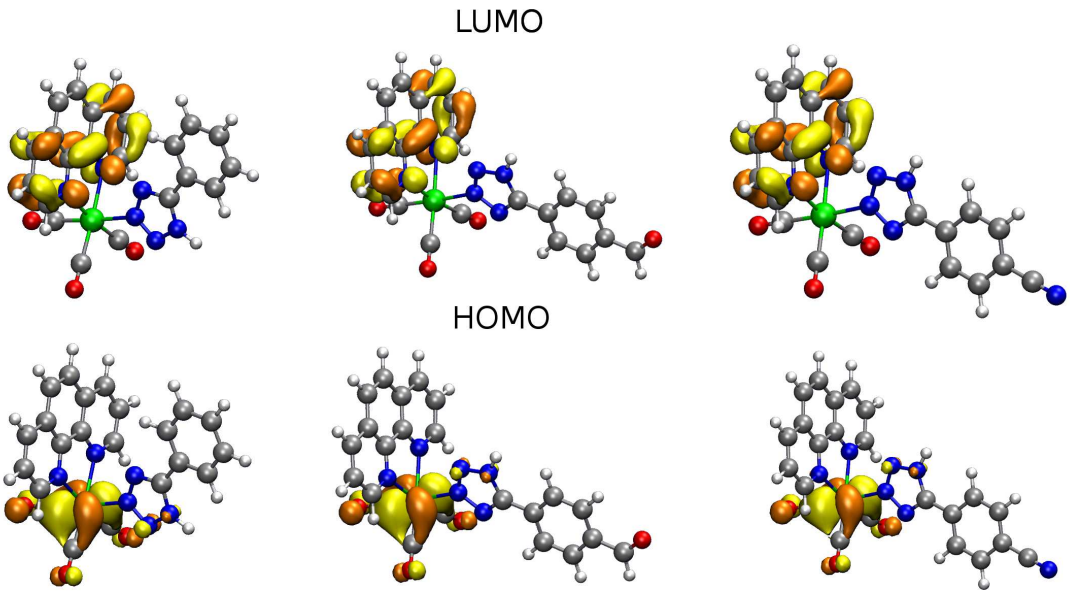


Figure 3.11: Localisation of the HOMO and LUMO for the protonated **phen** complexes (left to right); **21**, **23** and **25** .

Table 3.3.4 shows that the MLCT absorbance band for the **bipy** species are all red shifted with respect to their **phen** analogues. As was observed for the neutral **phen** complexes in Chapter Two, the LUMO is not delocalised over the entire diimine ligand (Figure 3.11) and therefore mimics a 2,2'-bipyridine-3,3'-dimethyl species.

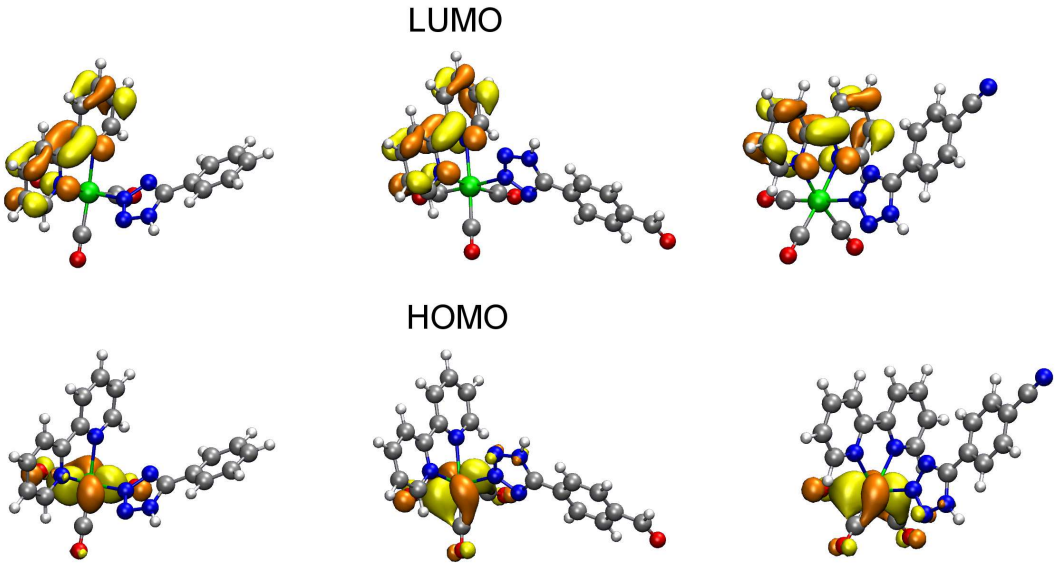


Figure 3.12: Localisation of the HOMO and LUMO for the protonated **bipy** complexes (left to right); **22**, **24** and **26**.

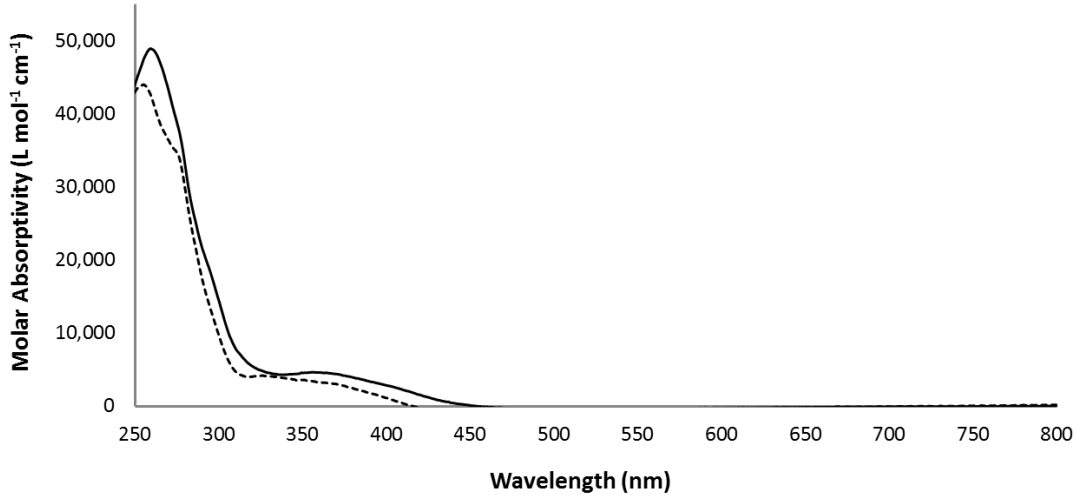


Figure 3.13: Absorption of the neutral rhenium complex, *fac*-[Re(**phen**)$(CO)_3$(**Tph**)] (**11**, solid line) compared to the absorption of the protonated species, *fac*-[Re(**phen**)$(CO)_3$(**TphH**)]$^+$ (**21**, dashed line) in DCM.

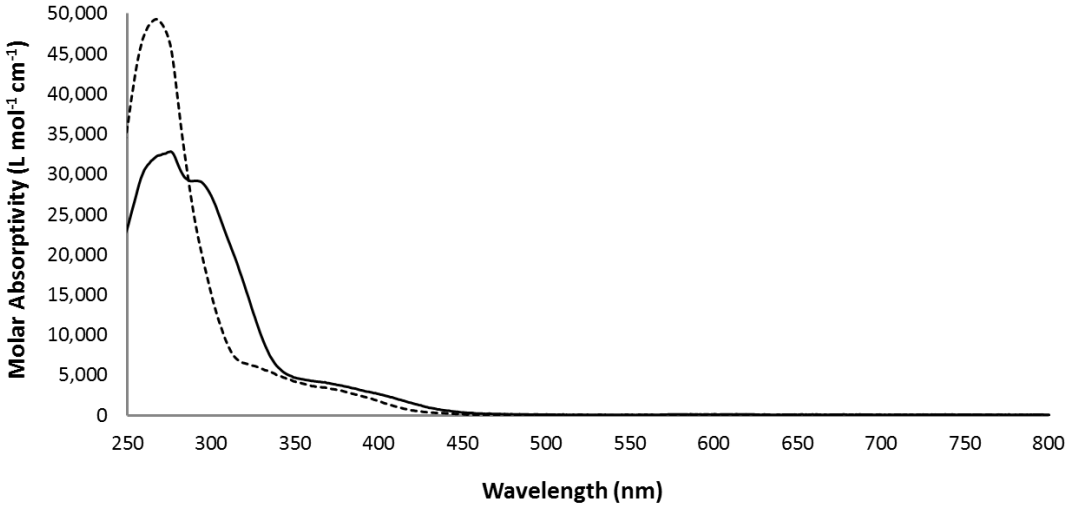


Figure 3.14: Absorption of the neutral rhenium complex, *fac*-[Re(**phen**)$(CO)_3$(**Tbz**)] (**13**, solid line) compared to the absorption of the protonated species, *fac*-[Re(**phen**)$(CO)_3$(**TbzH**)]$^+$ (**23**, dashed line) in DCM.

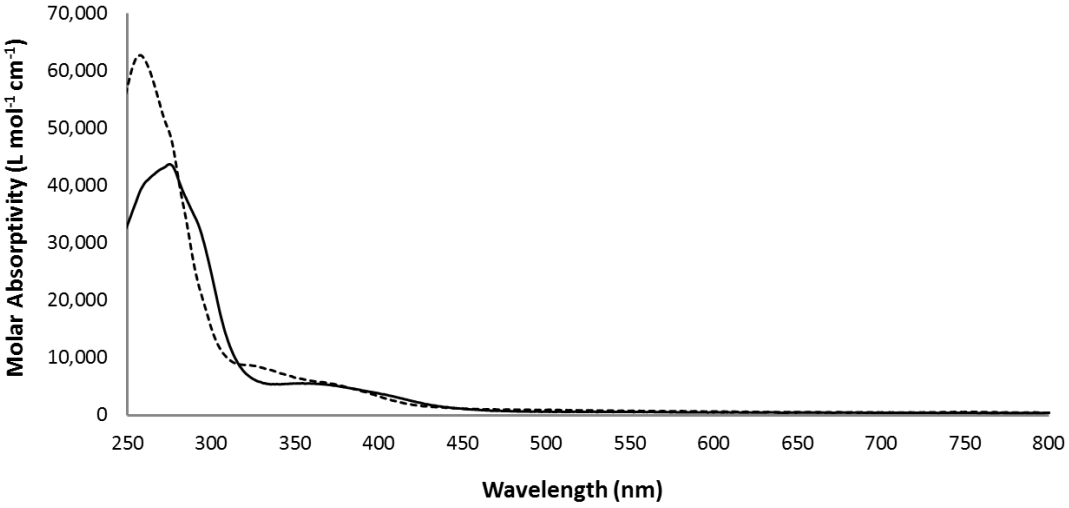


Figure 3.15: Absorption of the neutral rhenium complex, *fac*-[Re(**phen**)$(CO)_3$(**Tcya**)] (**17**, solid line) compared to the absorption of the protonated species, *fac*-[Re(**phen**)$(CO)_3$(**TcyaH**)]$^+$ (**25**, dashed line) in DCM.

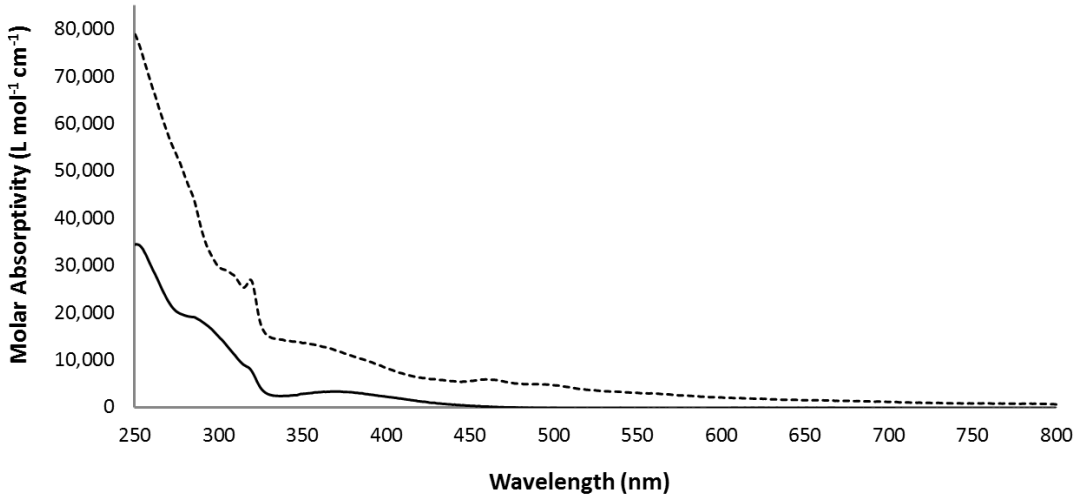


Figure 3.16: Absorption of the neutral rhenium complex, *fac*-[Re(**bipy**)$(CO)_3$(**Tph**)] (**12**, solid line) compared to the absorption of the protonated species, *fac*-[Re(**bipy**)$(CO)_3$(**TphH**)]$^+$ (**22**, dashed line) in DCM.

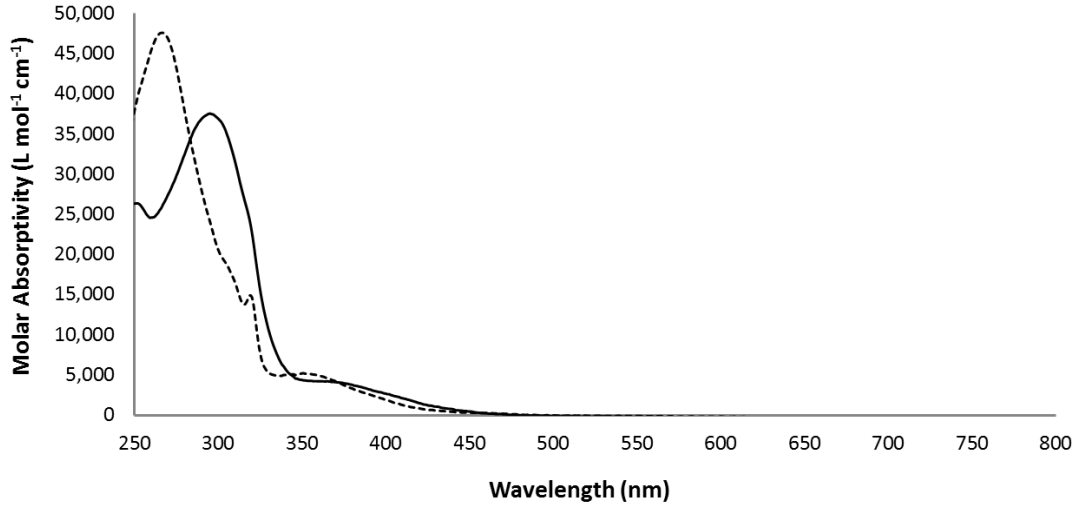


Figure 3.17: Absorption of the neutral rhenium complex, *fac*-[Re(**bipy**)$(CO)_3$(**Tbz**)] (**14**, solid line) compared to the absorption of the protonated species, *fac*-[Re(**bipy**)$(CO)_3$(**TbzH**)]$^+$ (**24**, dashed line) in DCM.

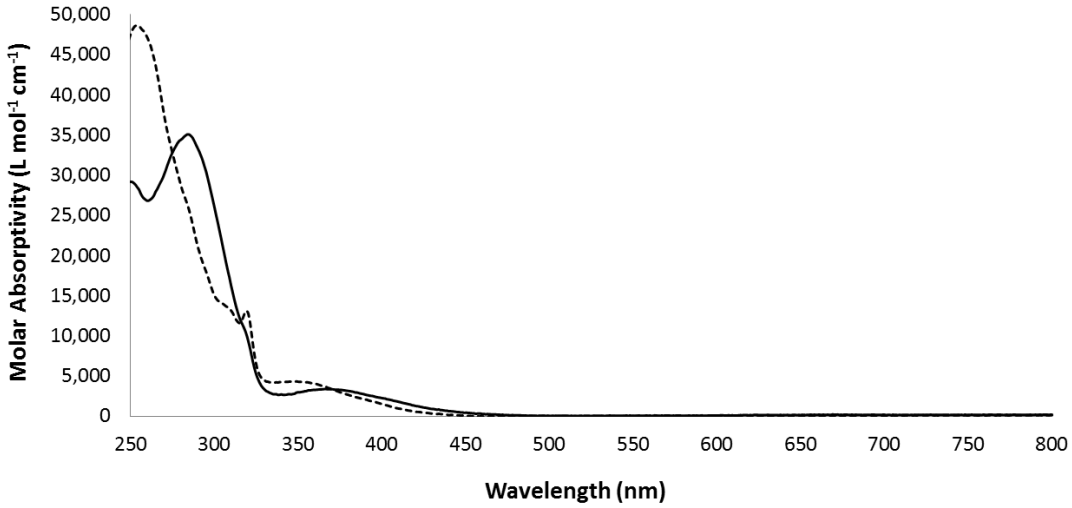


Figure 3.18: Absorption of the neutral rhenium complex, *fac*-[Re(**bipy**)$(CO)_3$(**Tcya**)] (**18**, solid line) compared to the absorption of the protonated species, *fac*-[Re(**bipy**)$(CO)_3$(**TcyaH**)]$^+$ (**26**, dashed line) in DCM.

Comparing the absorption profiles of the protonated and neutral species (Figure 3.13 to Figure 3.18), an expected hypsochromic shift of both the IL and CT bands is observed. This can be explained by protonation reducing the electron density around the Re metal centre (confirmed by IR spectroscopy). The decrease in electron density experienced by the tetrazole ring upon protonation causes indirect stabilisation of the HOMO type orbitals on the Re centre, leading to an increase in the HOMO-LUMO energy gap.

The emission profiles of the protonated rhenium species are from a pure $^3$MLCT state (disregarding the small contribution of the CO ligands to the HOMO) unlike the neutral complexes where emission was from a mixed $^3$MLLCT state. The contribution of the tetrazole to the lowest energy excited state has been removed in the protonated species. This explains why the emission profiles for the three **phen** complexes (Figure 3.19) and the three **bipy** complexes (Figure 3.20) are essentially the same.

The protonated rhenium complexes containing **phen** all have a blue shifted emission in comparison to the **bipy** analogues, as observed for the neutral complexes. Table 3.3.5 shows the emissive properties of the protonated Re(I) complexes. The $\tau$ of the protonated **phen** complexes are longer compared to the **bipy** analogues and the $\phi$ are generally higher.

This same trend was observed for the neutral complexes discussed in Chapter Two.

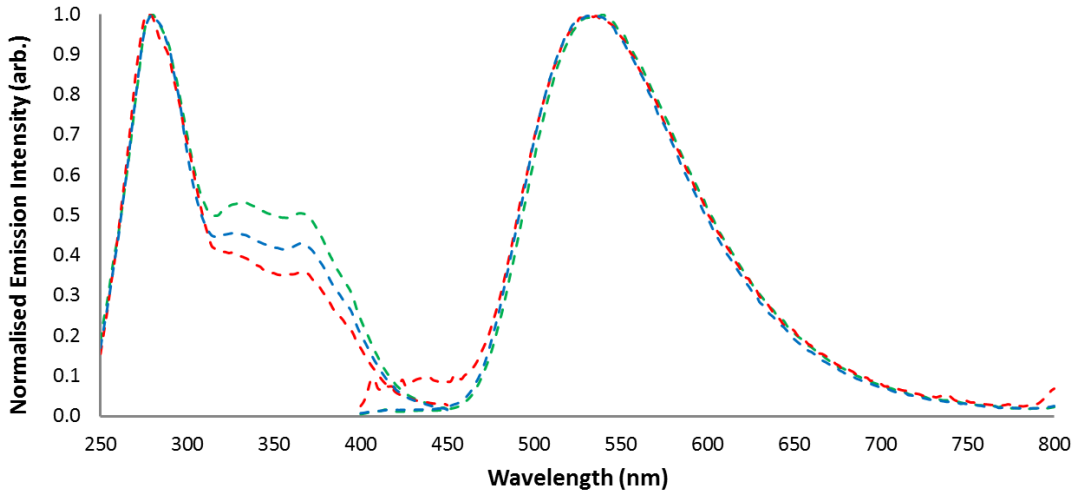


Figure 3.19: Excitation and emission of *fac*-[Re(**phen**)$(CO)_3$(**TphH**)]$^+$ (**21**, green), *fac*-[Re(**phen**)$(CO)_3$(**TbzH**)]$^+$ (**23**, red), and *fac*-[Re(**phen**)$(CO)_3$(**TcyaH**)]$^+$ (**25**, blue) in DCM.

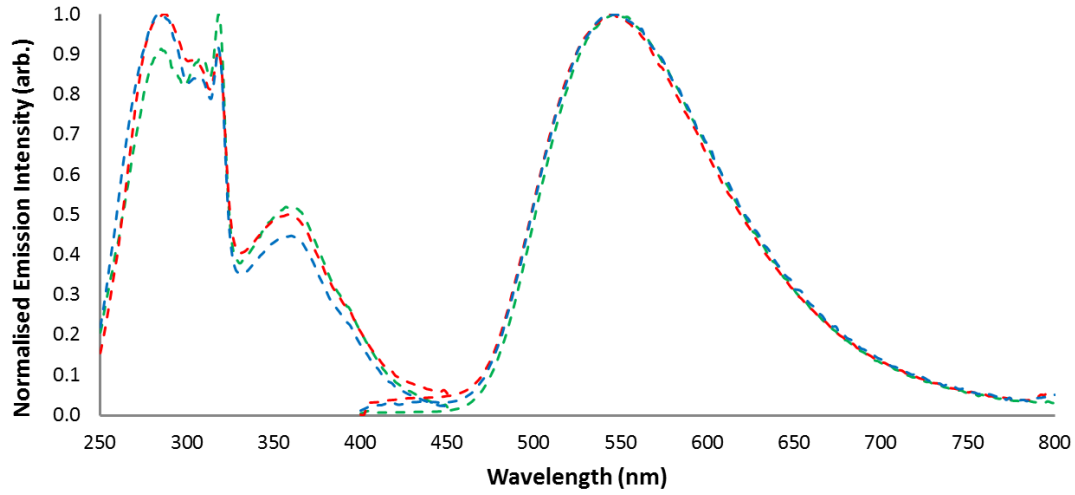


Figure 3.20: Excitation and emission of *fac*-[Re(**bipy**)$(CO)_3$(**TphH**)]$^+$ (**22**, green), *fac*-[Re(**bipy**)$(CO)_3$(**TbzH**)]$^+$ (**24**, red), and *fac*-[Re(**bipy**)$(CO)_3$(**TcyaH**)]$^+$(**26**, blue) in DCM.

The emission of the protonated species is sensitive to the presence of molecular oxygen, supporting the assignment of triplet state phosphorescence.[52,54] Upon de-oxygenating the solutions, the measured $\tau$ and $\phi$ increase (Table 3.3.5). The predominantly charge transfer nature of the emissive state is also supported by the rigidochromic effect observed upon freezing the solutions.[127,192,193] Table 3.3.6 illustrates the blue shifted $\lambda_{em}$ observed when DCM solutions are measured at 77 K.

Table 3.3.6: Emission data for the protonated rhenium tetrazolato complexes at 77 K in DCM.

| Rhenium Complex | Emission 77K | |
|---|---|---|
| | $\lambda_{max}$ (nm) | $\tau$ ($\mu$s) |
| *fac*-[Re(**phen**)(CO)$_3$(**TphH**)]$^+$ (**21**) | 500 | 5.25 |
| *fac*-[Re(**bipy**)(CO)$_3$(**TphH**)]$^+$(**22**) | 502 | 3.54 |
| *fac*-[Re(**phen**)(CO)$_3$(**TbzH**)]$^+$(**23**) | 496 | 9.57 |
| *fac*-[Re(**bipy**)(CO)$_3$(**TbzH**)]$^+$(**24**) | 502 | 3.38 |
| *fac*-[Re(**phen**)(CO)$_3$(**TcyaH**)]$^+$ (**25**) | 508 | 5.42 |
| *fac*-[Re(**bipy**)(CO)$_3$(**TcyaH**)]$^+$(**26**) | 534 | 2.32 (47%), 4.74 (53%) |

Unlike the comparison of the absorption profiles for the neutral and protonated complexes, there is a very obvious and significant change in the emission profiles upon protonation. The protonated complexes all still exhibit broad structureless emission profiles however they are significantly blue shifted and have increased intensity compared to the neutral precursors. Aliquots of triflic acid were sequentially added to dilute solutions of the neutral Re(I) complexes and emission spectra recorded after each addition. The top spectra in Figure 3.21 and Figure 3.23 shows the gradual change in emission occurring upon protonation of the complex. The bottom spectra show the normalised emission, highlighting the blue shift.

Upon excitation of the $^1$MLCT band at *ca*. 370 nm, the neutral **Re(I)** tetrazolato complexes display a single broad and structureless emission in the range of 584-606 nm (see Chapter Two). After formation of their conjugate acids (**[ReH]$^+$**), excitation of the $^1$MLCT band at *ca*. 368 nm, shifts the emission to bright green, between 534-548 nm for both the **phen** and **bipy** complexes.

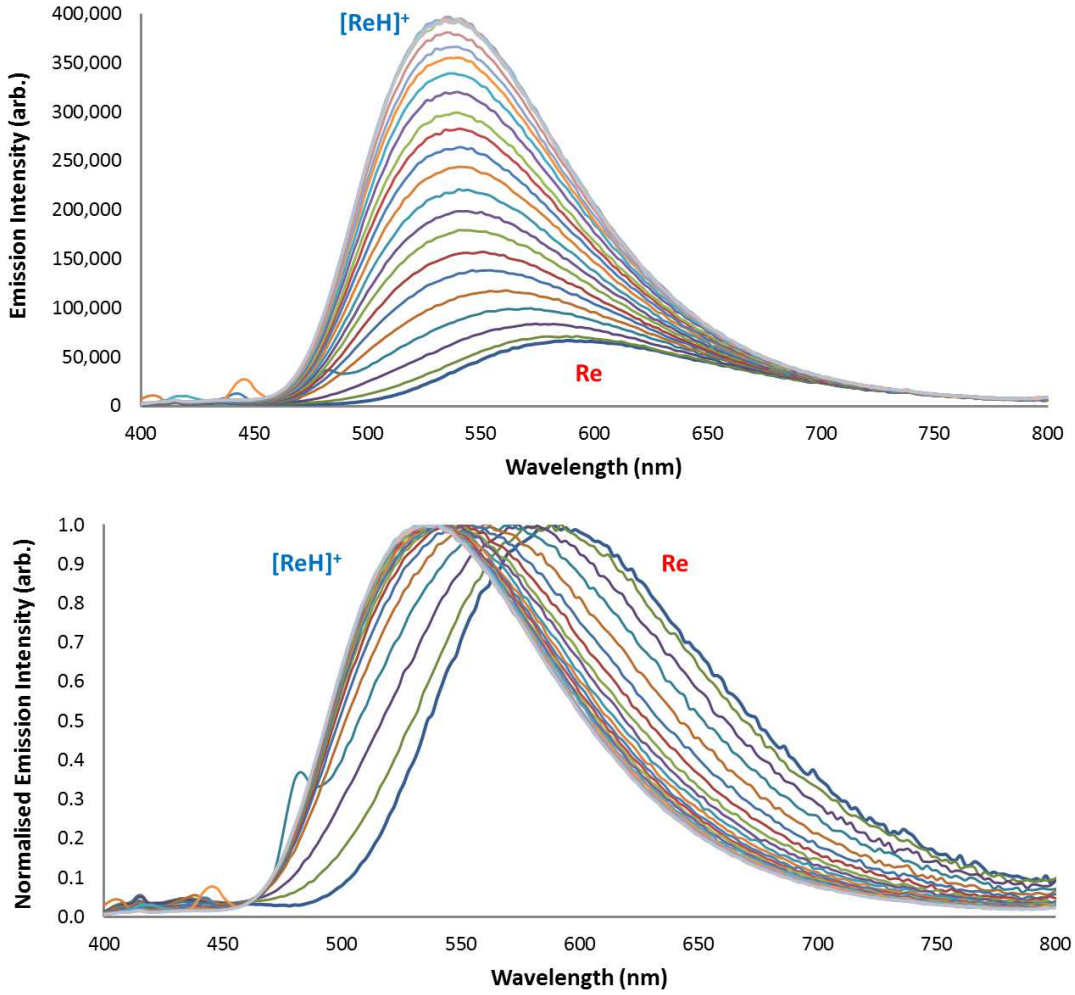


Figure 3.21: (Top) Steady state emission spectra showing the change occurring upon the sequential addition of triflic acid to *fac*-[Re(**phen**)$(CO)_3$(**Tph**)] (**11**, Re) to form the protonated complex, *fac*-[Re(**phen**)$(CO)_3$(**TphH**)]$^+$ (**21**, [ReH]$^+$). (Bottom) Normalised emission spectra to highlight the blue shift that occurs upon protonation.

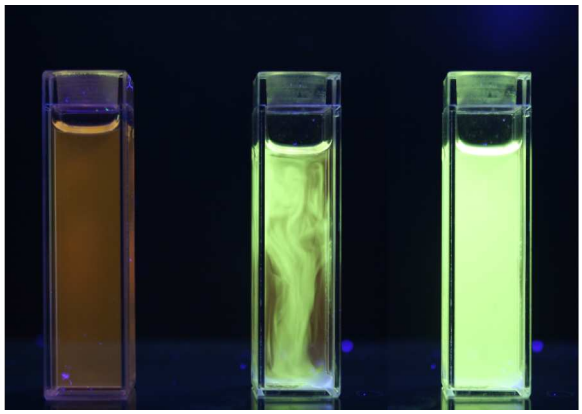

Figure 3.22: Cuvettes showing the starting complex, *fac*-[Re(**phen**)$(CO)_3$(**Tph**)] (**11**, left), the protonated *fac*-[Re(**phen**)$(CO)_3$(**TphH**)]$^+$ (**21**, right) and the intermediate mixture of the two complexes (middle).

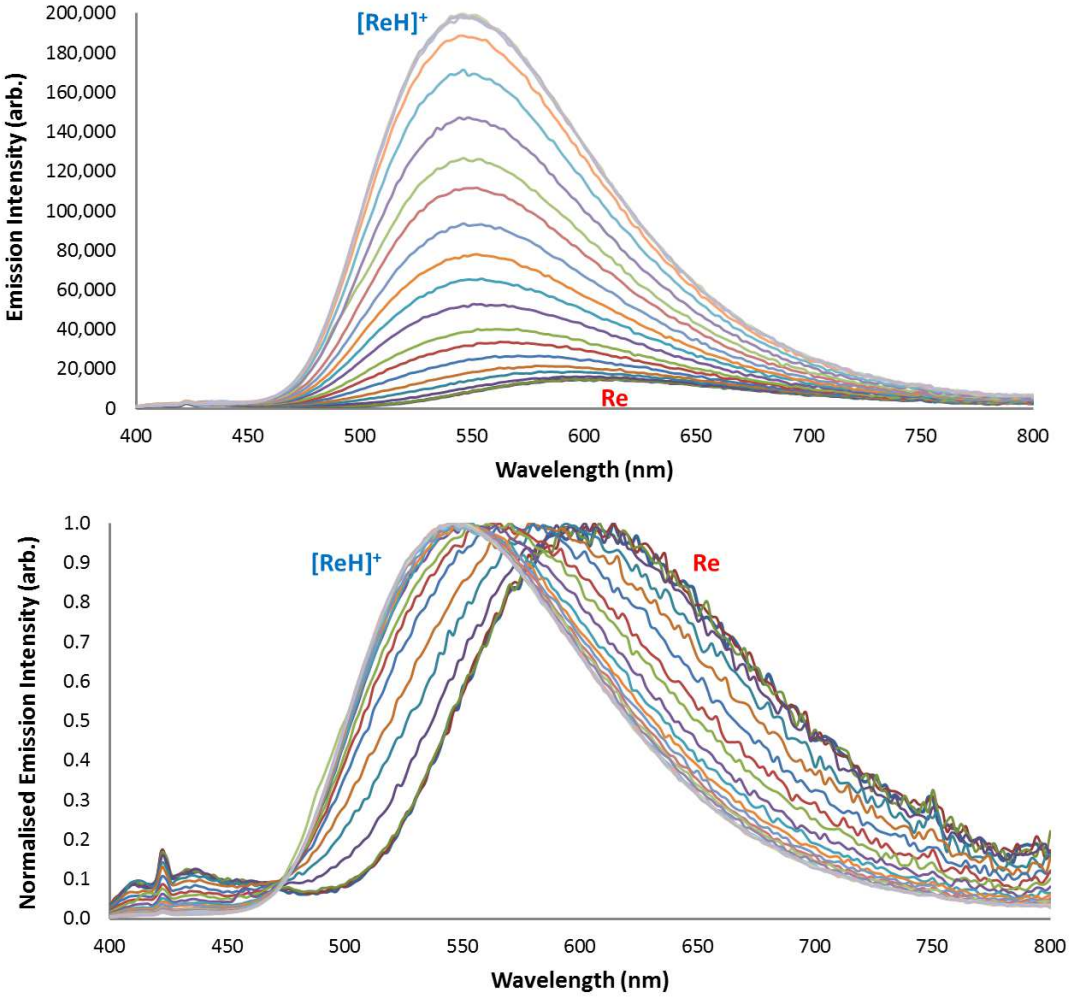


Figure 3.23: (Top) Steady state emission spectra showing the change occurring upon the sequential addition of triflic acid to *fac*-[Re(**bipy**)$(CO)_3$(**Tph**)] (**12**, Re) to form the protonated complex, *fac*-[Re(**bipy**)$(CO)_3$(**TphH**)]$^+$ (**22**, [ReH]$^+$). (Bottom) Normalised emission spectra to highlight the blue shift that occurs upon protonation.

This change in emission could be observed *in situ* by visualising the solutions under a UV lamp and sequentially adding triflic acid, Figure 3.22. The steady state emission spectra for the remainder of the complexes are shown in Figure 3.24 to Figure 3.27.

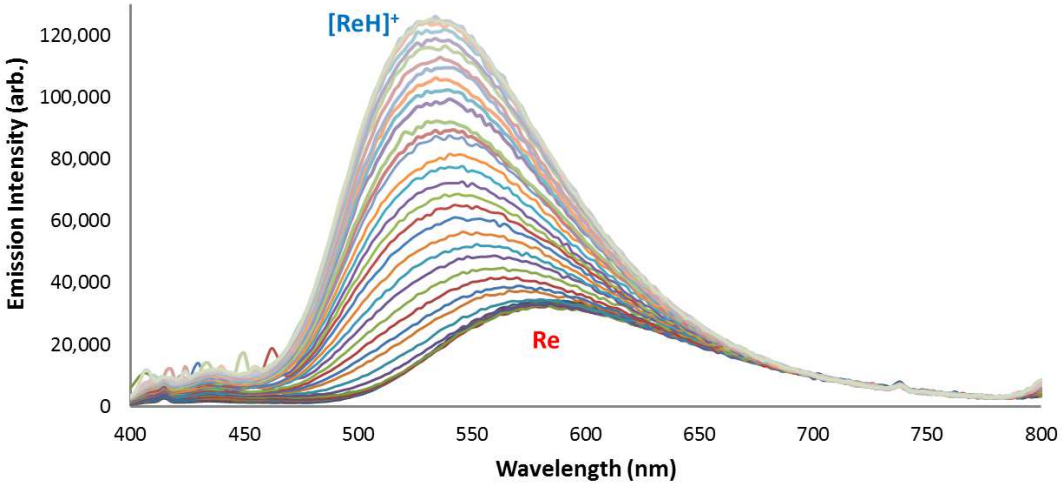


Figure 3.24: Steady state emission spectra showing the blue shift and increase in emission intensity occurring during the sequential addition of triflic acid to the neutral rhenium complex *fac*-[Re(**phen**)$(CO)_3$(**Tbz**)] (**13**, Re) to form the protonated complex, *fac*-[Re(**phen**)$(CO)_3$(**TbzH**)]$^+$(**23**, [ReH]$^+$).

The blue shift in the emission can be rationalised by the increased HOMO-LUMO energy gap caused by protonation of the tetrazole ring. To further understand this, the energies of the frontier molecular orbitals for *fac*-[Re(**phen**)$(CO)_3$(**Tph**)] (**11**) and *fac*-[Re(**phen**)$(CO)_3$(**Tph**H)]$^+$ (**21**) were plotted.

Figure 3.28 illustrates that protonation of the tetrazole ring causes stabilisation of the ground state (HOMO) by indirectly reducing the electron density on the Re centre. The LUMO is not greatly effected however there is an overall increase in the HOMO-LUMO energy gap, supporting the observed blue shifted emission.

Cationic rhenium complexes generally display greater photophysical output,[57] often rationalised by the energy gap law.[47,48] The $\phi$ of the cationic protonated complexes are 4-13 times higher than their neutral analogues and similarly, $\tau$ has been significantly elongated. Relative to the air-equilibrated neutral Re(I) complexes, lifetimes range from 270 to 518 ns for the **phen**-based and 85 to 107 ns for the **bipy**-based complexes. Comparatively the cationic species exhibit lifetimes between 1.3 and 1.8 $\mu$s for the **phen** complexes and between 595 and 655 ns and for the **bipy** complexes.

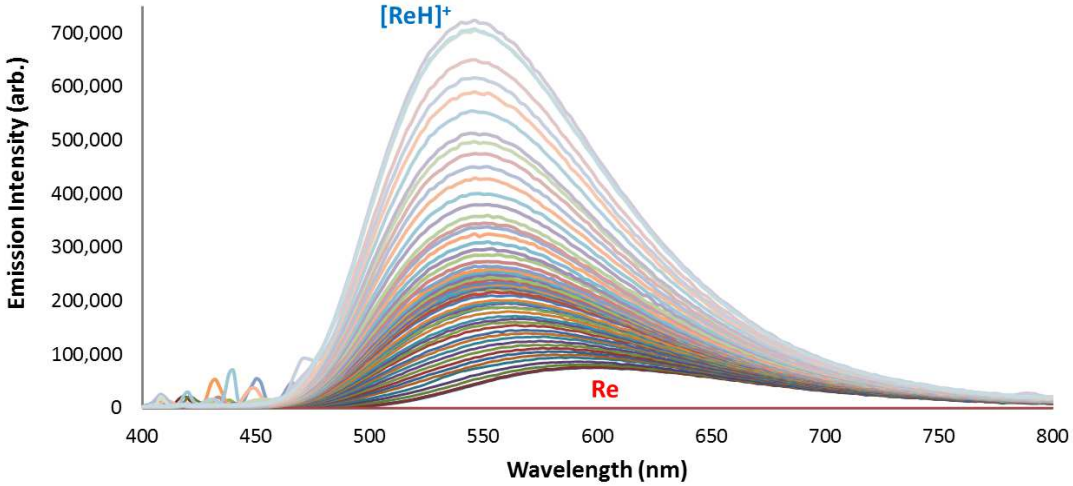


Figure 3.25: Steady state emission spectra showing the blue shift and increase in emission intensity occurring during the sequential addition of triflic acid to the neutral rhenium complex *fac*-[Re(**bipy**)$(CO)_3$(**Tbz**)] (**14**, Re) to form the protonated complex, *fac*-[Re(**bipy**)$(CO)_3$(**TbzH**)]$^+$(**24**, [ReH]$^+$).

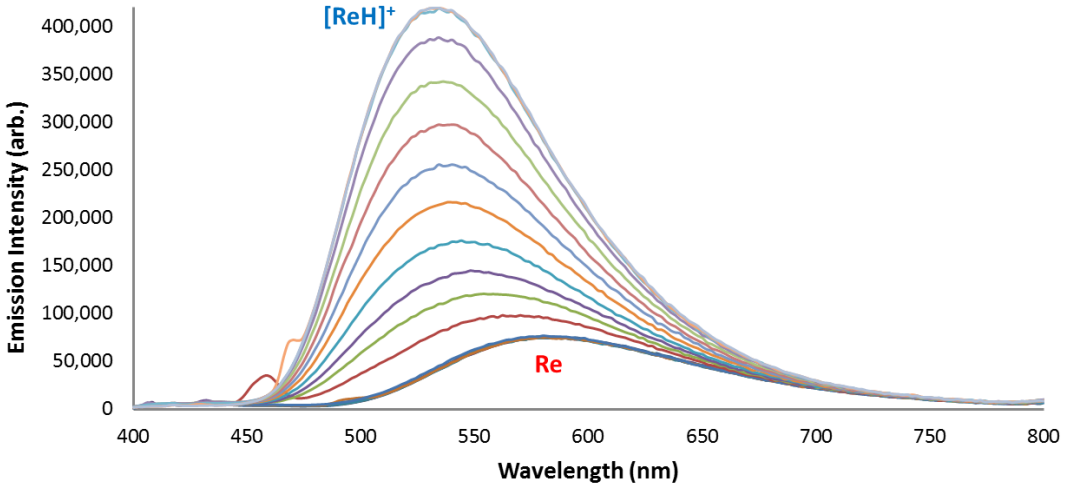


Figure 3.26: Steady state emission spectra showing the blue shift and increase in emission intensity occurring during the sequential addition of triflic acid to the neutral rhenium complex *fac*-[Re(**phen**)$(CO)_3$(**Tcya**)] (**17**, Re) to form the protonated complex, *fac*-[Re(**phen**)$(CO)_3$(**TcyaH**)]$^+$(**25**, [ReH]$^+$).

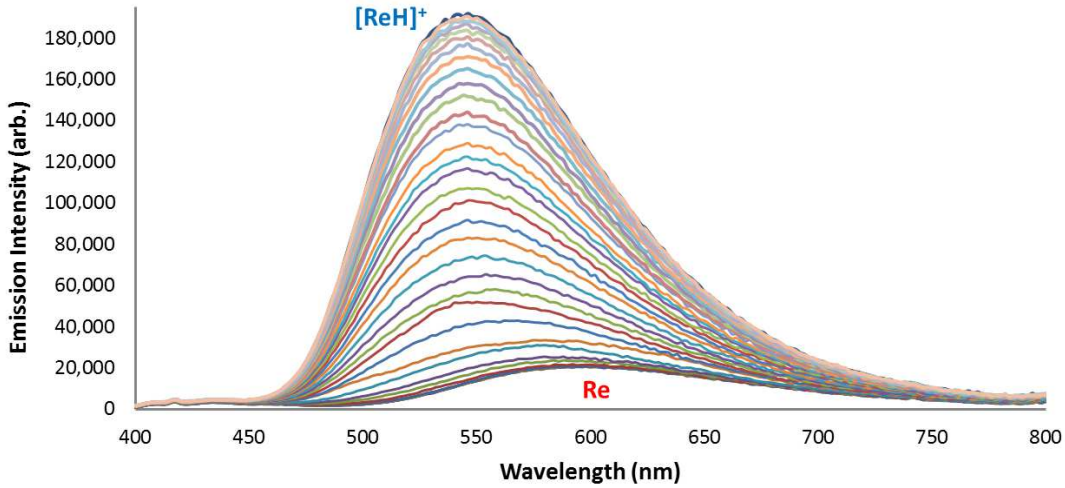


Figure 3.27: Steady state emission spectra showing the blue shift and increase in emission intensity occurring during the sequential addition of triflic acid to the neutral rhenium complex *fac*-[Re(**bipy**)$(CO)_3$(**Tcya**)] (**18**, Re) to form the protonated complex, *fac*-[Re(**bipy**)$(CO)_3$(**Tcya**H)]$^+$(**26**, $[ReH]^+$).

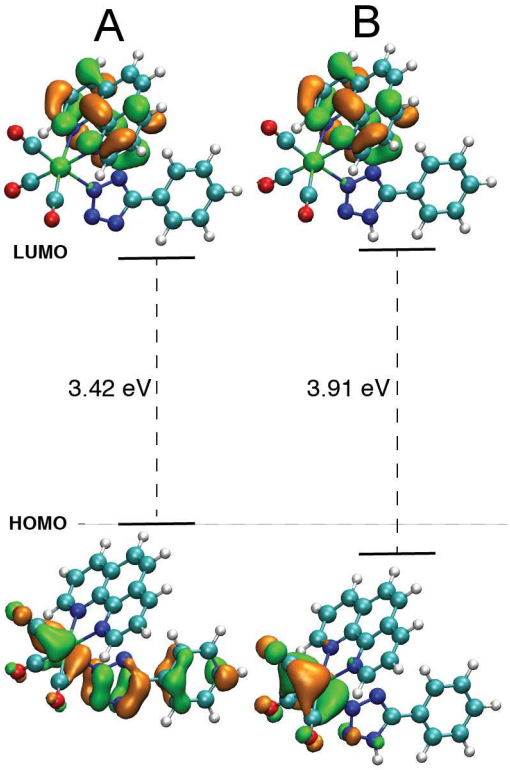


Figure 3.28: Calculated energy levels and orbital contours for the HOMO and LUMO of *fac*-[Re(**phen**)$(CO)_3$(**Tph**)], **11** (A) and the protonated analogue *fac*-[Re(**phen**)$(CO)_3$(**TphH**)]$^+$, **21** (B), obtained from DFT calculations.

Based on the calculations of the radiative and non-radiative decay constants it appears that the energy gap law is one factor explaining the improved luminescent output of the protonated species. For example, *fac*-[Re(**phen**)$(CO)_3$(**Tph**)] (**11**) exhibits a $k_r$ of $0.139\times10^6$ $s^{-1}$ and $k_{nr}$ of $1.79\times10^6$ $s^{-1}$ whereas the corresponding protonated complex (**21**) shows a slightly increased $k_r$ of $0.188\times10^6$ $s^{-1}$ and a significantly lower $k_{nr}$ value of $0.212\times10^6$ $s^{-1}$(see Table 3.3.7 for the $k_r$ and $k_{nr}$ of the protonated species and Table 2.3.8 on page 59 for the neutral species).

Table 3.3.7: Radiative and non-radiative decay constants ($k_r$ and $k_{nr}$) for the protonated rhenium complexes in degassed ($O_2$ free) DCM.

| **Rhenium Complex** | $k_r(10^6\ s^{-1})$ | $k_{nr}(10^6\ s^{-1})$ |
|---|---|---|
| *fac*-[Re(**phen**)$(CO)_3$(**Tph**H)]$^+$ (**21**) | 0.188 | 0.212 |
| *fac*-[Re(**bipy**)$(CO)_3$(**Tph**H)]$^+$(**22**) | 0.205 | 1.311 |
| *fac*-[Re(**phen**)$(CO)_3$(**Tbz**H)]$^+$(**23**) | 0.094 | 0.363 |
| *fac*-[Re(**bipy**)$(CO)_3$(**Tbz**H)]$^+$(**24**) | 0.335 | 0.878 |
| *fac*-[Re(**phen**)$(CO)_3$(**Tcya**H)]$^+$ (**25**) | 0.183 | 0.156 |
| *fac*-[Re(**bipy**)$(CO)_3$(**Tcya**H)]$^+$(**26**) | 0.233 | 0.911 |

It was noted that after complete protonation, the addition of triethylamine caused the photophysical output to revert back to that of the neutral complex. This was observed by a red shift and decrease in emission intensity. The luminescent features of the neutral Re(I) complexes are therefore able to undergo reversible modulation via a protonation-deprotonation regime.

## 3.4 Results and Discussion: Iridium

The results obtained from the protonation of neutral Re(I) complexes prompted us to investigate whether the reversible luminescent modulation might be a general feature of luminescent metal tetrazolato complexes. To explore the generality of this behaviour, the protonation of a previously reported cyclometalated Ir(III) tetrazolato complex[217] was investigated.

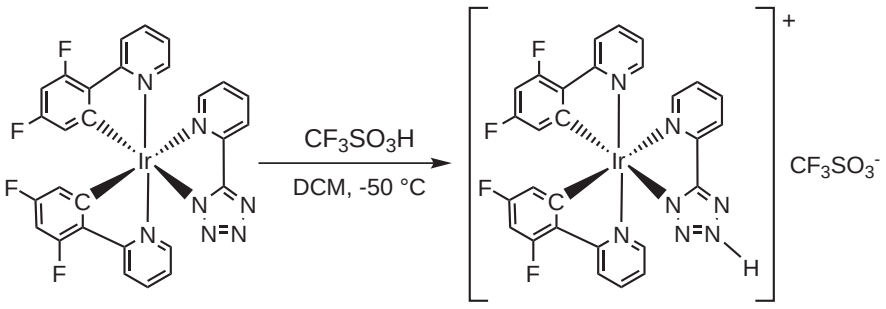


**27** [Ir(PyrTzF)] **28** $[Ir(PyrTzFH)]^+$

Scheme 3.3: Synthesis of the protonated iridium tetrazolato complex **28**.

Protonation was again performed by the addition of triflic acid to a DCM solution of the complex, as shown in Scheme 3.3. The starting complex, [Ir(PyrTzF)] (**27**) was already available at the University of Bologna. The final protonated species was analysed by $^1$H NMR and ESI-MS to confirm protonation.

Table 3.4.1: Absorbance data for the Ir(III) complexes at $10^{-5}$ M in DCM.

| Iridium Complex | Absorption $\lambda_{max}$/nm ($\varepsilon$ /$10^4$M$^{-1}$cm$^{-1}$) |
|---|---|
| [Ir(PyrTzF)] (**27**) | 248 (6.09), 310 (2.23), 370 (0.78) |
| $[Ir(PyrTzFH)]^+$(**28**) | 239 (5.45) 315 (2.13), 430 (0.194) |

The absorbance of the neutral iridium complex exhibits an intense transition in the high energy UV region at 250 nm and a low intensity band at 370 nm, Table 3.4.1 and Figure 3.29. Once again, the energetics and absorption spectra of the complexes were simulated with TD-DFT, using GAUSSIAN09.[181] Computational calculations reveal that the lowest energy transitions for [Ir(PyrTzF)] (**27**) appear to originate from HOMO→LUMO+*m* transitions, where *m* = 0-2. Figure 3.30 shows the localisation of the HOMO and LUMO on the Ir (III) complex. The lowest energy excited state

Table 3.4.2: Emission data for the iridium tetrazolato complexes.

| Iridium Complex[a] | Emission 298 K $\lambda$(nm) | $\tau$ ($\mu$s)[b] | $\tau$ ($\mu$s)[c] | $\phi$[b] | $\phi$[c] | Emission 77 K $\lambda_{max}$(nm) | $\tau$ ($\mu$s) |
|---|---|---|---|---|---|---|---|
| [Ir(PyrTzF)] (**27**) | 458, 488 | 0.105 | 0.161 | 0.034 | 0.056 | 450, 482 | 3.14 (26)<br>4.85 (74) |
| $[Ir(PyrTzFH)]^+$ (**28**) | 536 | 0.226 | 0.351 | 0.138 | 0.182 | 448, 478 | 4.23 |

[a]; All data for complexes in $10^{-5}$ M DCM solutions and all quantum yields measured against rhodamine 101, [b]; air-equilibrated samples, [c]; degassed ($O_2$ free) samples.

was therefore characterised as a mixture of MLCT and IL ($\pi$-$\pi^*$) states, with a small contribution from LLCT. The emission of [Ir(PyrTzF)] (**27**) is structured with $\lambda_{em}$ maxima at 458 and 488 nm (Table 3.4.2). This structured profile is caused by the close energy of the $^3$IL and $^3$MLCT emissive states and is common in these types of iridium complexes.[113] This is also supported by DFT which shows that the lowest energy excited state has both charge transfer and intraligand character. The emission maximum measured at 77 K for [Ir(PyrTzF)] (**27**) does not significantly differ from the maximum recorded at room temperature (Table 3.4.2) suggesting dominance of the $^3$IL ($\pi$-$\pi^*$) emissive state.[127,192]

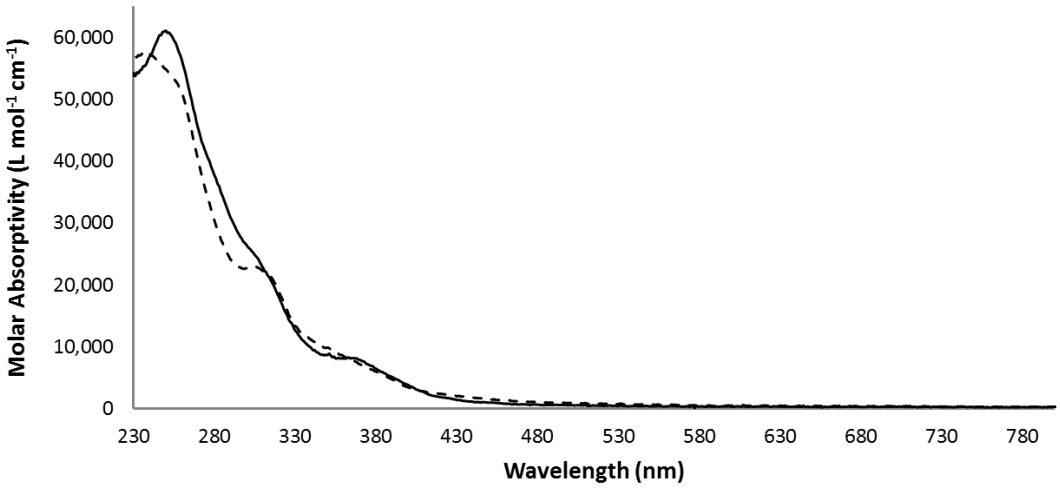


Figure 3.29: Absorption of the neutral iridium complex, [Ir(PyrTzF)] (**27**, solid line) compared to the corresponding protonated species, $[Ir(PyrTzFH)]^+$ (**28** dashed line) in DCM.

Figure 3.29 shows the absorbance profiles of both the neutral and protonated Ir complexes. There is not a significant change in the spectrum upon protonation. The lower energy bands are difficult to distinguish due to their broad nature however it appears

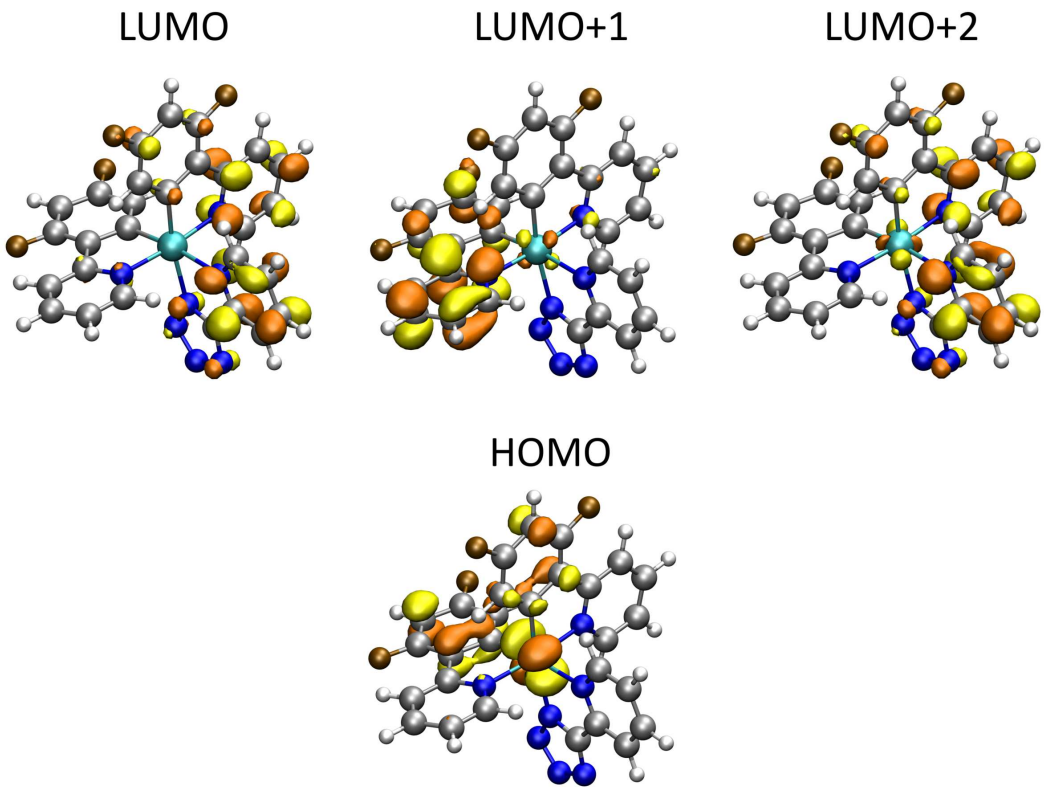


Figure 3.30: Localisation of the HOMO and LUMO for [Ir(PyrTzF)], **27**.

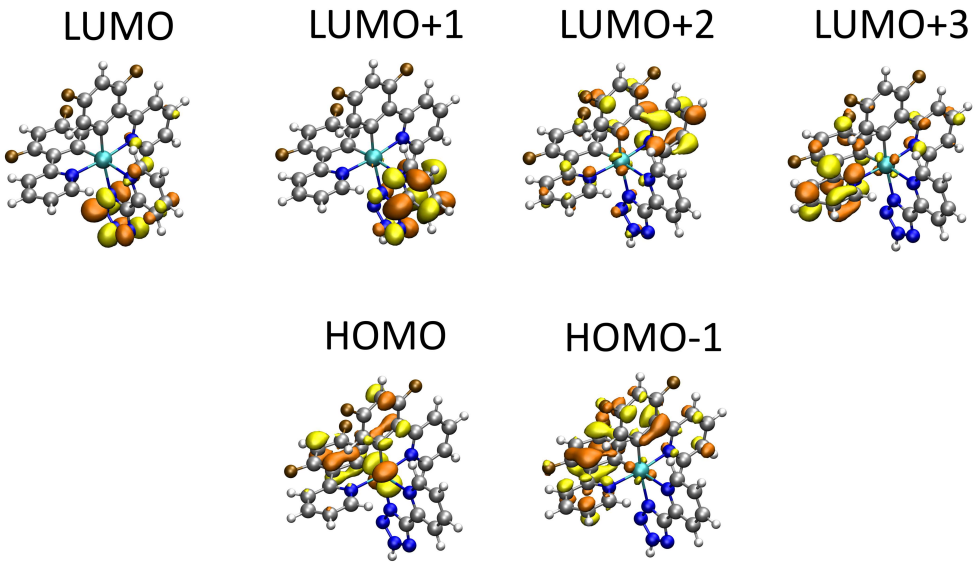


Figure 3.31: Localisation of the HOMO and LUMO for $[Ir(PyrTzFH)]^{+}$, **28**.

there is an overall red shift of the low intensity bands. Computational calculations of $[Ir(PyrTzFH)]^+$(**28**) indicate that the lowest energy excited state originates primarily from HOMO-*n*→LUMO+*m* transitions, where *n* = 0-1 and *m* = 0-3 (Figure 3.31). Based on the localisation of these orbitals, the lowest energy transition can be assigned to a mixture of MLCT and LLCT, with a significant reduction in the contribution from the IL ($\pi - \pi^*$) transition.

The emission of the protonated complex iridium complex is significantly different to that of the starting neutral species. As can be seen in Figure 3.32, the neutral blue-green emitting Ir(III) tetrazolato complex **[Ir(PyrTzF)]** is gradually transformed into the corresponding protonated species **$[Ir(PyrTzFH)]^+$**, displaying an increased intensity and red shifted emission. The structured profile observed for [Ir(PyrTzF)] (**27**) is lost upon protonation as evidenced in Figure 3.32, suggestive of emission from a more dominant charge transfer state.

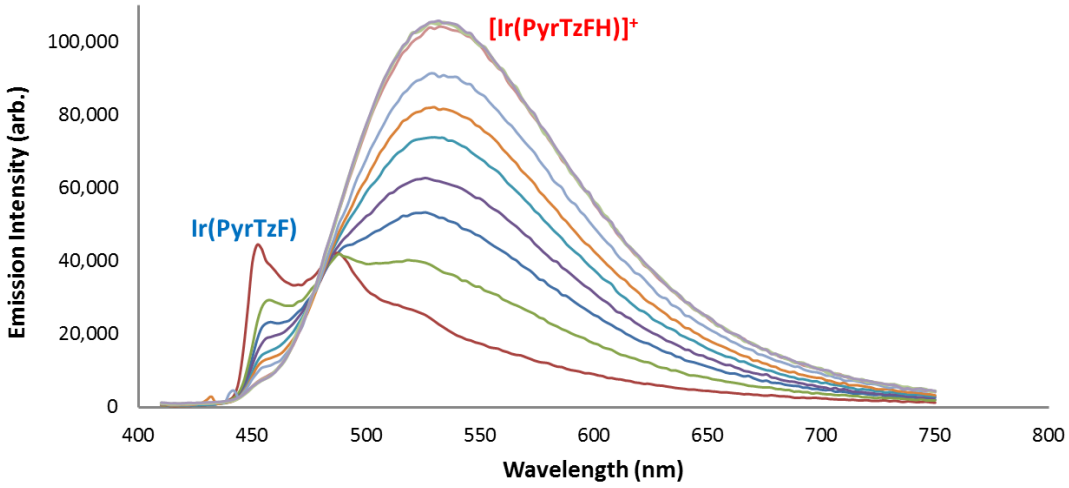


Figure 3.32: Steady state emission spectra showing the red shift and increase in emission intensity occurring upon addition of triflic acid to [Ir(PyrTzF)] (**27**), forming the protonated complex, $[Ir(PyrTzFH)]^+$ (**28**).

The loss of the IL contribution is also suggested by the blue-shifted emission maximum observed upon freezing the solution (Table 3.4.2). The rigidochromic effect is commonly seen for purely charge transfer emissive states (ie: not $\pi - \pi^*$ IL transitions).[192,193] The localisation of the frontier orbitals, as calculated using DFT, also shows a reduction in the IL contribution (Figure 3.31). The energies of the frontier molecular orbitals for [Ir(PyrTzF)] (**27**) and the corresponding protonated analogue, $[Ir(PyrTzFH)]^+$ (**28**) have been plotted and are shown in Figure 3.33. It is apparent

that the tetrazole ring is directly involved in the composition of the LUMO. Protonation therefore causes stabilisation of the LUMO, reducing the HOMO-LUMO energy gap and explaining the observed red shifted emission.

Table 3.4.4: Radiative and non-radiative decay constants ($k_r$ and $k_{nr}$) for the iridium complexes.

| Iridium Complex | $k_r(10^6\ s^{-1})$ | $k_{nr}(10^6\ s^{-1})$ |
|---|---|---|
| [Ir(PyrTzF)] (**27**) | 0.349 | 5.86 |
| $[Ir(PyrTzFH)]^+$(**28**) | 0.519 | 2.33 |

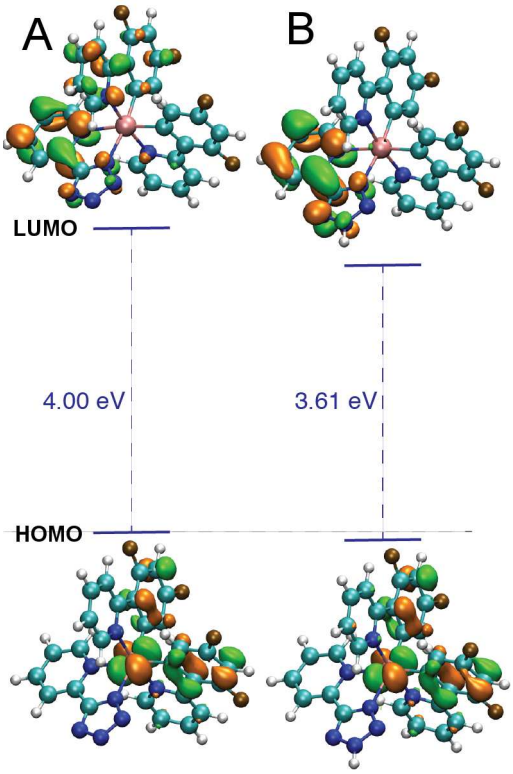


Figure 3.33: Calculated energy levels and orbital contours for the HOMO and LUMO of [Ir(PyrTzF)] (**27**, A) and the protonated analogue $[Ir(PyrTzFH)]^+$ (**28**, B), obtained from DFT calculations.

As observed with the Re complexes, the $\tau$ and $\phi$ for the protonated Ir complex is improved with respect to the corresponding neutral analogue (Table 3.4.2). The improved output is usually described by an increased HOMO-LUMO energy gap[47,48] however, the red shifted emission and the contour plots (Figure 3.33) show that this in not the case. Table 3.4.4 illustrates that in fact there is a significant reduction in the $k_{nr}$ upon

protonation which explains the improved $\tau$ and $\phi$. The improved output of the protonated complexes might be rationalised by the reduced $^3$IL contribution to the excited state however this is still uncertain. The increased $k_r$ is also expected upon a reduced contribution from the $^3$IL state.[218] The proton-induced modulation of the photophysics is once again reversible, with the addition of triethylamine.

## 3.5 Results and Discussion: Ruthenium

The final metal tetrazolato complex investigated was $[Ru(PyrTz)]^+$ (**29**). Protonation was again carried out through addition of triflic acid to a DCM solution of the complex (Scheme 3.4). The starting material was available from the University of Bologna and the final product was characterised by $^1$H NMR and ESI-MS to confirm protonation.

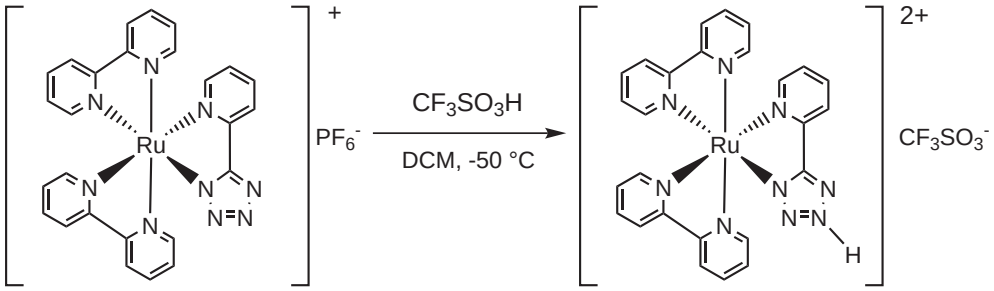


**29** $[Ru(PyrTz)]^+$ **30** $[Ru(PyrTzH)]^{2+}$

Scheme 3.4: Synthesis of the protonated ruthenium tetrazolato complex **30**.

Table 3.5.1: Absorbance data for Ru(II) complexes measured in DCM.

| Ruthenium Complex | Absorption $\lambda_{max}$/nm ($\varepsilon 10^{-4} M^{-1} cm^{-1}$) |
|---|---|
| $[Ru(PyrTz)]^+$(**29**) | 291 (1.701) 370 (0.272) 475 (0.311) |
| $[Ru(PyrTzH)]^{2+}$(**30**) | 287 (1.515) 441 (0.346) |

The absorbance of the starting Ru(II) complex exhibits intense transitions in the high energy UV region around 291 nm and a series of bands in the UV-visible range with the main peaks at 370 nm and 475 nm. The structure of the absorbance profile, as shown in Figure 3.34, is typical for this class of ruthenium complexes.[114,219] The absorption spectrum was simulated with TD-DFT using GAUSSIAN09.[181] Computational calculations indicates that the lowest energy excited states in the unprotonated ruthenium

Table 3.5.2: Photophysical data for the ruthenium tetrazolato complexes.

| Ruthenium | Emission 298 K | | | | | Emission 77 K | |
|---|---|---|---|---|---|---|---|
| Complex[a] | $\lambda_{max}$(nm) | $\tau$ ($\mu$s)[b] | $\tau$ ($\mu$s)[c] | $\phi^b$ | $\phi^c$ | $\lambda_{max}$(nm) | $\tau$ ($\mu$s) |
| $[Ru(PyrTz)]^+$ (**29**) | 653 | 0.077 | 0.220 | - | 0.04 | 597 | 5.23 |
| $[Ru(PyrTzH)]^{2+}$ (**30**) | - | - | - | - | - | - | - |

[a]; measurements in acetonitrile and data from work by Stagni *et al.*[219], [b]; air-equilibrated samples, [c]; degassed ($O_2$ free) samples.

complex (**29**) appear to originate from HOMO-*n* →LUMO+*m* transitions, where *n* = 0-2 and *m* = 0-1. The HOMO-*n* type orbitals predominantly localise on the 4d orbitals of the Ru center, whereas the LUMO+*m* are localised on both bipyridine ligands, as shown in Figure 3.35. The low energy transitions are therefore MLCT in character (Ru → **bipy**). The higher energy transitions can be assigned to $\pi - \pi^*$ IL transitions.[219]

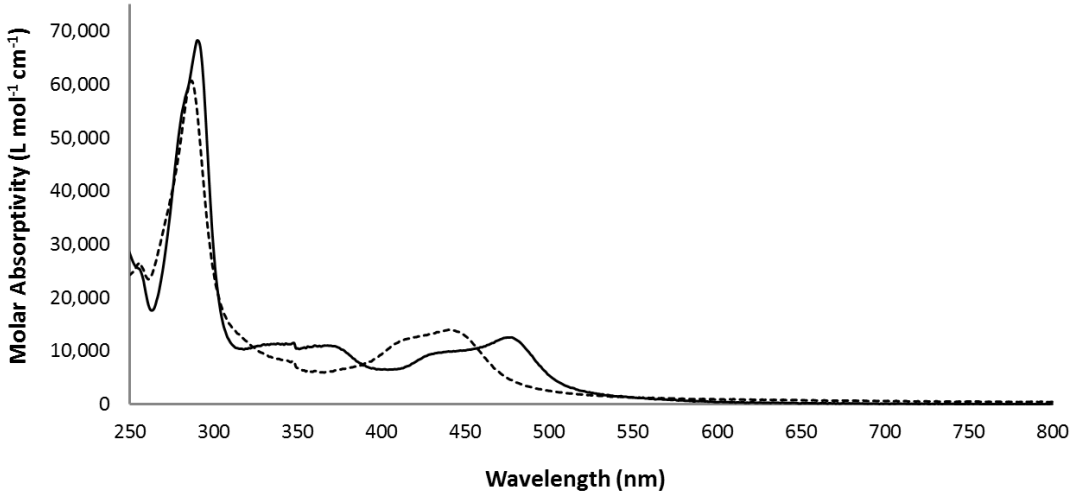


Figure 3.34: Absorption of the ruthenium complex, $[Ru(PyrTz)]^+$ (**29**, solid line) compared to the corresponding protonated species, $[Ru(PyrTzH)]^{2+}$ (**30**, dashed line) in DCM.

Emission of the unprotonated ruthenium complex is broad and structureless with a maximum at 653 nm in acetonitrile. The increased $\tau$ and $\phi$ measured for the Ru complex upon de-oxygenating the solution supports the assigned emission from a triplet MLCT state[52,54] (Table 3.5.2). Ru(II) emission measured in a frozen matrix blue shifted, suggestive of emission from a charge transfer state.[192,193] DFT indicates that there is a minor but notable contribution of 4d orbitals present in the LUMO type orbitals as illustrated in Figure 3.35. Their contribution is likely to be minor enough as

there is not significant deactivation of the $^3$MLCT (via the MC state) and emission is still observed.

The absorbance spectrum of the protonated species $[Ru(PyrTzH)]^{2+}$ (**30**) shows a broad low intensity transition at 441 nm and a sharp high intensity transition at 287 nm (Figure 3.34). Comparing the absorbance profiles of the starting and protonated ruthenium complexes (Figure 3.34), there has been a blue shift of the two low energy bands upon protonation. Based on TD-DFT/DFT calculations, the lowest energy excited state of **30**, appears to originate from HOMO→LUMO+*m* transitions, where *m* = 0-2. The orbitals involved are again the 4d orbitals of the Ru center (HOMO) and the bipyridine $\pi^*$ orbitals (LUMO), see Figure 3.36. Based on the localisation of the HOMO and LUMO, the low energy transition is assigned to an MLCT. The higher energy transitions can be assigned to $\pi - \pi^*$ IL transitions.[219]

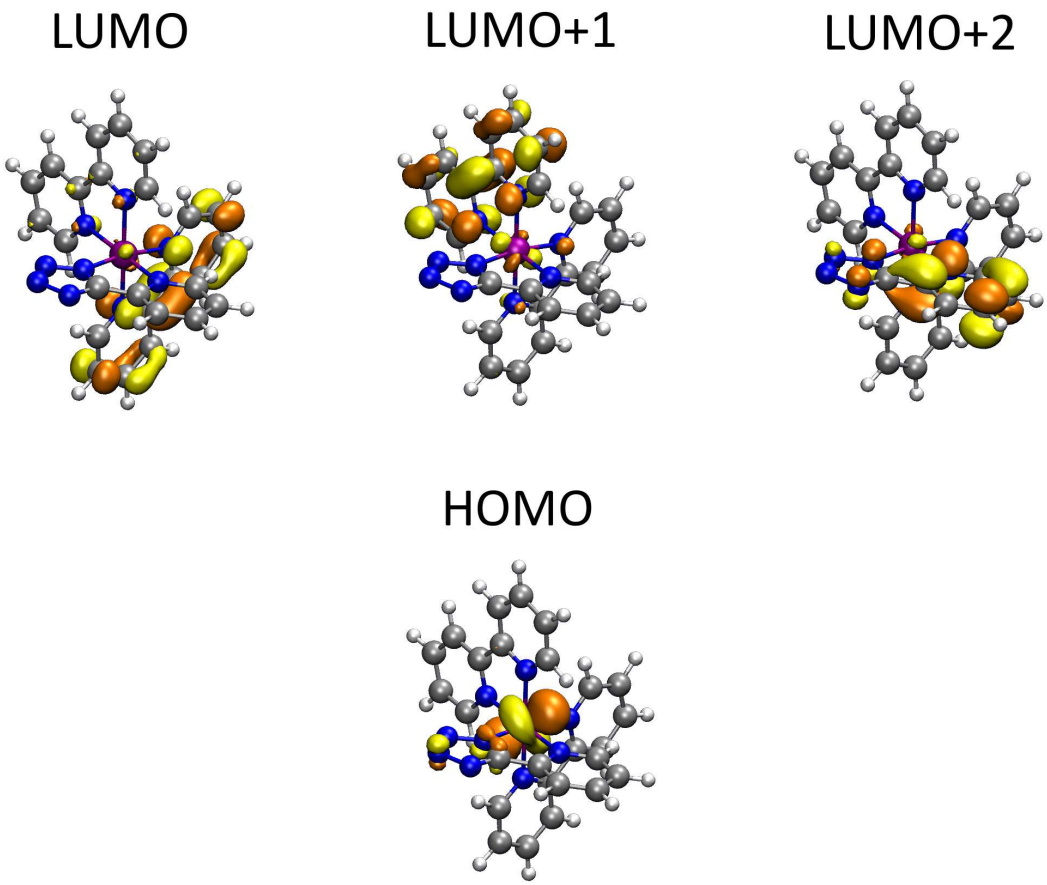


Figure 3.35: Localisation of the HOMO and LUMO for the ruthenium complex $[Ru(PyrTz)]^+$ (**29**).

Sequential addition of triflic acid was carried out on a DCM solution of $[Ru(PyrTz)]^+$

(**29**) and the emission maximum initially seen at 635 nm, was significantly quenched (and blue shifted) upon protonation as shown in Figure 3.37. Emission of the protonated complex is originating from a $^3$MLCT state and again, the DFT indicates that the LUMO+1 and LUMO+2 have a small contribution from the 4d Ru orbitals (Figure 3.36). The HOMO and LUMO contributions do not seem to change greatly between the starting and protonated ruthenium complex (Figure 3.35 and Figure 3.36). Even though upon protonation, there is a significant reduction in the emission of the Ruthenium complex the small blue shifted emission band observed was assigned to emission from a $^3$MLCT state. The blue shift in the complex can be rationalised by a stabilisation of the ground state (HOMO) orbitals, due to the indirect reduction in electron density on the metal centre from the protonation of the tetrazole ring. It is interesting that protonation of the tetrazolato ligand causes significant quenching as previous studies which have methylated this same complex, observe extension of lifetime but a reduction in quantum yield.[219]

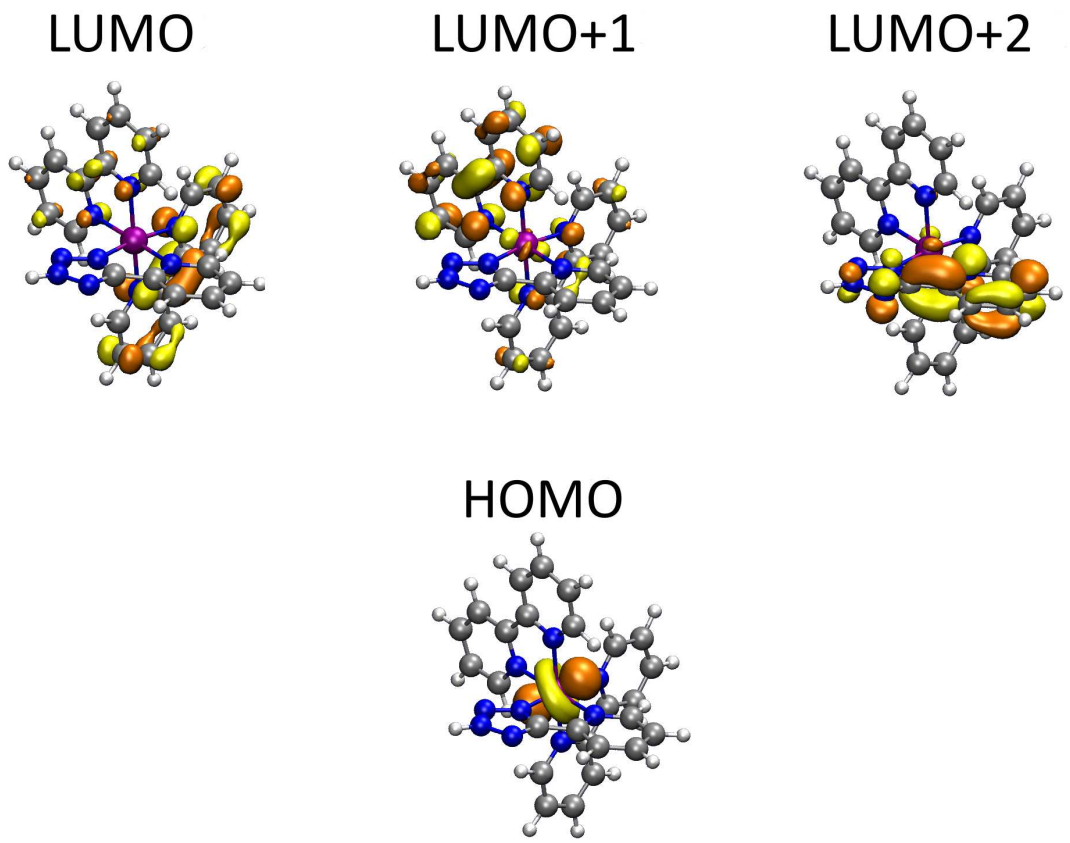


Figure 3.36: Localisation of the HOMO and LUMO for the ruthenium complex $[Ru(PyrTzH)]^{2+}$ (**30**).

The quenching mechanism is still not fully understood but other studies looking at the protonation of ruthenium azole complexes have observed similar quenching behaviour.[220] The rationalisation used to describe their quenched emission could be used herein. Duati *et al.* state that the pyridine tetrazole ligand is a good $\sigma$ donor, meaning it is a strong field ligand and can cause strong ligand field splitting of the complex. This caused the $e_g$ level (ie; MC state) of the ruthenium to rise, increasing the energy gap between the $^3$MC and $^3$MLCT states.[220] The rationalisation could also be used herein to describe the $^3$MLCT emission of $[Ru(PyrTz)]^+$ (**29**). However, upon protonation Duati *et al.* describe the azole ligand becoming a weaker sigma donor. The ligand field splitting strength has also been reduced and therefore $^3$MC and $^3$MLCT gap is smaller compared to the situation in the starting Ru complex. The closeness of the $^3$MC and $^3$MLCT causes thermal population of the deactivating $^3$MC state.[220] The low emission output observed herein, upon the formation of $[Ru(PyrTzH)]^{2+}$ (**30**) could also be caused by thermal population of the $^3$MC state. Temperature dependent lifetime measurements would need to be conducted in order to further understand if the theory of Duati *et al.* can explain the quenched emission of the ruthenium tetrazolato complexes reported herein.

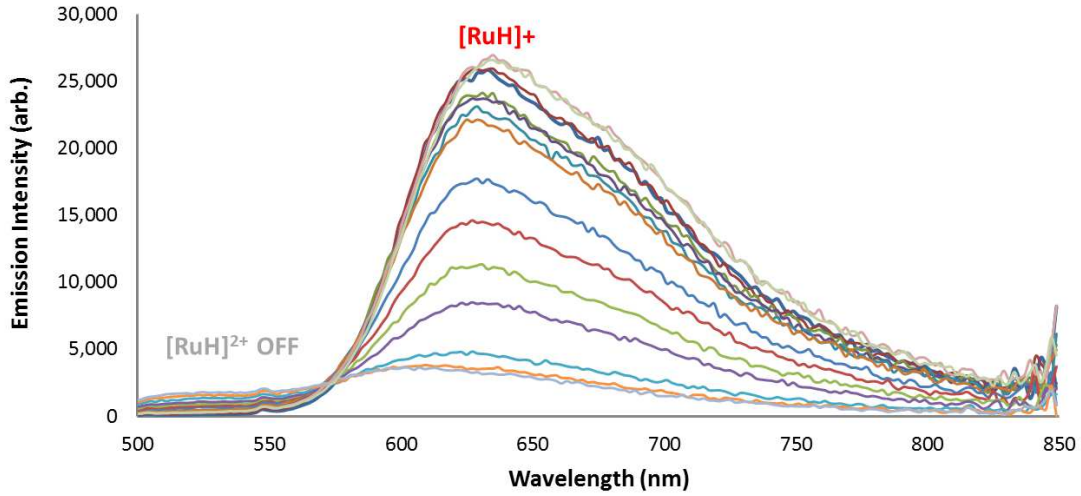


Figure 3.37: Steady state emission spectra showing the red shift and increase in emission intensity occurring upon addition of triflic acid to $[Ru(PyrTz)]^+$(**29**, $[RuH]^+$) forming the protonated complex, $[Ru(PyrTzH)]^{2+}$ (**30**, $[RuH]^{2+}$).

An acetonitrile solution of the protonated complex with a few drops of triflic acid was layered with diethyl ether to afford single crystals suitable for X-ray diffraction. The resolved structure was somewhat unexpected as shown in Figure 3.38. The pyridine

tetrazole is no longer present as a bidentate ligand but is mono-coordinating through the N2 atom of the tetrazole ring. In this case, the crystal structure shows acetonitrile coordinating as a sixth ligand. The proton is also shown on the pyridine ring, which is as pyridine is the stronger base compared to the tetrazole. Potential weakening of the Ru-N bond of the pyridine tetrazole ligand could be another reason why emission is quenched upon formation of **30**. Increased lability and movement of the tetrazole ligand could cause increased vibrations and therefore an increased contribution from $k_{nr}$ . $K_{nr}$ could not be calculated due to the lack of $\tau$ and $\phi$ data. Understandably, the photophysical measurements were carried out in dichloromethane, a non-coordinating solvent. Nonetheless, protonation could make the tetrazolato ligand labile enough for $CF_3SO_3^-$ to weakly coordinate (instead of solvent) however this has not been observed. As stated above, the precise cause of the quenched emission in the protonated ruthenium species is still not known and further experiments are required.

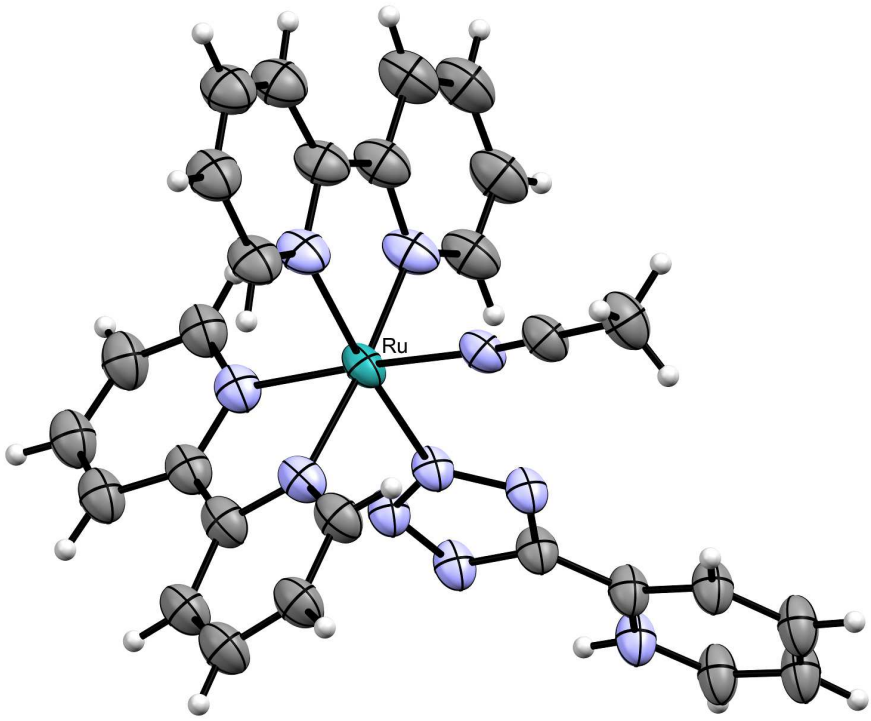


Figure 3.38: X-ray crystal structure of the protonated ruthenium complex where thermal ellipsoids have been drawn at 30% probability. The triflate counter ion has been omitted for clarity.

As a common feature discussed in Chapter Three, the emission of light from the protonated Ru(II) complex can be restored through the addition of triethylamine. Protonation of the Re(I), Ir(III) and Ru(II) tetrazolato complexes causes a unique modulation

of their photophysical properties. The tetrazolato ligand, which undergoes protonation, has a varied contribution to the excited state for each class of complex.

## 3.6 Conclusion

The reversible protonation reaction of Re(I) tetrazolato complexes has been investigated and the change in luminescence reported. Through protonation of the tetrazole ring, it was possible to significantly increase the intensity and blue shift the emission of the complexes. Protonation, which occurs on the tetrazolato ligand, indirectly creates a larger energy gap between the ground and excited states of the newly formed cationic complex. The protonated species are therefore characterised by a reduction in the value of $k_{nr}$ and hence improved $\phi$ and elongated $\tau$. Addition of triethylamine to the cationic complex causes deprotonation and the photophysical output returns to that of the neutral analogue.

The photophysical output of the Ir(III) tetrazolato complex was also modified upon protonation with a red shifted emission observed. The emitting excited state reversibly passes from a mixed $^3$LC/$^3$MLCT in the neutral species to a predominant $^3$MLCT excited state after protonation. A completely different behaviour is observed for the Ru(II) polypyridyl complex. Upon protonation, emission is quenched producing a reversible on-off switch of the luminescence.

The reversible modulation of luminescence observed for the Re(I) tetrazolato complexes shows they are sensitive to their environment. This fundamental study provides the proof of concept that these complexes or modified analogues may be further investigated as sensors or responsive probes.

## 3.7 Experimental

### 3.7.1 General Procedures

General procedures are as outlined in Chapter Two, section 2.5.1, unless otherwise stated.

Nuclear magnetic resonance spectra (consisting of $^{1}H$ and $^{13}C$ experiments) were recorded using a Varian Mercury Plus 400 instrument (400.1 MHz for $^{1}H$, 101.1 MHz for $^{13}C$) at room temperature. $^{1}H$ and $^{13}C$ chemical shifts were referenced to residual solvent resonances. The NMR referencing scheme for the assignments of peaks is as outlined in Scheme 2.8.

Infrared spectra were recorded as DCM solutions using a NaCl (5 mm) disc on a Perkin-Elmer Spectrum 2000 FT-IR spectrometer. The intensities of the IR bands were reported as strong (s), medium (m) or weak (w), with broad (br) bands and shoulders (sh) also indicated.

ESI-mass spectra were measured by Dr. Luca Zuppiroli at the University of Bologna, using a Waters ZQ-4000 instrument (ESI-MS, acetonitrile as the solvent).

### Photophysics

Absorption spectra were recorded at room temperature using a Perkin-Elmer Lambda 35 UV-vis spectrometer. Uncorrected steady-state emission and excitation spectra were recorded on an Edinburgh FLSP920 spectrometer equipped with a 450 W xenon arc lamp, double excitation and single emission monochromators and a Peltier-cooled Hamamatsu R928P photomultiplier tube (185-850 nm). Emission and excitation spectra were corrected for source intensity (lamp and grating) and emission spectral response (detector and grating) by a calibration curve supplied with the instrument. Emission lifetimes ($\tau$) were determined with the same Edinburgh FLSP920 spectrometer using pulsed picosecond LEDs (EPLED 360, FHWM <800 ps) as the excitation source, with repetition rates between 1 kHz and 1 MHz, and the above mentioned R928P PMT as the detector. Degassed solutions were prepared by gently bubbling argon gas into the prepared sample for 15 minutes before measurement.

## 3.7.2 Synthesis

### 3.7.2.1 General methodology for protonation of neutral *fac*-[Re(diim)(CO)$_3$(L)] complexes.

The preparation of the protonated *fac*-[Re(**diim**)(CO)$_3$(**L**)] complexes (**diim** = 1,10-phenanthroline or 2,2'-bipyridine) was carried out following procedures adapted from previously published work.[108,111]

Previously synthesised *fac*-[Re(**diim**)(CO)$_3$(**L**)] (1 eq) was added to DCM under argon atmosphere and the mixture was allowed to cool using an ethyl acetate/liquid nitrogen cool bath. Once the reaction vessel had cooled, trifluoromethanesulfonic acid (1.2 eq) in DCM was added. The reaction was stirred under nitrogen for approximately 30 minutes in the cool bath and was then allowed to come to room temperature and stirred overnight. The solvent was removed *in vacuo* to yield a yellow glassy looking solid that was identified as the expected protonated complex.

*fac*-[Re(**phen**)(CO)$_3$(**Tph**H)]$^+$

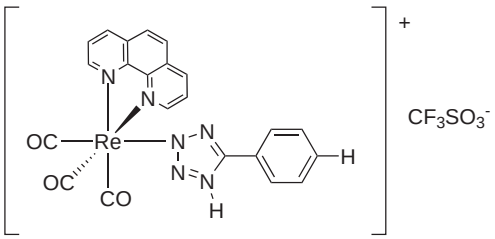


**21**

Yield of compound **21**: 0.051 g, 82%. ESI-MS (m/z) = 597 [M − $SO_3CF_3$]$^+$; 149 [$SO_3CF_3$]$^-$. $\nu_{max}$ (IR)/cm$^{-1}$, DCM, rt: 2039 s (CO, A´(1)), 1936 br (CO, A´(2)/A´´), 1606 w (tetrazole C=N). $^1$H NMR ($\delta$, ppm, Acetone-d$_6$): 9.75 (2H, d, $J$ = 4.8 Hz, phen $H_{2,9}$), 9.07 (2H, d, $J$ = 8.0 Hz, phen $H_{4,7}$), 8.37 (2H, s, phen $H_{5,6}$), 8.28−8.24 (2H, m, phen $H_{3,8}$), 7.69 (2H, d, $J$ = 7.6 Hz, $CN_4$-$C_6H_5$ $H_{ortho}$), 7.56−7.54 (1H, m, $CN_4$-$C_6H_5$ $H_{para}$), 7.43−7.39 (2H, m, $CN_4$-$C_6H_5$ $H_{meta}$). $^{13}$C NMR ($\delta$, ppm, Acetone-d$_6$): 197.0, 156.4, 156.2, 148.8, 141.8, 134.1, 132.7, 131.0, 129.6, 128.8, 128.5. Crystals suitable for X-ray analysis were obtained by slow diffusion of diethyl ether into a DCM solution of the complex with a few drops of dilute triflic acid solution. By using this procedure, two different crystals of the same complex were obtained; **21**, $C_{23}H_{14}F_3N_6O_6ReS$, and **21**· 0.25$Et_2O$, $C_{24}H_{16.5}F_3N_6O_{6.25}ReS$, respectively. These were distinguished by the absence and presence of diethyl ether in the unit cell.

*fac*-[Re(**bipy**)$(CO)_3$(**Tph**H)]$^+$

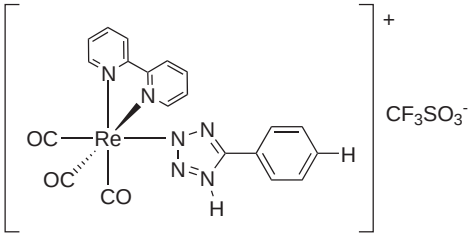


**22**

Yield of compound **22**: 0.045 g, 70%. ESI-MS (m/ z) = 573 [M − $SO_3CF_3$]$^+$; 149 [$SO_3CF_3$]$^-$. $\nu_{max}$ (IR)/cm$^{-1}$, DCM, rt: 2039 s (CO, A´(1)), 1936 br (CO, A´(2)/A´´), 1606 w (tetrazole C=N). $^1$H NMR (δ, ppm, Acetone-$d_6$): 9.31 (2H, d, *J* = 5.2 Hz, bipy $H_{6,6'}$), 8.78 (2H, d, *J* = 8.4 Hz, bipy $H_{3,3'}$), 8.43−8.39 (2H, m, bipy $H_{4,4'}$), 7.90−7.83 (4H, m, bipy $H_{5,5'}$ and $CN_4$-$C_6H_5$ $H_{ortho}$), 7.54−7.49 (3H, m, $CN_4$-$C_6H_5$ $H_{meta}$ and $H_{para}$). $^{13}$C NMR (δ, ppm, Acetone-$d_6$): 196.8, 194.3, 159.2, 157.5, 155.0, 141.9, 132.4, 130.1, 129.1, 127.9, 125.4, 123.3. Crystals suitable for X-ray analysis (identified as a dimeric Re species; $C_{34}H_{21}F_3N_8O_9Re_2S$) were obtained by slow diffusion of diethyl ether into a DCM solution of the complex with a few drops of dilute triflic acid solution.

*fac*-[Re(**phen**)$(CO)_3$(**Tbz**H)]$^+$

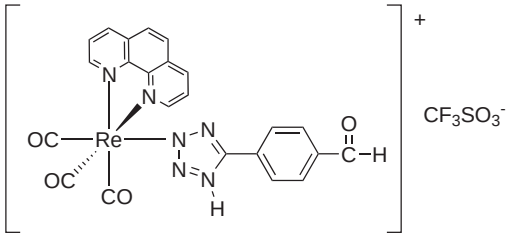


**23**

Yield of compound **23**: 0.042 g, 68%. ESI-MS (m/z) = 625 [M − $SO_3CF_3$]$^+$; 149 [$SO_3CF_3$]$^-$. $\nu_{max}$ (IR)/cm$^{-1}$, DCM, rt: 2040 s (CO, A´(1)), 1938 br (CO, A´(2)/A´´), 1709 s (aldehyde CO), 1607 w (tetrazole C=N). $^1$H NMR (δ, ppm, Acetone-$d_6$): 10.04 (1H, s, $CN_4$-$C_6H_4$-C*H*O), 9.74 (2H, d, *J* = 5.2 Hz, phen $H_{2,9}$), 9.04 (2H, d, *J* = 8.2 Hz, phen $H_{4,7}$), 8.36 (2H, s, phen $H_{5,6}$), 8.26−8.23 (2H, m, phen $H_{3,8}$), 7.95 (2H, d, *J* = 8.4 Hz, $CN_4$-$C_6H_4$ -CHO $H_{meta}$), 7.90 (2H, d, *J* = 8.4 Hz, $CN_4$-$C_6H_4$ -CHO $H_{ortho}$). $^{13}$C NMR (δ, ppm, Acetone-$d_6$): 192.3, 155.7, 148.2, 141.0, 139.3, 132.0, 130.9, 128.9, 128.5, 127.7. Crystals suitable for X-ray analysis (identified as **23**, $C_{24}H_{14}F_3N_6O_7ReS$) were obtained by slow diffusion of diethyl ether into a DCM solution of the complex with a few drops of dilute triflic acid solution.

*fac*-[Re(**bipy**)$(CO)_3$(**Tbz**H)]$^+$

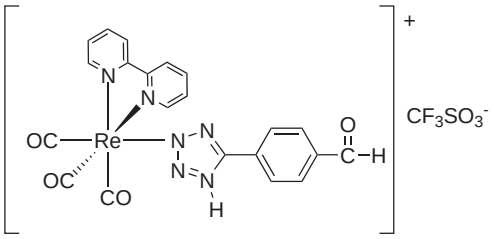

**24**

Yield of compound **24**: 0.035g, 56%. ESI-MS (m/z) = 601 [M − $SO_3CF_3$]$^+$; 149 [$SO_3CF_3$]$^-$. $\nu_{max}$ (IR)/cm$^{-1}$, DCM, rt: 2040 s (CO, A´(1)), 1937 br (CO, A´(2)/A´´), 1709 s (aldehyde CO), 1606 w (tetrazole C=N). $^1$H NMR (δ, ppm, Acetone-$d_6$): 10.11 (1H, s, $CN_4$-$C_6H_4$-C*H*O), 9.34 (2H, d, *J* = 5.6 Hz, bipy $H_{6,6'}$), 8.81 (2H, d, *J* = 8.2 Hz, bipy $H_{3,3'}$), 8.45−8.43 (2H, m, bipy $H_{4,4'}$), 8.07 (4H, s, $CN_4$-$C_6H_4$ -CHO $H_{meta,\ ortho}$), 7.91−7.88 (2H, m, bipy $H_{5,5'}$). $^{13}$C NMR (δ, ppm, Acetone-$d_6$): 196.4, 192.4, 157.5, 155.1, 154.9, 142.4, 142.1, 139.9, 131.0, 129.2, 129.0, 125.3. Crystals suitable for X-ray analysis (identified as **24**, $C_{22}H_{14}F_3N_6O_7ReS$) were obtained by slow diffusion of diethyl ether into a DCM solution of the complex with a few drops of dilute triflic acid solution.

*fac*-[Re(**phen**)$(CO)_3$(**Tcya**H)]$^+$

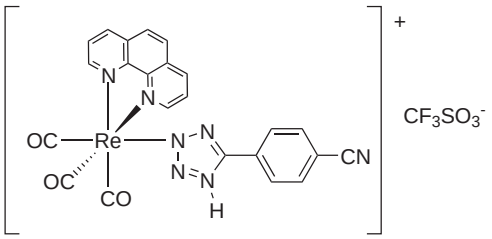

**25**

Yield of compound **25**: 0.039 g, 64%. ESI-MS (m/z) = 622 [M − $SO_3CF_3$]$^+$; 149 [$SO_3CF_3$]$^-$. $\nu_{max}$ (IR)/cm$^{-1}$, DCM, rt: 2233 w (CN), 2040 s (CO, A´(1)), 1937 br (CO, A´(2)/A´´), 1606 w (tetrazole C=N). $^1$H NMR (δ, ppm, Acetone-$d_6$): 9.76 (2H, d, *J* = 5.0 Hz, phen $H_{2,9}$), 9.07 (2H, d, *J* = 8.4 Hz, phen $H_{4,7}$), 8.37 (2H, s, phen $H_{5,6}$), 8.28−8.25 (2H, m, phen $H_{3,8}$), 7.91 (4H, s, $CN_4$-$C_6H_4$ -CN $H_{meta,\ ortho}$). $^{13}$C NMR (δ, ppm, Acetone-$d_6$): 196.3, 155.8, 148.1, 141.2, 134.1, 132.0, 129.0, 128.9, 127.8, 127.6, 126.8, 118.3, 116.5. Crystals suitable for X-ray analysis (identified as **25**, $C_{24}H_{13}F_3N_7O_6ReS$) were obtained by slow diffusion of diethyl ether into a DCM solution of the complex with a few drops of dilute triflic acid solution

*fac*-[Re(**bipy**)$(CO)_3$(**Tcya**H)]$^+$

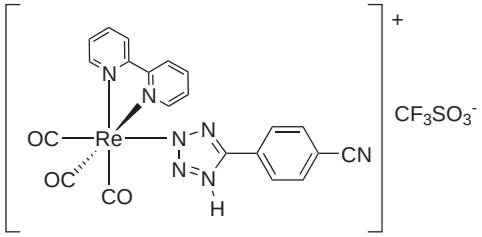

**26**

Yield of compound **26**: 0.026 g, 42%. ESI-MS (m/z) = 598 $[M - SO_3CF_3]^+$; 149 $[SO_3CF_3]^-$. $\nu_{max}$ (IR)/$cm^{-1}$, DCM, rt: 2233 w (CN), 2040 s (CO, A´(1)), 1938 br (CO, A´(2)/A´´), 1606 w (tetrazole C=N). $^1$H NMR (δ, ppm, Acetone-$d_6$): 9.32 (2H, d, *J* = 5.4 Hz, bipy $H_{6,6'}$), 8.78 (2H, d, *J* = 8.4 Hz, bipy $H_{3,3'}$), 8.44 (2H, t, *J* = 8.0 Hz, bipy $H_{4,4'}$), 8.04 (2H, d, *J* = 8.8 Hz, $CN_4$-$C_6H_4$ -CN $H_{meta}$), 7.94−7.88 (4H, m, $CN_4$-$C_6H_4$ -CN $H_{ortho}$ and bipy $H_{5,5'}$). $^{13}$C NMR (δ, ppm, Acetone-$d_6$): 157.5, 154.9, 154.1, 141.7, 140.7, 133.7, 129.0, 128.2, 125.0, 118.8, 114.5. Crystals suitable for X-ray analysis (identified as **26**, $C_{22}H_{13}F_3N_7O_6ReS$) were obtained by slow diffusion of diethyl ether into a DCM solution of the complex with a few drops of dilute triflic acid solution.

### 3.7.2.2 Protonation of the Ir(III) and Ru(II) Complexes.

$[Ir(PyrTzFH)]^+$

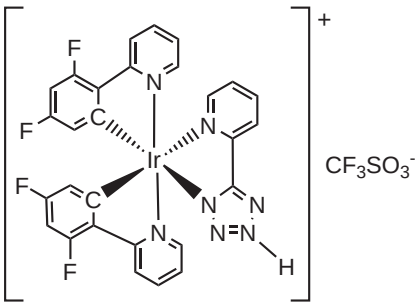

**28**

Protonation of [Ir(PyrTzF)] (**27**) was carried out according to previously published methods.[108,111] [Ir(PyrTzF)] (1 eq) was added to DCM and allowed to cool in an ethyl acetate/liquid nitrogen cool bath. Once the reaction vessel had cooled, trifluoromethanesulfonic acid (1.2 eq) in DCM was added. The reaction was stirred under argon for approximately 30 minutes in the cool bath and was then allowed to come to room temperature and stirred overnight. The solvent was removed *in vacuo* to yield a yellow residue that was identified as the expected protonated complex.

Yield of compound **28**: 0.048 g, 80 %. ESI-MS (m/z) = 719 $[M - SO_3CF_3]^+$. $^1H$ NMR (δ, ppm, Acetonitrile-$d_3$): 8.49 (1H, d, *J* = 7.6 Hz), 8.12-8.24 (3H, m), 8.01 (1H, d, *J* = 5.2 Hz), 7.92 (2H, t, *J* = 7.6Hz), 7.74 (1H, d, *J* = 5.6 Hz),7.66-7.59 (2H, m), 7.13-7.07 (2H, m), 6.72-6.65 (2H, m), 5.75-5.71 (2H, m).

$[Ru(PyrTzH)]^{2+}$

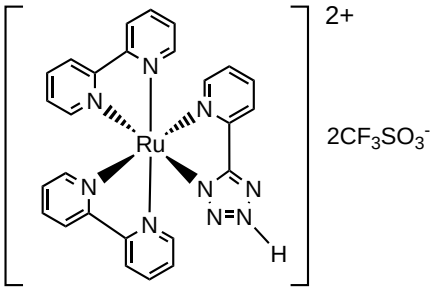


**30**

Protonation of $[Ru(PyrTz)]^+$(**29**) was carried out according to previously published methods.[108,111] $[Ru(PyrTz)]^+$ (1 eq) was added to DCM and allowed to cool in an ethyl acetate/liquid nitrogen cool bath. Once the reaction vessel had cooled, trifluoromethanesulfonic acid (1.2 eq) in DCM was added. The reaction was stirred under nitrogen for approximately 30 minutes in the cool bath and was then allowed to come to room temperature and stirred overnight. The solvent was removed *in vacuo* to yield a red residue that was identified as the expected protonated complex.

Yield of compound **30**: (0.045 g, 75%). ESI-MS (m/z) = 280 $[M^{2+}]$; 145 $[PF_6]^-$, 149 $[SO_3CF_3]^-$. $^1H$ NMR (δ, ppm, Acetonitrile-$d_3$): 8.49 (2H, t, *J* = 7.2 Hz), 8.44-8.41 (1H, m, 2H), 8.35 (1H, d, *J* = 7.6 Hz), 8.05-7.94 (5H, m), 7.87-7.83 (2H, m), 7.79 (1H, d, *J* = 5.6 Hz), 7.69 (1H, d, *J* = 5.2 Hz), 7.62 (1H, d, *J* = 5.2 Hz), 7.41-7.29 (5H, m).

### 3.7.3 X-ray Crystallography

X-ray Crystallography for all of the complexes presented in Chapter Three were carried out by Associate Professor Stefano Zacchini from the University of Bologna. Diffraction data for **21**, **22**, **23**, **24**, **25** and **26** can be found in previously published work.[201]

### 3.7.4 Computational Calculations

The TD-DFT/DFT calculations were performed by Mr. Phillip Wright of Curtin University using GAUSSIAN09.[181] The calculations were done using the B3LYP functional,[221] the Stuttgart-Dresden effective core potential for Re,[222] and the 6-311++G** basis set for the other atoms. The presence of solvent was then mimicked by using the PCM implicit model[223] with parameters appropriate for dichloromethane.

# Chapter 4

# Methylation of Rhenium Tetrazolato Complexes

## 4.1 Abstract

Methylation reactions on a series of neutral *fac*-[Re(**diim**)$(CO)_3$(**L**)] complexes caused an irreversible modulation of photophysical output, in terms of elongated lifetimes and higher quantum yields. The emission maximum was also blue shifted upon methylation. IR studies and photophysical characterisation suggested the formation of only one methylated rhenium species, NMR analysis revealed that two cationic rhenium species were present in solution. X-ray crystallography was used to identify these products as both the Re-N2 and Re-N1 linkage isomers. Although these complexes displayed superior luminescent output, the tetrazolato ligand became labile upon methylation, causing the overall stability of the complex to be lost.

## 4.2 Introduction

The 5-substituted aryl tetrazolato ligand has been increasingly explored in a series of organometallic complexes, spanning more than a decade.[111–114,170,174,219,224–227] For those luminescent complexes, the contribution of the tetrazole ligand can play an important role in determining the extent of the HOMO-LUMO gap which directly influences the luminescent output. As was observed in Chapter Three, the luminescence of a series of *fac*-[Re(**diim**)$(CO)_3$(**L**)] complexes was reversibly altered upon reaction with the most simple electrophile, $H^+$. The $CH_3{}^+$ group is another electrophile which can react with the nitrogen atoms of the tetrazole ring and potentially modulate the photophysical output of the complexes.

Previous reports on metal tetrazolato complexes have demonstrated that methylation can significantly influence the luminescent properties of these complexes. In particular, methylation of a mono-coordinated aryl tetrazolato ligand caused a "turn-on" effect for a Ru(II) metal complex.[114] The same reaction performed on cyclometalated Ir(III)-tetrazolate complexes caused a red shift of the emission maximum of over 50 nm,[113] similar to the outcome of protonating the Ir(III)-tetrazolato complex discussed in Chapter Three. Interestingly, the methylation of a deep blue emitting Pt(II)-cyclophane complex significantly altered the emitting excited state as was evidenced by a notable reduction in the luminescent output and an increase of the $k_{nr}$ value.[224]

The results from the protonation reactions carried out in Chapter Three were encouraging, with the Re(I) complexes showing detectable responses to changes in their surrounding environment. Methylation is an irreversible reaction and could offer a more straight forward way to purify and isolate the positively charged rhenium complexes.

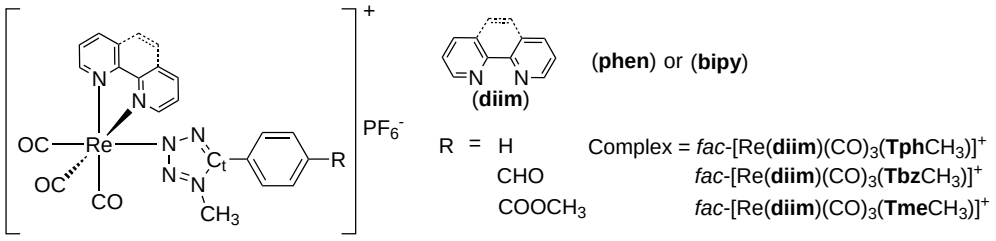


Scheme 4.1: Codes and abbreviations used for the methylated Re(I) complexes reported in Chapter Four.

The work described in this Chapter is based around the methylation of a series of

neutral *fac*-[Re(**diim**)$(CO)_3$(**L**)] complexes. The fundamental changes occurring at a chemical and photophysical level were investigated in response to this structural modification. The complexes described in this Chapter are outlined in Scheme 4.1

## 4.3 Results

### 4.3.1 Synthesis

Methylation of the neutral rhenium complexes was carried out according to previously published methods[108,111–113,219,224] as demonstrated in Scheme 4.2. The tetrazole ring has three potential sites for methylation which are the three free nitrogen atoms of the tetrazole ring. Scheme 4.2 shows the three possible methylation products. The reaction was carried out at low temperatures (-50 ºC), to favour methylation at the less hindered N4 atom, Scheme 4.2 C.

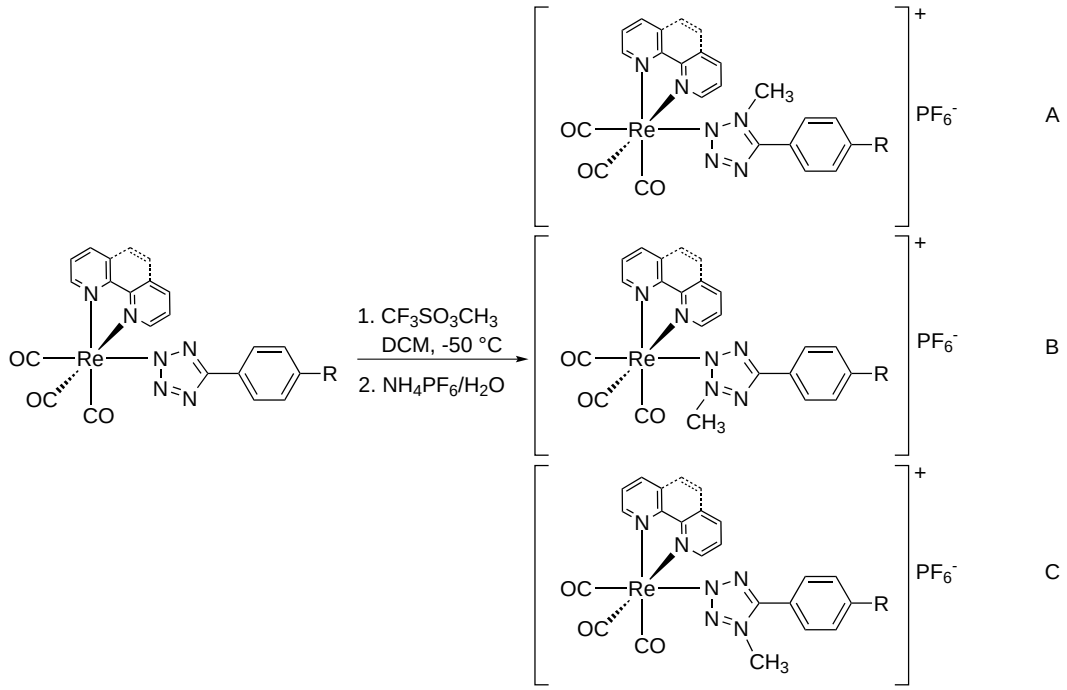


Scheme 4.2: Synthesis of the methylated rhenium tetrazolato complexes showing potential methylation at N1 (A), N3 (B) or N4 (C).

Following the addition of a slight excess of methyl triflate and stirring overnight at room temperature, the cationic rhenium complexes were formed and subsequently isolated as their $PF_6^-$ salts. The six complexes synthesised (Scheme 4.1) were purified by reprecipitation from dichloromethane and diethyl ether.

### 4.3.2 Infrared Spectroscopy

The formation of the expected compounds was first confirmed by solid state IR spectroscopy. Intense CO signals were observed between 2028 and 2032 $cm^{-1}$ and broader signals between 1897 and 1917 $cm^{-1}$, Table 4.3.1. In some of the **bipy** complexes, the CO A´(2) and A´´ are collapsed, which is not uncommon in these type of rhenium complexes.[178] The totally symmetric in phase stretching band A´(1), has shifted from values of 2018-2021 $cm^{-1}$ in the neutral rhenium complexes to 2028-2032 $cm^{-1}$ in the methylated species (Table 4.3.1). The A´(2) and A´´ CO bands also shift to higher wavenumbers upon methylation due to the reduced electron density on the rhenium metal centre caused by methylation of the tetrazolato ligand.

Table 4.3.1: Solid state FT-IR measurements comparing the CO stretching frequencies ($cm^{-1}$) in the neutral rhenium complexes and their corresponding methylated analogues.

| Stretching frequency ($cm^{-1}$) | CO A´(1) | CO A´(2) | CO A´´ |
|---|---|---|---|
| *fac*-[Re(**phen**)$(CO)_3$(**Tph**)] (**11**) | 2019 | 1909 | 1881 |
| *fac*-[Re(**phen**)$(CO)_3$(**Tph**$CH_3$)]$^+$ (**31**) | 2032 | 1911 | 1897 |
| *fac*-[Re(**bipy**)$(CO)_3$(**Tph**)] (**12**) | 2018 | 1893 | |
| *fac*-[Re(**bipy**)$(CO)_3$(**Tph**$CH_3$)]$^+$(**32**) | 2031 | 1931 | 1898 |
| *fac*-[Re(**phen**)$(CO)_3$(**Tbz**)] (**13**) | 2020 | 1916 | 1892 |
| *fac*-[Re(**phen**)$(CO)_3$(**Tbz**$CH_3$)]$^+$(**33**) | 2032 | 1929 | 1922 |
| *fac*-[Re(**bipy**)$(CO)_3$(**Tbz**)] (**14**) | 2021 | 1885 | |
| *fac*-[Re(**bipy**)$(CO)_3$(**Tbz**$CH_3$)]$^+$(**34**) | 2028 | 1929 | 1901 |
| *fac*-[Re(**phen**)$(CO)_3$(**Tme**)] (**15**) | 2020 | 1912 | 1887 |
| *fac*-[Re(**phen**)$(CO)_3$(**Tme**$CH_3$)]$^+$(**35**) | 2031 | 1931 | 1917 (1897sh) |
| *fac*-[Re(**bipy**)$(CO)_3$(**Tme**)] (**16**) | 2020 | 1902 | |
| *fac*-[Re(**bipy**)$(CO)_3$(**Tme**$CH_3$)]$^+$(**36**) | 2030 | 1908 (1925 sh) | |

### 4.3.3 NMR

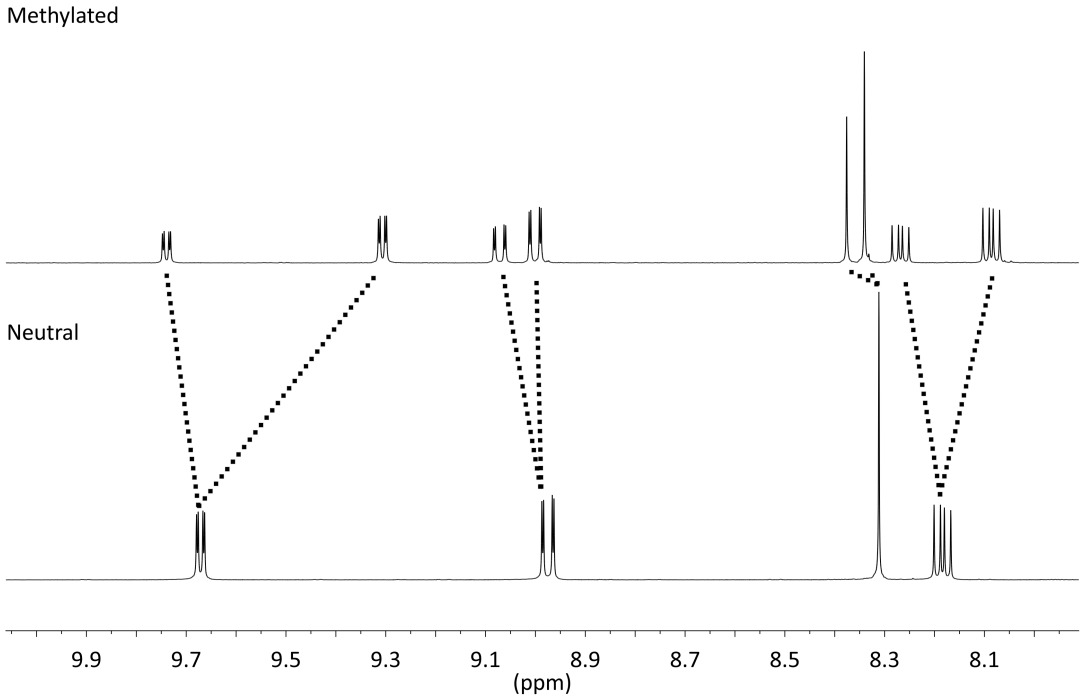


Figure 4.1: Comparison of the aromatic region in the $^{1}$H NMR spectrum of the neutral rhenium complex **11** (bottom) and the corresponding methylated species **31** (top).

Upon $^{1}$H and $^{13}$C NMR analysis of the methylated Re(I) species (acetone-$d_6$) two distinct signal patterns were observed. Figure 4.1 shows the aromatic region of the $^{1}$H NMR spectra illustrating the change in the number and position of the phenanthroline peaks upon methylation. In the neutral species there is one set of phenanthroline resonances (Figure 4.1, bottom) whereas after methylation, two sets are present (Figure 4.1, top). This could be suggestive of two rhenium species present in solution. The reaction may have produced two separate rhenium complexes or, in solution an equilibrium exists. Figure 4.2 to Figure 4.7 show the NMR spectra of the neutral and corresponding methylated Re(I) complexes. The integration of the $^{1}$H NMR spectra (in acetone-$d_6$) for the methylated species, indicated the two products were occurring in a ratio ranging from 1:0.65 to 1:0.97 (a:b; where “a” was assigned to the resonance with the higher integration ratio). This a:b ratio is specified in each of the Figures. The $^{1}$H NMR figures also show two new upfield singlets, suggestive of a methylated species.

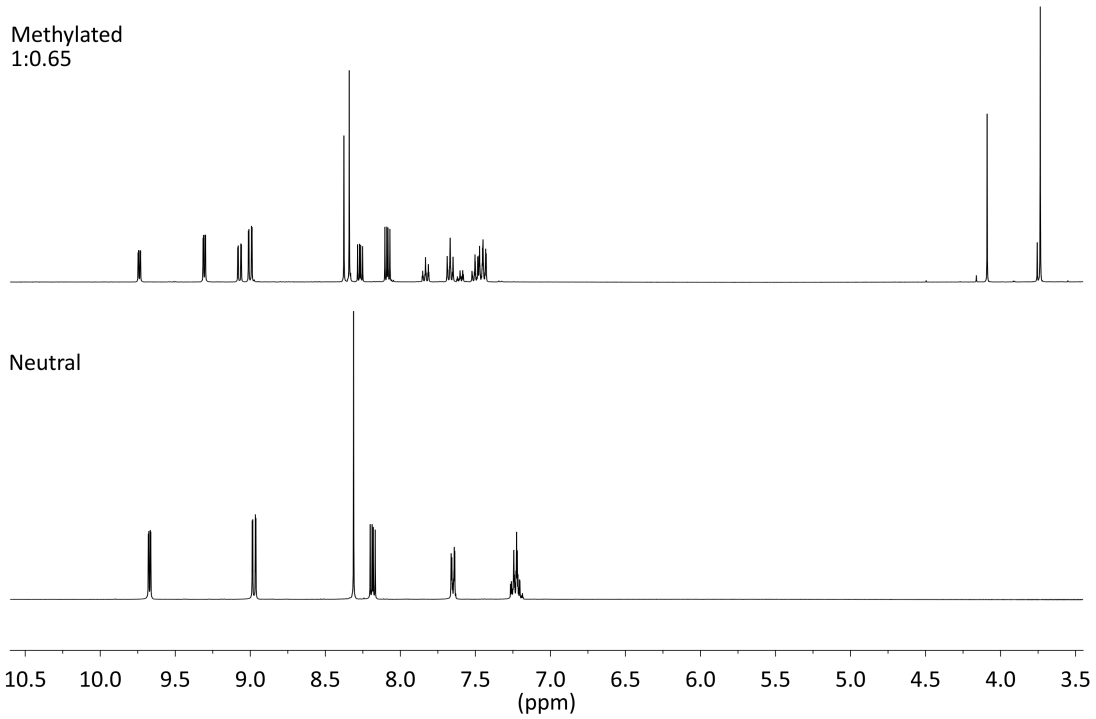


Figure 4.2: $^{1}$H NMR spectra of the neutral complex *fac*-[Re(**phen**)$(CO)_3$(**Tph**)], **11** (bottom) compared to the methylated species, *fac*-[Re(**phen**)$(CO)_3$(**TphCH$_3$**)]$^{+}$, **31** (top).

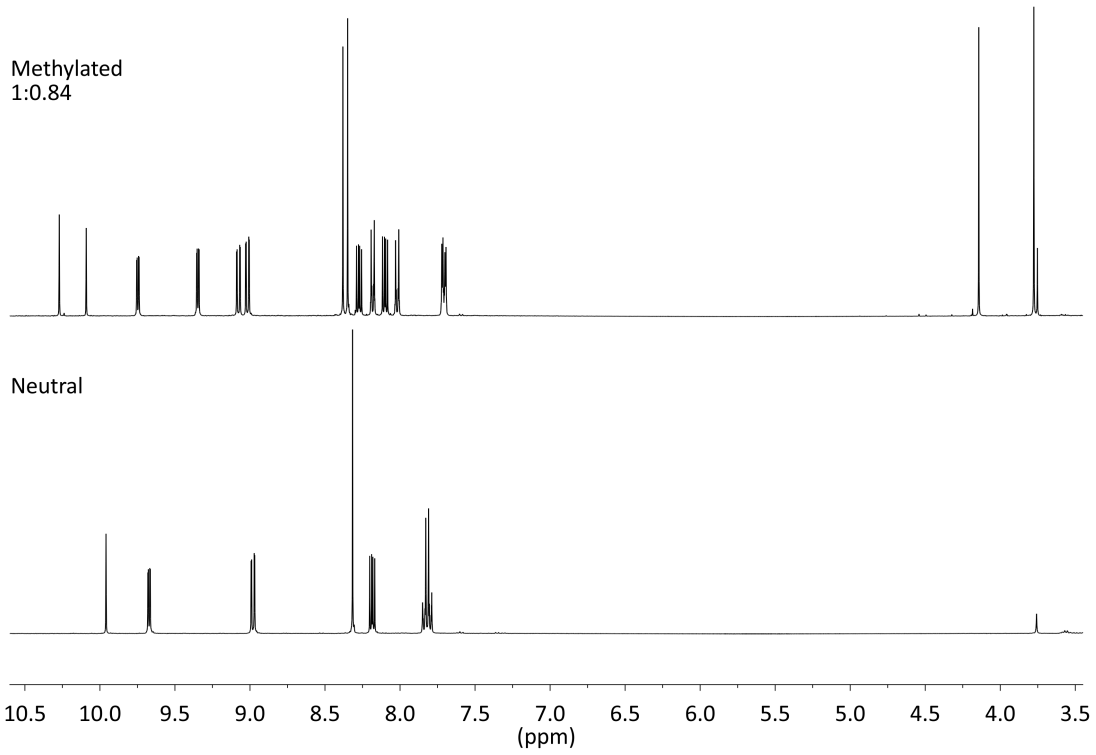


Figure 4.3: $^{1}$H NMR spectra of the neutral complex *fac*-[Re(**phen**)$(CO)_3$(**Tbz**)], **13** (bottom) compared to the methylated species, *fac*-[Re(**phen**)$(CO)_3$(**Tbz**$CH_3$)]$^{+}$, **33** (top).

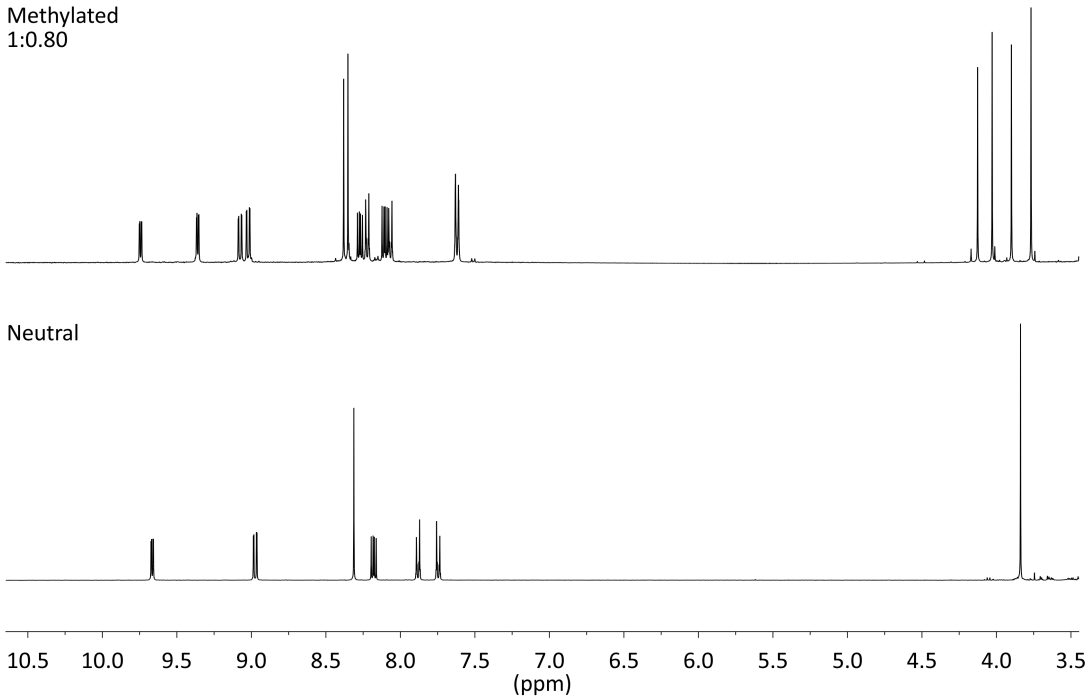


Figure 4.4: $^{1}$H NMR spectra of the neutral complex *fac*-[Re(**phen**)$(CO)_3$(**Tme**)], **15**, (bottom) compared to the methylated species, *fac*-[Re(**phen**)$(CO)_3$(**Tme**$CH_3$)]$^{+}$, **35** (top).

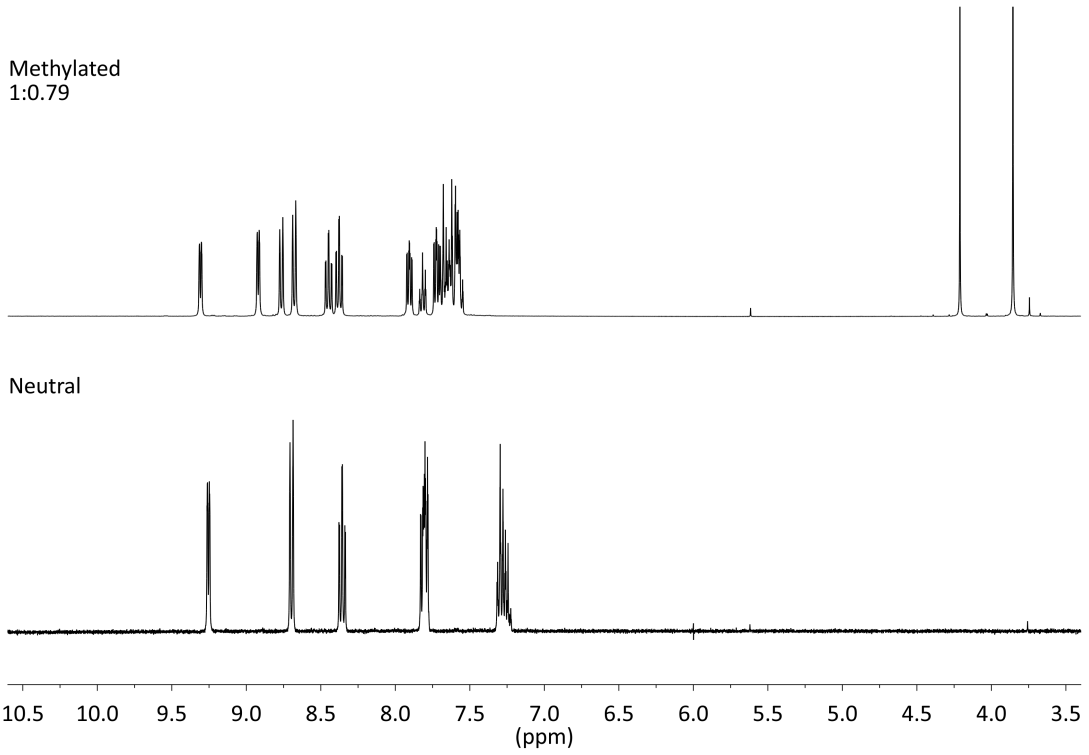


Figure 4.5: $^{1}$H NMR spectra of the neutral complex *fac*-[Re(**bipy**)$(CO)_3$(**Tph**)], **12** (bottom) compared to the methylated species, *fac*-[Re(**bipy**)$(CO)_3$(**Tph**$CH_3$)]$^{+}$, **32** (top).

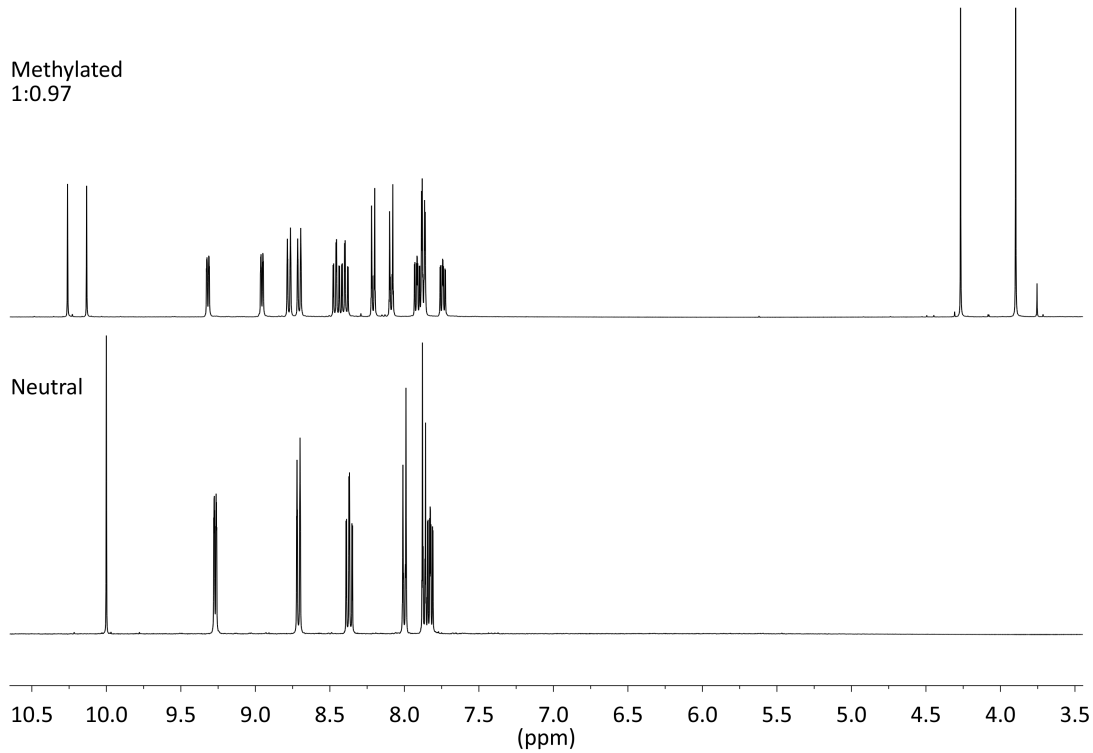


Figure 4.6: $^{1}$H NMR spectra of the neutral complex *fac*-[Re(**bipy**)$(CO)_3$(**Tbz**)], **14** (bottom) compared to the methylated species, *fac*-[Re(**bipy**)$(CO)_3$(**Tbz**$CH_3$)]$^+$, (**34**, top).

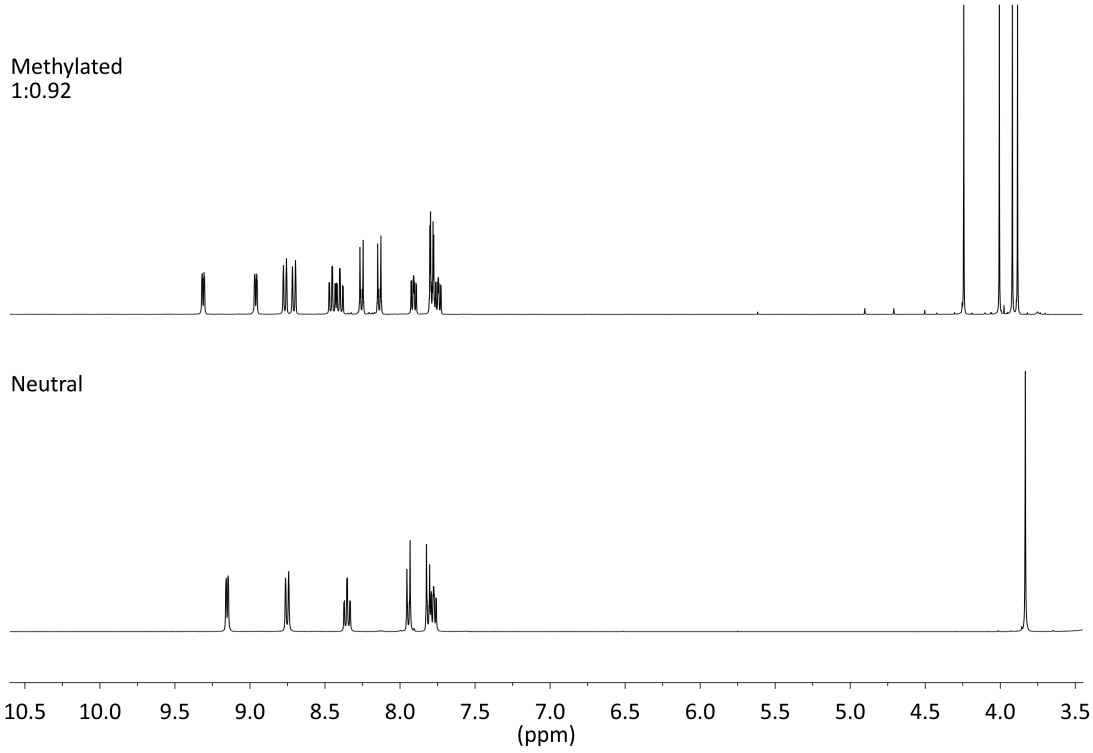


Figure 4.7: Comparison of the $^{1}$H NMR spectra of the neutral *fac*-[Re(**bipy**)$(CO)_3$(**Tme**)], **16** (bottom) with that of the methylated species, *fac*-[Re(**bipy**)$(CO)_3$(**Tme**$CH_3$)]$^+$, **36** (top).

Table 4.3.2 shows a comparison of the $H_{meta}$ and $H_{ortho}$ signals before and after methylation of the Re(I) complexes. Table 4.3.2 and the corresponding Figures, show that for the methylated complexes, the $H_{ortho}$ resonances for both species are collapsed, forming either a singlet or a multiplet. For those complexes with an electron withdrawing -R group in the *para* position, the $H_{meta}$ signals have been deshielded and two separate signals are observed. This is consistent with the two distinct sets of resonances observed for the methylated complexes. The $H_{ortho}$ resonances in the methylated species have been deshielded to a lesser extent than the $H_{meta}$ signals.

Table 4.3.2: Comparison of the $^1$H NMR signals relative to the *ortho* and *meta* protons before and after methylation. NMR data from acetone-$d_6$ solutions.

| **Rhenium Complex** | **Neutral / Methylated** | $\delta H_o$ | $\delta H_m$ |
|---|---|---|---|
| *fac*-[Re(**phen**)$(CO)_3$(**Tph**)] | **11** | 7.63 | 7.22-7.20[a] |
| *fac*-[Re(**phen**)$(CO)_3$(**Tph**$CH_3$)]$^+$ | **31** | - | - |
| *fac*-[Re(**bipy**)$(CO)_3$(**Tph**)] | **12** | 7.82−7.79[c] | 7.32−7.24[a] |
| *fac*-[Re(**bipy**)$(CO)_3$(**Tph**$CH_3$)]$^+$ | **32** | - | - |
| *fac*-[Re(**phen**)$(CO)_3$(**Tbz**)] | **13** | 7.80 | 7.84 |
| *fac*-[Re(**phen**)$(CO)_3$(**Tbz**$CH_3$)]$^+$ | **33** | 7.72-7.69 | 8.18, 8.02 |
| *fac*-[Re(**bipy**)$(CO)_3$(**Tbz**)] | **14** | 7.87 | 8.01 |
| *fac*-[Re(**bipy**)$(CO)_3$(**Tbz**$CH_3$)]$^+$ | **34** | 7.88 | 8.21, 8.09 |
| *fac*-[Re(**phen**)$(CO)_3$(**Tme**)] | **15** | 7.75 | 7.88 |
| *fac*-[Re(**phen**)$(CO)_3$(**Tme**$CH_3$)]$^+$ | **35** | 7.62 | 8.52, 8.19-8.06[b] |
| *fac*-[Re(**bipy**)$(CO)_3$(**Tme**)] | **16** | 7.91 | 7.95 |
| *fac*-[Re(**bipy**)$(CO)_3$(**Tme**$CH_3$)]$^+$ | **36** | 7.80-7.78 | 8.26, 8.14 |

[a]; Peak range includes the resonances for $H_m$ and $H_p$,[b]; Peak range includes the resonance for phen $H_{3,8}$, [c];Peak range includes the resonance for bipy $H_{4,4'}$, [-]; the $H_o$ and $H_m$ signals for the methylated complexes with the phenyltetrazole ligand could not be distinguished and have therefore been omitted.

Isolated crystals that were grown of some of the methylated complexes, were analysed by NMR. In each case, the crystal structures indicated the presence of one system in

the solid state (section 4.3.4) by assessing the unit cell parameters of several crystals in the same batch. However, the $^{1}$H NMR showed the presence of the two sets of resonances, again suggesting that in solution, two species are present.

#### 4.3.3.1 Temperature Dependent NMR

Temperature dependent NMR studies were carried out to further understand the nature of the two products observed for the methylated Re(I) complexes. Temperature dependent NMR experiments were carried out on *fac*-[Re(**phen**)$(CO)_3$(**Tbz**$CH_3$)]$^+$ (**33**) in DMSO-$d_6$ and acetonitrile-$d_3$. The experiment using DMSO-$d_6$ was performed using

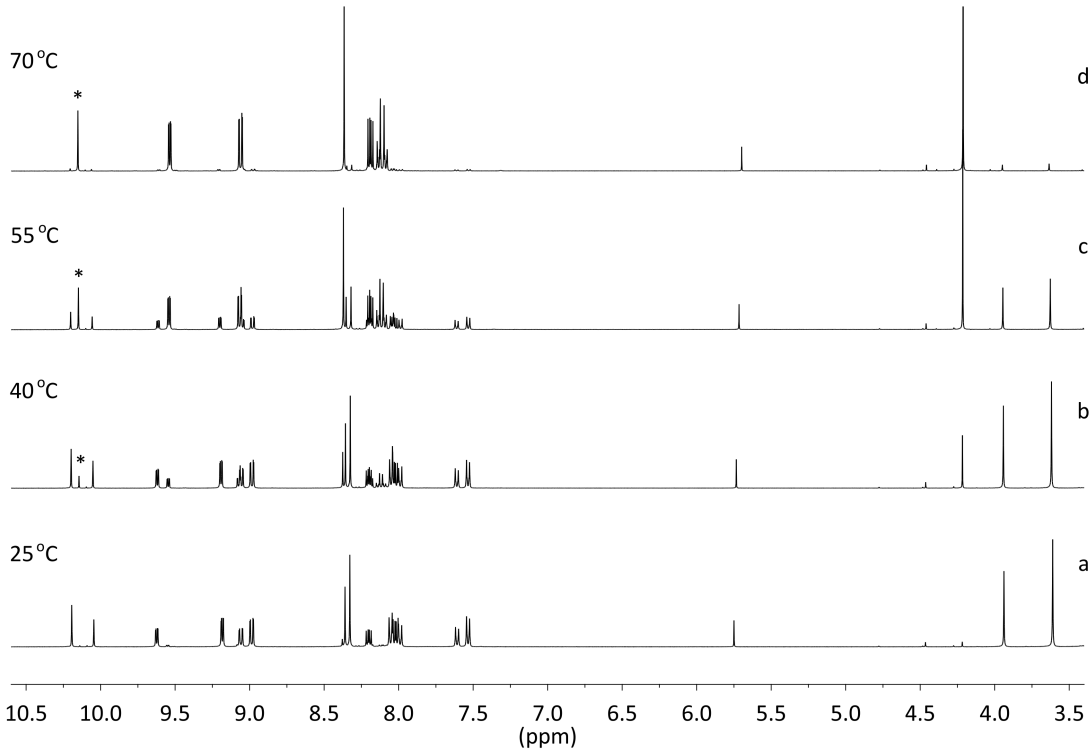


Figure 4.8: $^{1}$H NMR spectrum of *fac*-[Re(**phen**)$(CO)_3$(**Tbz**$CH_3$)]$^+$ (**33**) at 25 ºC (a), 40 ˚C (b), 55 ºC (c) and 70 ºC (d) in DMSO-$d_6$.

the variable temperature function of the NMR. The sample was steadily heated to 70 ºC with spectra being recorded at various intervals. Figure 4.8 shows the NMR spectra of **33** recorded at sequentially increasing temperatures between 25 and 70 ºC. At 40 ºC, there is the emergence of a new set of peaks which increase in intensity as the temperature rises (marked by the * in Figure 4.8). As this new system becomes more prevalent, the two sets of original peaks disappear. Upon reaching 70 ºC the new system predominates, with only minor traces of any other species observed. Heating the

sample has produced a single *new* product. The NMR, still containing the sample was slowly cooled back to the starting temperature of 25 ºC. Multiple spectra were recorded as the sample was cooled however each subsequent spectra, even the one taken at room temperature, looked identical to that in Figure 4.8 d (at 70 ºC).

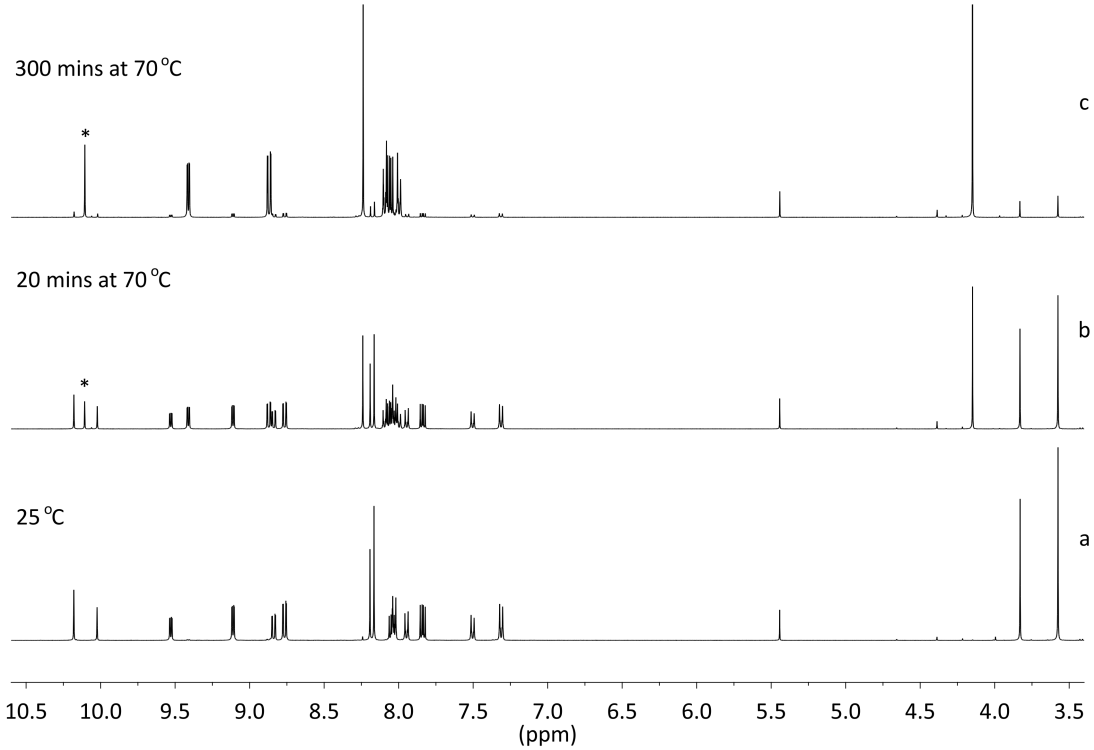


Figure 4.9: $^{1}$H NMR spectra of *fac*-[Re(**phen**)$(CO)_3$(**Tbz**$CH_3$)]$^+$ (**33**) at 25 ˚C (a), after being heated at 70 ˚C for 20 minutes (b) and after being heated at 70 ˚C for 300 minutes (c) in acetonitrile-$d_3$.

To further investigate these observations, an NMR sample of the same complex (**33**) in acetonitrile-$d_3$ was heated straight to 70 ˚C in an oil bath. NMR spectra were recorded at different time intervals. After 20 minutes of heating the sample, the emergence of a third, new set of peaks are observed (Figure 4.9). After heating to 70 ˚C for five hours, the NMR spectrum only showed one set of peaks, similar to that observed in DMSO-$d_6$.

Although the original resonances observed at room temperature eventually disappear; they were still present in the same ratios throughout the entire heating process (while they could still be observed).

### 4.3.3.2 Solvent effects

NMR were carried out in different solvents to analyse if there was a change in the relative integration ratios of the two systems present. The NMR spectra of *fac*-[Re(**phen**)$(CO)_3$(**Tph**$CH_3$)]$^+$ (**31**) was recorded in acetone-$d_6$. Subsequently, the solvent was removed (without heating) and the same sample was measured in acetonitrile-$d_3$. The integration ratio of the two rhenium systems (a:b) in acetone-$d_6$ was 1:0.52 whereas the same sample in acetonitrile-$d_3$ gave an integration ratio of 1:0.72 (a:b), see Figure 4.10.

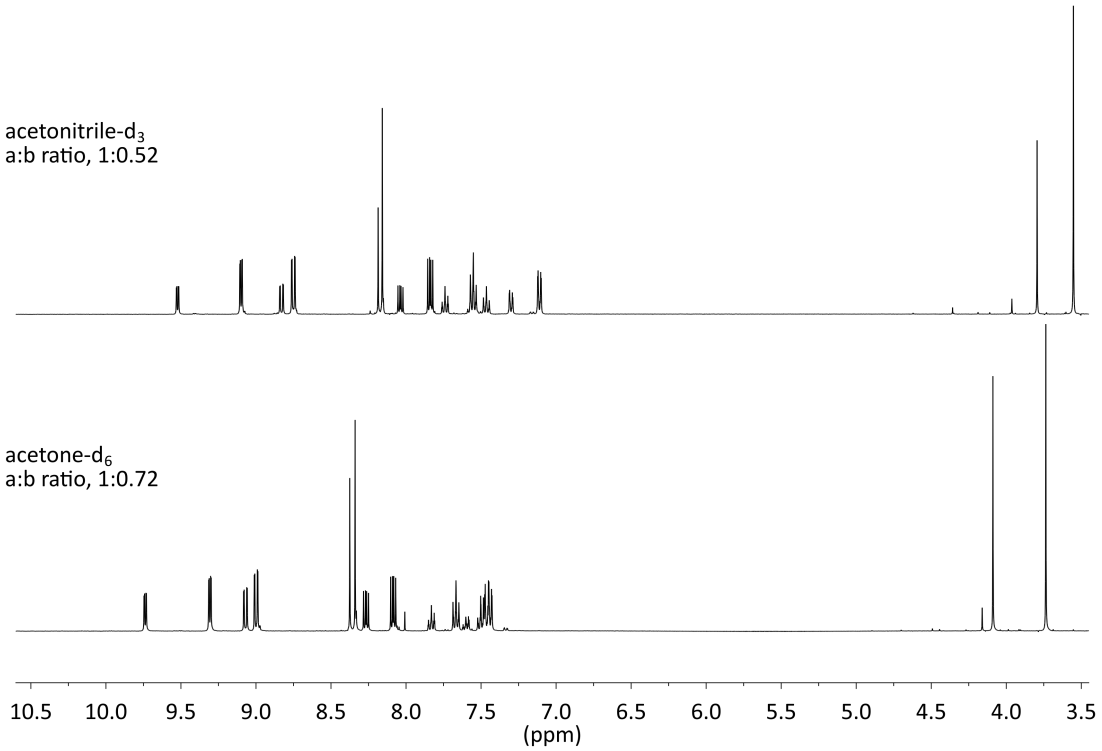


Figure 4.10: $^1$H NMR spectra of *fac*-[Re(**phen**)$(CO)_3$(**Tph**$CH_3$)]$^+$, **31** in acetonitrile-$d_3$ (top) compared to the spectrum recorded in acetone-$d_6$ (bottom).

The same experiment was conducted on *fac*-[Re(**phen**)$(CO)_3$(**Tbz**$CH_3$)]$^+$(**33**). The integration ratio of the two systems in acetone-$d_6$was 1:0.86 whereas when the NMR was recorded in acetonitrile-$d_3$, the a:b ratio was 1:0.68, see Figure 4.11.

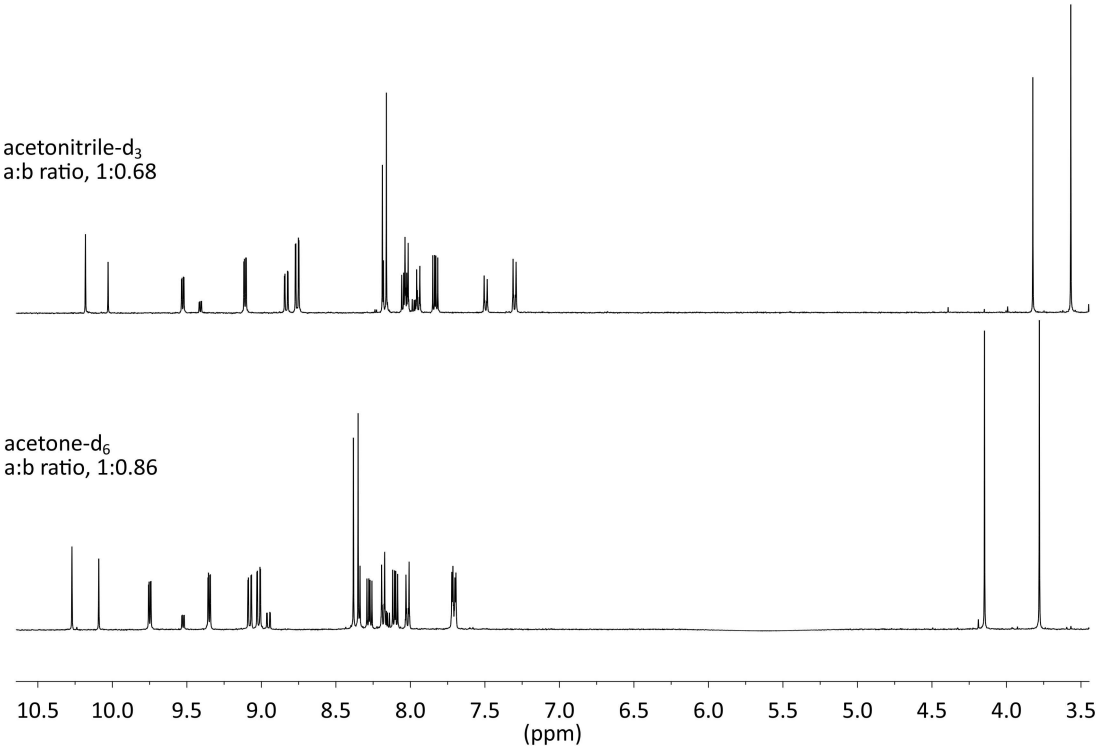


Figure 4.11: $^{1}H$ NMR spectra of *fac*-[Re(**phen**)$(CO)_3$(**Tbz**$CH_3$)]$^+$, **33** in acetonitrile-$d_3$ (top) compared to the spectrum recorded in acetone-$d_6$ (bottom).

### 4.3.4 X-ray Crystallography

Single crystals of all prepared complexes were grown. In each case, the product isolated from the crystallisation experiments was the one showing methylation occurring at the N4 atom. Interestingly, coordination of the aryl tetrazolato ligand to the rhenium centre was not always via the N2 atom as observed for the previously discussed Re(I) complexes in Chapters Two and Three. Figure 4.12 and Figure 4.13 show the crystal structures isolated for each of the methylated **phen** and **bipy** complexes respectively. All of the methylated **phen** complexes, **31**, **33** and **35** were isolated as the N1 linkage isomer. The crystals that were isolated for the methylated **bipy** complexes were a mixture of both N1 (**36**) and N2 (**33**, **32**) linkage isomers, see Table 4.3.3.

Table 4.3.3: Deviation from coplanarity between the aryl and tetrazole rings in the methylated Re(I) complexes.

| Rhenium Complex/N1 or N2 | Linkage Isomer | Deviation from Coplanarity (˚) (tetrazole and aryl ring) |
|---|---|---|
| *fac*-[Re(**phen**)$(CO)_3$(**Tph**$CH_3$)]$^+$ (**31**) | N1 | 72.75 |
| *fac*-[Re(**bipy**)$(CO)_3$(**Tph**$CH_3$)]$^+$(**32**) | N2 | 48.24 |
| *fac*-[Re(**phen**)$(CO)_3$(**Tbz**$CH_3$)]$^+$(**33**) | N1 | 86.98 |
| *fac*-[Re(**bipy**)$(CO)_3$(**Tbz**$CH_3$)]$^+$(**34**) | N2 | 39.80 |
| *fac*-[Re(**phen**)$(CO)_3$(**Tme**$CH_3$)]$^+$(**35**) | N1 | 84.55 |
| *fac*-[Re(**bipy**)$(CO)_3$(**Tme**$CH_3$)]$^+$(**36**) | N1 | 79.46 |

The torsion angle between the tetrazole and aryl ring was used to calculate the deviation from coplanarity (ie: deviation from 0˚ or 180˚). These calculated values are displayed in Table 4.3.3. The N2 coordinated species have torsion angles which indicate a smaller deviation from coplanarity compared to the N1 coordinated complexes. None of the crystal structures isolated for the synthesised complexes show any hydrogen bonding or significant $\pi$-$\pi$ interactions.

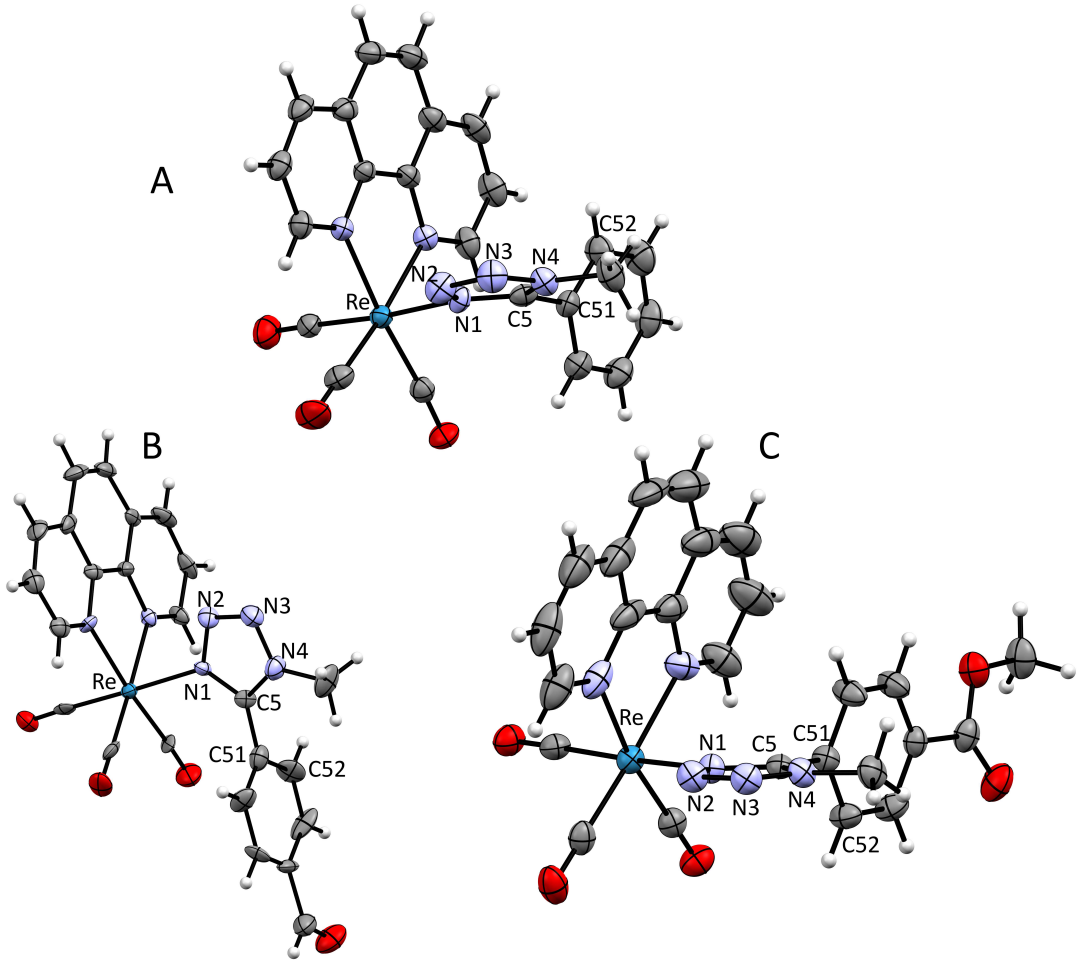


Figure 4.12: X-ray crystal structures of *fac*-[Re(**phen**)$(CO)_3$(**Tph**$CH_3$)]$^+$ (**31**, A), *fac*-[Re(**phen**)$(CO)_3$(**Tbz**$CH_3$)]$^+$ (**33**, B), and *fac*-[Re(**phen**)$(CO)_3$(**Tme**$CH_3$)]$^+$ (**35**, C) where thermal ellipsoids have been drawn at 50% probability (except for A, at 30% probability). The hexafluorophosphate counter ion has been omitted for clarity.

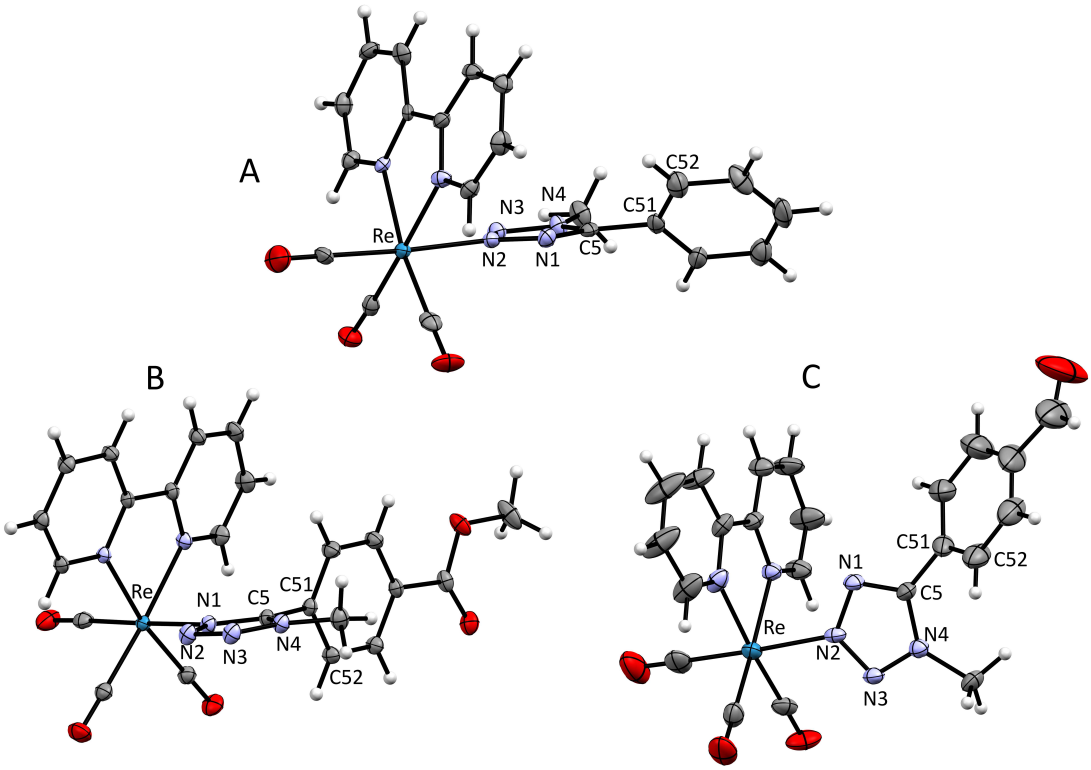


Figure 4.13: X-ray crystal structures of *fac*-[Re(**bipy**)$(CO)_3$(**Tph**$CH_3$)]$^+$ (**32**, A), *fac*-[Re(**bipy**)$(CO)_3$(**Tbz**$CH_3$)]$^+$ (**34**, B), and *fac*-[Re(**bipy**)$(CO)_3$(**Tme**$CH_3$)]$^+$ (**36**, C) where thermal ellipsoids have been drawn at 50% probability. The hexafluorophosphate counter ion has been omitted for clarity.

### 4.3.5 Photophysics

Table 4.3.4: Absorbance data for the methylated rhenium tetrazolato complexes at $10^{-5}$ M in DCM.

| Rhenium Complex | Absorption $\lambda_{max}$/nm ($\varepsilon/10^4 M^{-1}cm^{-1}$) |
|---|---|
| *fac*-[Re(**phen**)(CO)$_3$(**Tph**CH$_3$)]$^+$ (**31**) | 256 (3.93), 276 (3.83), 335 (0.87), 380 (0.60) |
| *fac*-[Re(**bipy**)(CO)$_3$(**Tph**CH$_3$)]$^+$(**32**) | 242 (5.22), 319 (2.56), 350 (1.20) |
| *fac*-[Re(**phen**)(CO)$_3$(**Tbz**CH$_3$)]$^+$(**33**) | 256 (4.22), 331 (0.67), 366 (0.43) |
| *fac*-[Re(**bipy**)(CO)$_3$(**Tbz**CH$_3$)]$^+$(**34**) | 246 (3.98), 314 (1.5), 350 (0.5) |
| *fac*-[Re(**phen**)(CO)$_3$(**Tme**CH$_3$)]$^+$(**35**) | 230 (5.77), 254 (4.64), 333 (0.78), 380 (0.41) |
| *fac*-[Re(**bipy**)(CO)$_3$(**Tme**CH$_3$)]$^+$(**36**) | 265 (4.14), 320 (1.28), 350 (0.47) |

Table 4.3.5: Photophysical data for the methylated rhenium tetrazolato complexes.

| Rhenium | Emission 298 K | | | | |
|---|---|---|---|---|---|
| Complex[a] | $\lambda_{max}$ (nm) | $\tau$ ($\mu$s)[b] | $\tau$ ($\mu$s)[c] | $\phi^b$ | $\phi^c$ |
| *fac*-[Re(**phen**)(CO)$_3$(**Tph**CH$_3$)]$^+$ (**31**) | 536 | 1.20 | 2.00 | 0.28 | 0.50 |
| *fac*-[Re(**bipy**)(CO)$_3$(**Tph**CH$_3$)]$^+$(**32**) | 546 | 0.61 | 1.00 | 0.22 | 0.36 |
| *fac*-[Re(**phen**)(CO)$_3$(**Tbz**CH$_3$)]$^+$(**33**) | 536 | 1.30 | 3.37 | 0.25 | 0.53 |
| *fac*-[Re(**bipy**)(CO)$_3$(**Tbz**CH$_3$)]$^+$(**34**) | 546 | 0.63 | 0.99 | 0.28 | 0.48 |
| *fac*-[Re(**phen**)(CO)$_3$(**Tme**CH$_3$)]$^+$(**35**) | 538 | 1.40 | 3.20 | 0.23 | 0.57 |
| *fac*-[Re(**bipy**)(CO)$_3$(**Tme**CH$_3$)]$^+$(**36**) | 546 | 0.64 | 1.02 | 0.20 | 0.34 |

[a]; All data for complexes in $10^{-5}$ M DCM solutions and all quantum yields measured against rhodamine 101, [b]; air-equilibrated samples, [c]; degassed ($O_2$ free) samples.

Table 4.3.6: Emission data for the methylated rhenium tetrazolato complexes at 77 K in DCM.

| Rhenium Complex | Emission 77K | |
|---|---|---|
| | $\lambda_{max}$(nm) | $\tau$ ($\mu$s) |
| *fac*-[Re(**phen**)$(CO)_3$(**Tph**$CH_3$)]$^+$ (**31**) | 492 | 9.80 |
| *fac*-[Re(**bipy**)$(CO)_3$(**Tph**$CH_3$)]$^+$(**32**) | 490 | 4.05 (84%), 8.42 (16%) |
| *fac*-[Re(**phen**)$(CO)_3$(**Tbz**$CH_3$)]$^+$(**33**) | 492 | 10.90 |
| *fac*-[Re(**bipy**)$(CO)_3$(**Tbz**$CH_3$)]$^+$(**34**) | 508 | 4.15 |
| *fac*-[Re(**phen**)$(CO)_3$(**Tme**$CH_3$)]$^+$(**35**) | 508 | 9.13 |
| *fac*-[Re(**bipy**)$(CO)_3$(**Tme**$CH_3$)]$^+$(**36**) | 500 | 4.38 |

Table 4.3.7: Radiative and non-radiative decay constants ($k_r$ and $k_{nr}$) for the methylated rhenium complexes in degassed ($O_2$ free) solutions of DCM.

| **Rhenium Complex** | $k_r$ ($10^6$ $s^{-1}$) | $k_{nr}$ ($10^6$ $s^{-1}$) |
|---|---|---|
| *fac*-[Re(**phen**)$(CO)_3$(**Tph**$CH_3$)]$^+$ (**31**) | 0.250 | 0.250 |
| *fac*-[Re(**bipy**)$(CO)_3$(**Tph**$CH_3$)]$^+$(**32**) | 0.360 | 0.640 |
| *fac*-[Re(**phen**)$(CO)_3$(**Tbz**$CH_3$)]$^+$(**33**) | 0.157 | 0.139 |
| *fac*-[Re(**bipy**)$(CO)_3$(**Tbz**$CH_3$)]$^+$(**34**) | 0.485 | 0.525 |
| *fac*-[Re(**phen**)$(CO)_3$(**Tme**$CH_3$)]$^+$(**35**) | 0.178 | 0.134 |
| *fac*-[Re(**bipy**)$(CO)_3$(**Tme**$CH_3$)]$^+$(**36**) | 0.333 | 0.647 |

The absorption profiles for the methylated rhenium complexes generally show high energy absorption bands in the UV region at 230 nm, tailing off around 320 nm. There is also a lower energy band around 330-480 nm. As observed for the previously synthesised Re(I) complexes, the low energy absorption bands for the methylated **phen** complexes are blue shifted with respect to the **bipy** ones. This blue shift makes them appear broader as they tail off into high energy transitions. The methylated species generally have a blue shifted absorption profile when compared to the neutral analogues, as seen in Figure 4.14 to Figure 4.19.

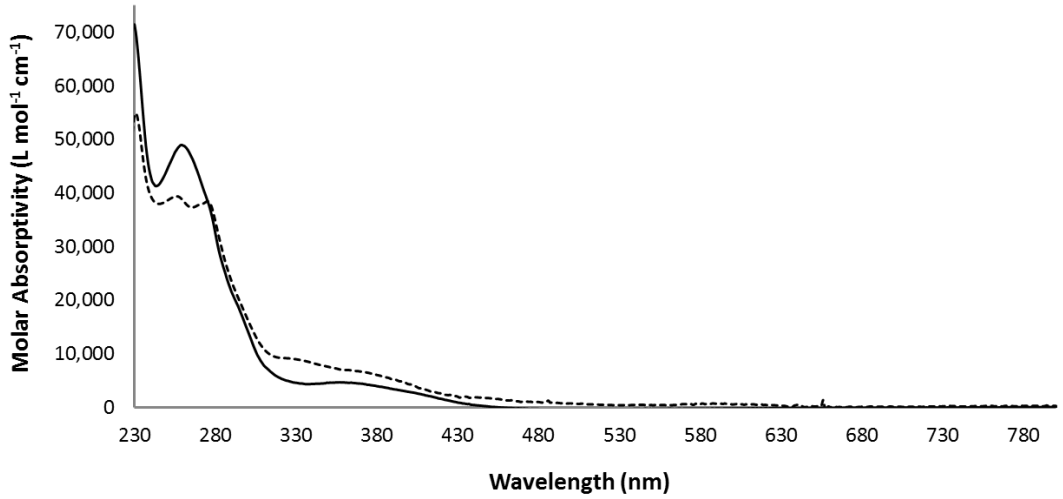


Figure 4.14: Absorption of the neutral rhenium complex, *fac*-[Re(**phen**)$(CO)_3$(**Tph**)] (**11**, solid line) compared to the corresponding methylated complex, *fac*-[Re(**phen**)$(CO)_3$(**Tph**$CH_3$)]$^+$ (**31**, dashed line) in DCM.

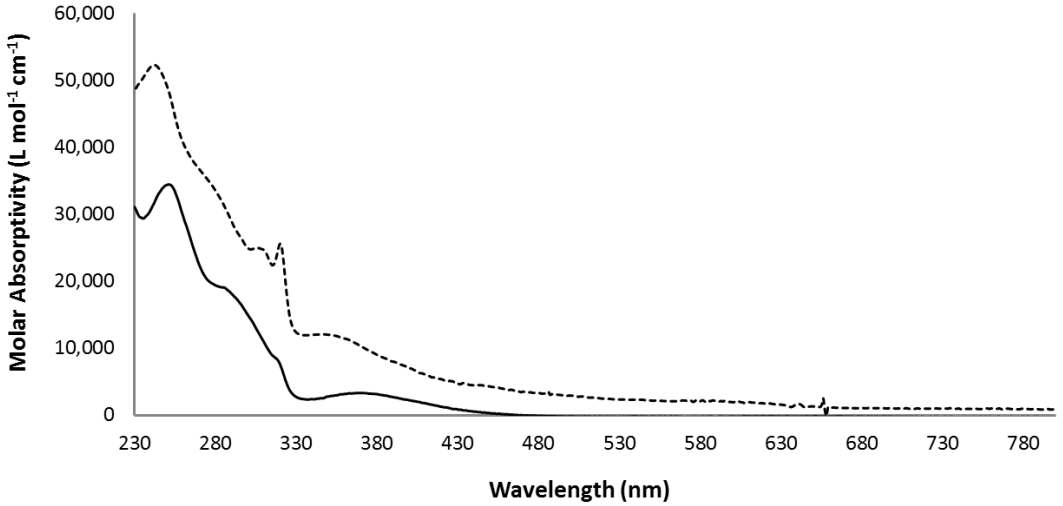


Figure 4.15: Absorption of the neutral rhenium complex, *fac*-[Re(**bipy**)$(CO)_3$(**Tph**)] (**12**, solid line) compared to the corresponding methylated complex, *fac*-[Re(**bipy**)$(CO)_3$(**Tph**$CH_3$)]$^+$ (**32**, dashed line) in DCM.

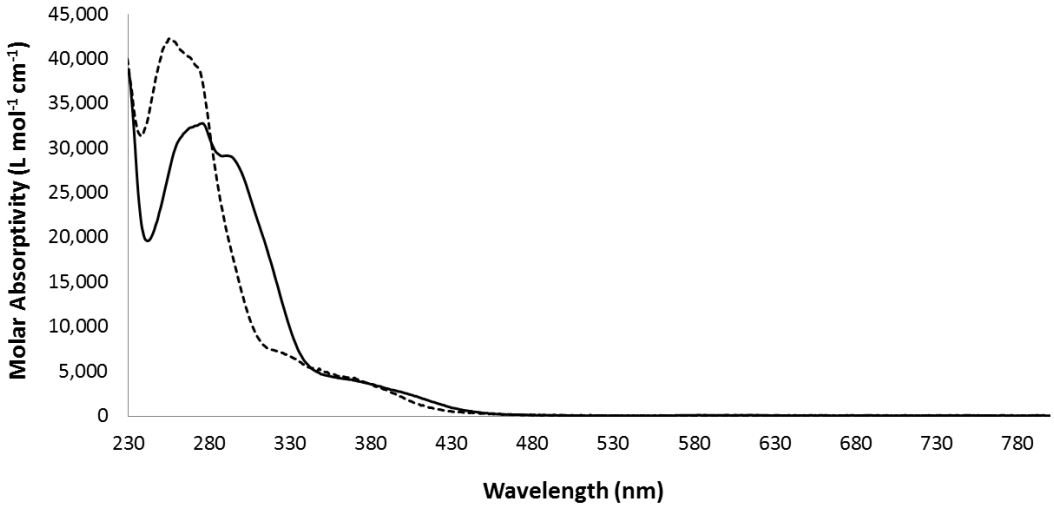


Figure 4.16: Absorption of the neutral rhenium complex, *fac*-[Re(**phen**)$(CO)_3$(**Tbz**)] (**13**, solid line) compared to the corresponding methylated complex, *fac*-[Re(**phen**)$(CO)_3$(**TbzCH**$_3$)]$^+$ (**33**, dashed line) in DCM.

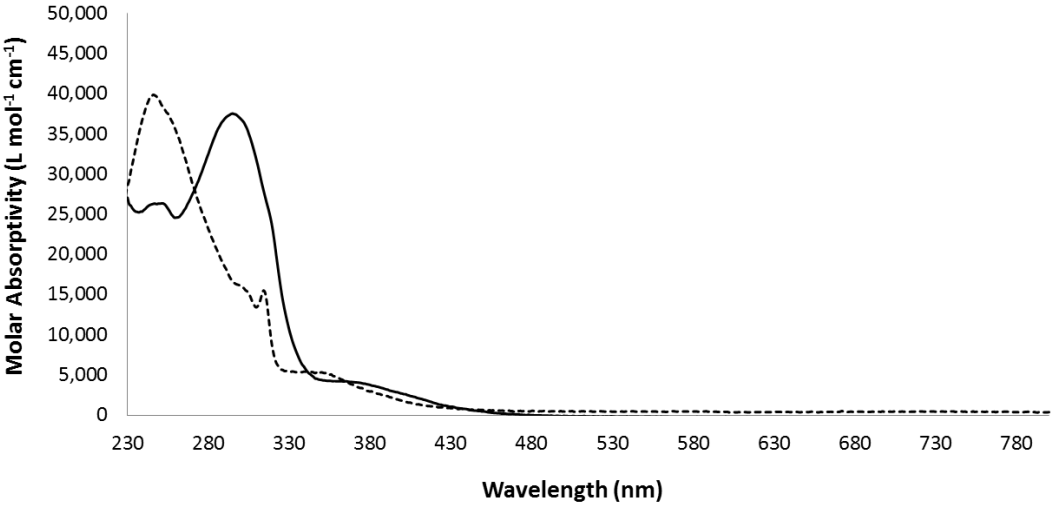


Figure 4.17: Absorption of the neutral rhenium complex, *fac*-[Re(**bipy**)$(CO)_3$(**Tbz**)] (**14**, solid line) compared to the corresponding methylated complex, *fac*-[Re(**bipy**)$(CO)_3$(**Tbz**$CH_3$)]$^+$ (**34**, dashed line) in DCM.

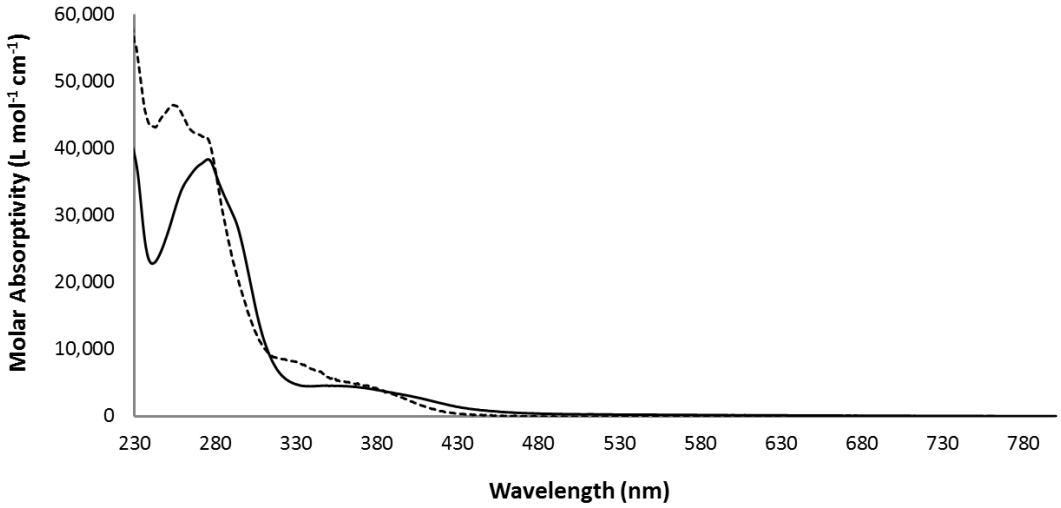


Figure 4.18: Absorption of the neutral rhenium complex, *fac*-[Re(**phen**)$(CO)_3$(**Tme**)] (**15**, solid line) compared to the corresponding methylated complex, *fac*-[Re(**phen**)$(CO)_3$(**Tme**$CH_3$)]$^+$ (**35**, dashed line) in DCM.

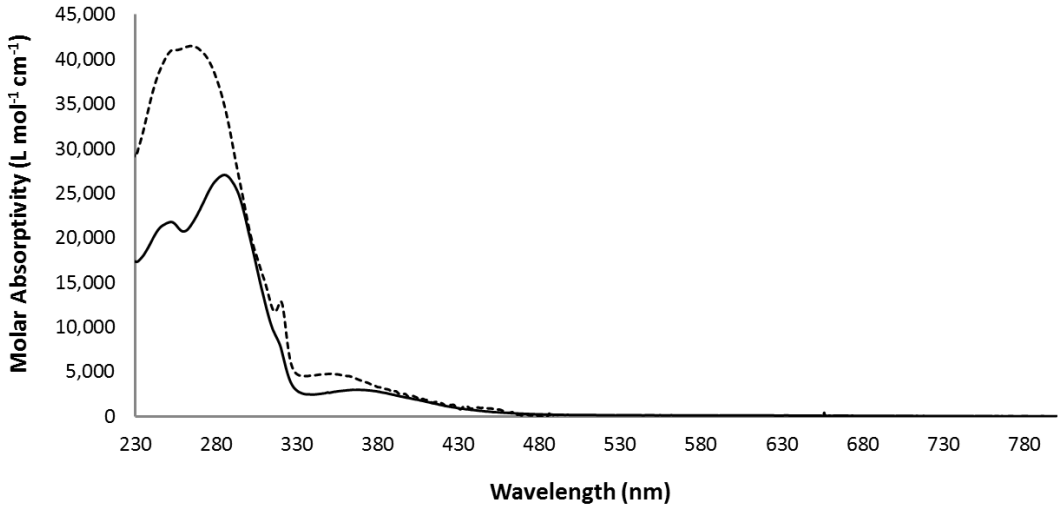


Figure 4.19: Absorption of the neutral rhenium complex, *fac*-[Re(**bipy**)$(CO)_3$(**Tme**)] (**16**, solid line) compared to the corresponding methylated complex, *fac*-[Re(**bipy**)$(CO)_3$(**Tme**$CH_3$)]$^+$ (**36**, dashed line) in DCM.

The emission profiles of the methylated rhenium complexes at room temperature in dilute DCM solutions are broad and structureless. All of the complexes within the same diimine group have the same emission maxima, see Table 4.3.5, Figure 4.20 and Figure 4.21. The methylated **phen** complexes have a maximum emission wavelength at 536-538 nm and the **bipy** complexes at 546 nm. The emission profiles measured are wavelength independent suggestive of emission from a single excited state, as predicted by Kasha's law. Again, as was observed for the absorption spectra, the emission maxima of the **phen** complexes are blue shifted with respect to the **bipy** analogues.

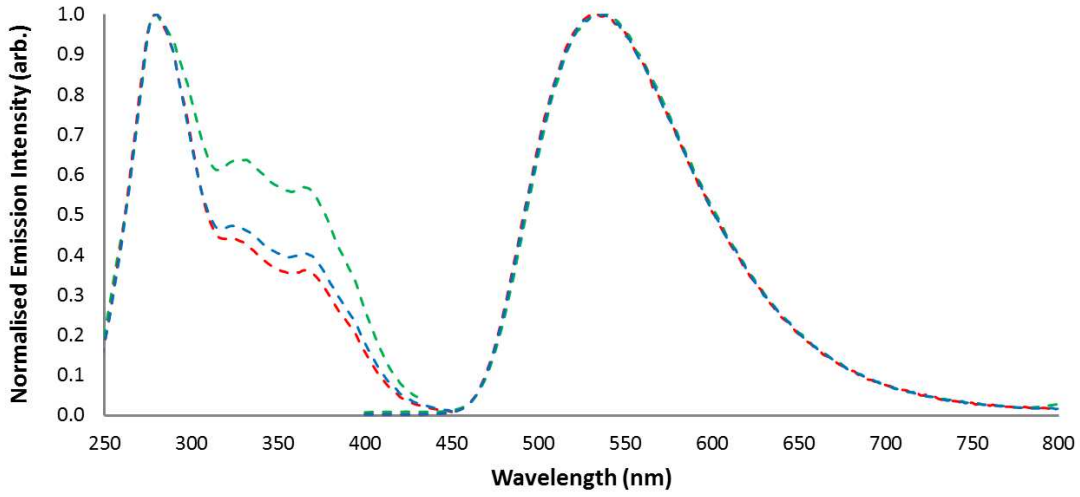


Figure 4.20: Excitation and emission of *fac*-[Re(**phen**)$(CO)_3$(**Tph**$CH_3$)]$^+$ (**31**, green), *fac*-[Re(**phen**)$(CO)_3$(**Tbz**$CH_3$)]$^+$ (**33**, red), and *fac*-[Re(**phen**)$(CO)_3$(**Tme**$CH_3$)]$^+$ (**35**, blue) in DCM.

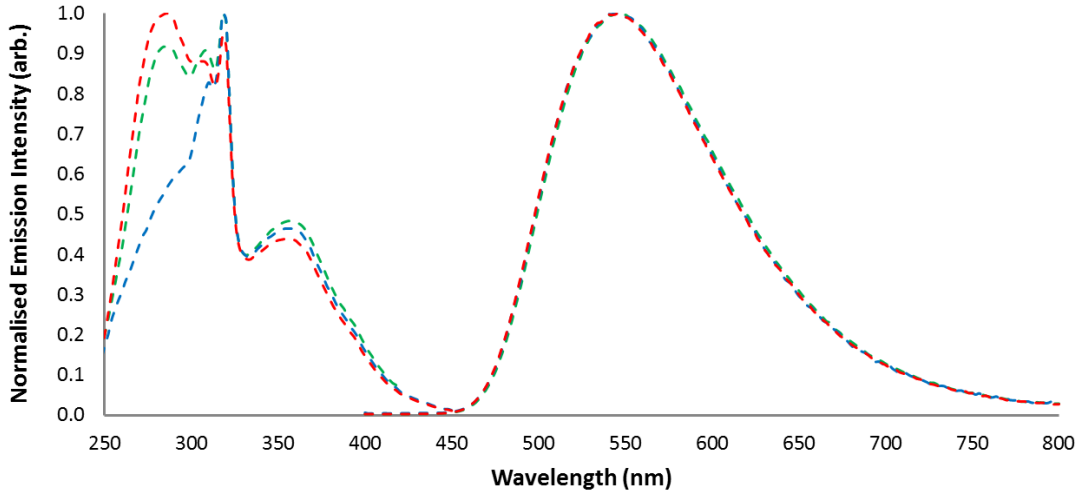


Figure 4.21: Excitation and emission of *fac*-[Re(**bipy**)$(CO)_3$(**Tph**$CH_3$)]$^+$ (**32**, green), *fac*-[Re(**bipy**)$(CO)_3$(**Tbz**$CH_3$)]$^+$ (**34**, red), and *fac*-[Re(**bipy**)$(CO)_3$(**Tme**$CH_3$)]$^+$(**36**, blue) in DCM.

The luminescent properties of the methylated complexes compared to the corresponding neutral precursors shows similar trends to those observed for the protonated species discussed in Chapter Three. The emission of the methylated complexes have been significantly blue shifted, between 48 and 60 nm. Figure 4.22 shows an example of the blue shifted emission observed for the methylated complexes, with respect to their neutral analogues. The quantum yields of the methylated complexes have improved

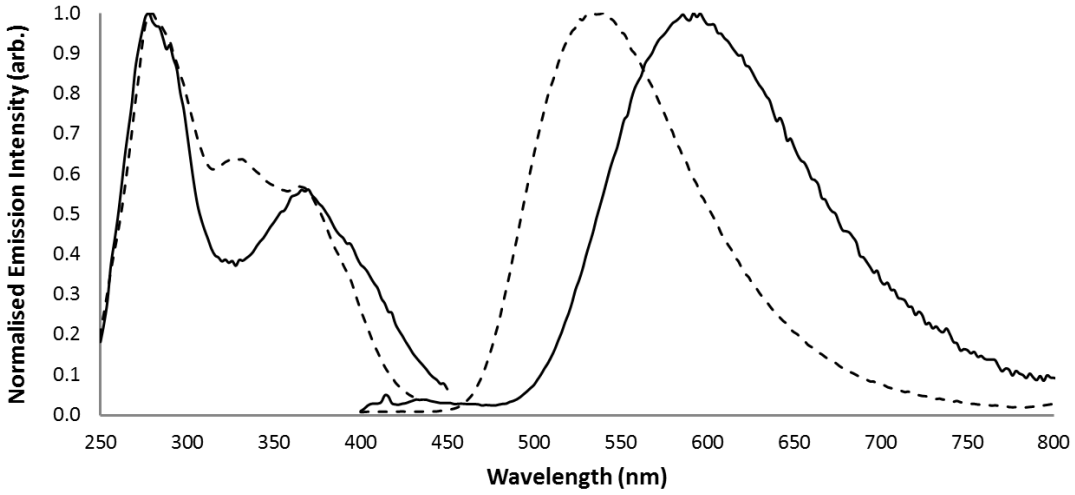


Figure 4.22: Excitation and emission of *fac*-[Re(**phen**)$(CO)_3$(**Tph**$CH_3$)]$^+$ (**31**, dashed line) comapred to the neutral *fac*-[Re(**phen**)$(CO)_3$(**Tph**)] (**11**, solid line).

23 fold and the lifetime has been elongated 4-10 times, with respect to the neutral analogues. In line with these observations are the values calculated for $k_r$ and $k_{nr}$, Table 4.3.7. There has been a significant reduction, up to 15 times, in the non radiative decay constant upon methylation of the rhenium complexes compared to the neutral analogues, see Table 2.3.8 on page 59, Chapter Two.

#### 4.3.5.1 Methylation using Methyl-$d_3$ Trifluoromethanesulfonate

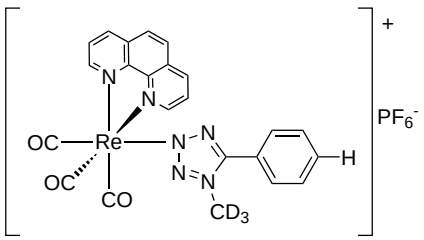


**37**

C-H vibrations and rotation around the C-N bond, are potential sources of quenching in luminescent molecules. To understand if the introduction of the methyl group

Table 4.3.8: Photophysical data of *fac*-[Re(**phen**)$(CO)_3$(**Tph**$CH_3$)]$^+$ (**31**) compared to *fac*-[Re(**phen**)$(CO)_3$(**Tph**$CD_3$)]$^+$(**37**).

| Rhenium Complex[a] | Emission 298 K | | | | | Decay Constants ($10^6$ $s^{-1}$) | |
|---|---|---|---|---|---|---|---|
| | $\lambda_{max}$(nm) | $\tau$ ($\mu$s)[b] | $\tau$ ($\mu$s)[c] | $\phi$[b] | $\phi$[c] | $k_r$ | $k_{nr}$ |
| $CH_3$ (**31**) | 536 | 1.18 | 1.83 | 0.14 | 0.26 | 0.142 | 0.404 |
| $CD_3$ (**37**) | 536 | 1.26 | 1.86 | 0.11 | 0.23 | 0.124 | 0.414 |

[a]; All data for complexes in $10^{-5}$ M DCM solutions and all quantum yields measured against quinine sulfate, [b]; air-equilibrated samples, [c]; degassed ($O_2$ free) samples.

has caused any significant vibrational quenching, *fac*-[Re(**phen**)$(CO)_3$(**Tph**)](**11**) was methylated using methyl-$d_3$ trifluoromethane sulfonate. The photophysical properties of complex *fac*-[Re(**phen**)$(CO)_3$(**Tph**$CD_3$)]$^+$ (**37**) were compared to the non-deuterated analogue (**31**) and are presented in Table 4.3.8. The emission maximum has not changed upon substituting the $CH_3$ group for a $CD_3$. Similarly, the $\tau$ and $\phi$ observed for the two complexes are not significantly different. This is also reflected in the $k_{nr}$ values which are similar for both complexes.

### 4.3.6 Computational Calculations

To further support the interpretation of the photophysical results, the energetics and absorption spectra of the complexes were simulated with time-dependent density functional theory using GAUSSIAN09.[181] It is generally known that the high energy transitions observed in the UV-Vis spectra are from IL $\pi - \pi^*$ transitions.[174] The DFT was used to further classify the lower energy transitions.

As discussed in Chapter Two, the lowest energy excited state for the neutral rhenium complexes was assigned to a $^3$MLLCT, with the HOMO localised over both the Re 5d metal orbitals and the $\pi$ orbitals on the tetrazole ligand. In the case of the methylated complexes, the lowest energy excited state appears to originate predominantly from HOMO-*n*→LUMO+*m* transitions, where *n* = 0-2 and *m* = 0-2. Figure 4.23 and Figure 4.24 show the localisation of the HOMO and LUMO for the methylated Re(I) complexes. Only the HOMO and LUMO are only shown here for clarity however Figure A3.1 and Figure A3.2 show the extended orbital localisation for the HOMO-*n*

and LUMO+*m* orbitals. The calculated low energy transitions are tabulated and can be found in Appendix A3.3.

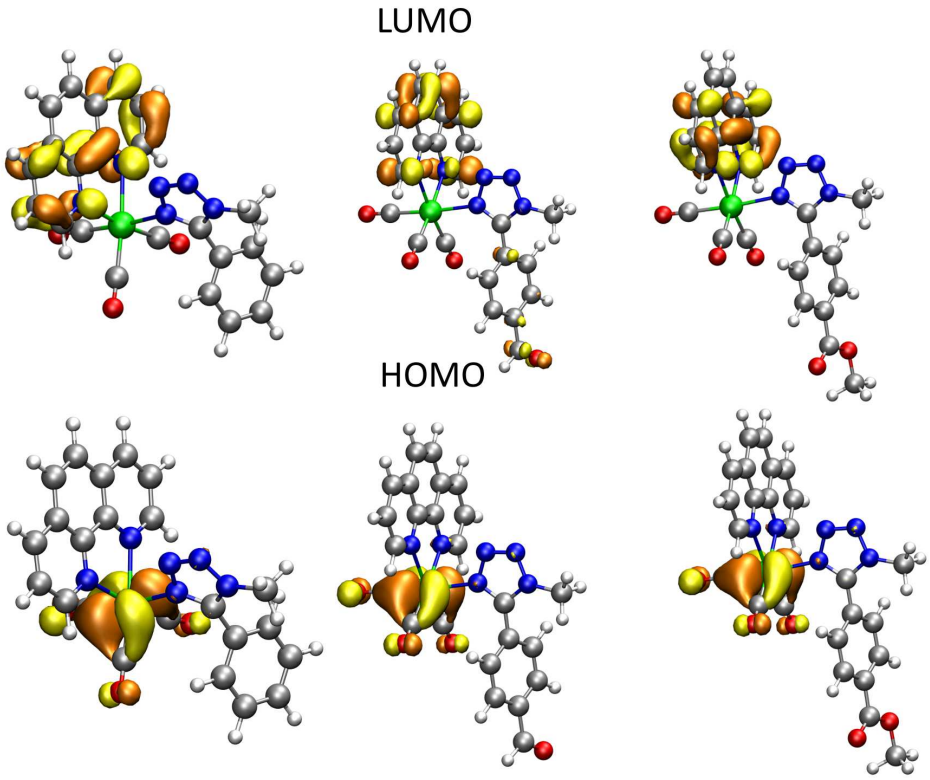


Figure 4.23: Localisation of the HOMO and LUMO for the methylated **phen** complexes (left to right); *fac*-[Re(**phen**)$(CO)_3$(**Tph**$CH_3$)]$^+$ (**31**), *fac*-[Re(**phen**)$(CO)_3$(**Tbz**$CH_3$)]$^+$ (**33**) and *fac*-[Re(**phen**)$(CO)_3$(**Tme**$CH_3$)]$^+$ (**35**).

Based on the localisation of these orbitals (Figure 4.23 and Figure 4.24) it appears that the lowest energy transition is an MLCT (Re→diimine) with a small contribution of LLCT (CO→diimine). The extended HOMO and LUMO images (Figure A3.1 and Figure A3.2 ) illustrate that there is negligible contribution of the tetrazolato ligand to the HOMO based orbitals.

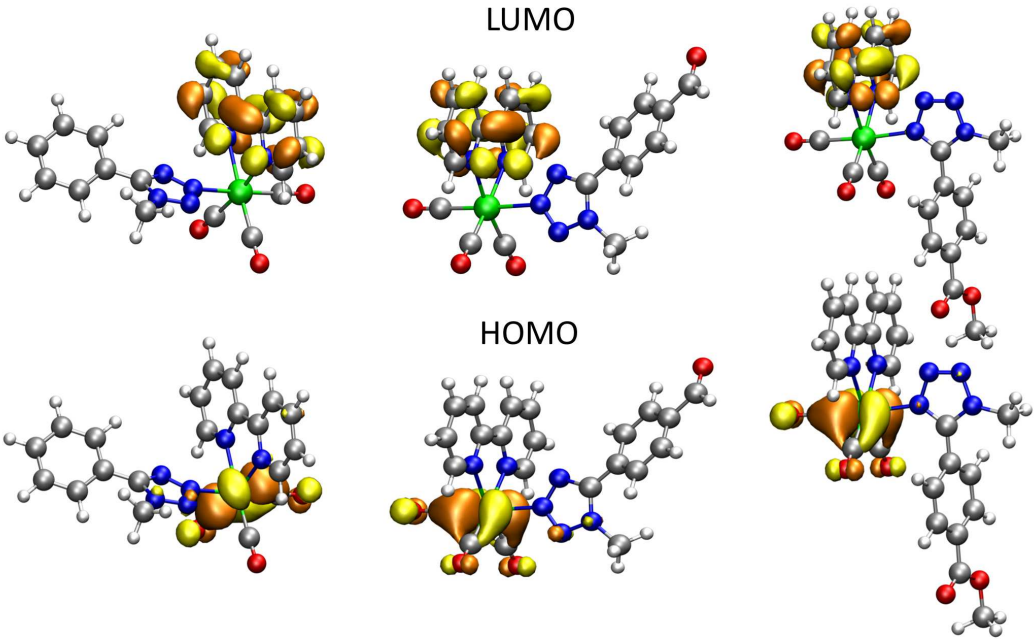


Figure 4.24: Localisation of the HOMO and LUMO for the methylated **bipy** complexes (left to right); *fac*-[Re(**bipy**)$(CO)_3$(**Tph**$CH_3$)]$^+$ **32**, *fac*-[Re(**bipy**)$(CO)_3$(**Tbz**$CH_3$)]$^+$(**34**) and *fac*-[Re(**bipy**)$(CO)_3$(**Tme**$CH_3$)]$^+$(**36**).

## 4.4 Discussion

### 4.4.1 Synthesis and Purification

The methylation reactions proceeded to give moderate to good yields of the final complexes (51-80 %). Solid state IR spectroscopy was used to probe the outcome of the methylation reactions. Spectra suggested the obtainment of one cationic rhenium complex in a *facial* configuration, with a $PF_6^-$ counter anion. The CO bands in the methylated rhenium complexes are the main feature used to observe the formation of a cationic complex. The CO stretching frequencies are effected by the electron density on the rhenium metal centre. The A´(1) CO band in the methylated complexes shifts to significantly higher wavenumbers (Table 4.3.1) compared to their neutral analogues, which is consistent with the formation of a positively charged species.[108] Increased CO stretching frequencies is consistent with a reduction in electron density on the rhenium centre, which therefore reduces the amount of backbonding onto the CO ligands.

The crude NMR indicated the presence of two main products but in some instances, there was a third set of minor peaks present in the baseline. Firstly, column chromatography was used to understand if the two main products observed in the crude NMR were separable. *fac*-[Re(**phen**)$(CO)_3$(**Tme**$CH_3$)]$^+$(**35**) was passed through an acidic alumina column and three separate fractions were isolated. The first fraction showed the presence of a phenanthroline system in the $^1$H NMR, however there was no sign of the tetrazolato ligand attached. The specific identity of this first fraction was not determined as the mass collected was negligible. The $^1$H NMR of the second fraction looked very similar to that of the crude product, with two rhenium systems present in a 1:0.88 ratio. This fraction was recovered with a yield of approximately 60% but there were still minor impurities present in the baseline of the NMR. The recovery of fraction two also reveals the inseparable nature of the two original species observed in the crude NMR. The final fraction appeared to contain three distinct rhenium complexes as there was an extra set of **phen** signals compared to the crude product. The new signal observed was in a comparable proportion to the other two systems. This final fraction was passed through another column (neutral alumina) to try and identify the new system present. Two fractions were recovered from this second column. The first fraction eluted with ethyl acetate (100 %) and the second fraction with DCM/methanol (9:1).

NMR revealed that the second fraction was again a mixture of three systems. The $^{1}$H NMR of fraction one did not contain any **phen** signals and appeared to be mostly free, methylated ester tetrazole (ie: benzoic acid-4-(1-methyl-1*H*-tetrazole-5-yl)-methyl ester). Crystallisation using liquid liquid diffusion of petroleum spirits into a chloroform solution of fraction one, isolated benzoic acid-4-(1-methyl-1*H*-tetrazole-5-yl)-methyl ester, as shown in Figure 4.25.

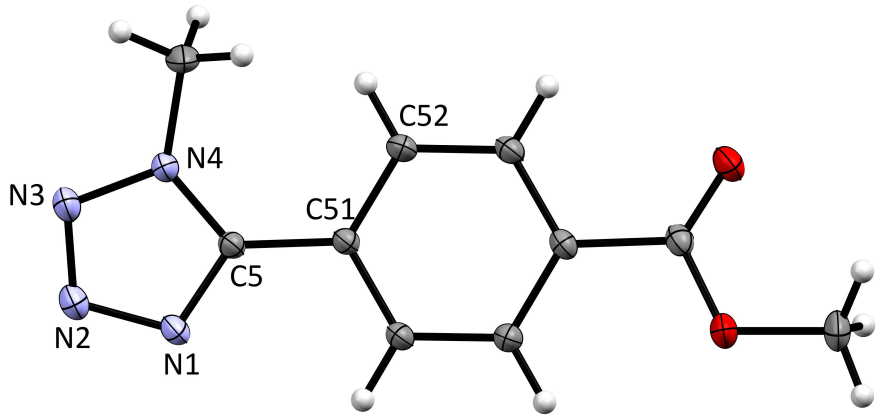


Figure 4.25: X-ray crystal structure of benzoic acid-4-(1-methyl-1*H*-tetrazole-5-yl)-methyl ester, where thermal ellipsoids have been drawn at 50% probability.

Alumina-filled column chromatography was an unsuitable method for purification, as a third *new* system was formed, as observed in the $^{1}$H NMR. This third system could be the result of ligand exchange or loss, as suggested by the recovery of a free methylated tetrazole ligand. The alumina could be promoting ligand dissociation. Purification was eventually achieved through reprecipitation of the crude product from DCM and diethyl ether. Purification was unable to separate the two species observed in the NMR but the minor baseline peaks were successfully removed.

### 4.4.2 Spectroscopic Characterisation

As mentioned above, upon analysis of the solid state IR spectroscopy (Table 4.3.1) it seemed plausible to assume the obtainment of one single methylation product for each reaction. However, in the NMR spectra two inseparable products were observed.

Based on the chemical shifts and integration ratios, both systems appeared to be methylated rhenium complexes, not simply a mixture of neutral starting material and methylated product. Figure 4.2 to Figure 4.7 highlight the changes to the NMR spectra that occur upon methylation. Firstly, the appearance of two new singlets between 3.5 and 4.5 ppm with integration ratios of 3H, suggests that methylation has occurred but also supports the idea that there are two *methylated* rhenium systems present.[228] 2D NMR experiments including COSY, HMBC and HSQC were used to classify the signals into two separate systems, a and b; where a was assigned to the set of resonances with the relatively higher integration ratio. This also confirmed that the two systems present were both singly methylated rather than one of the systems undergoing alkylation at two sites on the tetrazole.

To identify the nature of the two species observed in the $^{1}$H NMR, single crystals were grown of the final methylated products. Figure 4.12 and Figure 4.13 show the crystal structures isolated for each of the methylated **phen** and **bipy** complexes respectively. Coordination of the tetrazole ligand to the rhenium centre was observed through both the N2 and N1 atoms of the tetrazole ring. N1 coordination has not been observed for

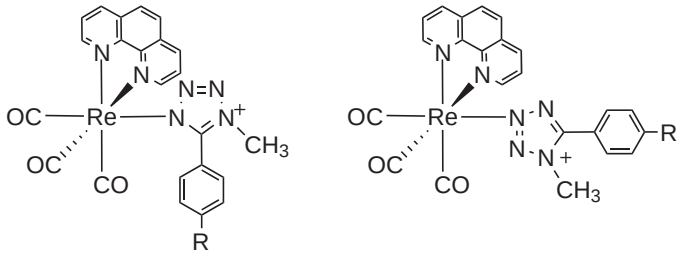


N1 linkage isomer N2 linkage isomer

Scheme 4.3: N1 and N2 linkage isomers of the methylated tetraozlto complexes.

any of the previously synthesised neutral or protonated rhenium complexes. Based on the isolated crystals, it was hypothesised that the two sets of signals observed in the NMR could belong to the N1 and N2 linkage isomers, as shown in Scheme 4.3. It was not possible to identify which system in the NMR belonged to the N1 or N2 linkage isomer.

Interestingly, upon methylation of iron and ruthenium tetrazolato complexes, only one linkage isomer (N2) has ever been observed.[111,229] Reports on cobalt(III) tetrazolato complexes observe both N1 and N2 linkage isomers, however no methylation reaction was carried out.[230] The two linkage isomers in the study by Hall *et al.* are not in

equilibrium with each other[230] but this can not be ruled out for the methylated Re(I) complexes reported herein.

#### 4.4.2.1 Investigation into the Two Re(I) Systems

**$^1$H NMR of Single Crystals**

$^1$H NMR analysis was carried out on isolated crystals grown from some methylated complexes. In each case, where the crystal structures indicated the presence of one system in the solid state, the NMR showed the presence of the two sets of resonances. This suggests that in solution, the Re-N1 and Re-N2 complexes both exist. This could mean that the two isomers are in equilibrium. Their formation could also be due to the lability of the tetrazole ligand. A possible dissociative-associative type mechanism could be occurring where the ligand can reattach in the N2 or N1 form. It can not be ruled out that both the N1 and N2 linkage isomers crystallise out of solution, however even upon analysis of multiple crystals from each batch, only one linkage isomer was ever observed in the solid state.

A study of dinuclear Re(I) systems with a tetrazolate bridging ligand has in fact observed a similar situation in the NMR. In particular, Wright *et al*. isolated a dinuclear species of the type [Re-L-Re]$^+$ in which both Re(I) fragments coordinated to the tetrazolate ring.[174] In this case, the crystals isolated showed the Re(I) metal centre binding to the N1 and N4 atoms of the tetrazole ligand however, upon NMR analysis, both N1-N4 and N2-N4 linkage isomers were observed, as illustrated in Figure 4.26.[174] This was ascribed to an equilibrium situation, which may also be used to describe what is observed for the synthesised methylated Re(I) complexes.

**Temperature Dependent NMR**

Temperature dependent NMR studies were carried to understand if a change in the integration ratios of the two systems could be observed. Previous studies by Butler *et al*. on a series of 5-substituted aryl tetrazoles indicate that temperature can effect the equilibrium position between the N1 and N2 tautomers (ie: the proton on the N1 or N2 atom of the tetrazole ring).[167]

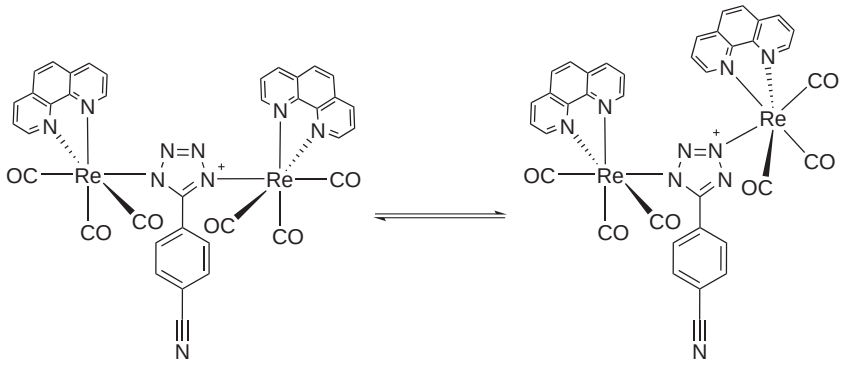


Figure 4.26: Equilibrium between linkage isomers of a dinuclear rhenium species.[174]

*fac*-[Re(**phen**)$(CO)_3$(**Tbz**$CH_3$)]$^+$ (**33**) was used in a series of temperature dependent experiments in both DMSO-$d_6$ and acetonitrile-$d_3$ (Figure 4.8 and Figure 4.9). Upon heating (in both solvents), the two original sets of *fac*-[Re(**phen**)$(CO)_3$(**Tbz**$CH_3$)]$^+$ resonances disappeared and a single new set of peaks were finally observed in the spectra. It was found that for the acetonitrile-$d_3$ experiments, the methylated tetrazole ligand had dissociated and acetonitrile coordinated in its place. Formation of the acetonitrile solvate was confirmed by synthesising this complex, *fac*-[Re(**phen**)$(CO)_3(CH_3CN)]^+$ and comparing NMR spectra . The phenanthroline signals of *fac*-[Re(**phen**)$(CO)_3$(**Tbz**$CH_3$)]$^+$ (**33**) after being heated for five hours at 70 ˚C appear to match with those of the acetonitrile solvate, Figure 4.27. It is likely that a solvate is also forming upon heating **33** in DMSO-$d_6$. The methylated tetrazolato ligand is displaced by the coordinating solvent upon heating and becomes free in the solution. It appears that the Re-N backbonding (already fairly weak in the neutral complexes) is further reduced upon methylation, therefore weakening the bond. The position of the tetrazole peaks also appear to shift downfield, consistent with the free neutral ligand.[170] Ligand dissociation is also supported by the fact that upon column chromatography, the free methylated ester tetrazole ligand (benzoic acid-4-(1-methyl-1*H*-tetrazole-5-yl)-methyl ester) was isolated from a column of *fac*-[Re(**phen**)$(CO)_3$(**Tme**$CH_3$)]$^+$, as discussed earlier.

**Solvent Effects**

The studies of Butler *et al*. also looked at the effect of solvents on the tautomeric equilibrium in a series of substituted aryl tetrazoles.[167] They note that for these compounds, the difference in ring conformations and therefore interannular conjugation should

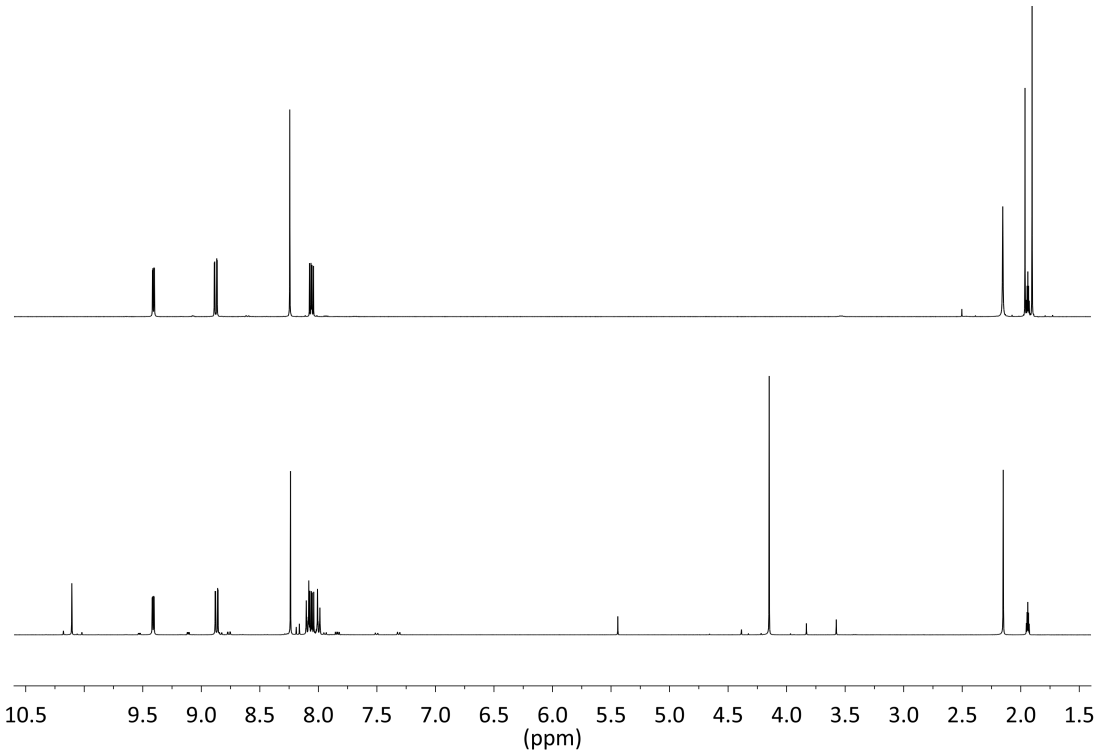


Figure 4.27: $^{1}$H NMR spectrum of *fac*-[Re(**phen**)(CO)$_3$(**Tbz**CH$_3$)]$^+$ (**33**) after being heated at 70 ˚C for 300 minutes (bottom) compared to the synthesised *fac*-[Re(**phen**)(CO)$_3$(**CH$_3$CN**)]$^+$(top) in acetonitrile-d$_3$.

cause differences in energies and solvation effects between the N1 and N2 tautomeric forms.[167] Their observations show that the more polar, N1 form, is more prominent in the polar solvent DMSO whereas the relative abundance of the N1 tautomer reduces in the less polar solvent, dioxane.[167] If the synthesised methylated Re(I) complexes are in fact in a state of dynamic equilibrium (in solution) between the N1 and N2 isomers, then solvent changes could affect their relative abundance. The NMR of *fac*-[Re(**phen**)(CO)$_3$(**Tph**CH$_3$)]$^+$ (**31**) was measured in acetonitrile-d$_3$ (giving an integration ratio of 1:0.72, ie: 58% system a and 41% system b) and acetone-d$_6$ (integration of 1:0.52, ie: 65% system a and 34% system b). There was also a change observed for *fac*-[Re(**phen**)(CO)$_3$(**Tbz**CH$_3$)]$^+$(**33**) with an integration ratio of 1:0.68 (60% to 40%) in acetonitrile-d$_3$ and 1:0.86 (54% to 46%) in acetone-d$_6$. Although the difference in percentage abundance of the two systems does not greatly change with the change in solvent, the differences are within the range that Butler observed for 2-methyl-5-phenyltetrazole upon changing from DMSO to dioxane. The abundance of the N1 tautomer was 86% in DMSO and 73% in dioxane.[167] Acetonitrile is more polar than acetone, therefore it is likely that the less abundant signals (based on integration) can

be assigned to the less polar linkage isomer. Based on Butler's studies this may be ascribed to the Re-N2 complex[167] however is it still not certain as to which signals correspond to which isomer. By observing a change in the integration ratios of the two rhenium systems upon changing solvents, the idea of having the N1 and N2 linkage isomers in dynamic equilibrium is supported.

#### 4.4.2.2 $^{13}$C NMR

Analysis of the $^{13}$C NMR spectra also showed two distinct sets of signals. The values of the tetraozolic carbon ($C_t$) in each case are in the range of 158.5-156.8 ppm (Table 4.4.1).

The studies conducted by Butler *et al*. on 5-substituted aryl tetrazoles indicate that a tetrazolic carbon value of 152-156 ppm is indicative of the N1 tautomer and values in the range of 162-165 ppm indicate the N2 tautomer. Although it is hypothesised that both N1 and N2 linkage isomers of the methylated Re(I) complexes are present in solution, the fact that the methyl group is also coordinated to the tetrazole ring must be taken into consideration. The tetrazole ring has sites occupied at two of the four N atoms. The values of the $C_t$ for all of the methylated species are generally the same and in fact lie closer to those values which represent the N1 linkage isomer. This could suggest that the methylation occurring at the N4 position is actually more responsible for the $C_t$ values, than whether the Re is coordinated via the N1 or N2 atom.[166,167]

Table 4.4.1: Linkage isomer observed in the crystal strucure and the $C_t$ signals for the methylated complexes in $d_6$-acetone.

| Complex | Re coordination observed in the Crystal Structure | $C_t$ signal observed in the NMR (ppm). |
|---|---|---|
| *fac*-[Re(**phen**)$(CO)_3$(**TphCH$_3$**)]$^+$ (**31**) | N1 | 158.2, 157.4 |
| *fac*-[Re(**bipy**)$(CO)_3$(**TphCH$_3$**)]$^+$(**32**) | N2 | 158.5, 157.6 |
| *fac*-[Re(**phen**)$(CO)_3$(**TbzCH$_3$**)]$^+$(**33**) | N1 | 157.6, 156.8 |
| *fac*-[Re(**bipy**)$(CO)_3$(**TbzCH$_3$**)]$^+$(**34**) | N2 | 157.7, 157.0 |
| *fac*-[Re(**phen**)$(CO)_3$(**TmeCH$_3$**)]$^+$(**35**) | N1 | 157.7, 156.8 |
| *fac*-[Re(**bipy**)$(CO)_3$(**TmeCH$_3$**)]$^+$(**36**) | N1 | 157.8, 157.0 |

It is also possible that the $C_t$ value is not useful in determining tetrazole coordination to the rhenium (ie, through N1 or N2). In fact, the $C_t$ value may provide more insight into the sight of alkylation. Reports by Stagni *et al.*[114] on ruthenium complexes bearing a mono coordinated 5-substituted aryl tetrazole observed similar NMR trends upon methylation. Even though the ruthenium is coordinated via the N2 atom on the tetrazole, methylation causes a significant upfield shift of the $C_t$ which they have ascribed to the methyl substituent being regioselective for the nitrogen atom adjacent to the $C_t$ .[114] Their claims are supported in the solid state with the deviation from coplanarity between the aryl and tetrazole rings being 61.4 º. Based on the study of Stagni *et al.*[114], the $C_t$ resonances for our methylated Re(I) complexes, suggest the methyl is on the N atom adjacent to the tetrazole ring, even if the rhenium is coordinated via the N2 atom.

The deviation from colplanarity between the aryl and tetrazole rings in the methylated complexes are discussed in section 4.4.3 and there is a significant increase in the degree of twisting between the rings, compared to the neutral analogues. The N1 linkage isomer or "tautomer" in the studies of Butler, usually gives rise to the aryl and tetrazole rings taking on a twisted conformation (Scheme 2.5).[165–167] The shielded nature of the $C_t$ in the methylated complexes compared to their neutral analogues is suggestive of this twisted conformation as there is a reduction in the +M from the tetrazole ring, explained by poor overlap of the p orbitals on the two rings (Scheme 2.4).

### 4.4.3 X-ray Crystallography

The solid state studies of the Re(I) methylated complexes show that the methyl resides on the N4 in the solid state. This supports the observed $C_t$ values discussed above.

The torsion angle between the aryl and tetrazole rings was calculated to assess their degree of coplanarity. A large deviation from coplanarity correlates to an increased twisting of the aryl and tetrazole rings. For all of the complexes that displayed the N1 linkage isomer in the solid state (**31**, **33**, **35** and **36**) a significant deviation from coplanarity was calculated (72-87 ˚). Interestingly, for all of the complexes that displayed the N2 linkage isomer in the solid state (**32** and **34**) the degree of twisting observed between the aryl and tetrazole rings is reduced (48.24-39.8 ˚, Table 4.3.3). This is not

unexpected as coordination of the Re to the tetrazole ligand through the N1 is sterically unfavourable therefore causing out of plane rotation of the phenyl and tetrazole rings. However, the degree of twisting observed in the solid state for either of the linkage isomers is still significantly larger than what has been calculated for the neutral analogues. Table 2.3.4 (Chapter Two) shows that the deviation from coplanarity for the neutral Re(I) complexes is between 2.03 and 26.47 º. The slight twisting was suggested to be predominantly due to a solid state effect and computational studies showed that in solution, this angle relaxed to values closer to zero.

Interestingly, although there is an obvious comparison that can be made for the torsion angles in the solid state between the Re-N1 and Re-N2, the NMR $C_t$ values are indiscernible. This might be rationalised by the rings becoming more relaxed in solution, irrespective of whether or not the Re is coordinated to the N1 or N2 atom of the tetrazole. Therefore the $C_t$ values (being closer to that indicative of N1) may be predominantly caused by the methyl group at N4. In the solid state the twisting of the aryl and tetrazole rings appears to be a combination of the both the tetrazole coordination to the Re (N1 or N2) and also the position of the methyl group on the tetrazole ring.

### 4.4.4 Photophysics

The observed blue shift in the absorption for the **phen** complexes compared to the **bipy** can be rationalised by the fact that the 1,10-phenanthroline ligand is not fully conjugated over the three rings (as was discussed in Chapter Two). A reduced HOMO-LUMO energy gap also explains the blue shifted emission of the **phen** complexes compared to the **bipy**.

When compared to the starting neutral complexes, the UV-Vis absorption spectra of the methylated species display an expected hypsochromic shift of the MLCT transition, which is accompanied by an analogous shift of the $\pi - \pi^*$ absorption bands (see Figure 4.14 to Figure 4.19). This observation can be rationalised by methylation reducing the electron density on the rhenium centre (confirmed by IR spectroscopy, see Table 4.3.1) due to a reduced $\sigma$ donation of the alkylated tetrazole ligand and/or an increased $\pi$ acceptance. This causes indirect stabilisation of the HOMO-*n* orbitals which increases the HOMO-LUMO energy gap and therefore a blue shift in the absorption

bands is expected. Figure 4.28 illustrates this concept and shows how the energy gap between the HOMO and LUMO increases upon methylation.

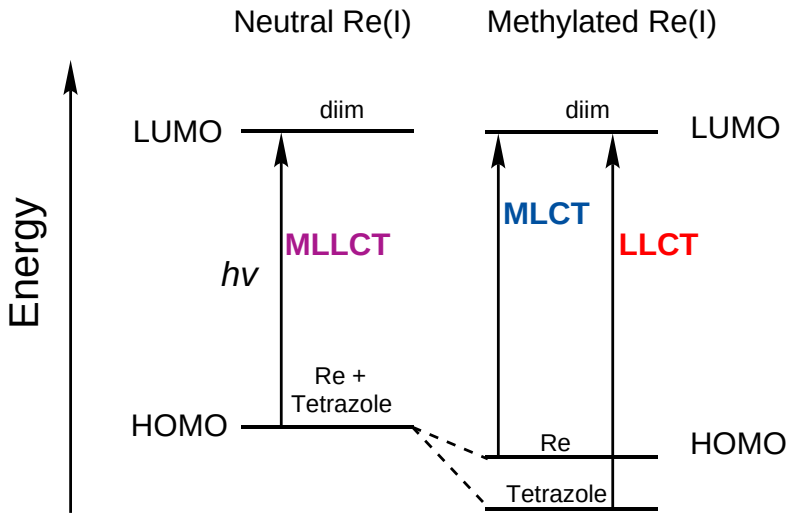


Figure 4.28: Energy level diagram illustrating the differences in the HOMO-LUMO gap for the neutral and cationic rhenium complexes.

The emission of the methylated rhenium complexes at room temperature, which have to be considered as a mixture of N1 and N2 coordination isomers, are brightly emissive. Upon excitation at the $^{1}$MLCT, each complex displays a broad and structureless band consistent with emission from a $^{3}$MLCT excited state. This also indicates that emission from the two isomers is indistinguishable. Support for emission from a triplet state can be found in Table 4.3.5 as the synthesised complexes exhibit sensitivity to molecular oxygen. There is an observed increase in $\tau$ and $\phi$ upon de-oxygenating the solutions before measurement. Also, there is a rigidochromic blue shift observed in the emission bands of the complexes upon passing from room temperature to 77 K, suggestive of emission from a charge transfer state.[127,192,193] The monoexponential nature of the lifetimes at room temperature is also suggestive that the photophysical properties of the N1 and N2 linkage isomers are indiscernible.

Computational calculations (TD-DFT and DFT) can offer rationalisation as to why all of the complexes within the same diimine group (**phen** or **bipy**) have the same emission maxima. Upon alkylation, the contribution of the tetrazole ligand to the HOMO type orbitals becomes negligible (see Figure A3.1 and Figure A3.2). The *para* substituent on the tetrazole ligand is the only differentiating factor between the complexes within the same diimine group. As the tetrazole is not involved in the HOMO-*n*→LUMO+*m*

transitions, emission of the complexes within their respective diimine classes is the same. This concept is also illustrated in Figure 4.28, using a simplified energy level diagram. There has been stabilisation of the tetrazole orbitals in the methylated complex and therefore contribution of the LLCT to the lowest excited state is lost.

The blue shifted emission observed for the methylated complexes, with respect to their neutral analogues can also be rationalised by stabilised HOMO type orbitals. The luminescence output of the methylated complexes (in terms of $\tau$ and $\phi$) is also greater which can again be linked with an increased HOMO-LUMO energy gap, compared to the neutral starting complexes. The energy gap law is one factor that can explain the observed improvement in luminescent output of the synthesised cationic complexes.[47,48,57] The increased HOMO-LUMO gap is also supported by a reduction in $k_{nr}$ upon methylation (Table 4.3.7). A similar trend was discussed for the protonated rhenium complexes in Chapter Three.

The improved luminescence of the methylated complexes is similar to the output observed for the protonated species in Chapter Three. In this case however the methylation reaction and therefore the increased luminescent output is irreversible.

#### 4.4.4.1 Methylation using Methyl-$d_3$ Trifluoromethanesulfonate

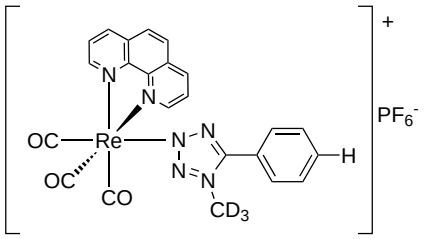


**37**

It is important to consider that the addition of the methyl groups could be a potential source of C-H vibrational quenching that was not present in the neutral analogues. The stretching frequencies of C-D occur at lower wavenumbers than C-H, as the deuterium is heavier than the proton. This means that higher overtones are needed to be reached before quenching of rhenium emission can occur. The intensity of the C-D stretching frequency is reduced as higher overtones are reached, making quenching from $CD_3$ less likely than $CH_3$. The photophysical properties of **37** were compared with the $CH_3$ analogue, **31**. The photophysical properties of both complexes are in fact comparable,

indicating that the $CH_3$ is not involved in quenching of the $^3$MLCT exited state of the rhenium complexes. As mentioned above, the TD-DFT provides evidence that the tetrazolato ligand is not directly involved in the excited state of the complexes, reducing the likelihood of quenching from the methyl on the tetrazolato ligand.

## 4.5 Conclusion

Methylation of the neutral *fac*-[Re(**diim**)$(CO)_3$(**L**)] complexes has been carried out and the cationic $PF_6^-$ complexes isolated. The product of the reaction is an inseparable mixture of Re-N1 and Re-N2 coordinated complexes with methylation regioselective for the N4 atom on the tetrazole. This was confirmed in solution through NMR and in the solid state using X-ray diffraction. Methylation of the tetrazole ring is irreversible. Upon heating the complex in a coordinating solvent, the methylated tetrazolato ligand becomes labile and the solvent coordinates as the ancillary ligand. It is still unclear as to whether or not the Re-N1 and Re-N2 linkage isomers exist in equilibrium however some of the experimental data supports this conclusion.

Although two rhenium linkage isomers are observed in the NMR they do not appear to be distinguishable by their photophysical properties. The emission of the methylated complexes are blue shifted and the $\tau$ and $\phi$ values are increased compared to the neutral analogues. Methylation, which occurs on the tetrazolato ligand, indirectly creates a larger energy gap between the ground and excited states which has reduced the contribution from $k_{nr}$ of these complexes. Upon comparison of the $CH_3$ and $CD_3$ complexes, no significant change in the photophysical properties was observed. TD-DFT supports this observation as the contribution of the tetrazolato ligand to the HOMO type orbitals is negligible.

This study has explored the interesting Re-N1 and Re-N2 linkage isomers that form upon methylation of the neutral Re(I) complexes. This fundamental investigation shows the potential for these complexes to be explored as highly emissive optical imaging agents however, the increased lability of the methylated tetrazolato ligand must be taken into account for possible “reactivity” in biological environments.

## 4.6 Experimental

### 4.6.1 General procedures

General procedures are as outlined in Chapter Two, section 2.5.1 unless otherwise stated.

Solid state IR measurements were carried out using an attenuated total reflectance Perkin Elmer Spectrum 100 FT-IR with a diamond stage.

Elemental analyses were performed by Dr Thomas Rodemann at the Central Science Laboratory, University of Tasmania or by Robert Herman at the Department of Chemistry, Curtin University.

### Photophysics

Absorption spectra were recorded at room temperature using a Perkin-Elmer Lambda 35 UV/Vis spectrometer. Uncorrected steady-state emission and excitation spectra were recorded on an Edinburgh FLSP920 spectrometer equipped with a 450 W xenon arc lamp, double excitation and single emission monochromators and a Peltier-cooled Hamamatsu R928P photomultiplier tube (185-850 nm). Emission and excitation spectra were corrected for source intensity (lamp and grating) and emission spectral response (detector and grating) by a calibration curve supplied with the instrument. Emission lifetimes ($\tau$) were determined with the same Edinburgh FLSP920 spectrometer using pulsed picosecond LEDs ( EPLED 360, FHWM <800 ps) as the excitation source, with repetition rates between 1 kHz and 1 MHz, and the above mentioned R928P PMT as detector. Degassed solutions were prepared by gently bubbling argon gas into the prepared sample for 15 minutes before measurement.

#### 4.6.1.1 General methodology for the methylation of the neutral *fac*-[Re(diim)(CO)$_3$(L)] complexes

The preparation of the methylated *fac*-[Re(**diim**)(CO)$_3$(**L**)] complexes (**diim** = 1,10-phenanthroline or 2,2'-bipyridine) was carried out following procedures adapted from previously published work.[108,111–113,219,224,229]

Previously synthesised *fac*-[Re(**diim**)$(CO)_3$(**L**)] (1 eq) was added to DCM and the mixture was allowed to cool using an ethyl acetate/liquid nitrogen cool bath. Once the reaction vessel had cooled, methyl trifluoromethanesulfonate (1.2 eq) in DCM was added. The reaction was stirred under nitrogen for approximately 30 minutes in the cool bath and was then allowed to come to room temperature and stirred overnight. An excess of $NH_4PF_6$ in water was added to the reaction and stirred for 45 minutes. The reaction was then extracted using DCM (3 × 15 mL) and the organic components combined and dried over anhydrous $MgSO_4$. The solvent was removed *in vacuo* to yield a yellow glassy looking solid. Each of the complexes showed two distinct systems in the the NMR which have been assigned to system a or b; where system a has the higher integration ratio. Some of the signals were collapsed in the $^{13}C$ NMR spectra, ie: two signals appeared as one.

*fac*-[Re(**phen**)$(CO)_3$(**Tph**$CH_3$)]$^+$

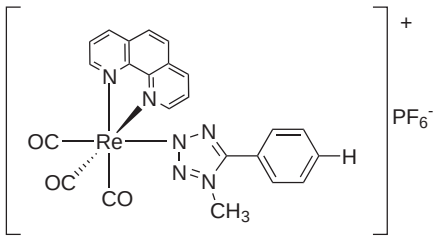


**31**

Compound **31** was purified by reprecipitation from DCM and diethyl ether. Yield 0.064 g (61%). M.p. 284 ºC (dec.). Elemental analysis for $C_{23}H_{16}F_6N_6O_3PRe{\cdot}0.5H_2O$: calculated: C 36.13, H 2.24, N 10.99; found: C 36.03 , H 1.86, N 10.85. $\nu_{max}$ (ATR)/$cm^{-1}$: 3095 w, 2032 s (CO, A′(1)), 1911 s (CO, A′(2)), 1897 s (CO, A″), 1699 w, 1524 w, 1463 w, 1431 w, 1207 w, 1152 w, 832 m, 777 w, 721 w. The ratio of system a:b is 1:0.65.$^1H$ NMR (δ, ppm, Acetone-$d_6$): 9.73 (2H, d, $J$ = 5.2 Hz, phen $H_{2,9}$)$^b$, 9.30 (2H, d, $J$ = 5.0 Hz, phen $H_{2,9}$)$^a$, 9.06 (2H, d, $J$ = 8.2 Hz, phen $H_{4,7}$)$^b$, 8.99 (2H, d, $J$ = 8.2 Hz, phen $H_{4,7}$)$^a$, 8.37 (2H, s, phen $H_{5,6}$)$^b$, 8.33 (2H, s, phen $H_{5,6}$)$^a$ , 8.28-8.24 (2H, m, phen $H_{3,8}$)$^b$, 8.09-8.06 (2H, m, phen $H_{3,8}$)$^a$ , 7.85-7.80 (2H, m, $CN_4$-$C_6H_5$), 7.68-7.64 (3H, m, $CN_4$-$C_6H_5$)$^b$, 7.61-7.57 (1H, m, $CN_4$-$C_6H_5$), 7.52-7.42 (4H, m, $CN_4$-$C_6H_5$), 4.08 (3H, s, $CH_3$)$^b$, 3.73 (3H, s, $CH_3$)$^a$. $^{13}C$ NMR (δ, ppm, Acetone-$d_6$): 196.3 (*C*O), 196.0 (*C*O), 158.2 (*C*$N_4$-$C_6H_5$), 157.4 (*C*$N_4$-$C_6H_5$), 155.7, 155.4, 148.1, 147.9, 141.2, 140.9, 133.5, 133.0, 132.0 (collapsed), 130.5 (collapsed), 130.1, 129.6,

128.9 (collapsed), 127.8, 127.6, 122.6, 122.1, 36.9 ($CH_3$), 35.6 ($CH_3$). Crystals suitable for X-ray analysis (identified as **31**, $C_{23}H_{16}F_6N_6O_3PRe$) were obtained by liquid liquid diffusion of diethyl ether into a DCM solution of the complex.

*fac*-[Re(**bipy**)$(CO)_3$(**Tph**$CH_3$)]$^+$

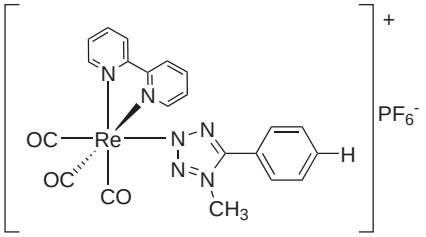


**32**

Compound **32** was purified by reprecipitation from DCM and diethyl ether. Yield 0.79 g (79%). M.p. 230 ºC. Elemental analysis for $C_{21}H_{16}F_6N_6O_3PRe{\cdot}0.5H_2O$: calculated: C 34.06, H 2.31, N 11.35; found: C 33.84, H 1.97, N 11.12 . $\nu_{max}$ (ATR)/$cm^{-1}$: 3127 w, 2031 s (CO, A′(1)), 1931 m (CO, A′(2)), 1898 s (CO, A″), 1606 w, 1550 w, 1474 w, 1447 w, 1318 w, 1247 w, 1163 w, 1111 w, 1074 w, 1027 w, 902 w, 834 s, 768 m, 732 w, 698 w. The ratio of system a:b is 1:0.79. $^1$H NMR (δ, ppm, Acetone-$d_6$): 9.32 (2H, d, *J* = 5.4 Hz, bipy $H_{6,6'}$ )$^b$ , 8.93 (2H, d, *J* = 5.2 Hz, bipy $H_{6,6'}$ )$^a$ , 8.78 (2H, d, *J* = 8.4 Hz, bipy $H_{3,3'}$ )$^b$ , 8.70 (2H, d, *J* = 8.4 Hz, bipy $H_{3,3'}$ )$^a$ , 8.46 (2H, t, *J* = 8.0 Hz, bipy $H_{4,4'}$ )$^b$, 8.39 (2H, t, *J* = 8.0 Hz, bipy $H_{4,4'}$ )$^a$, 7.93-7.90 (2H, m, bipy $H_{5,5'}$ )$^b$, 7.84-7.80 (1H, m, $CN_4$-$C_6H_5$), 7.75-7.71 (2H, m, bipy $H_{5,5'}$ )$^a$, 7.69-7.55 (9H, m, $CN_4$-$C_6H_5$), 4.22 (3H, s, -$CH_3$)$^b$ , 3.86 (3H, s, -$CH_3$)$^a$. $^{13}$C NMR (δ, ppm, Acetone-$d_6$): 158.5 ( $CN_4$-$C_6H_5$), 157.6 ($CN_4$-$C_6H_5$), 157.5, 157.3, 155.1, 154.8, 142.1, 141.8, 133.5, 133.1, 130.7, 130.6, 130.2, 129.8, 129.2, 129.0, 125.2, 125.1, 122.7, 122.2, 37.1 ($CH_3$), 35.8 ($CH_3$). Crystals suitable for X-ray analysis (identified as **32**, $C_{23}H_{18}C_{l2}F_3N_6O_6ReS$) were obtained by liquid liquid diffusion of diethyl ether into a DCM solution of the complex.

*fac*-[Re(**phen**)$(CO)_3$(**Tbz**$CH_3$)]$^+$

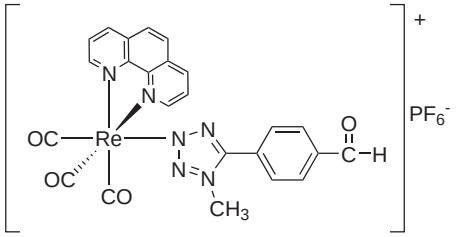

**33**

Compound **33** was purified by reprecipitation from DCM and diethyl ether. Yield 0.057 g (53%). M.p. 234 ºC (dec.). Elemental analysis for $C_{24}H_{16}F_6N_6O_4PRe{\cdot}0.5H_2O$: calculated: C 36.37, H 2.16, N 10.60; found: C 36.31, H 1.89, N 10.48. $\nu_{max}$ (ATR)/cm$^{-1}$: 3083 (w), 2032 s (CO, A′(1)), 1929 s (CO, A′(2)), 1922 s (CO, A″), 1699 m, 1548 w, 1520 w, 1430 m, 1310 w, 1206 w, 1179 w, 1146 w, 826 m, 722 w. The ratio of system a:b is 1:0.84.$^1$H NMR (δ, ppm, Acetone-$d_6$): 10.27 (1H, s, $CN_4$-$C_6H_4$-C*H*O)$^a$, 10.09 (1H, s, $CN_4$-$C_6H_4$-C*H*O)$^b$ , 9.74 (2H, d, *J* = 5.2 Hz, phen $H_{2,9}$)$^b$, 9.34 (2H, d, *J* = 6.3 Hz, phen $H_{2,9}$)$^a$, 9.07 (2H, d, *J* = 8.4 Hz, phen $H_{4,7}$)$^b$ , 9.01 (2H, d, *J* = 8.2 Hz, phen $H_{4,7}$)$^a$ , 8.38 (2H, s, phen $H_{5,6}$ )$^b$, 8.34 (2H, s, phen $H_{5,6}$ )$^a$, 8.28-8.25 (2H, m, phen $H_{3,8}$ )$^b$, 8.18 (2H, d, *J* = 8.8 Hz, $CN_4$-$C_6H_4$-CHO $H_{meta}$)$^a$, 8.19-8.08 (2H, m, phen $H_{3,8}$ )$^a$ , 8.02 (2H, d, *J* = 8.4 Hz, $CN_4$-$C_6H_4$-CHO $H_{meta}$)$^b$, 7.72-7.69 (4H, m, $CN_4$-$C_6H_4$-CHO $H_{ortho}$)$^{a,b}$, 4.13 (3H, s, -C$H_3$)$^b$, 3.77 (3H, s, -C$H_3$)$^a$ . $^{13}$C NMR (δ, ppm, Acetone-$d_6$): 196.2 (*C*O), 196.0 (*C*O), 192.6 (*C*HO), 192.4 (*C*HO), 157.6 (*C*$N_4$-$C_6H_4$-CHO), 156.8 (*C*$N_4$-$C_6H_4$-CHO), 155.8, 155.5, 148.1, 147.9, 141.2, 141.0, 140.1, 139.6, 132.0, 131.6, 131.0, 130.7, 130.5, 129.0 (collapsed), 127.8, 127.7, 127.6, 127.4, 37.1 (*C*$H_3$), 35.7 (*C*$H_3$). Crystals suitable for X-ray analysis (identified as **33**·$CDCl_3$, $C_{24}H_{16}F_6N_6O_4PRe{\cdot}CDCl_3$) were obtained by vapour diffusion of petroleum spirits (40-60 ºC) into a $CDCl_3$ solution of the complex.

*fac*-[Re(**bipy**)$(CO)_3$(**Tbz**$CH_3$)]$^+$

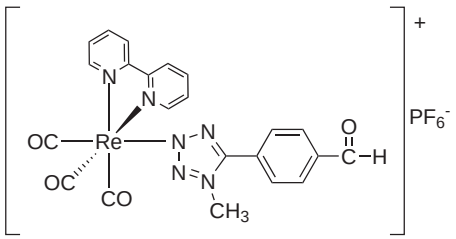

**34**

Compound **34** was purified by reprecipitation from chloroform and diethyl ether. Yield 0.066 g (61%). M.p. 225 ºC (dec.). Elemental analysis for $C_{22}H_{16}F_6N_6O_4PRe{\cdot}0.4CHCl_3$:

calculated: C 33.32, H 2.05, N 10.41; found: C 33.57, H 1.73, N 10.39 (a corresponding singlet for $CHCl_3$was observed in the NMR spectrum of **34**). $\nu_{max}$ (ATR)/$cm^{-1}$: 3087 w, 2841 w, 2028 s (CO, A′(1)), 1929 s (CO, A′(2)), 1901 s (CO, A″), 1706 m, 1606 w, 1554 w, 1473 w, 1447 w, 1314 w, 1202 w, 834 m, 769 m, 731 w. The ratio of system a:b is 1:0.97. $^1$H NMR (δ, ppm, Acetone-$d_6$): 10.26 (1H, s, $CN_4$-$C_6H_4$-C*H*O)$^b$, 10.13 (1H, s, $CN_4$-$C_6H_4$-C*H*O)$^a$, 9.32 (2H, d, *J* = 5.6 Hz, bipy $H_{6,6'}$ )$^a$, 8.96 (2H, d, *J* = 5.6 Hz, bipy $H_{6,6'}$)$^b$, 8.78 (2H, d, *J* = 7.6 Hz, bipy $H_{3,3'}$ )$^a$, 8.72 (2H, d, *J* = 8.4 Hz, bipy $H_{3,3'}$)$^b$, 8.46 (2H, t, *J* = 8 Hz, bipy $H_{4,4'}$)$^a$, 8.41 (2H, t, *J* = 8 Hz, bipy $H_{4,4'}$)$^b$, 8.21 (2H, d, *J* = 6.4 Hz, $CN_4$-$C_6H_4$-CHO $H_{meta}$)$^b$, 8.09 (2H, d, *J* = 6.4 Hz, $CN_4$-$C_6H_4$-CHO $H_{meta}$)$^a$, 7.94-7.90 (2H, m, bipy $H_{5,5'}$ )$^a$, 7.88 (4H, d, J = 6.8 Hz, $CN_4$-$C_6H_4$-CHO $H_{ortho}$)$^{a,b}$, 7.77-7.73 (2H, m, bipy $H_{5,5'}$)$^b$, 4.27 (3H, s, -C$H_3$)$^a$, 3.90 (3H, s, -C$H_3$)$^b$. $^{13}$C NMR (δ, ppm, Acetone-$d_6$): 196.3 (*C*O), 196.1 (*C*O), 192.6 (*C*HO), 192.4 (*C*HO), 157.7 (*C*$N_4$-$C_6H_4$-CHO), 157.5, 157.3, 157.0 (*C*$N_4$-$C_6H_4$-CHO), 155.1, 154.9, 142.2, 141.9, 140.2, 139.7, 131.8, 131.0, 130.7 (collapsed), 129.3, 129.1, 127.7, 127.5, 125.2 (collapsed), 37.3 (*C*$H_3$), 35.9 (*C*$H_3$). Crystals suitable for X-ray analysis (identified as **34**· $CHCl_3$, $C_{22}H_{16}F_6N_6O_4PRe{\cdot}CHCl_3$) were obtained by vapour diffusion of petroleum spirits (40-60 ºC) into a $CHCl_3$ solution of the complex.

*fac*-[Re(**phen**)$(CO)_3$(**Tme**$CH_3$)]$^+$

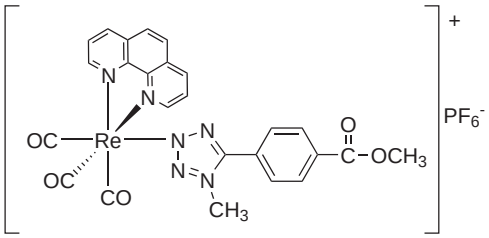


**35**

Compound **35** was purified by reprecipitation from DCM and diethyl ether. Yield 0.016 g (80%). M.p.195-197 ºC (dec.). Elemental analysis for $C_{25}H_{18}F_6N_6O_5PRe{\cdot}0.5H_2O$: calculated: C 36.50, H 2.33, N 10.22; found: C 36.66 , H 1.96 , N 10.10 . $\nu_{max}$ (ATR)/$cm^{-1}$: 3099 w, 2031 s (CO, A′(1)), 1931 s (CO, A′(2)), 1917 (1897 sh) s (CO, A″), 1713 w, 1637 w, 1604 w, 1524 w, 1465 w, 1433 m, 1286 w, 1207 w, 1150 w, 1120 w, 834 m, 721 w. The ratio of system a:b is 1:0.8. $^1$H NMR (δ, ppm, Acetone-$d_6$): 9.74 (2H, d, *J* = 5.0 Hz, phen $H_{2,9}$)$^b$ , 9.35 (2H, d, *J* = 5.0 Hz, phen $H_{2,9}$)$^a$ , 9.07 (2H, d, *J* = 8.2 Hz, phen $H_{4,7}$)$^b$ , 9.02 (2H, d, *J* = 8.2 Hz, phen $H_{4,7}$)$^a$ , 8.38 (2H,

s, phen $H_{5,6}$)[b], 8.35 (2H, s, phen $H_{5,6}$)[a], 8.28-8.25 (2H, m, phen $H_{3,8}$)[b], 8.52 (2H, d, $J$ = 8.8 Hz, $CN_4$-$C_6H_4$-$COOCH_3$ $H_{meta}$)[a], 8.19-8.06 (4H, m, phen $H_{3,8}$and $CN_4$-$C_6H_4$-$COOCH_3$ $H_{meta}$)[a,b], 7.62 (4H, d, $J$ = 8.6 Hz, $CN_4$-$C_6H_4$-$COOCH_3$ $H_{ortho}$)[a,b], 4.12 (3H, s, -C$H_3$)[b] , 4.03 (3H, s, -OC$H_3$)[a], 3.90 (3H, s, -OC$H_3$)[b], 3.77 (3H, s, -C$H_3$)[a]. $^{13}$C NMR (δ, ppm, Acetone-$d_6$): 166.3 (*C*$OCH_3$), 166.1 (*C*$OCH_3$), 157.7 (*C*$N_4$-$C_6H_4$-$COOCH_3$), 156.8 (*C*$N_4$-$C_6H_4$-$COOCH_3$), 155.8, 155.6, 148.1, 148.0, 141.2, 141.0, 134.8, 134.2, 132.01 (collapsed), 131.1 (collapsed), 130.8, 130.0, 129.0 (collapsed), 127.8, 127.7, 126.7, 126.4, 53.1 (-O*C*$H_3$), 52.9 (-O*C*$H_3$), 37.1 (*C*$H_3$), 35.7 (*C*$H_3$). Crystals suitable for X-ray analysis (identified as **35**, $C_{25}H_{18}F_6N_6O_5PRe$) were obtained by liquid liquid diffusion of petroleum spirits (60-80 ºC) into a DCM solution of the complex.

*fac*-[Re(**bipy**)$(CO)_3$(**Tme**$CH_3$)]$^+$

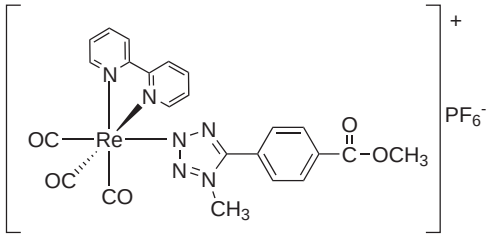


**36**

Compound **36** was purified by reprecipitation from DCM and diethyl ether. Yield 0.072 g (57%). M.p. 242-243 ºC. Elemental analysis for $C_{23}H_{18}F_6N_6O_5PRe$: calculated: C 34.99, H 2.30, N 10.64; found: C 35.11 , H 2.38, N 10.45. $\nu_{max}$ (ATR)/cm$^{-1}$: 3091 w, 2952 w, 2030 s (CO, A′(1)), 1908 (1925 sh) s (CO, A′(2)/A″), 1706 m, 1607 w, 1463 w, 1451 w, 1433 w, 1294 w, 1207 w, 1122 w, 834 m, 775 w, 732 w. The ratio of system a:b is 1:0.92. $^1$H NMR (δ, ppm, Acetone-$d_6$): 9.31 (2H, d, $J$ = 4.9 Hz, bipy $H_{6,6'}$)[b] , 8.96 (2H, d, $J$ = 5.6 Hz, bipy $H_{6,6'}$)[a] , 8.77 (2H, d, $J$ = 7.8 Hz, bipy $H_{3,3'}$)[b] , 8.71 (2H, d, $J$ = 8.0 Hz, bipy $H_{3,3'}$)[a] , 8.48-8.43 (2H, m, bipy $H_{4,4'}$)[b] , 8.43-8.38 (2H, bipy $H_{4,4'}$)[a] , 8.26 (2H, d, $J$ = 8.2 Hz, $CN_4$-$C_6H_4$ -$COOCH_3$ $H_{meta}$)[a] , 8.14 (2H, d, $J$ = 8.8 Hz, $CN_4$-$C_6H_4$-$COOCH_3$ $H_{meta}$)[b], 7.93-7.89 (2H, m, bipy $H_{5,5'}$)[b], 7.80-7.78 (4H, d, $J$ = 8.8 Hz, $CN_4$-$C_6H_4$-$COOCH_3$ $H_{ortho}$)[a,b], 7.77-7.73 (2H, m, bipy $H_{5,5'}$)[a], 4.25 (3H, s, -C$H_3$)[b], 4.01 (3H, s, -OC$H_3$)[a], 3.92 (3H, s, -OC$H_3$)[b], 3.89 (3H, s, -C$H_3$)[a]. $^{13}$C NMR (δ, ppm, Acetone-$d_6$): 196.3 (*C*O), 196.1 (*C*O), 166.3 (*C*$OCH_3$), 166.2 (*C*$OCH_3$), 157.8 (*C*$N_4$-$C_6H_4$-$COOCH_3$), 157.5, 157.3, 157.0 (*C*$N_4$-$C_6H_4$-$COOCH_3$),

155.1, 154.9, 142.1, 141.9, 134.8, 134.2, 131.3, 131.1, 130.8, 130.2, 129.2, 129.0, 126.8, 126.5, 125.2 (collapsed), 53.0 (-O*C*$H_3$), 52.9 (-O*C*$H_3$), 37.24 (*C*$H_3$), 35.91 (*C*$H_3$). Crystals suitable for X-ray analysis (identified as **36**, $C_{23}H_{18}F_6N_6O_5PRe$) were obtained by liquid liquid diffusion of petroleum spirits (60-80 ºC) into a DCM solution of the complex.

*fac*-[Re(**phen**)$(CO)_3$(**Tph**$CD_3$)]$^+$

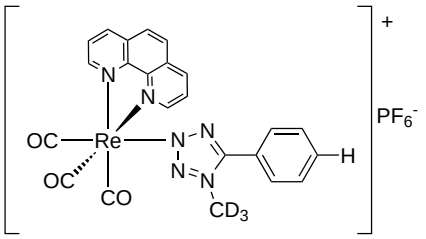


**37**

Compound **37** was synthesised according to the general procedure however, methyl-$d_3$ trifluoromethanesulfonate was used and purification was via neutral alumina filled column chromatography giving a yield of 0.019 g (43%). $\nu_{max}$ (ATR)/cm$^{-1}$: 3102 w, 2925 w, 2854 w, 2032 s (CO, A′(1)), 1929 s (CO, A′(2)), 1894 s (CO, A″), 1609 w, 1587 , 1522.7w, 1481 w, 1457 w, 1431 m, 1328 w, 1227 w, 1153 w, 1080 w, 1020 w, 832 m, 770 m, 752 w, 722 m, 701 w. The ratio of system a:b is 1:0.71. $^1$H NMR (δ, ppm, Acetone-$d_6$): 9.74 (2H, d, *J* = 5.0 Hz, phen $H_{2,9}$)$^b$ , 9.31 (2H, d, *J* = 5.0 Hz, phen $H_{2,9}$)$^a$ , 9.07 (2H, d, *J* = 8.2 Hz, phen $H_{4,7}$)$^b$ , 9.00 (2H, d, *J* = 8.2 Hz, phen $H_{4,7}$)$^a$ , 8.37 (2H, s, phen $H_{5,6}$)$^b$, 8.34 (2H, s, phen $H_{5,6}$)$^a$, 8.28-8.25 (2H, m, phen $H_{3,8}$)$^b$, 8.10-8.07 (2H, m, phen $H_{3,8}$)$^a$, 7.85-7.81 (2H, m, $CN_4$-$C_6H_5$), 7.69-7.65 (3H, m, $CN_4$-$C_6H_5$), 7.60-7.58 (1H, m, $CN_4$-$C_6H_5$), 7.58-7.43 (4H, m, $CN_4$-$C_6H_5$).

## 4.6.2 X-ray Crystallography

X-ray Crystallography for all of the complexes presented in Chapter Four were carried out by Dr. Brian Skelton at the University of Western Australia. Diffraction data were collected at 100(2) K on an Oxford Diffraction Gemini diffractometer fitted with Mo K$\alpha$ radiation. Following analytical absorption corrections and solution by direct methods, the structure was refined against $F^2$ with full-matrix least-squares using the program SHELXL-97.[202]

For **58** the benzaldehyde group was modelled as being disordered over two sets of sites with site occupancies constrained to 0.5 after trial refinement. For **34**, the $CHCl_3$ solvent molecule was modelled as being disordered over two sets of sites with occupancies of the two components each constrained to 0.5 after trial refinement. The $PF_6^-$ anion was also disordered over two sets of sites but with occupancies refined to 0.889(12) and its complement.

All H-atoms were added at calculated positions and refined by use of a riding model with isotropic displacement parameters based on those of the parent atoms. Anisotropic displacement parameters were employed throughout for the non-hydrogen atoms.

All crystallographic data can be found in Table A3.1, Table A3.2 and Table A3.3 in Appendix 3.

### 4.6.3 Computational Calculations

Computational (TD-DFT/DFT) calculations were performed by Mr. Phillip Wright of Curtin University using GAUSSIAN09.[181] The TD-DFT calculations were done using the B3LYP functional,[221] the Stuttgart-Dresden effective core potential for Re,[222] and the 6-311++G** basis set for the other atoms. The presence of solvent was then mimicked by using the PCM implicit model[223] with parameters appropriate for dichloromethane.

# Chapter 5

# Biological Investigation of Rhenium Complexes in HeLa Cells

## 5.1 Abstract

HeLa cells were incubated with a series of Re(I) complexes, to final concentrations of 20 $\mu$M and imaged on a confocal microscope using excitation at 405 nm. The three neutral Re(I) tetrazolato complexes, *fac*-[Re(**phen**)$(CO)_3$(**Tph**)] (**11**), *fac*-[Re(**phen**)$(CO)_3$(**Tbz**)] (**13**) and *fac*-[Re(**phen-S-PEG**)$(CO)_3$(**Tph**)] (**41**) showed good uptake and diffuse cytoplasmic localisation in the HeLa cells. The methylated complexes *fac*-[Re(**phen**)$(CO)_3$(**Tph**$CH_3$)]$^+$ (**31**) and *fac*-[Re(**phen**)$(CO)_3$(**Tbz**$CH_3$)]$^+$(**33**) did not exhibit observable cellular uptake. These complexes were also unsuitable imaging agents due to their instability in coordinating solvents. Confocal images of the *fac*-[Re(**phen-RS**)$(CO)_3$(Cl)] (**39**) and *fac*-[Re(**phen-S-PEG**)$(CO)_3$(Cl)] (**40**) suggested that they did pass into the HeLa cells but the signal detected appeared significantly weaker than those complexes containing the tetrazolato ancillary ligand. Phototoxic effects were observed for some of the complexes when illuminated continuously, for more than two minutes.

## 5.2 Introduction

Live cell imaging experiments were conducted by incubating a selection of prepared Re(I) complexes with HeLa cells. These experiments were carried out to determine the behaviour of the complexes in a biological environment and assess how small structural changes might affect uptake, localisation and/or toxicity within cells.

### 5.2.1 Cell Culture

The growth of separated cells from animal tissue (or plants) is known as cell or tissue culture. Under the correct conditions, cells will grow in an artificial environment, ie: *in vitro.*[231] One requirement for cell sustainability is an appropriate culture media generally containing energy sources (carbohydrates), amino acids (for nutrients), essential metals and minerals, buffering agents (to maintain pH ~ 7.4) and indicators (for pH change).[232] External conditions, such as temperature and humidity levels, are also important for cell growth. External conditions are controlled using an incubator, to closely mimic the environment experienced by cells *in vivo*. The optimal temperature for mammalian cell culturing is 37 ºC with 100% humidity (to avoid culture media evaporation). A $CO_2$ atmosphere (5%) is generally required to maintain the pH of the cell culture media. It works by acting as a buffer system with the sodium bicarbonate present in the media, to sustain pH ~ 7.4.[232] Herein, standard conditions refer to incubation with these particular requirements (or settings).

Primary culture refers to cells when they have been taken directly from a subject, for example through a biopsy or from tissue/organ samples. This primary cell culture is then grown *in vitro* until it reaches confluence (ie: the cells cover approximately 80-95% of the base of the flask). Once confluent, cells are detached from their original flask, then divided into new flasks in order to expand the culture and continue that cell line.[233]

#### HeLa Cells

HeLa cells are a human cervical cancer cell line, that was first isolated in the 1950s from a woman named Henrietta Lacks. HeLa are the first example of an immortal hu-

man cell line. “Normal” cells have a finite number of divisions they can undergo before they become senescent (stop dividing).[234] This is known as they Hayflick limit.[235] Immortal cell lines such as HeLa can be grown outside the human body with an apparent unlimited capacity for population doubling. HeLa cells were quickly distributed all over the world and have been extensively used in biomedical research ever since.[236]

### 5.2.2 Light Microscopy

Light microscopy is a powerful technique used in biology to analyse cellular structure, physiology and function. Compound microscopes contain multiple lenses. The magnification of these lenses is compounded (multiplied) to increase overall magnification of a sample, compared to simple microscopes which use only one lens. The two main configurations of microscopes include upright (where the objective lenses are located above the sample and light source illuminates from underneath) and inverted (where the objective lenses are below the sample and the light source is above). The objective lens is the first part of the microscope to collect light from the sample.[237] Here, live cell imaging experiments were carried out using MatTek glass bottom petri dishes, on an inverted microscope. The glass coverslip at the base of the dish is necessary as the objective lenses are positioned below the sample.

The resolution of a microscope is defined as its ability to resolve fine detail in the sample being imaged. It can be expressed as the smallest distance between two close points, at which they can still be recognised as two *separate* entities. The resolution of a microscope is directly related to the wavelength of light used to illuminate the sample and is inversely proportional to the numerical aperture (NA).[237] This relationship is outlined in the equation below, where $d$ is the smallest resolvable distance (resolution).

$$d = \frac{0.61\lambda}{NA}$$

In these experiments, an oil immersion objective lens (60×, NA 1.4) was used where the medium between the objective lens and the glass coverslip is oil (rather than air). Oil is used as it has a similar refractive index (n) to the glass coverslip on the base of the MatTek petri dish. Therefore the system has a higher NA and improved resolution (n $\propto$NA).[237,238]

**Confocal Microscopy**

In conventional light or fluorescence microscopy the entire depth of a sample is constantly illuminated meaning out of focus light is still being detected ( Figure 1.12 on page 18), which can make image detail difficult to interpret.[239] Comparatively, confocal microscopy allows imaging of thin optical sections as any out of focus light is not detected, reducing the issue of out-of-focus information.[240] This is possible due to the use of two pinholes, the first located at the point of illumination, see Figure 5.1. Light

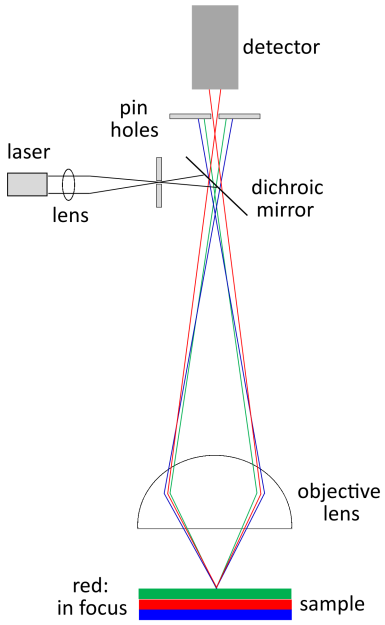


Figure 5.1: Basic schematic of a confocal microscope.[241]

passes through the first pinhole and is directed to the sample by a highly reflective dichroic mirror. Light is focused onto the specimen by passing through the objective lens which then forms an image of the specimen onto the second pinhole (located before the detector).[242] In other terms, the illumination and detection systems are focused at the same point on the sample; ie: they are confocal (Figure 5.1).[240]

The diameter of the pinhole can be controlled and smaller pinhole sizes lead to thinner optical sections and high resolution along the z-axis is achieved. The z-axis is the optical plane perpendicular to the sample (Figure 5.2), whereas the x and y axes are parallel to the coverslip. An example of optical sectioning is shown in Figure 5.2, taken from the research of Dan and co-workers.[243] By increasing the pinhole radius, a thicker optical section is imaged and although a brighter signal is detected, resolution along the z-axis is reduced.[240] In all imaging experiments a balance between sensitivity,

spatial and temporal resolution needs to be considered. Confocal imaging also has the advantage of being able to produce images in the xy and z planes allowing 3-D images to be constructed. In z-stack imaging, multiple images are taken as the sample is moved to different focal planes along the z-axis. This can then be viewed as a whole stack or 3-D image. Figure 5.2 shows how optical sectioning (or z-stack imaging) can be used to generate 3D images.

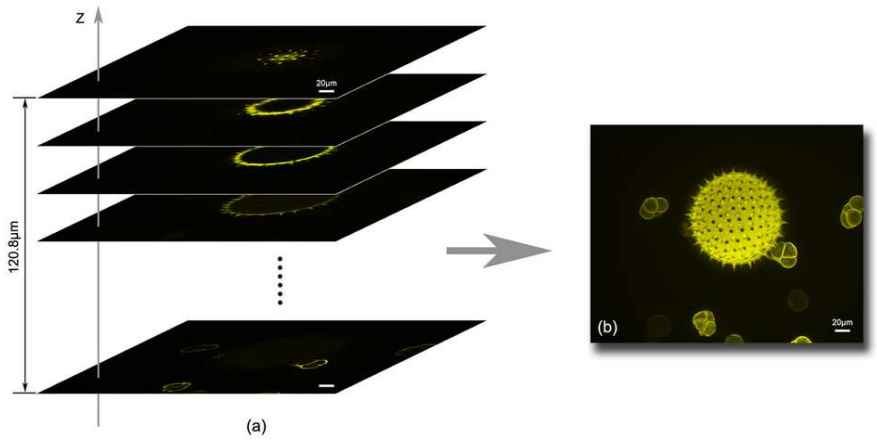


Figure 5.2: Optical sectioning of pollen grains where (a) shows a stack of optically sectioned images and (b) shows the constructed 3D image.[243]

**Multiphoton Microscopy**

Multiphoton excitation (MPE) was discussed in Chapter One, sections 1.3.1 and 1.3.2.2. Many microscope systems have integrated MPE capabilities where high energy pulsed lasers (in the femtosecond range) are used to image the specimen.[244] The importance of MPE in optical imaging is that lower energy light can be used to excite the probe. This is less damaging to the sample than high energy radiation. Generally, low energy light has improved tissue penetration[63] due to reduced scattering. Another advantage of MPE is that it provides excitation of the sample only at the focal point of incident light and therefore confocal type imaging is achieved without the use of pinholes.[57] Also, there is usually less photobleaching as the sample is only illuminated at the plane of focus.[60]

**Spectral Detection Imaging**

In generic confocal imaging, filters can be used to avoid spectral bleed-through artifacts. However, many dye combinations can become complex to distinguish, especially when their excitation profiles also overlap.[245] Spectral imaging is a technique which allows the spectral profile of fluorophores within the sample to be detected and collected *in situ*, on a pixel by pixel basis. This technique is incorporated into some confocal imaging systems and is often combined with spectral unmixing. Labels which have overlapping excitation and/or emission profiles, making them difficult to separate with filters alone, can be discriminated with spectral unmixing. Spectral imaging collects many images of the same view at different wavelengths. The Nikon A1Si confocal microscope system (used in this research) contains a 32 channel spectral detector and for the experiments reported herein, a 10 nm Si grating resolution was used. This means that there is one signal point detected for each 10 nm step. A larger step is required to detect a greater range of the spectrum however spectral resolution is reduced. To improve resolution, the Si grating can be reduced (ie: 10 nm to 2.5 nm), however this means that less of the spectrum can be collected.

In relation to this research, the spectral detection capability of the confocal microscope was used to detect and identify the emission of the rhenium complexes incubated with HeLa cells. It was also used to identify the rhenium signal against any autofluorescence or noise. Autofluorescence is discussed in section 1.2.2 on page 9. Due to the very broad emission profile of the rhenium complexes, the 10 nm grating was used to ensure a sufficient portion of the visible spectrum could be analysed *in vitro* (approximately 400-700 nm).

## 5.3 Results and Discussion

### 5.3.1 Sample preparation

*fac*-[Re(**phen**)$(CO)_3$(**Tph**)] (**11**) and *fac*-[Re(**phen**)$(CO)_3$(**Tbz**)] (**13**) were the first complexes used for live cell imaging experiments. Only the **phen** analogues are investigated due to their superior photophysical performance (as discussed in Chapter Two). The Re(I) complexes are not completely water soluble and therefore dimethylsulfoxide (DMSO) was used to dissolve them into aqueous cellular media. DMSO is commonly used in biology to make up stock solutions of powdered fluorophores.[240] It is often advised to maintain DMSO concentrations in cell samples ≤0.1 %.[240] However, many publications looking at the application of metal complexes (eg: Ir, Re and Ru) as optical imaging agents use concentrations of DMSO in cell cultures anywhere between 1%[99,246,247], 2%[76] and even 5%.[154] Herein, the concentration of DMSO used is ≤1%, with exact concentrations specified for each experiment. Control samples, containing the same DMSO concentrations used for each rhenium experiment, were always prepared in parallel. Blank samples were also used, in which nothing was added to the cell culture.

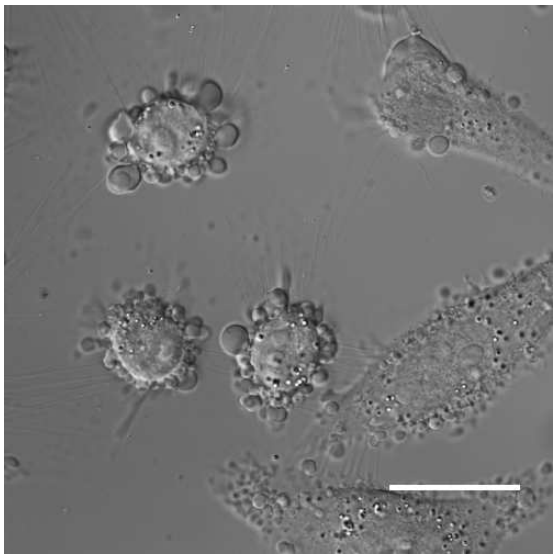

Figure 5.3: HeLa cells showing membrane blebbing, as indicated by the presence of small bulges around the cells. Scale bar, 25 $\mu$M.

The first sets of experiments were conducted by adding rhenium complexes (in DMSO) *directly* onto the cell culture, contained in a glass bottom MatTek petri dish with media.

In these experiments, some cells were observed undergoing a process known as blebbing of the plasma membrane. Cell blebs are irregular bulges that protrude from cell membranes and the bulges appear like clear bubbles under the microscope.[248,249] Blebbing is often a sign of cells undergoing membrane damage or apoptosis (programmed cell death) and can be in response to intracellular and extracellular damage and/or specific physiological signals.[248,250–252] The loss of structural integrity is a stress response of the cells, easily observable in transmission images, as illustrated in Figure 5.3. It is therefore important to present both fluorescent and transmission images as the morphology of cells and therefore the presence of membrane blebs is not obvious in fluorescent images (unless specific stains are used). Transmission imaging can include brightfield, phase contrast or differential interference contrast (DIC) optics. DIC is used herein, as it provides an increased contrast of the cells with high resolution.[237]

It was hypothesised that some cells were showing membrane blebs in response to the highly localised concentration of DMSO being added directly onto the cells. A DMSO control experiment was carried out to determine the cause of stress on the cells. HeLa cells in a glass bottom MatTek petri dish were placed on the microscope and confocal images were taken. DMSO was directly added to the centre of the cell culture dish and further images were taken. Cells blebbed less than four minutes after DMSO addition. Only cells directly "hit" by the DMSO showed blebbing. Figure 5.4 A and B shows HeLa cells before and after the addition of DMSO. White arrows in image B indicate

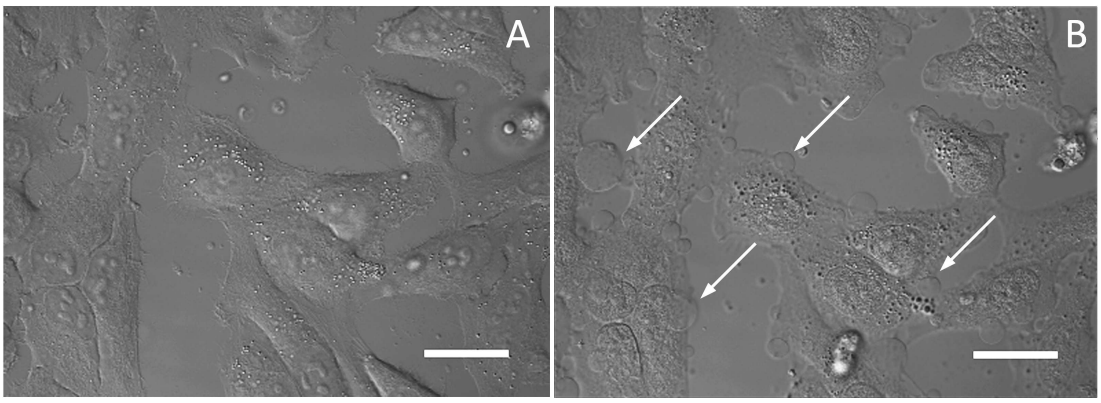


Figure 5.4: DIC images of HeLa Cells before (A) and after (B) the direct addition of DMSO to the culture. Arrows show the presence of blebs in image B. Scale bar, 25 $\mu$m.

the presence of blebs. Upon moving the field of view away from where DMSO was

directly added, cells morphology appeared unchanged (similar to before the addition of DMSO, ie: no blebs observed). The remainder of the imaging experiments were therefore conducted by pre mixing the rhenium solutions (or DMSO) in culture media. The homogenous solution was then added to HeLa cells. Improved cell response was observed as the DMSO was evenly dispersed throughout the culture and cells were not experiencing a highly localised concentration.

### 5.3.2 Imaging of *fac*-[Re**(phen)**$(CO)_3$**(Tph)] (11) and *fac*-[Re(phen)$(CO)_3$(Tbz)] (13)**

Confocal images were collected on a Nikon Ti-E inverted motorised microscope with a Nikon A1Si confocal microscope system to assess uptake and localisation of the rhenium complexes in HeLa cells.

HeLa cells were incubated under standard conditions with *fac*-[Re(**phen**)$(CO)_3$(**Tph**)] (**11**) to a final concentration of 20 $\mu$M and 0.4% (v/v) DMSO, for three hours before imaging. HeLa cells displayed good uptake of the applied rhenium complex with confocal imaging indicating cytoplasmic localisation. Figure 5.5 A-C shows the DIC, fluorescence and merged images respectively. **11** appears to have entered the cells and is localising in the cytoplasm. Bright punctate signals are observed in the fluorescence image which could suggest organelle localisation however co-localisation experiments would be required to support this. The black hole in the middle of the cells (Figure 5.5) is indicative of the cell nucleus. Confocal images only take a thin optical section and therefore Figure 5.5 B illustrates that the complex is entering cells and not just adhering to the external cell surface.

The DIC image shows the majority of cells in culture appear comparable to cells in the DMSO control and blank dishes. Cells show no signs of altered morphology, suggesting the rhenium complexes are non-toxic within the experimental time frame. It is unclear if specific cellular organelles are preferentially targeted. Intracellular localisation of the rhenium compound appears diffuse, suggestive of non-specific localisation.

*fac*-[Re(**phen**)$(CO)_3$(**Tbz**)] (**13**) was incubated with HeLa cells for two hours, under standard conditions (section 5.2.1 on page 172). For the images shown in Figure 5.6, *fac*-[Re(**phen**)$(CO)_3$(**Tbz**)] (**13**) was incubated to a final concentration of 20 $\mu$M and

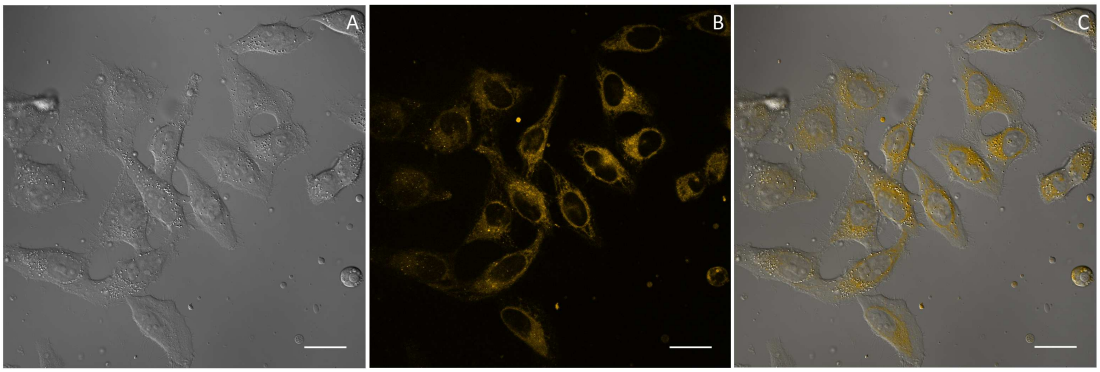


Figure 5.5: HeLa cells incubated with *fac*-[Re(**phen**)$(CO)_3$(**Tph**)] (**11**). DIC (A) shows the structural integrity of the cells where the fluorescence (B) and merged (C) images illustrate the cellular uptake and cytoplasmic localisation of **11**. Scale bar, 25 $\mu$m.

0.4% (v/v) DMSO. Diffuse cytoplasmic localisation was again observed.

HeLa cells did not show signs of stress suggesting *fac*-[Re(**phen**)$(CO)_3$(**Tbz**)] (**13**) is non toxic during imaging experiments.

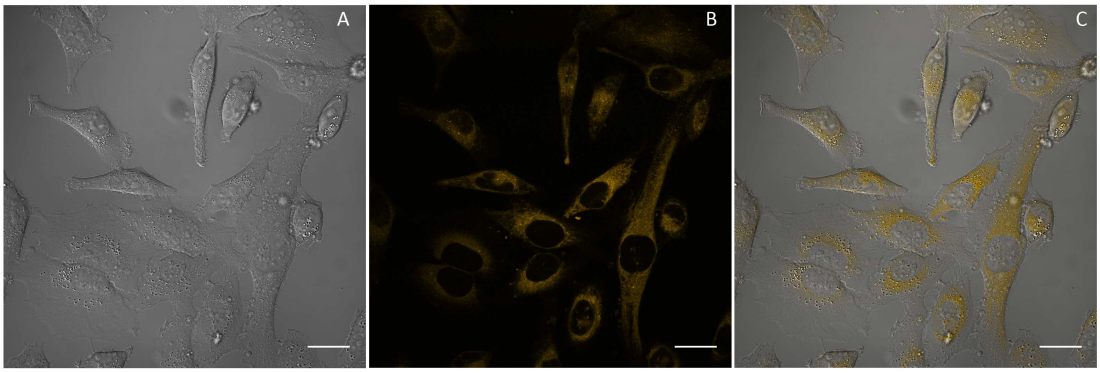


Figure 5.6: HeLa cells incubated with *fac*-[Re(**phen**)$(CO)_3$(**Tbz**)] (**13**). DIC (A) shows the structural integrity of the cells where the fluorescence (B) and merged (C) images illustrate the cellular uptake and perinuclear localisation of **13**. Scale bar, 25 $\mu$m

The times of incubation quoted for each complex in HeLa cells (two to three hours) are for the specific images shown. Uptake of both complexes **11** and **13** has clearly been observed after incubation times of one hour.

#### 5.3.2.1 Spectral Detection

As mentioned above, control and blank samples were always prepared to gauge the status of cells without rhenium additives. In some instances, low levels of cellular

autofluorescence were detected whilst imaging the DMSO control and unlabelled cell samples. This is not unexpected due to the presence of naturally occurring fluorescent biological compounds (eg: flavinoids, aromatic amino acids). To ensure that the luminescent signal detected for the experiments above, was in fact due to the presence of rhenium, spectral images were collected followed by spectral analysis.

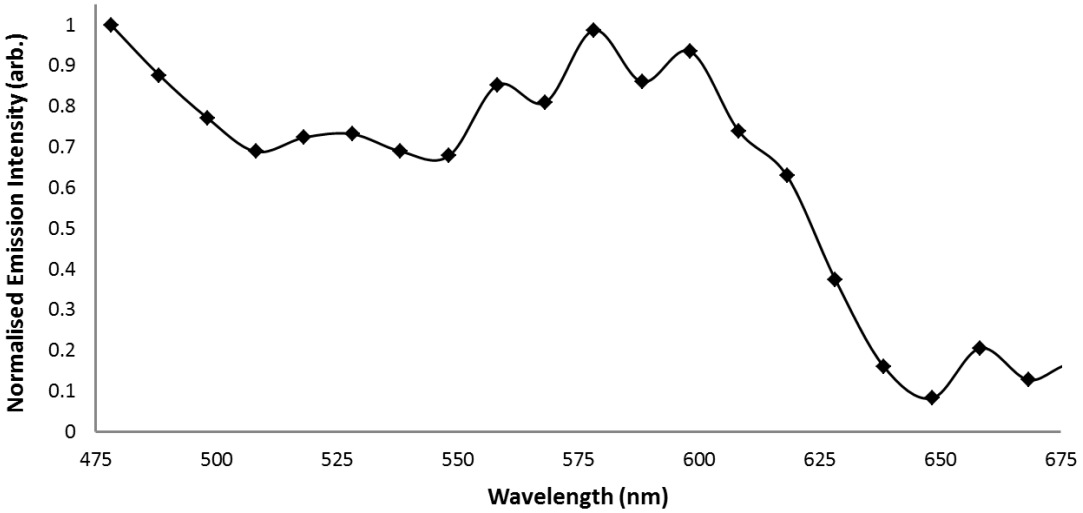


Figure 5.7: Spectral detection emission profile measured from a blank HeLa cell.

To perform spectral analysis, a spectral image of cells without additives (blank sample) was first collected. Regions of interest were selected inside the cytoplasm of cells and then spectrally analysed. Figure 5.7 shows the normalised emission profile generated from a region of interest (ROI) inside the cytoplasm of a blank HeLa cell. There is a slight maximum observed between 575 and 600 nm however the profile does not have a Gaussian shape. This profile is representative of background noise and autofluorescent signal.

Spectral references of the Re(I) complexes were measured on the confocal using DMSO stock solutions. From the spectral image, a specific ROI was selected and an emission profile generated. The emission was collected using a 32 channel spectral detector and 10 nm Si grating resolution. The spectral profiles generated from DMSO solutions of *fac*-[Re(**phen**)$(CO)_3$(**Tph**)] (**11**) and *fac*-[Re(**phen**)$(CO)_3$(**Tbz**)] (**13**) are shown in Figure 5.8. The emission spectra have Gaussian profiles which is expected, based on the measurements made in Chapter Two (section 2.3.4 on page 49).

HeLa cells were incubated with *fac*-[Re(**phen**)$(CO)_3$(**Tph**)] (**11**) to a final concentration of 10 $\mu$M and 0.5% (v/v) DMSO, for two hours before imaging. Spectral images

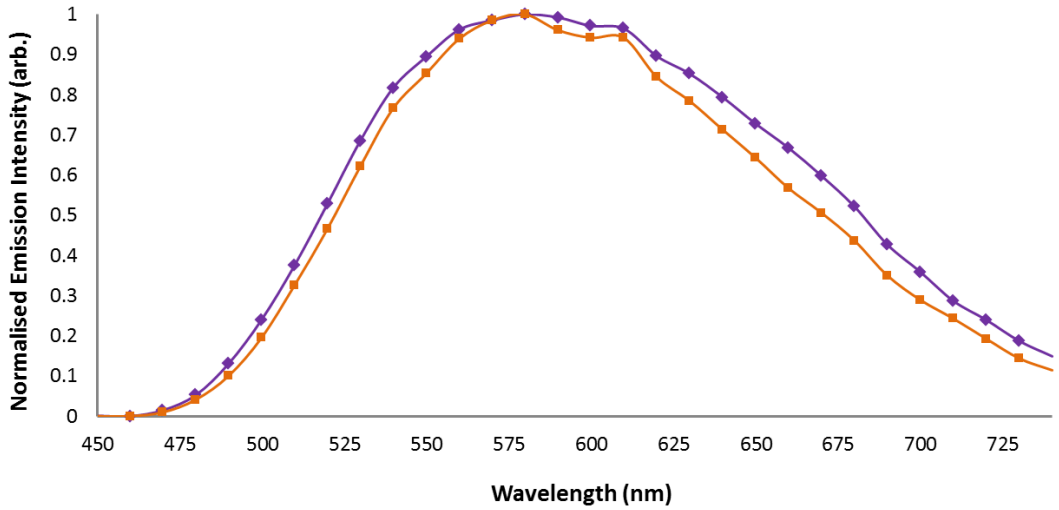


Figure 5.8: Spectral detection emission profiles measured from DMSO solutions of *fac*-[Re(**phen**)$(CO)_3$(**Tph**)] (**11**, purple) and *fac*-[Re(**phen**)$(CO)_3$(**Tbz**)] (**13**, orange).

were taken and from these, a ROI inside the cytoplasm of the cell was chosen. The ROI selected was a circle with an approximate diameter of 7 $\mu$m. The white arrow in Figure 5.9 indicates the area where the ROI was selected. The spectral profile was analysed and is shown in Figure 5.10.

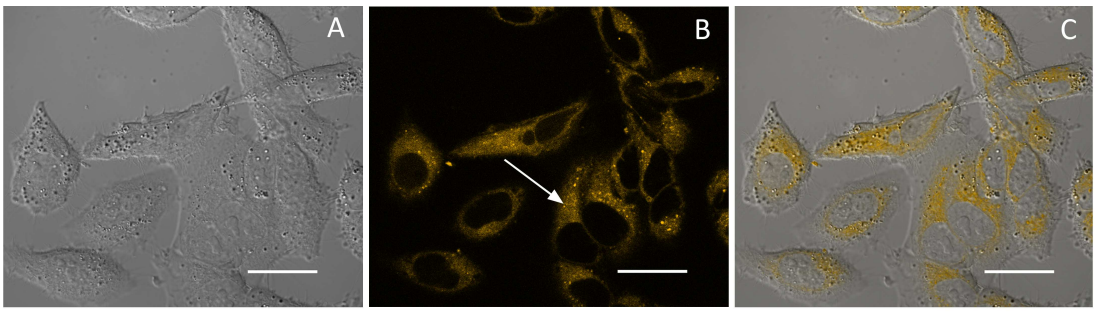


Figure 5.9: HeLa cells incubated with *fac*-[Re(**phen**)$(CO)_3$(**Tph**)] (**11**). The white arrow shows the area in which a ROI was selected for spectral analysis. DIC (A), fluorescence (B) and merged (C) images. Scale bar, 25 $\mu$m.

Emission spectra from the confocal microscope are not as "smooth" as those taken with a spectrofluorometer and therefore a definite emission maximum is difficult to identify. The general shape and approximate emission maximum shown in Figure 5.10 is consistent with that measured from the DMSO stock solution of **11** on the microscope (Figure 5.8).

The same experiments were carried out incubating HeLa cells with *fac*-[Re(**phen**)$(CO)_3$(**Tbz**)]

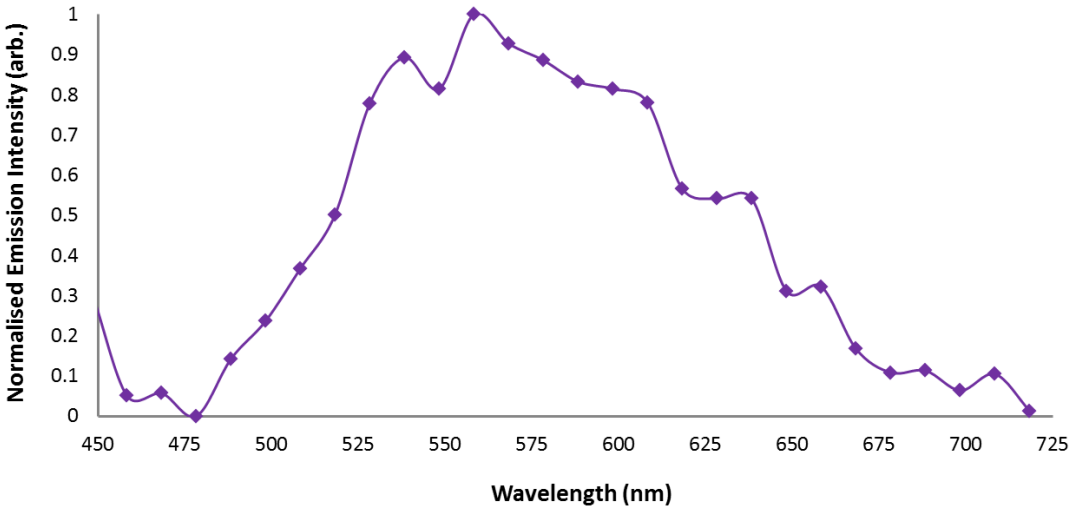


Figure 5.10: Spectral detection emission profile taken from inside HeLa cells incubated with *fac*-[Re(**phen**)$(CO)_3$(**Tph**)] (**11**). The area in which a ROI was selected is indicated by the white arrow in Figure 5.9.

(**13**) to a final concentration of 20 $\mu$M and 0.4% (v/v) DMSO, for two hours before imaging. Spectral images were taken and from these, a ROI inside the cytoplasm of the cell was chosen. The ROI was a circle with an approximate diameter of 7 $\mu$m and the white arrow in Figure 5.11 indicates where the ROI was located. Spectral analysis produced the profile shown in Figure 5.12. The emission profile is again comparable to that taken from a DMSO solution of *fac*-[Re(**phen**)$(CO)_3$(**Tbz**)] (**13**), using the microscope (Figure 5.8). There is a slight blue shift noted for the detection of both complexes (**11** and **13**), inside the HeLa cells compared to that of the DMSO solution however this is not unexpected. Upon changing to more polar solvents, the emission maxima of the prepared rhenium complexes are known to undergo a blue shift. The reference spectra were recorded in DMSO but once incubated with the cells the complex is in a more aqueous (polar) environment. The hypsochromic shift that occurs upon increasing solvent polarity is illustrated in Appendix 5, Figure A5.1.

The emission profiles collected *in vitro* from HeLa cells incubated with rhenium complexes (**11** and **13**) indicate that there is cellular uptake with cytoplasmic localisation. When regions of interest were positioned outside cells or inside the nucleus, the emission profiles were significantly weaker and the shape was not comparable to the DMSO control (Figure 5.8). Based on the similarity of the reference and *in vitro* emission profiles, it could be suggested that the Re(I) complexes remain unchanged upon incubation with HeLa cells.

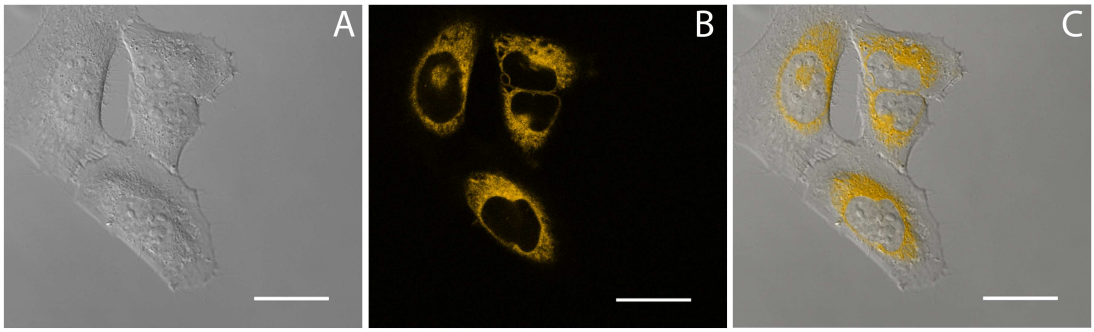


Figure 5.11: HeLa cells incubated with *fac*-[Re(**phen**)$(CO)_3$(**Tbz**)] (**13**). The white arrow shows the area in which a ROI was selected for spectral analysis. DIC (A), fluorescence (B) and merged (C) images. Scale bar, 25 $\mu$m.

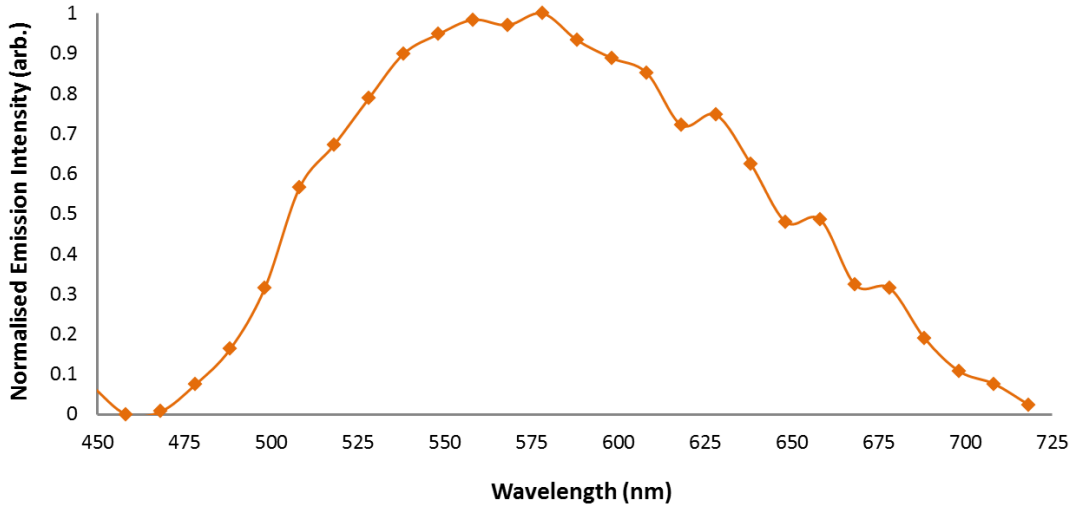


Figure 5.12: Spectral detection emission profile taken from inside HeLa cells incubated with *fac*-[Re(**phen**)$(CO)_3$(**Tbz**)] (**13**).The area in which a ROI was selected is indicated by the white arrow in Figure 5.11. Scale bar, 25 $\mu$m.

Further support for the stability of neutral Re(I) complexes in biological environments is discussed in a study by Bader *et al.*[115] The two Re(I) tetrazolato complexes used in Bader's study exhibit different localisation patterns attributed to the different tetrazole ancillary ligands. Bader *et al.* indicate that if the structures of the complexes were to change upon incubation, for example by detachment of the tetrazolato ligand, then it would be unlikely for the different complexes to exhibit unique localisation.

#### 5.3.2.2 Intensity Profiles

Intensity profile plots were used to confirm the localisation of rhenium complexes inside the cytoplasm of cells. FIJI (ImageJ) was used to draw a line across the cell

and an intensity profile along this line was plotted. The profiles for cells incubated with *fac*-[Re(**phen**)$(CO)_3$(**Tph**)] (**11**) and *fac*-[Re(**phen**)$(CO)_3$(**Tbz**)] (**13**) are shown in Figure 5.13, along with the cells they were collected from. The normalised pro-

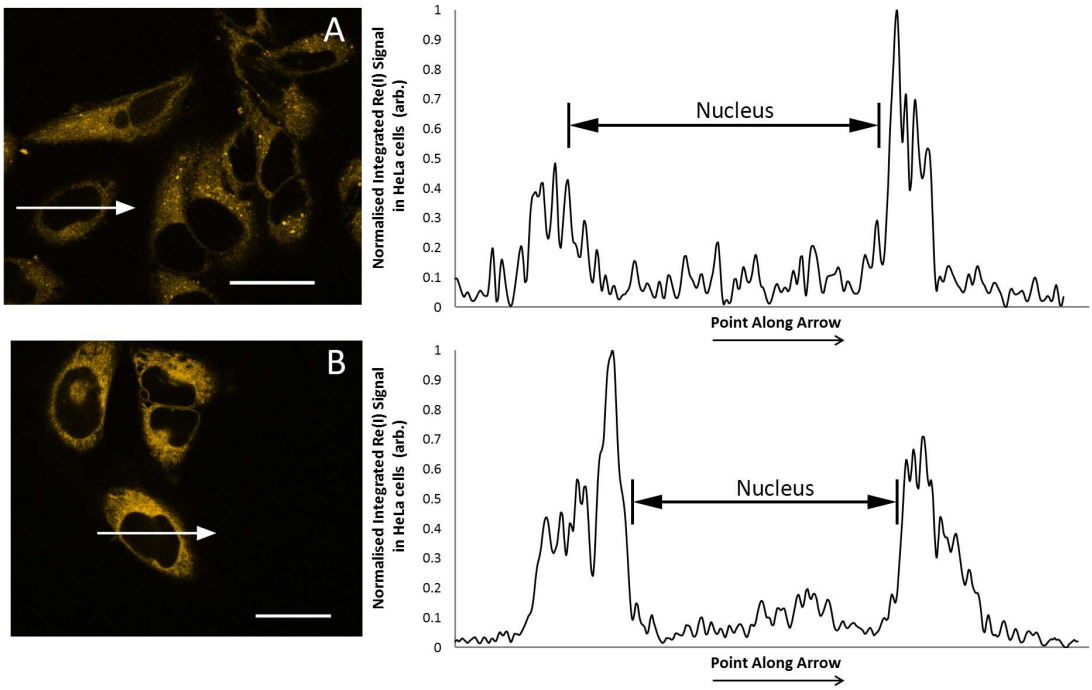


Figure 5.13: HeLa cells incubated with *fac*-[Re(**phen**)$(CO)_3$(**Tph**)] (**11**, A) and *fac*-[Re(**phen**)$(CO)_3$(**Tbz**)] (**13**, B) and their corresponding integrated intensity profiles collected along the white arrow. Intensity profiles show that the most intense signal is originating from the cytoplasm of HeLa cells. Scale bar, 25 $\mu$m.

files are reported to demonstrate the *relative* luminescence intensities in various parts of the cell culture. Figure 5.13 illustrates the increased luminescence intensity in the cytoplasmic regions of the cells, compared to inside the nucleus or in the extracellular space. Only one cell profile is reported for each complex however each example is representative of all cells in culture. Confocal images of the HeLa cells incubated with the two neutral rhenium complexes (**11** and **13**), as well as the emission profiles analysed demonstrate consistent cellular uptake. The predominant cytoplasmic localisation was supported by analysis of the intensity profile plots across the cells. These results show the potential for **11** and **13** to be further investigated as optical imaging agents.

#### 5.3.2.3 Multiphoton Excitation

To evaluate the ability of *fac*-[Re(**phen**)$(CO)_3$(**Tph**)] (**11**) to undergo multiphoton excitation, a thin film of the sample was imaged on a confocal microscope equipped with

a pulsed infrared laser (700-1000 nm). The sample was excited with the infrared laser at wavelengths between 720 and 800 nm. Figure 5.14 shows the signal from a thin film of **11**, imaged using 720 nm pulsed excitation. The white arrow in Figure 5.14 indicates the edge of the thin film, illustrating that the observed luminescence is originating from the Re(I) sample. Although no cellular images were taken using multiphoton excitation, the possibility for Re(I) complexes to be excited using NIR light has been demonstrated (Figure 5.14).

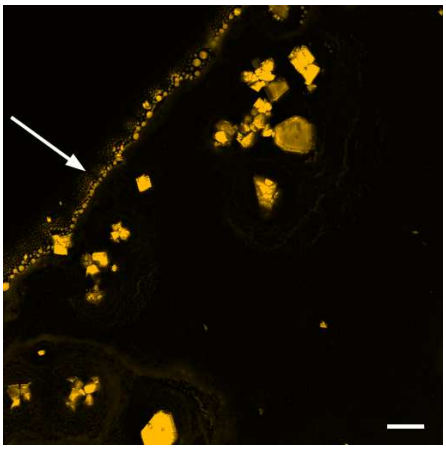

Figure 5.14: Thin film of *fac*-[Re(**phen**)$(CO)_3$(**Tph**)] (**11**), demonstrating multiphoton excitation. Scale bar, 25 $\mu$m.

#### 5.3.2.4 Photoinduced Cytotoxicity

Z-stack images were taken with the aim to produce 3D images of the rhenium containing HeLa cells. Upon collection of z-stacks cells appeared to become stressed (which was not observed during single image capture over a period of hours). *fac*-[Re(**phen**)$(CO)_3$(**Tph**)] (**11**) was added to HeLa cells at a concentration of 20 $\mu$M and 1% (v/v) DMSO. Cytoplasmic uptake of the complex was observed. However, upon acquiring a z-stack series over a time of 3 minutes and 35 seconds, cells were clearly being affected by the increased light exposure. In the z-stack images, cells progressively withdraw, round up and form blebs. Figure 5.15 B shows a snap shot taken from the illuminated area immediately after z-stack acquisition where cells have rounded up and formed blebs. Although Figure 5.15 B was taken at the end of a 3 minute and 35 second z-stack, the cells appeared stressed even after one minute. Interestingly, when a non-illuminated filed of view was examined cell morphology appeared unaltered with no evidence of bleb formation.

To investigate the main cause of stress to the cells, 1% (v/v) DMSO control sample was analysed using similar laser exposure conditions. After five minutes of illumination through acquisition of a z-stack series, a snap shot was taken of the illuminated area, as shown in Figure 5.15 A. Overall, cellular morphology did not appear to be altered with few rounded cells and no blebbing visible. Figure 5.15 shows evidence that *fac*-[Re(**phen**)$(CO)_3$(**Tph**)] (**11**) is having a toxic effect on cells that are continually illuminated with 405 nm laser for one minute or more.

It is known that UV light radiation has damaging effects on cells[65,66] and the 405 nm laser source is classified as UVA radiation.[253] However, it is unlikely that the 405 nm laser is the sole cause of damage to HeLa cells as the (DMSO) control cells do not show signs of stress. It is probable that the combination of both the laser light and rhenium complex is causing the toxic effects to the cells.

It was rationalised that the formation of singlet oxygen ($^1O_2$) could be contributing to the toxic response observed in the cells being illuminated. $^1O_2$ is commonly associated with photoinduced cytotoxicity from phosphorescent metal complexes.[104] The mechanism of $^1O_2$ formation is discussed in Chapter One. The diffusion distance of singlet oxygen in cells has been calculated between 70 and 300 nm.[254,255] This relatively short

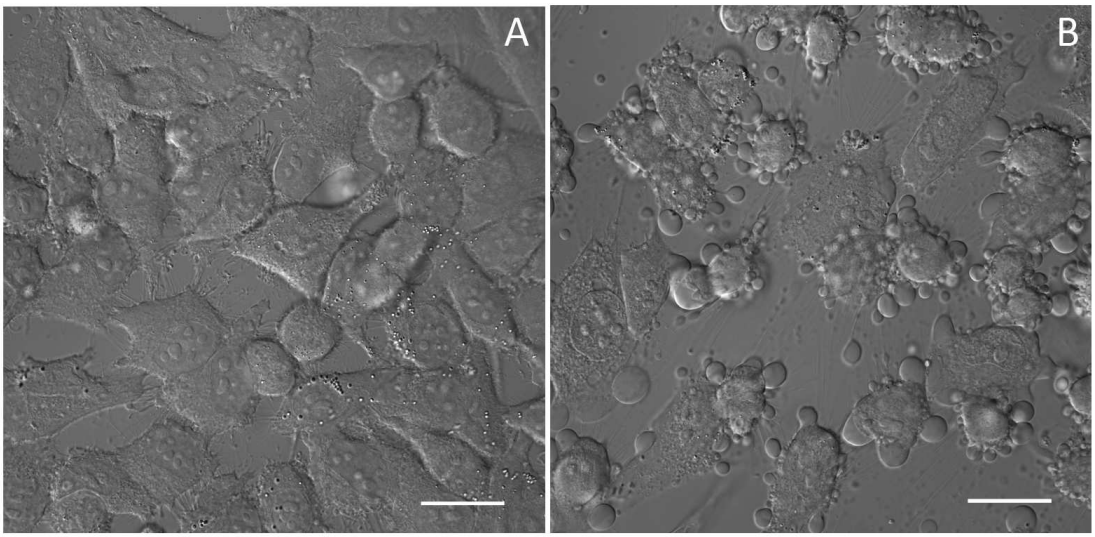


Figure 5.15: DIC images of HeLa cells after z-stack images. HeLa cells incubated with 1% (v/v) DMSO (A) and HeLa cells incubated with *fac*-[Re(**phen**)$(CO)_3$(**Tph**)] (**11**, B). Control cells (A) do not show signs of altered behaviour. However cells incubated with **11** (B) have rounded up and show evidence of bleb formation. Scale bar, 25 $\mu$m.

diffusion distance is the reason that only directly illuminated cells show signs of stress. The singlet oxygen produced upon irradiation does not travel far enough to damage surrounding cells. One way to detect the production of singlet oxygen is directly through monitoring its emission in the near infrared (NIR) region of the spectra. The spectral detector on the confocal does not have the capacity for NIR detection. Emission studies using the FLS980 spectrofluorometer coupled to an NIR detector were carried out. $^1O_2$ is known to exhibit an emission peak around 1270 nm[254–257] and this peak has been directly detected for a series of previously published Re(I) complexes.[55]

Emission of the prepared rhenium complexes, *fac*-[Re(**phen**)$(CO)_3$(**Tph**)] (**11**) and *fac*-[Re(**phen**)$(CO)_3$(**Tbz**)] (**13**) in DCM, was monitored in the NIR, using an excitation wavelength of 370 nm (as was determined in Chapter Two). A peak at 1274 nm was observed for both complexes as illustrated in Figure 5.16. This is a direct indicator of the ability of **11** and **13**, to generate singlet oxygen. Interestingly, the $^1O_2$ peak was not observed for the complexes when measured in 1% (v/v) DMSO in $H_2O$. The measurement was also conducted in 100% DMSO and again, no $^1O_2$ emission was observed. The generation of $^1O_2$ can not be ruled out for aqueous or DMSO solutions. The production of $^1O_2$ may be reduced in these solvents or the emission at 1274 nm could be quenched. Difficulties in obtaining reliable data from aqueous solutions have

been previously reported.[258] A study by Leonidova *et al.* also noted that upon changing solvents from acetonitrile to water, the production of $^1O_2$ from the Re(I) complexes was reduced.[55]

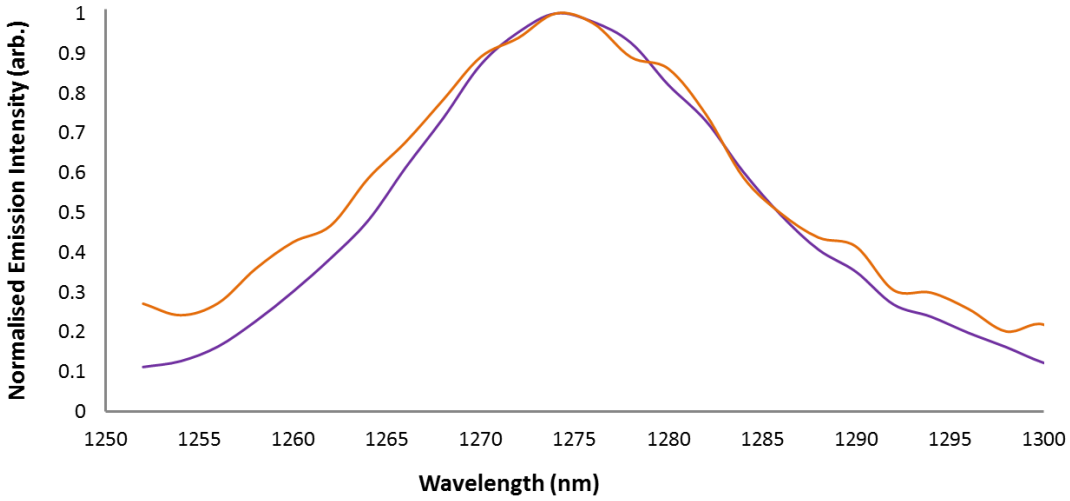


Figure 5.16: Near infrared emission spectra of *fac*-[Re(**phen**)$(CO)_3$(**Tph**)] (**11**, purple) and *fac*-[Re(**phen**)$(CO)_3$(**Tbz**)] (**13**, orange) in DCM. $\lambda_{ex}$: 360 nm.

There is a correlation between the solvent (or medium in which the $^1O_2$ is being generated) and the excited state lifetime decay (and therefore emission intensity) of $^1O_2$. Studies by Merkel show that the lifetime of $^1O_2$ emission ranges from 700 $\mu$s in carbon tetrachloride to 12 $\mu$s in ethanol and 2 $\mu$s in water.[256] The relationship is related to the ability of the solvent to absorb at 7880 and 6280 $cm^{-1}$ (1269 and 1592 nm respectively), which correspond to O-H and C-H vibrations.[256] These vibrational energies also correspond to the 0-0 and 0-1 emission transitions of $^1O_2$. The stronger the solvent absorbs in these regions, the more $^1O_2$ emission is quenched. The quenching described by Merkel *et al.* could rationalise the absence of the $^1O_2$ peak in rhenium DMSO and water solutions.

Production of $^1O_2$ in a biological environment is always going to be an issue for triplet state emitters (as discussed in 1.3.1.1), such as these Re(I) phosphorescent complexes. Further studies are required to understand the extent of $^1O_2$ production and the damage caused herein. During most imaging experiments no obvious phototoxic effects were observed and it was only when the sample was continually irradiated that damage was observed. Therefore, the neutral Re(I) complexes, *fac*-[Re(**phen**)$(CO)_3$(**Tph**)] (**11**) and *fac*-[Re(**phen**)$(CO)_3$(**Tbz**)] (**13**) still show potential to be investigated as optical

imaging agents. However, these complexes also demonstrate the ability to become phototoxic under certain conditions.

**Photodynamic Therapy**

Photodynamic therapy is still a fairly new procedure that is used in the treatment of cancerous tumours.[259] It involves the administration of a photosensitising agent which, to avoid side effects, must be non-toxic in the dark.[260] This agent is then irradiated with a specific wavelength of light which, through a series of photochemical, photophysical and photobiological processes (including the generation of $^1O_2$ ), causes cytotoxic damage.[261] Selectivity comes from the ability of the photosensitiser to localise in specific tumour cells and also from the targeted delivery of light.[260] The phosphorescent Re(I) metal complexes, *fac*-[Re(**phen**)$(CO)_3$(**Tph**)] (**11**) and *fac*-[Re(**phen**)$(CO)_3$(**Tbz**)] (**13**) are cytotoxic upon continuous irradiation with 405 nm light. These rhenium complexes show potential to be further explored as mulitmodal agents combining imaging and phototherapeutics.

### 5.3.3 Imaging of *fac*-[Re**(phen)**$(CO)_3$**(TphCH$_3$)]$^+$ (31) and *fac*-[Re(phen)$(CO)_3$(TbzCH$_3$)]$^+$(33)**

#### 5.3.3.1 Anion Exchange

The methylated rhenium complexes *fac*-[Re(**phen**)$(CO)_3$(**TphCH$_3$**)]$^+$ (**31**) and *fac*-[Re(**phen**)$(CO)_3$(**TbzCH$_3$**)]$^+$(**33**) were used in cellular experiments as a direct comparison to their neutral analogues. As described in Chapter Four, the methylated complexes were isolated as their $PF_6^-$ salts (exchanged from $CF_3SO_3^-$). For biological applications this anion may not be optimal in terms of size and solubility. Water solubility could potentially be improved by exchanging the $PF_6^-$ counter ion for $Cl^-$. The smaller anion may also improve cellular uptake.[262]

Anion exchange was trialled using a DOWEX®-Cl mesh column.[263]
*fac*-[Re(**phen**)$(CO)_3$(**TphCH$_3$**)]$^+$ (**31**) was passed through a DOWEX®-Cl column and an NMR taken of the product. Interestingly, instead of observing the expected two sets of rhenium signals (see section 4.3.3 on page 128) there appeared to be a third

system present. Separation of this mixture was attempted using acidic alumina-filled column chromatography. IR and NMR suggested that the first product eluted was *fac*-[Re(**phen**)$(CO)_3$(Cl)] (**7**). The IR spectrum showed two intense CO stretches at 2013 and 1861 $cm^{-1}$matching with **7** (see section 2.5.2.2 on page 66). The $^1$H NMR spectrum also matched well with previously synthesised *fac*-[Re(**phen**)$(CO)_3$(Cl)] (**7**) as shown in Figure 5.17. There also appears to be excess free methylated tetrazole ligand present in the NMR. The second product collected from the acidic alumina column still showed the presence of three rhenium systems.

Based on these preliminary experiments it was concluded that the DOWEX®-Cl mesh column was not appropriate to exchange the $PF_6^-$counter ion for $Cl^-$. The tetrazole ligand appears to be exchanging for the chloro as well as or instead of the $PF_6^-$ anion. This is not unexpected due to the lability of the methylated tetrazole ligand, discussed in Chapter Four. The complexes were therefore left with the $PF_6^-$ counter ion for imaging experiments.

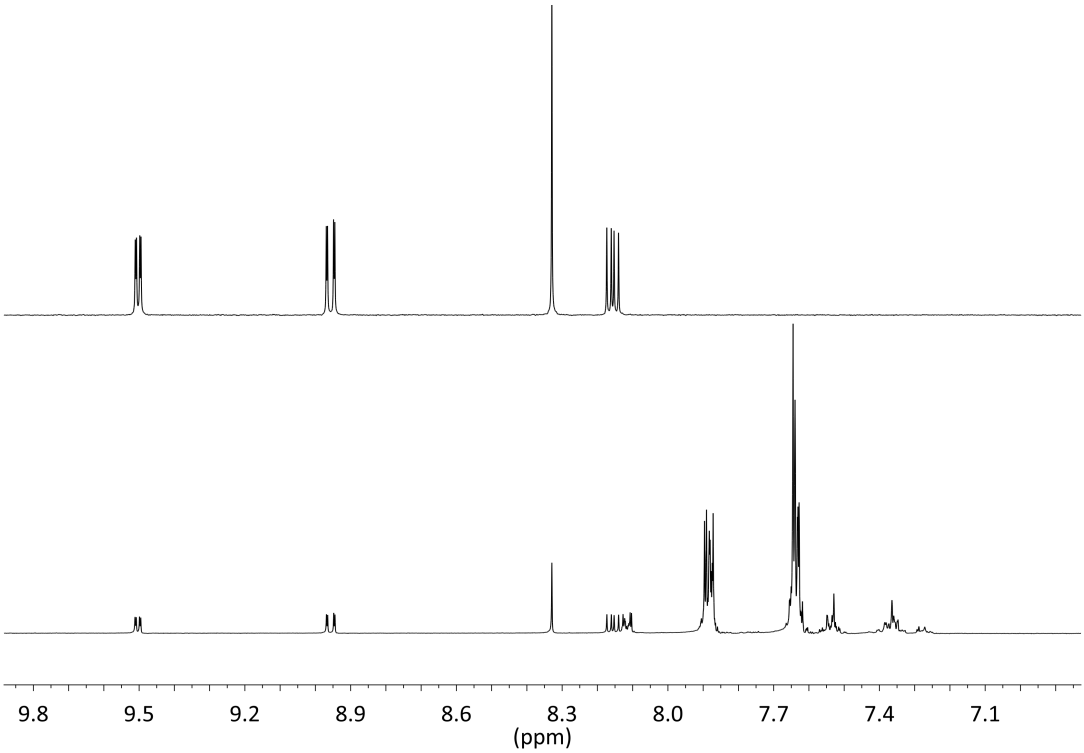


Figure 5.17: NMR of *fac*-[Re(**phen**)$(CO)_3$(**Cl**)] (top) and fraction one recovered from the acidic alumina column (bottom), in acetone-$d_6$.

### 5.3.3.2 Confocal Imaging and Spectral Detection

HeLa cells were incubated under standard conditions with *fac*-[Re(**phen**)$(CO)_3$(**TphCH$_3$**)]$^+$ (**31**) and *fac*-[Re(**phen**)$(CO)_3$(**TbzCH$_3$**)]$^+$(**33**) to final concentrations of 20 $\mu$M and 0.4% (v/v) DMSO, for one to two hours before imaging. The same general imaging conditions used for the neutral Re(I) complexes were employed. Interestingly, no obvious luminescence signal was observed in HeLa cells incubated with either **31** or **33**.

It was hypothesised that there could be some ligand reactivity or exchange process occurring due to the labile nature of the methylated tetrazolato ligand. Temperature dependent NMR experiments carried out in Chapter Four revealed that at 40 ºC the cationic Re(I) complexes start to undergo ligand exchange with coordinating solvents (see Figure 4.8 on page 133). *fac*-[Re(**phen**)$(CO)_3$(**TphCH$_3$**)]$^+$ (**31**) in DMSO-$d_6$ was heated at 37 ºC (incubation conditions) and analysed by NMR at various time intervals, as shown in Figure 5.18.

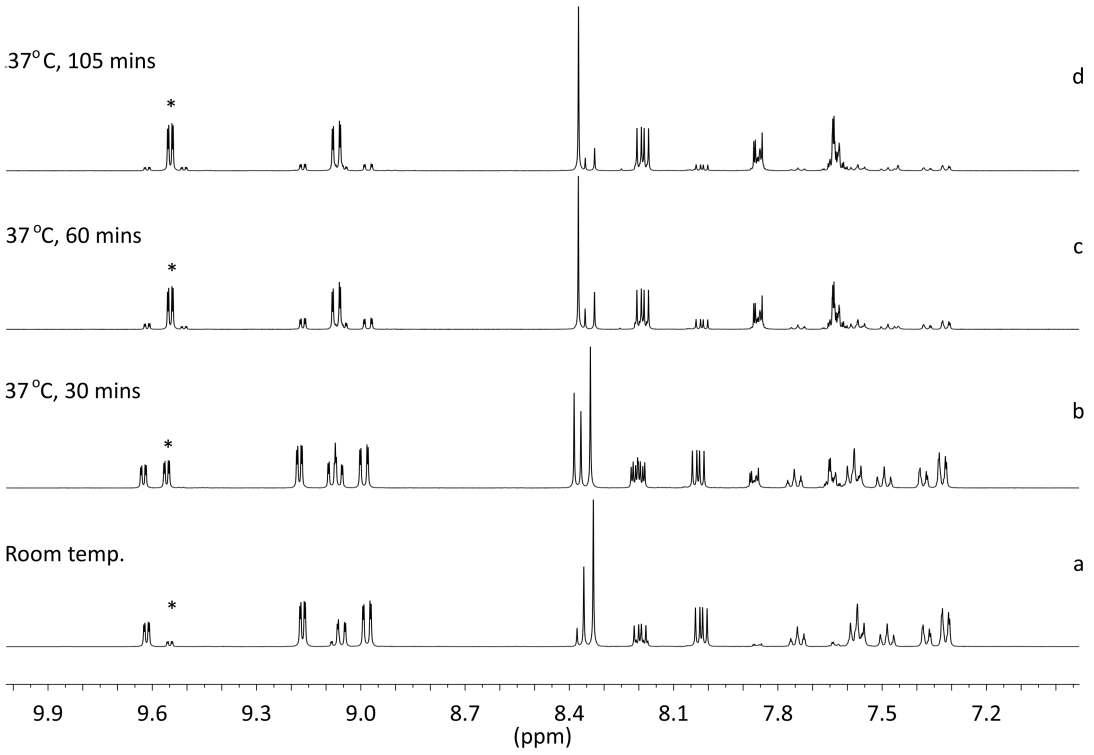


Figure 5.18: $^1$H NMR spectrum of *fac*-[Re(**phen**)$(CO)_3$(**TphCH$_3$**)]$^+$ (**31**) at room temperature (a) and after being heated at 37 ºC for 30 minutes (b), 60 minutes (c) and 105 minutes (d) in DMSO-$d_6$.

After 60 minutes of heating at 37 ºC in DMSO-$d_6$, the DMSO solvate (identified by

the * in Figure 5.18) was the main complex present. It is therefore likely that in cell culture media at 37 ºC the ligand could start exchanging with compounds or even water present in cellular media. The solvato complex is even present at room temperature (Figure 5.18). Nonetheless live cell imaging experiments were attempted at room temperature as ligand exchange seemed to occur slower than at 37 ºC.

The cultured HeLa cells and media were stabilised at room temperature after which *fac*-[Re(**phen**)$(CO)_3$(**TphCH$_3$**)]$^+$ (**31**) was added to achieve a final concentration of 20 $\mu$M and 0.4% (v/v) DMSO. Cells with the complex were allowed to sit at room temperature for 90 minutes before imaging. Some signal was detected inside HeLa cells however it was very weak compared to the signal produced by the analogous neutral complex *fac*-[Re(**phen**)$(CO)_3$(**Tph**)] (**11**). Localisation was mainly observed in the perinuclear region of cells with a focal appearance. A weak diffuse signal was also detected, as illustrated in Figure 5.19. HeLa cells shown in Figure 5.19 A, do not show any signs of phototoxicity and cellular morphology is consistent with the control/blank samples (also at room temperature). This indicates that the complexes were non-toxic towards HeLa cells within the parameters used during these imaging experiments.

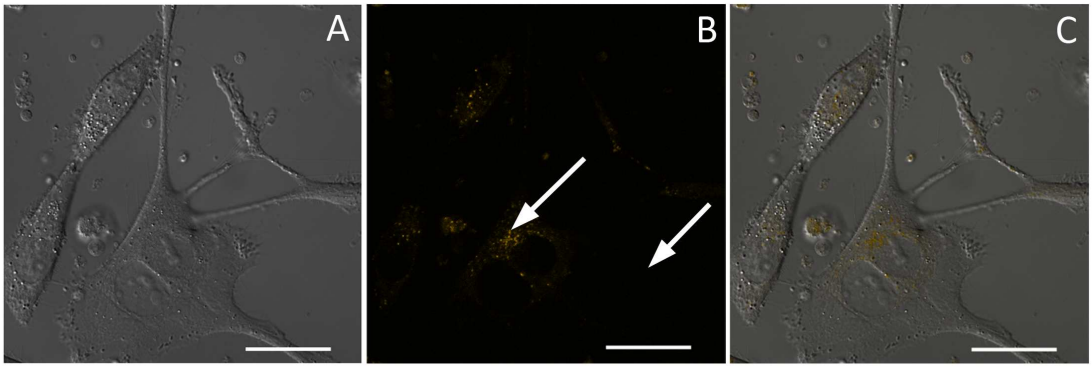


Figure 5.19: HeLa cells incubated with *fac*-[Re(**phen**)$(CO)_3$(**TphCH$_3$**)]$^+$ (**31**). DIC (A) shows the structural integrity of the cells. Fluorescence (B) and merged (C) images illustrate the weak signal observed in the perinuclear regions of HeLa cells incubated with **31**. White arrows show areas in which ROIs were selected for spectral analysis. Scale bar, 25 $\mu$m.

*fac*-[Re(**phen**)$(CO)_3$(**TbzCH$_3$**)]$^+$(**33**) was added to HeLa cells in the same way as described above (for complex **31**). Similar results were observed. Figure 5.20 shows a weak signal apparent in the perinuclear/cytoplasmic region of cells. The apparent brighter signal of **33** compared to **31** could be attributed to the increased gain

settings used during image acquisition. Based on the morphology of the cells, *fac*-[Re(**phen**)$(CO)_3$(**TbzCH$_3$**)]$^+$(**33**) appears to be non-toxic toward HeLa cells during the imaging experiments.

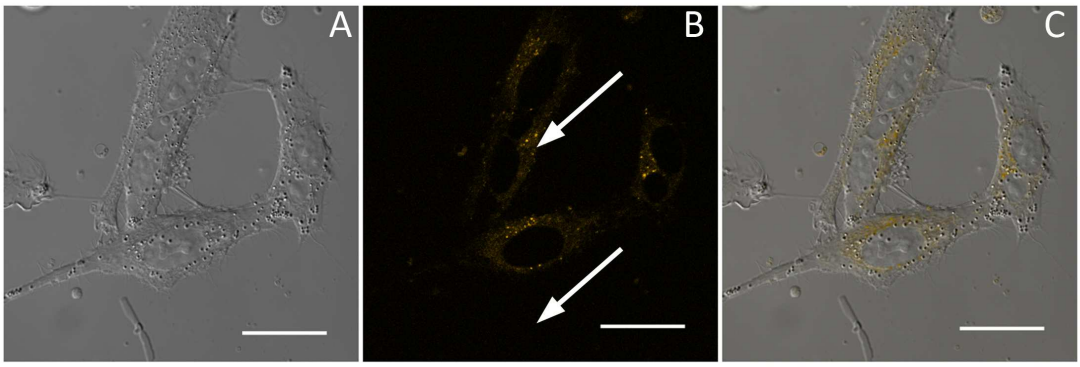


Figure 5.20: HeLa cells incubated with *fac*-[Re(**phen**)$(CO)_3$(**TbzCH$_3$**)]$^+$(**33**). DIC (A) illustrates the structural integrity of the HeLa cells where the fluorescence (B) and merged (C) images show the weak signal observed in the perinuclear regions of HeLa cells incubated with **33**. White arrows show areas in which ROIs were selected for spectral analysis. Scale bar, 25 $\mu$m.

Confocal images of HeLa cells containing no complex were collected under the same conditions used for **31**. Some autofluorescent signal was observed for blank cells however it appeared weaker than the signal detected for HeLa cells containing **31**. To confirm the signal from cell incubated with **31** or **33** was originating from a Re(I) species, spectral imaging was trialled. Unfortunately, spectral imaging was unsuccessful due to the very weak signal intensity from both blank and experimental cells.

It was also hypothesised that the low signal intensity from cells incubated with **31** or **33** may have been due to low molar absorptivity of *fac*-[Re(**phen**)$(CO)_3$(**TphCH$_3$**)]$^+$(**31**) and *fac*-[Re(**phen**)$(CO)_3$(**TbzCH$_3$**)]$^+$(**33**) at 405 nm. Molar absorptivity directly relates to the probability of a complex absorbing light (absorption cross section). As discussed in Chapter Four, methylated Re(I) complexes have blue shifted absorbances therefore their absorbance cross section at 405 nm may be reduced compared to the neutral analogues. Molar absorptivity values for both neutral and methylated Re(I) complexes in DCM are presented in Table 5.3.1. The absorbance cross sections are comparable between the neutral and methylated species. Therefore, a low absorbance cross section at 405 nm is unlikely to be the reason that signal from *fac*-[Re(**phen**)$(CO)_3$(**TphCH$_3$**)]$^+$(**31**) and *fac*-[Re(**phen**)$(CO)_3$(**TbzCH$_3$**)]$^+$ (**33**) in HeLa cells is extremely weak.

Table 5.3.1: Molar Absorptivity (L $mol^{-1}$ $cm^{-1}$) for Re(I) complexes at 405 nm.

| Rhenium Complex | Molar Absorptivity at 405 nm (L $mol^{-1}$ $cm^{-1}$) |
|---|---|
| *fac*-[Re(**phen**)$(CO)_3$(**Tph**)] (**11**) | 2555 |
| *fac*-[Re(**phen**)$(CO)_3$(**Tbz**)] (**13**) | 2375 |
| *fac*-[Re(**phen**)$(CO)_3$(**TphCH$_3$**)]$^+$(**31**) | 3701 |
| *fac*-[Re(**phen**)$(CO)_3$(**TbzCH$_3$**)]$^+$ (**33**) | 1696 |

Reference spectra of the methylated rhenium complexes, *fac*-[Re(**phen**)$(CO)_3$(**TphCH$_3$**)]$^+$ (**31**) and *fac*-[Re(**phen**)$(CO)_3$(**TbzCH$_3$**)]$^+$(**33**) in DMSO were measured on the microscope and the spectral profiles are shown in Figure 5.21. The collection of these

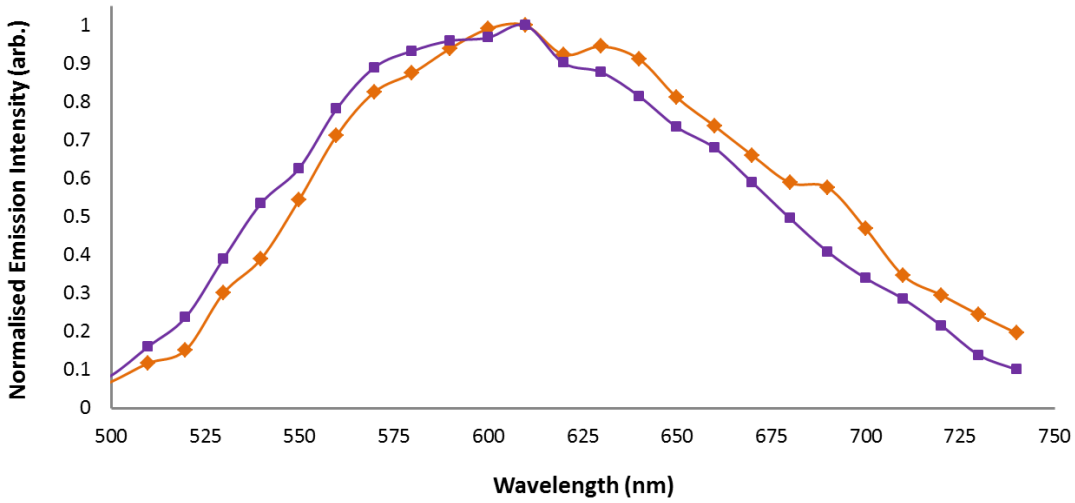


Figure 5.21: Spectral detection emission profiles measured from DMSO solutions of *fac*-[Re(**phen**)$(CO)_3$(**TphCH$_3$**)]$^+$ (**31**, purple) and *fac*-[Re(**phen**)$(CO)_3$(**TbzCH$_3$**)]$^+$(**33**, orange).

profiles illustrate that the 405 nm laser is able to sufficiently excite the complexes to produce a detectable signal. The low signal intensity observed *in vitro* could be due to poor cellular uptake and/or that the identity of the methylated Re(I) complexes are significantly changing upon incubation. If the structure of the complexes is altered the photophysical properties, including $\lambda_{ex}$ and $\lambda_{em}$ are likely to change.

From these preliminary experiments, it is clear that *fac*-[Re(**phen**)$(CO)_3$(**TphCH$_3$**)]$^+$ (**31**) and *fac*-[Re(**phen**)$(CO)_3$(**TbzCH$_3$**)]$^+$(**33**) do not show potential for further investigation as optical imaging agents. The complexes are unstable in solution, even at room temperature. The lability of the ligand could be causing structural alterations to

the complexes once incubated into HeLa cells. Although these complexes are highly emissive compared to their neutral analogues, their lack of stability makes them unsuitable to be used in a biological context.

### 5.3.4 Imaging of *fac*-[Re(**phen-RS**)$(CO)_3$**(**Cl**)] (39) and *fac*-[Re(**phen-S-PEG**)$(CO)_3$**(**Cl**)] (40)**

Imaging experiments were carried out on *fac*-[Re(**phen-RS**)$(CO)_3$(Cl)] (**39**) and *fac*-[Re(**phen-S-PEG**)$(CO)_3$(Cl)] (**40**). These complexes were synthesised as precursors to the final tetrazolato complex, *fac*-[Re(**phen-S-PEG**)$(CO)_3$(**Tph**)] (**41**), (section 5.3.5). Live HeLa cell imaging experiments were performed to assess if altering the ancillary ligand and/or functionalising the diimine group would effect the behaviour of rhenium complexes in a biological environment.

#### 5.3.4.1 Confocal Imaging and Spectral Detection

*fac*-[Re(**phen-RS**)$(CO)_3$(Cl)] (**39**) and *fac*-[Re(**phen-S-PEG**)$(CO)_3$(Cl)] (**40**) were incubated with HeLa cells to a final concentration of 20 $\mu$M and 0.4% (v/v) DMSO for 90-120 minutes under standard culture conditions (as outlined in section 5.2.1 on page 172). Figure 5.22 shows confocal images of HeLa cells incubated with **39** (images A-C) and **40** (images D-F).

HeLa cells show uptake of the complexes with an apparent cytoplasmic localisation for both **39** and **40**. Again, the localisation was very diffuse and therefore it is unclear if specific organelles are preferentially targeted. The localisation of **39** and **40** appears similar to *fac*-[Re(**phen**)$(CO)_3$(**Tph**)] (**11**) and *fac*-[Re(**phen**)$(CO)_3$(**Tbz**)] (**13**), discussed in section 5.3.2. The main difference observed was the signal strength. Under the same imaging conditions, complexes containing the chloro ancillary ligand appeared to show a weaker signal in the cytoplasm compared to **11** and **13**. The molar absorptivity of **39** and **40** at 405 nm (3378 and 4136 L $mol^{-1}$ $cm^{-1}$ respectively) are in fact comparable to **11** and **13** (see Table 5.3.1). Again, these measurements are in DCM and could be different in aqueous solvents. DIC images in Figure 5.22 illustrate that the majority of cells in culture have morphological structure comparable

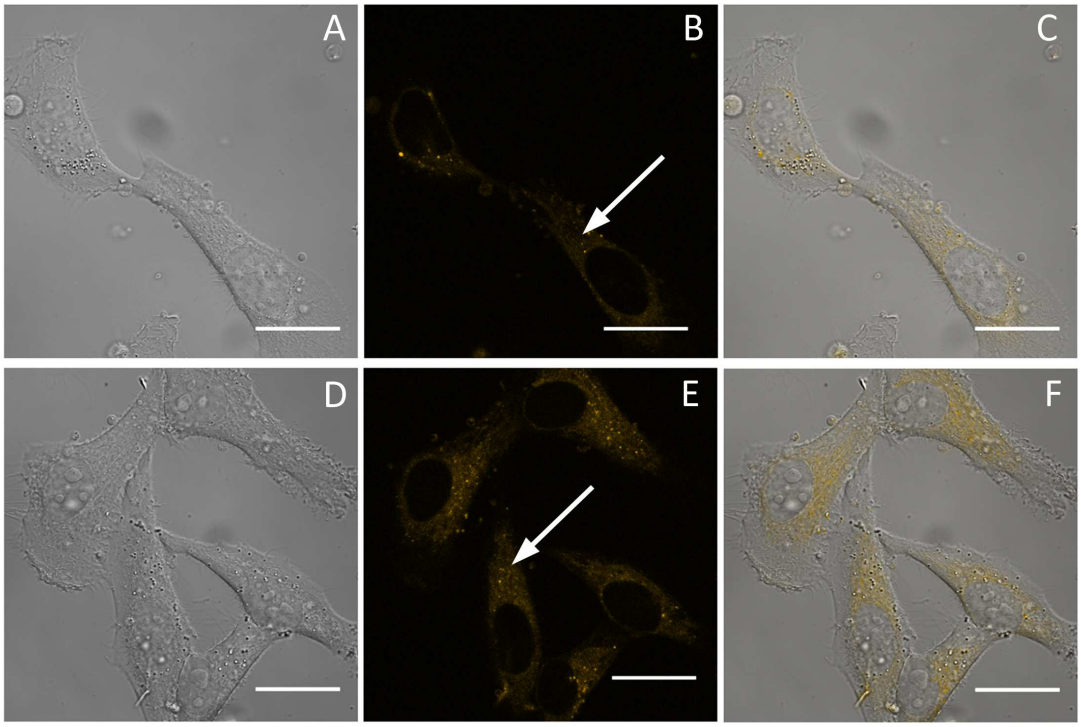


Figure 5.22: HeLa cells incubated with *fac*-[Re(**phen-RS**)$(CO)_3$(Cl)] (**39**, images A-C) and *fac*-[Re(**phen-S-PEG**)$(CO)_3$(Cl)] (**40**, images D-F). DIC (A and D) images show the structural integrity of cells where fluorescence (B and E) and merged (C and F) images illustrate the uptake and cytoplasmic localisation of HeLa cells. Scale bar, 25 $\mu$m.

to the (DMSO) control and blank cells. They do not appear to be showing signs of stress, indicating the non-toxic nature of *fac*-[Re(**phen-RS**)$(CO)_3$(Cl)] (**39**) and *fac*-[Re(**phen-S-PEG**)$(CO)_3$(**Cl**)] (**40**) during imaging experiments.

To further confirm the observed signal was originating from *fac*-[Re(**phen-RS**)$(CO)_3$(Cl)] (**39**) or *fac*-[Re(**phen-S-PEG**)$(CO)_3$(Cl)] (**40**) and not simply from autofluorescence/noise, spectral imaging was carried out. Firstly, DMSO stock solutions of **39** and **40** were measured as a reference. The spectra are shown in Figure 5.23 and have an expected broad Gaussian shape, with maxima just above 600 nm.

Figure 5.24 shows the spectral profiles collected from circular ROIs (approximately 7 $\mu$m diameter) inside HeLa cells incubated with **39** and **40**. The ROIs were located in areas indicated by the white arrows in Figure 5.22 B and E. The emission profiles collected *in vitro* are comparable with the reference DMSO solutions.

There was a significant difference in the profiles measured from regions of interest inside the cytoplasm and in the extracellular space.

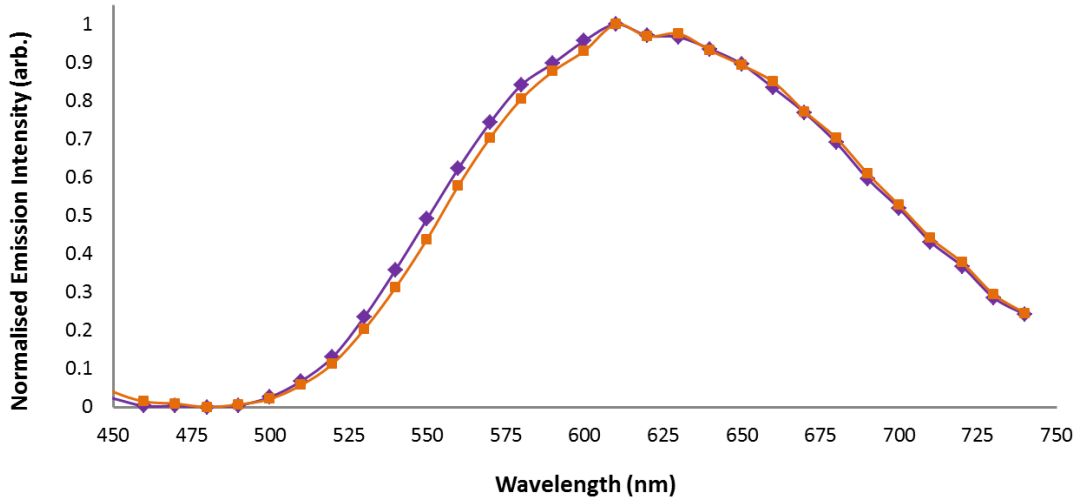


Figure 5.23: Spectral detection emission profiles measured from DMSO solutions of *fac*-[Re(**phen-RS**)$(CO)_3$(Cl)] (**39**, purple) and *fac*-[Re(**phen-S-PEG**)$(CO)_3$(Cl)] (**40**, orange).

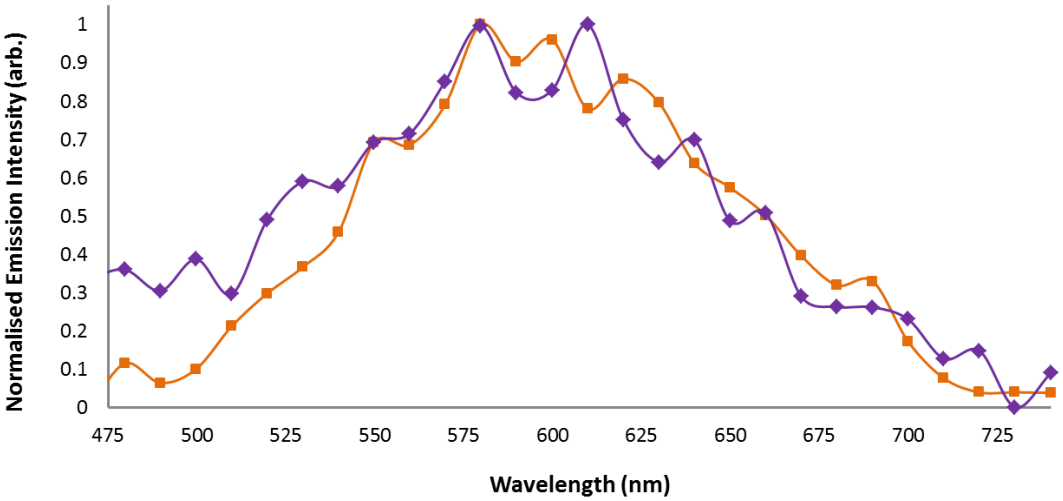


Figure 5.24: Spectral detection emission profile taken from inside HeLa cells incubated with *fac*-[Re(**phen-RS**)$(CO)_3$(Cl)] (**39**, purple) and *fac*-[Re(**phen-S-PEG**)$(CO)_3$(Cl)] (**40**, orange).

The spectra lost its Gaussian-like shape and a significant reduction in intensity was observed. Although the observed signal from HeLa cells incubated with **39** and **40** is relatively weak, spectral analysis suggests that both complexes are taken into HeLa cells and localise in the cytoplasm.

It does not appear that modifications on the diimine ligand or the change in ancillary ligand is having a significant effect on the localisation of Re(I) complexes in HeLa cells. One difference observed for *fac*-[Re(**phen-RS**)$(CO)_3$(Cl)] (**39**) and *fac*-[Re(**phen-S-PEG**)$(CO)_3$(Cl)] (**40**) is that the signal detected in the cytoplasmic region of HeLa cells is weaker compared to the two Re(I) complexes discussed in section 5.3.2. This could be an indication of reduced cellular uptake which may be rationalised by their low lipophilicity in comparison to rhenium *tetrazolato* complexes (see section **??** on page ??). The weaker signal observed for the chloro complexes (compared to the tetrazolato) could also be rationalised by their relatively lower quantum yield.

### 5.3.5 Imaging of *fac*-[Re(**phen-S-PEG)**$(CO)_3$(**Tph**)] **(41)**

Motivation behind the synthesis of *fac*-[Re(**phen-S-PEG**)$(CO)_3$(**Tph**)] (**41**) was to improve water solubility compared to the unsubstituted rhenium phenanthroline analogue. Improved water solubility may facilitate reduced DMSO concentrations during cell culture. As discussed in Chapter Five (section **??** on page ??), the small PEG chain was of insufficient length to modify the lipophilicity of the complexes. Nonetheless, **41** was analysed in HeLa cells.

#### 5.3.5.1 Confocal Imaging and Spectral Detection

HeLa cells were incubated with **41** to a final concentration of 20 $\mu$M and 0.4% (v/v) DMSO, for 40 minutes before imaging. Confocal imaging illustrates uptake of **41** into HeLa cells, resulting in a diffuse cytoplasmic localisation. Figure 5.25 A-C shows the DIC, fluorescence and merged images. In the fluorescence image, small bright spots within the cytoplasm are observed. This could be indicative of preferential organelle localisation (eg: lysosomes or mitochondria) however further experiments would be

required to confirm this. The signal from **41** in HeLa cells does appear stronger, compared to many of the other Re(I) complexes imaged herein. This might be rationalised by the molar absorptivity calculated for *fac*-[Re(**phen-S-PEG**)$(CO)_3$(**Tph**)] (**41**) at 405 nm (in DCM). The value is 6936 $Lmol^{-1}cm^{-1}$, which corresponds to the highest absorption cross section out of all complexes studied in HeLa cells. The morphology and overall appearance of cells shown in Figure 5.25 A, is comparable to the control/blank cells. This is suggestive of the non-toxic nature of **41** in HeLa cells during the incubation period and at the time of imaging.

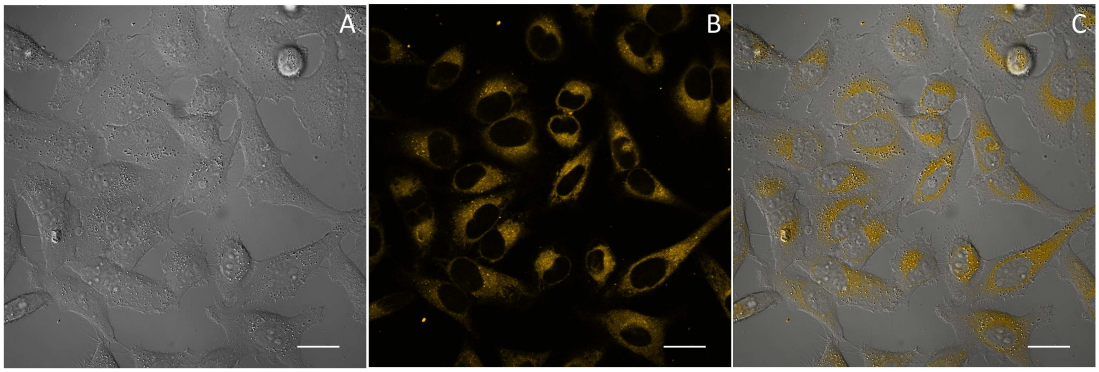


Figure 5.25: HeLa cells incubated with *fac*-[Re(**phen-S-PEG**)$(CO)_3$(**Tph**)] (**41**). DIC image (A) shows the structural integrity of HeLa cells where the fluorescence (B) and merged (C) images illustrate the uptake and cytoplasmic localisation of the **41** in HeLa cells. Scale bar, 25 $\mu$m.

Spectral imaging was used to probe the identity of the emitting species localised inside the cytoplasm of the HeLa cells. First, as a reference, the DMSO stock solution of *fac*-[Re(**phen-S-PEG**)$(CO)_3$(**Tph**)] (**41**) was placed into a MatTek dish and a spectral image was recorded. Spectral analysis produced the profile shown in Figure 5.26. The broad structureless emission with a maximum around 590 nm is expected, based on the photophysical characterisation of **41** carried out in Chapter Five, section **??**.

The same HeLa cells incubated with *fac*-[Re(**phen-S-PEG**)$(CO)_3$(**Tph**)] (**41**) were used to collect spectral images. The white arrow in Figure 5.27 indicates the area where a circular ROI (approximately 7 $\mu$m diameter) was positioned for spectral analysis. This particular ROI gave the profile shown in Figure 5.28. Upon moving the ROI to other parts of the cytoplasm where signal was observed, a similar spectrum was always generated with the emission maximum around 575 nm, comparable to that of the DMSO reference, Figure 5.26.

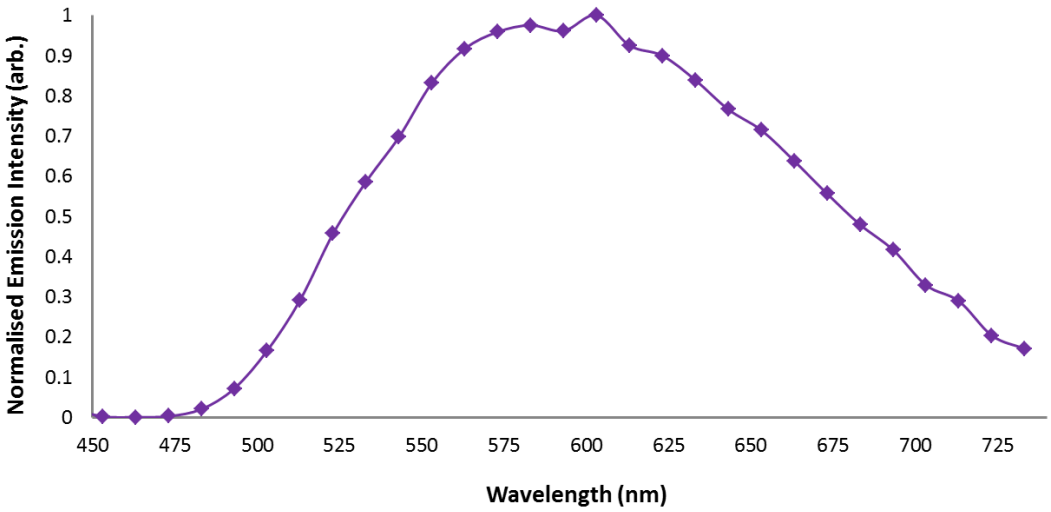


Figure 5.26: Spectral detection emission profile measured from a DMSO solution of *fac*-[Re(**phen-S-PEG**)$(CO)_3$(**Tph**)] (**41**).

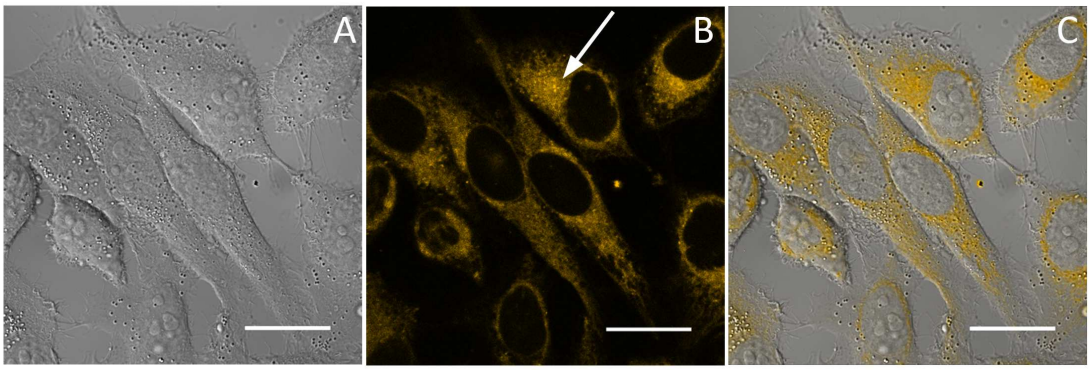


Figure 5.27: HeLa cells incubated with *fac*-[Re(**phen-S-PEG**)$(CO)_3$(**Tph**)] (**41**). DIC (A), fluorescence (B) and merged (C) images. The white arrow shows the area in which a ROIs was selected for spectral analysis. Scale bar, 25 $\mu$m.

When comparing the profile collected *in vitro* (Figure 5.28) to that of the DMSO reference (Figure 5.26), a slight blue shift in the maximum is observed. This can again be rationalised by the change in solvent. When the ROI was moved to a location in the extracellular space, the spectral profile reduced in intensity, lost the Gaussian-like shape and therefore did not resemble typical Re(I) emission.

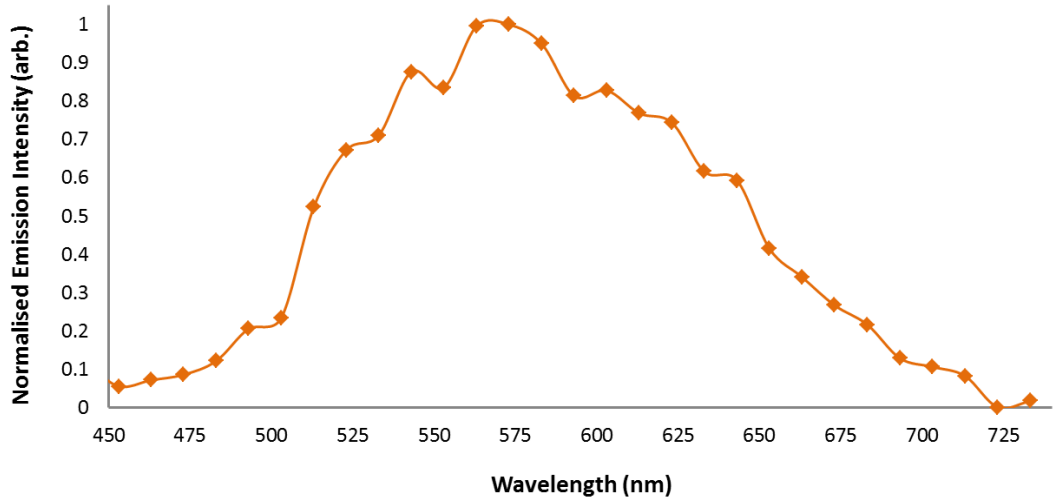


Figure 5.28: Spectral detection emission profile measured from the cytoplasm of HeLa cells incubated with *fac*-[Re(**phen-S-PEG**)$(CO)_3$(**Tph**)] (**41**).

#### 5.3.5.2 Photoinduced Cytotoxicity

During live imaging of HeLa cells incubated with *fac*-[Re(**phen-S-PEG**)$(CO)_3$(**Tph**)] (**41**), phototoxicity was observed. For the other rhenium complexes, phototoxicity was only observed during continuous illumination. This was also observed for HeLa cells incubated with *fac*-[Re(**phen-S-PEG**)$(CO)_3$(**Tph**)] (**41**). However, cytotoxicity was also observed when multiple images were taken of the same area, even with breaks/recovery time between each image.

Time lapse imaging was carried out to confirm this phototoxic effect. HeLa cells were

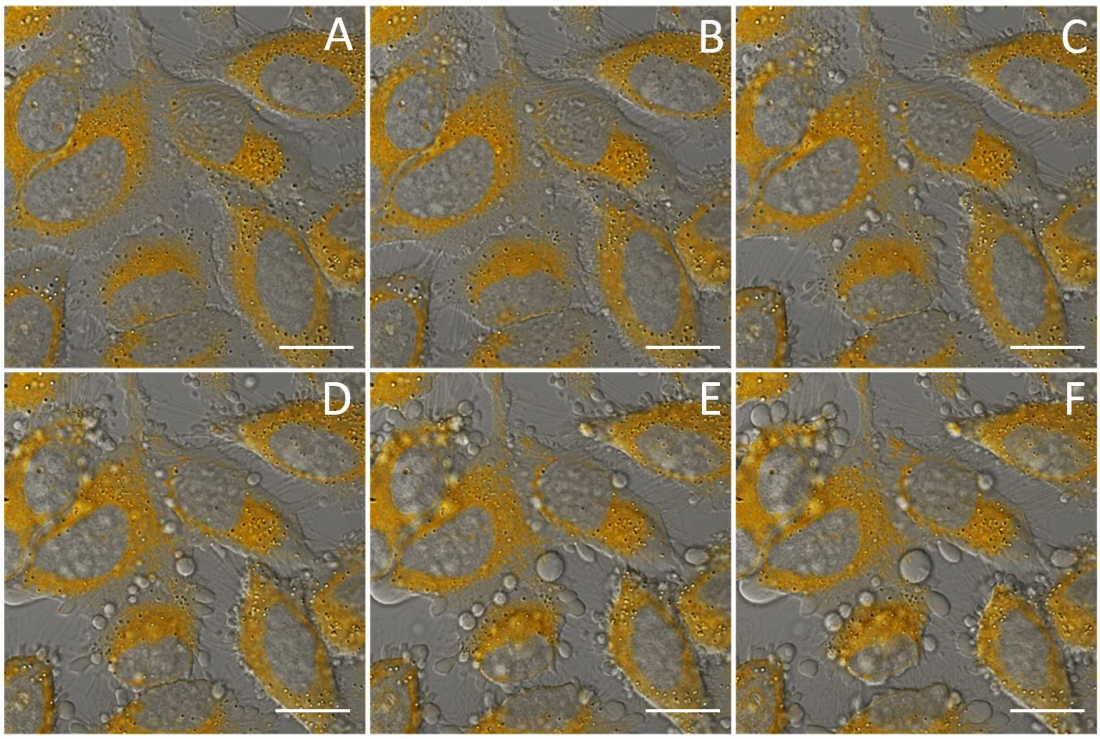


Figure 5.29: Merged DIC and confocal fluorescence images from a five minute time lapse experiment of HeLa cells incubated with *fac*-[Re(**mercaptophenPEG**)$(CO)_3$(**Tph**)] (**41**). An image was taken every 30 seconds for five minutes and the images shown were taken at t=0 (A), t=1 min (B), t=2 min (C), t=3 min (D), t=4 min (E) and t=5 min (F). Blebs are apparent at t=2 min (C). Scale bar, 25 $\mu$m.

incubated with 20 $\mu$M of *fac*-[Re(**phen-S-PEG**)$(CO)_3$(**Tph**)] (**41**) with a 0.4% (v/v) DMSO concentration. After incubation for one hour, the time lapse experiment was started. The laser power and gain settings were all consistent with the images taken previously for this and other rhenium complexes. Imaging was carried out over five minutes with a single image captured every 30 seconds. The progress of images are

shown in Figure 5.29. After two minutes, corresponding to a total of five scans, (Figure 5.29 C) cells start to show a stress response. This is slower than when cells are continually illuminated, where a stress response is observed after only one minute. The slower phototoxic effect during time lapse imaging can be ascribed to the recovery time cells have between each image acquisition when the cells are not illuminated. Despite this recovery time, HeLa cells still suffered from phototoxicity after the acquisition of five images. Cells started to round up with some small membrane blebs observed. These observations are consistent with phototoxicity.[264] At completion of the time lapse experiment, nearly all of the cells in view had blebs present and many of them had completely rounded up. The stress response exhibited by cells was again ascribed to the production of singlet oxygen. Further experiments would need to be carried out to determine the exact cause of the stress response but as discussed in section 5.3.2.4, these type of Re(I) species emit from the triplet state and can generate singlet oxygen in solution. The NIR emission spectra of *fac*-[Re(**phen-S-PEG**)$(CO)_3$(**Tph**)] (**41**) in DCM was measured. A peak is observed at 1274 nm (Figure 5.30), corresponding to

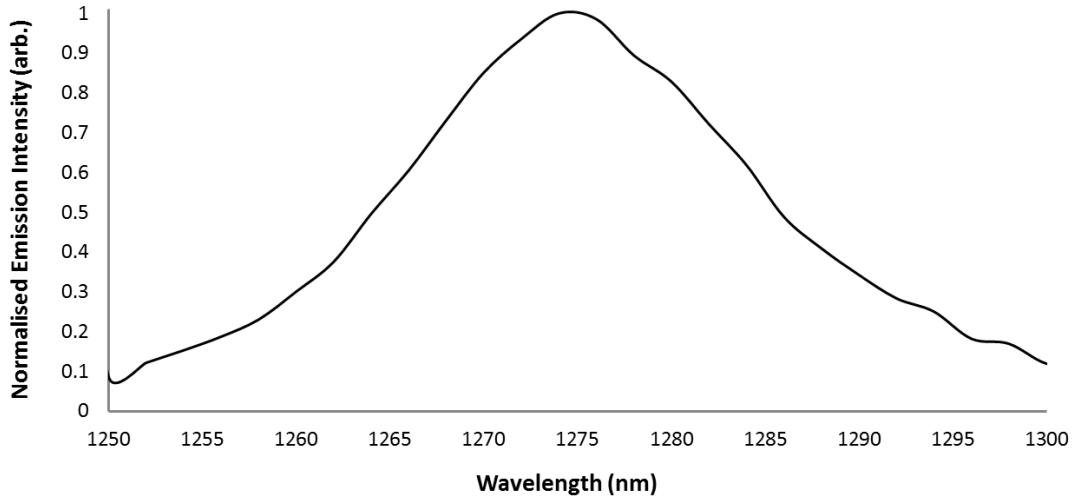


Figure 5.30: Near infrared emission spectra of *fac*-[Re(**phen-S-PEG**)$(CO)_3$(**Tph**)] (**41**) in DCM.

$^1O_2$. As the complexes show uptake into the cells, it is not unlikely that the production of this cytotoxic species ($^1O_2$) would cause an apoptotic response.

The same time lapse settings were used on a dish of HeLa cells where no complex was added. This was done as a control to gauge if the cause of the cells distress was the complex. The images shown in Figure 5.31 are from scans taken at time zero

(A), 2 min 30 sec (B) and 5 min (C). These cells do not illustrate any morphological changes over time suggesting that **41** is likely playing a direct role in causing the HeLa cells to bleb and round up upon illumination. These observations are consistent with continuous illumination effects shown in section 5.3.2.4.

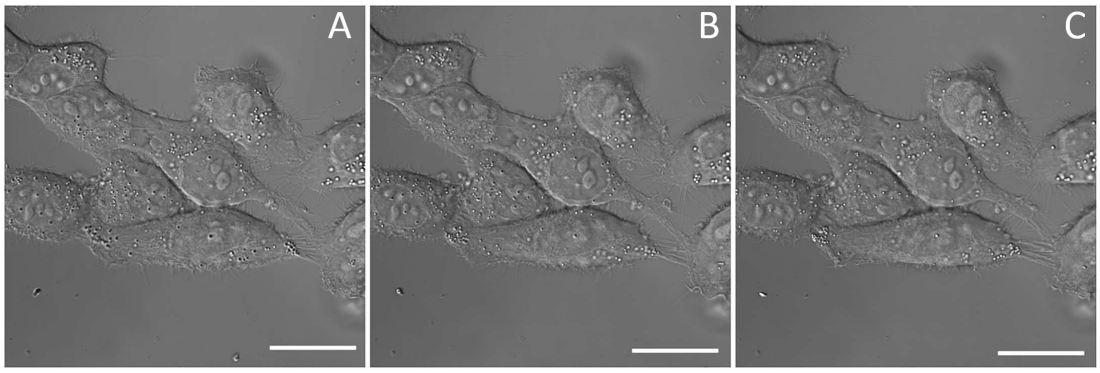


Figure 5.31: DIC images from a five minute time lapse of HeLa cells without any rhenium complex or DMSO additives. Images were acquired every 30 seconds for five minutes. DIC images show the structural integrity of HeLa cells where: t=0 (A), t=2.5 min (B) and t=5 min (C). Scale bar, 25 $\mu$m.

Time lapse experiments were also carried out on cells incubated with *fac*-[Re(**phen**)$(CO)_3$(**Tph**)] (**11**), *fac*-[Re(**phen**)$(CO)_3$(**Tbz**)] (**13**), *fac*-[Re(**phen-RS**)$(CO)_3$(**Cl**)] (**39**) or *fac*-[Re(**phen-S-PEG**)$(CO)_3$(**Cl**)] (**40**). For each of these experiments phototoxic effects, with bleb formation were observed. However, the response was slower and less pronounced compared to **41**. This could be attributed to a greater uptake of *fac*-[Re(**phen-S-PEG**)$(CO)_3$(**Tph**)] (**41**) into the HeLa cells compared to the other complexes or simply a greater production of $^1O_2$. Further experiments are required to completely understand the different phototoxic effects exhibited by each of the complexes. All of the neutral Re(I) complexes studied in HeLa cells are phototoxic upon extended illumination, however it appears that *fac*-[Re(**phen-S-PEG**)$(CO)_3$(**Tph**)] (**41**) is having the greatest phototoxic effect.

As seen with many of the Re(I) complexes studied in this Chapter, *fac*-[Re(**phen-S-PEG**)$(CO)_3$(**Tph**)] (**41**) shows potential as an imaging agent however its phototoxic nature could lead to potential applications as a multi-modal luminescent imaging and phototherapeutic agent.

## 5.4 Conclusion

Neutral Re(I) tetrazolato complexes, *fac*-[Re(**phen**)$(CO)_3$(**Tph**)] (**11**), *fac*-[Re(**phen**)$(CO)_3$(**Tbz**)] (**13**) and *fac*-[Re(**phen-S-PEG**)$(CO)_3$(**Tph**)] (**41**), showed cellular uptake and exhibited a diffuse perinuclear localisation in HeLa cells without apparent localisation to any particular organelles. Spectral imaging and analysis of cells incubated with the Re(I) complexes confirmed the signal observed in the cytoplasm, was originating from the Re(I) species. Further investigation could employ techniques such as ICP-MS and/or GF-AAS to quantify the uptake of Re(I) complexes in HeLa cells.

Apparent toxicity of the Re(I) complexes is very dependent on imaging protocol. When taking multiple images over extended time periods with breaks between each scan, the cells appeared to resemble the morphology of those cells in the control and blank samples. Under these experimental conditions, the rhenium complexes are non-toxic. However, HeLa cells did exhibit an observable phototoxic response during acquisition of z-stacks, where the sample is illuminated, almost continuously. Phototoxicity was attributed to the excessive production of singlet oxygen, a cytotoxic species. The non-toxic nature of the Re(I) complexes observed during "normal" image acquisition can be ascribed to the significant recovery time the cells have between each scan.

Weak luminescent signals were identified in the perinuclear regions of HeLa cells incubated with *fac*-[Re(**phen-RS**)$(CO)_3$(**Cl**)] (**39**) and *fac*-[Re(**phen-S-PEG**)$(CO)_3$(**Cl**)] (**40**). This weaker signal could be attributed to reduced uptake of **39** and **40** which might be explained by the reduced lipophilicity of these complexes.

Methylated complexes *fac*-[Re(**phen**)$(CO)_3$(**TphCH$_3$**)]$^+$ (**31**) and *fac*-[Re(**phen**)$(CO)_3$(**TbzCH$_3$**)]$^+$(**33**) were originally designed to be highly emissive optical imaging labels. Uptake and localisation patterns were unclear as a luminescent signal was not detected and spectral analysis was unsuccessful due to the weak signal. These methylated Re(I) complexes were not stable enough to be utilised in a biological context.

Further studies using *fac*-[Re(**phen**)$(CO)_3$(**Tph**)] (**11**), *fac*-[Re(**phen**)$(CO)_3$(**Tbz**)] (**13**) and *fac*-[Re(**phen-S-PEG**)$(CO)_3$(**Tph**)] (**41**) are required to grasp their full potential as optical imaging agents.

## 5.5 Experimental

### 5.5.1 Cell Culture

Human cervical carcinoma cells, HeLa, (company, location) were cultured in DMEM cell medium (Gibco, Australia), 10% Fetal Bovine Serum (Gibco, Australia), and 1% penicillin-streptomycin at 37 °C under a 5% $CO_2$ atmosphere, in T75 culture flasks. When the cells were ready to be split for imaging, they were done so using 1 mL of trypsin (0.25 %) and seeded into 35 mm diameter MatTek glass bottom petri dishes for 24 hours before imaging, to give a cell confluency of 50-60% unless otherwise stated. DMSO solutions of the prepared complexes were added to 2 mL of culture media. This solution was then added to cell culture to give final concentrations of the rhenium complexes between 10-20 $\mu$M. The DMSO concentration for each experiment was 0.4-1% in culture media, as specified.

### 5.5.2 Confocal Imaging

All confocal imaging and spectral detection experiments were carried out on a Nikon Ti-E inverted motorised microscope with a Nikon A1Si confocal microscope system. Köhler alignment was carried out before each imaging experiment and differential interference contrast (DIC) imaging was always employed.

The Nikon A1Si confocal microscope system was equipped with four PMT detectors, a spectral detector and 50mW solid state lasers of the following wavelengths: 405 nm, 488 nm, 561 nm and 638 nm. The 405 nm laser was used for excitation and the images were collected in channels 2, 3 and 4 with spectral ranges of 500-550 nm, 570-620 nm and 633-738 nm respectively. For live cell imaging experiments, a Tokai Hit stage top incubation system was used, unless otherwise stated. Images were collected using a Nikon PlanApo 60× oil immersion objective (NA 1.4). In cases where spectral detection was carried out, 32-channel spectral images were collected using a 10 nm Si grating resolution and the 405 nm laser for excitation. All images were collected at a resolution of 0.21 $\mu$m/pixel (1024×1024 pixels) or 0.41$\mu$m/pixel (512×512 pixels).

#### 5.5.2.1 Image Processing

Confocal images were exported from the Nikon software NIS-Elements as 16 bit mono colour images. FIJI (ImageJ, http://fiji.sc/Fiji) was used to add channels 2, 3 and 4 together. The resultant image was imported into Adobe Photoshop and converted to an RGB image. The contrast and brightness of the image was increased. Colour was added by altering the relative values of the each RGB channel. Each fluorescence image was processed using the same brightness/contrast and RGB values for consistency. The DIC image was also imported into Adobe Photoshop and the brightness/contrast adjusted. The DIC and fluorescence images were overlaid. The fluorescent layer (top) was converted to "color" using the blending options which gave the final merged image. The final images were converted to 8 bit and saved as TIFF files.

### 5.5.3 Multiphoton Excitation Confocal Imaging

All multiphoton microscopy was carried out on a Nikon Ti-E inverted motorised microscope with a Nikon A1R confocal microscope system equipped with four PMT detectors and 20mW solid state lasers of the following wavelengths: 405 nm, 488 nm, 561 nm and 638 nm. The system also contained a Coherent Chameleon II infrared laser (700-1000 nm) for two photon excitation.

### 5.5.4 Near-Infrared Luminescence

The photophysical measurements were carried out as described in Chapter Two, section 2.5.1. Singlet oxygen analysis was measured using the Hamamatsu R5509-42 photomultiplier detector for detection of NIR radiation (spectral range 800-1400 nm).

### 5.5.5 Anion Exchange

DOWEX®-Cl (1×8, 200-400 mesh, $Cl^-$ form) was swollen in ethanol and packed into a column. An acetonitrile solution of *fac*-[Re(**phen**)$(CO)_3$(**TphCH$_3$**)]$^+$ (**59**) was passed through the column and eluted with acetonitrile until all the yellow solution

had eluted. The yellow solution was concentrated *in vacuo* to yield a mixture of rhenium complexes as characterised by $^{1}$H NMR. This mixture was passed through an acidic alumina-filled column. Fraction one was eluted with ethyl acetate (100%) and fraction two eluted with an ethyl acetate/methanol (9.5:0.5) solvent system. IR and $^{1}$H NMR revealed fraction one was *fac*-[Re(**phen**)$(CO)_3$(**Cl**)] (**7**) and fraction two was a mixture.

# Chapter 6

# Conclusions and Future Work

This study reports on the design, synthesis and investigation of a library of rhenium tetrazolato complexes for applications in optical imaging. Small structural changes were made to assess how the chemical, photophysical and biological properties of the complexes would be effected. The neutral complexes were of the form; *fac*-[Re(**diim**)$(CO)_3$(**L**)], where **diim** is either 1,10-phenanthroline (**phen**) or 2,2'-bipyridine (**bipy**) and **L** is one of a series of 5-substituted aryl tetrazoles. The first set of structural changes involved altering the diimine ligand from **bipy** to **phen** as well as modification of the *para* substituent on the aryl tetrazolato ligand. NMR, IR and X-ray crystallographic analysis indicated the chemical similarity between the synthesised neutral Re(I) complexes; each complex was in a *facial* configuration and the tetrazolato ligand was coordinated to rhenium via the N2 atom. The photophysical output of the Re(I) **phen** complexes demonstrated longer $\tau$ and higher $\phi$ compared to the **bipy** analogues. The photophysical output could be fine tuned by altering the *para* substituent on the tetrazolato ligand. Computational calculations (DFT) indicated that as the electron withdrawing strength of the *para* substituent increased, the contribution of the aryl ring to the HOMO reduced; rationalising the minor photophysical change observed. Therefore these tetrazolato ligands can be further functionalised without significantly altering the photophysical output. When *fac*-[Re(**phen**)$(CO)_3$(**Tph**)] (**11**) and *fac*-[Re(**phen**)$(CO)_3$(**Tbz**)] (**13**) were incubated with HeLa cells, live imaging experiments revealed their good uptake and perinuclear localisation. There was no obvious difference in the behaviour of **11** and **13** in HeLa cells, despite the difference in *para* substituents. These complexes were also found to be non-toxic during incubation

and imaging however upon acquisition of z-stacks (continuous imaging, <4 min), cells showed signs of blebbing. It is likely that *fac*-[Re(**phen**)$(CO)_3$(**Tph**)] (**11**) and *fac*-[Re(**phen**)$(CO)_3$(**Tbz**)] (**13**) are phototoxic due to the production of singlet oxygen.

Protonation of the neutral Re(I) tetrazolato complexes with triflic acid produced a blue shifted and increased emission intensity as well as elongated $\tau$ and higher $\phi$. These experiments provide proof of concept that Re(I) tetrazolato complexes demonstrate a detectable response to a change in environment and may therefore be further explored as sensing agents/responsive probes. Protonation of [Ir(PyrTzF)](**60**) lead to a change in the composition of the excited state. The neutral Ir(III) complex has a structured emission profile and upon protonation emission red shifts and becomes structureless. The emission of $[Ru(PyrTzH)]^{2+}$(**61**) was significantly quenched with respect to the unprotonated species. Photophysical modulation of the metal tetrazolato complexes was completely reversible through addition of triethylamine.

The improved photophysical output of the Re(I) complexes was harnessed in an irreversible way by carrying out methylation on the tetrazolato ligand. The photophysical output increased in a similar way as observed for the protonated species, however the chemical stability of the complexes decreased. In coordinating solvents, the methylated ligand became labile and a solvato-complex was formed, even at 37 ºC (cell incubation temperature). Live cell imaging experiments were conducted with HeLa cells incubated with *fac*-[Re(**phen**)$(CO)_3$(**Tph**$CH_3$)]$^+$
(**59**) and *fac*-[Re(**phen**)$(CO)_3$(**Tbz**$CH_3$)]$^+$(**33**) however limited uptake was observed. The lack of cellular uptake and the instability of the methylated Re(I) complexes, suggests they are unsuitable for biological imaging.

*fac*-[Re(**phen-S-PEG**)$(CO)_3$(**Tph**)] (**41**) was synthesised in an attempt to improve the water solubility of the Re(I) tetrazolato complexes. Analysis of the *n*-octanol/water distribution coefficient suggests the addition of a small PEG chain was insufficient to significantly improve water solubility. Although the concentration of DMSO used during the live cell imaging experiments was generally kept below 0.5%, it is important to minimise cytotoxic effects and alterations to "normal" physiological state. Future modifications to the complexes will aim to reduce DMSO to below 0.1% (as recommended). This may involve the attachment of a longer and/or more PEG chains to the diimine ligand. Functionalisation of the diimine ligand with PEG did not lead to

significant structural changes nor significant photophysical changes at room temperature. **41** was incubated with HeLa cells and live cell imaging showed good uptake with diffuse perinuclear localisation. Functionalisation did not appear to effect localisation however **41** did exhibit increased phototoxicity. This could be attributed to increased singlet oxygen production and/or increased cellular uptake.

This study has gained fundamental insight into how structural changes to Re(I) tetrazolato complexes can influence their chemical, photophysical and biological properties. The photophysical properties are conserved upon functionalisation of both the diimine ligand (with a thioether chain) and the *para* substituted tetrazolato ligand. This provides opportunities for conjugation to molecules aiming to improve or direct cellular uptake and localisation without altering emission properties.

Future work will focus on live cell imaging in a range of other cell lines, including normal human cells. This will extend understanding of uptake, localisation and toxicity. To reveal the Re(I) complexes preferential organelle localisation or simply confirm their non-specific nature co-localisation experiments will be carried out using labels known to stain cytoplasmic organelles. A recent publication by Bader *et al*.[115] studied the uptake and localisation of two Re(I) complexes, **17** and **62** in *Drosophila* larval adipose tissues and human adipose 3T3-L1 cells.

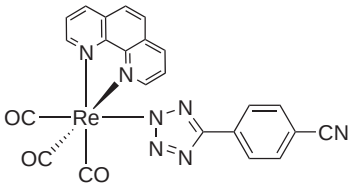


**17**

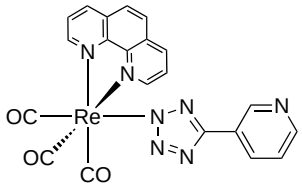


**62**

The cellular uptake and localisation suggested a relationship between the structure of the Re(I) tetrazolato complexes and their behaviour in a biological environment. Collaborations with this research group at the University of South Australia are continuing. Investigations will look at cellular uptake and localisation of other Re(I) complexes reported in this work.

The toxicity of the Re(I) comlpexes can be further explored through a range of tests. MTT testing as well as the utilisation of flow cytometry can quantify the relative toxicity of Re(I) complexes against a range of cell lines. The production of singlet oxygen by phosphorescent metal complexes is not commonly addressed in the literature, with only a few studies reporting on this issue.[80,104] Therefore, it is important that the phototoxic nature of the Re(I) complexes be further explored. The quantum yield of singlet oxygen production is a way to quantify the efficiency of a photodynamic probe and will be a necessary parameter to calculate for the Re(I) complexes. The photodynamic efficiency of the Re(I) complexes will assess their potential to be explored as therapeutic agents. Selectivity of the complex could be conferred through functionalisation with a compound exhibiting specificity towards cancerous or diseased cells. A range of strategies exist to form targeted imaging or therapeutic agents with examples including conjugation of antibody conjugates, tumour surface proteins (ie: receptor binding ligands) and peptides.[265] Conjugation to either the tetrazolato or diimine ligand of the Re(I) complexes would offer specificity without significantly altering photophysical and therefore the phototoxic properties.

The sensing abilities of Re(I) complexes (which was fundamentally studied in Chapter Three) should be further investigated. It is important to be able to monitor the levels of certain molecules and cations within cells. A range of metals within the body are responsible for life processes and their levels can be used as a marker for the health status of cells.[213] The Re(I) complexes should be analysed by UV-visible and emission spectrophotometric titrations with metal cations such zinc, calcium and cadmium. If no selective response is noted structural changes to the Re(I) tetrazolato complex can improve the coordination site for cations. If the aryl group on the ligand is substituted for a pyridine to form *fac*-[Re(**phen**)$(CO)_3$(**TPyr**)] (**63**), cations may coordinate between the nitrogen on the pyridine.

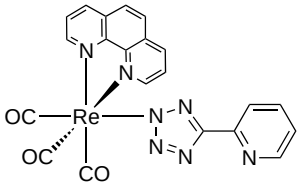


**63**

If *fac*-[Re(**phen**)$(CO)_3$(**TPyr**)] (**63**) exhibits a selective and detectable response to any cation(s), the investigation can be extended to *in vitro* studies.

Despite the numerous studies of phosphorescent metal complexes in bio-imaging, their specific design is not trivial. To advance their use in optical imaging, systematic studies need to continue, to gauge an understanding of what structural changes govern their chemical, photophysical and biological properties. Heavy metal complexes generally exhibit chemical stability and advantageous photophysical properties. These properties are tunable through simple synthetic modifications. The variety of optical imaging experiments available has been greatly expanded with the employment of phosphorescent heavy metal complexes. This study, along with many others, has shown the potential of metal complexes to be applied in optical imaging in both a diagnostic and therapeutic context.

# Appendix

# A1.1 Appendix: Chapter Two

Table A1.1: Crystallographic data for *fac*-[Re(**phen**)$(CO)_3$(**TIod**)] (**20**) and *fac*-[Re(**phen**)$(CO)_3$(**TBr**)] (**19**).

| Identification code | **20** | **19** |
|---|---|---|
| Empirical formula | $C_{22}H_{12}I\ N_6O_3Re$ | $C_{22}H_{12}Br\ N_6O_3Re$ |
| Formula weight | 721.48 | 674.49 |
| Temperature | 100(2) K | 100(2)K |
| Wavelength | 0.71073 Å | 1.54178 Å |
| Crystal system | Monoclinic | Monoclinic |
| Space group | $P2_{1/n}$ | $P2_{1/c}$ |
| Unit cell dimensions | a = 7.0191(3) Å | a = 6.8071(3) Å |
| | b = 18.0476(8) Å | b = 18.4161(8) Å |
| | c = 16.9652(6) Å | c = 17.0264(7) Å |
| | $\beta$= 99.850(3)° | $\beta$=102.607(3)° |
| Volume | 2117.44(15) $Å^3$ | 2082.97(15) $Å^3$ |
| Z | 4 | 4 |
| Density (calculated) | 2.263 $Mg/m^3$ | 2.151 $Mg/m^3$ |
| $\mu$ | 7.236 $mm^{-1}$ | 7.792 $mm^{-1}$ |
| Crystal size | 0.46 x 0.31 x 0.02 $mm^3$ | 0.53 x 0.24 x 0.035 $mm^3$ |
| $\theta$ range for data collection | 2.99 to 30.00° | 3.66 to 28.00° |
| Index ranges | -19<=h<=9, -25<=k<=25, | -8<=h<=8, -23<=k<=24, |
| | -23<=l<=23 | -22<=l<=18 |
| Reflections collected | 21406 | 20685 |
| Independent reflections | 6157 [*R*(int) = 0.0448] | 5005 [*R*(int) = 0.0585] |
| Completeness to $\theta$ max | 99.9 % | 99.8 % |
| Absorption correction | Analytical | Analytical |
| Max. and min. transmission | 0.855 and 0.219 | 0.758 and 0.217 |
| Refinement method | Full-matrix least-squares on $F^2$ | Full-matrix least-squares on $F^2$ |
| Data / restraints / parameters | 6157 / 0 / 298 | 5005 / 0 / 298 |
| Goodness-of-fit on F2 | 1.129 | 1.069 |
| Final R indices [I>2$\sigma$(I)] | *R*1 = 0.0372, *wR2* = 0.0787 | *R*1 = 0.0340, *wR2* = 0.0800 |
| R indices (all data) | *R*1 = 0.0448, *wR2* = 0.0815 | *R*1 = 0.0399, *wR2* = 0.0827 |
| Largest diff. peak and hole | 2.204 and -0.802 $e.Å^{-3}$ | 2.862 and -2.081 $e.Å^{-3}$ |

## A2.2 Appendix: Chapter Three

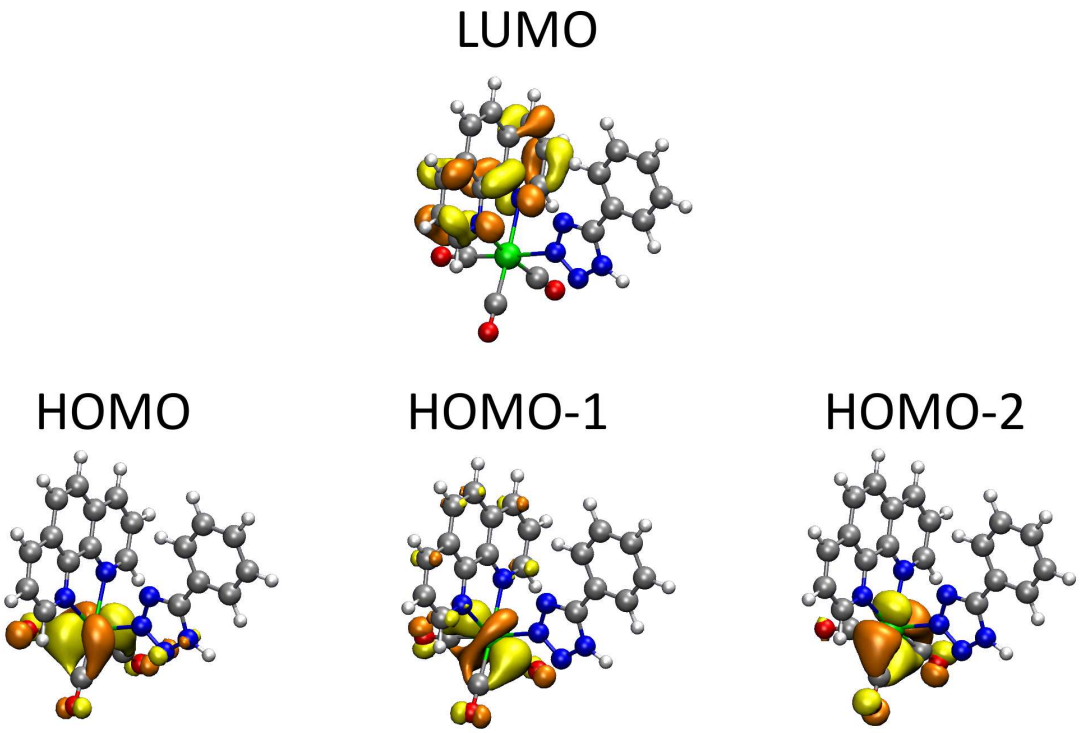


Figure A2.1: Localisation of the HOMO and LUMO for *fac*-[Re(**phen**)$(CO)_3$(**TphH**)]$^+$ (**21**).

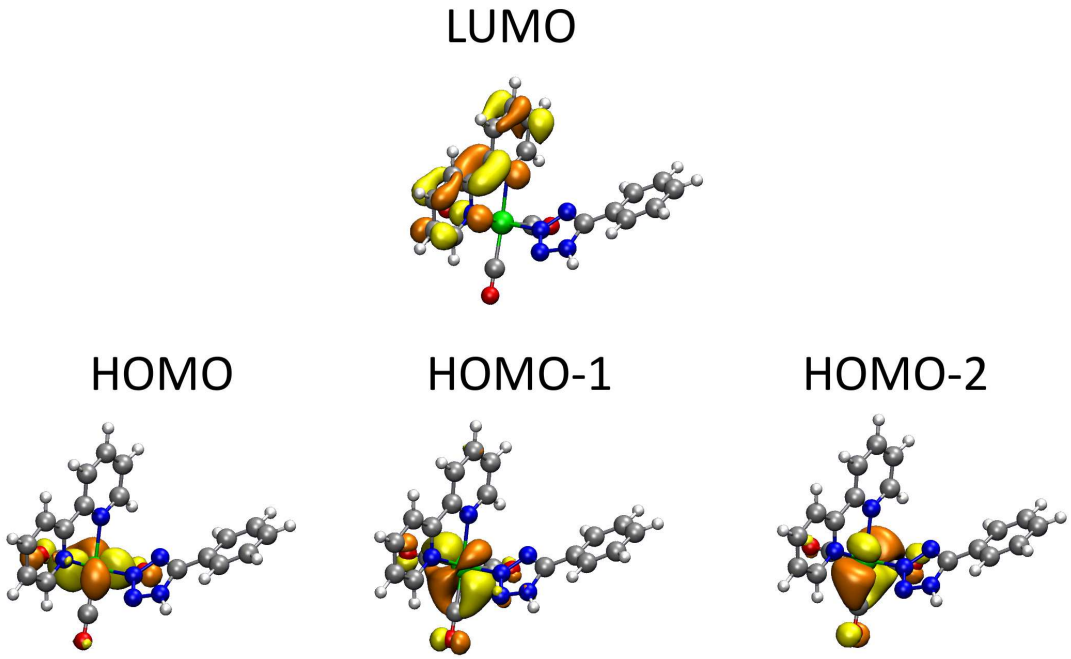


Figure A2.2: Localisation of the HOMO and LUMO for *fac*-[Re(**bipy**)(CO)$_3$(**TphH**)]$^+$ (**22**).

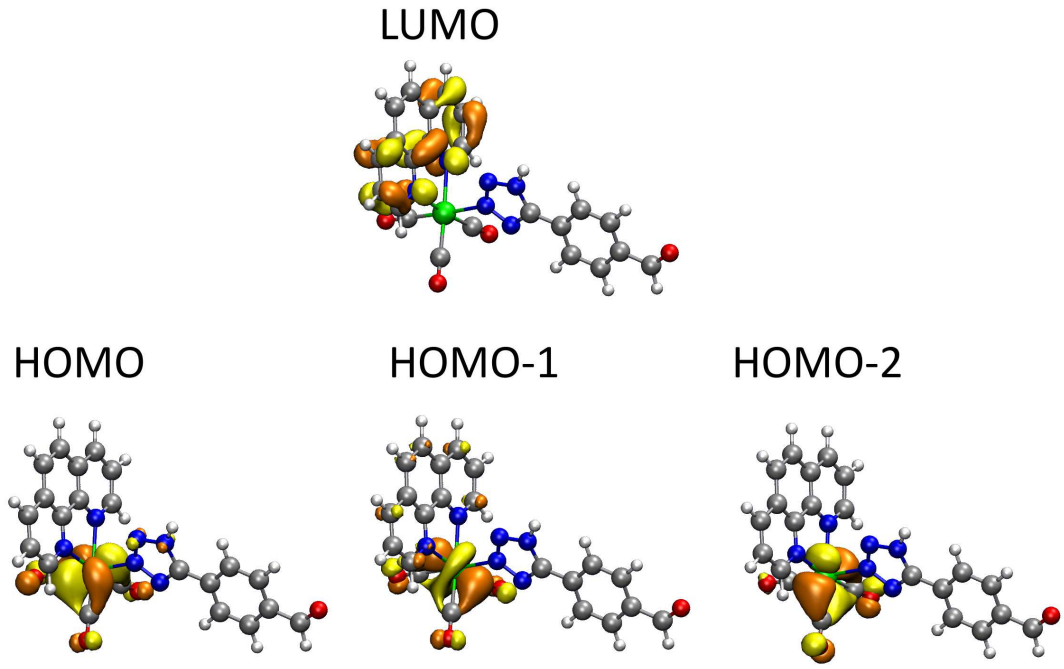


Figure A2.3: Localisation of the HOMO and LUMO for *fac*-[Re(**phen**)(CO)$_3$(**TbzH**)]$^+$ (**23**).

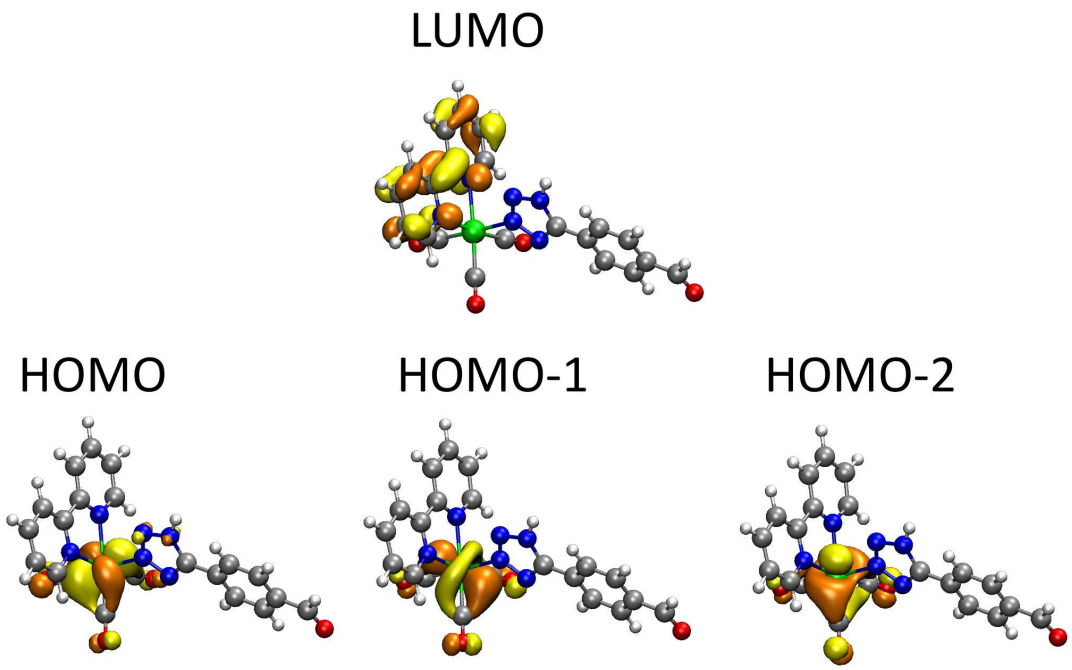


Figure A2.4: Localisation of the HOMO and LUMO for *fac*-[Re**bipy**$(CO)_3$(**TbzH**)]$^+$ (**24**).

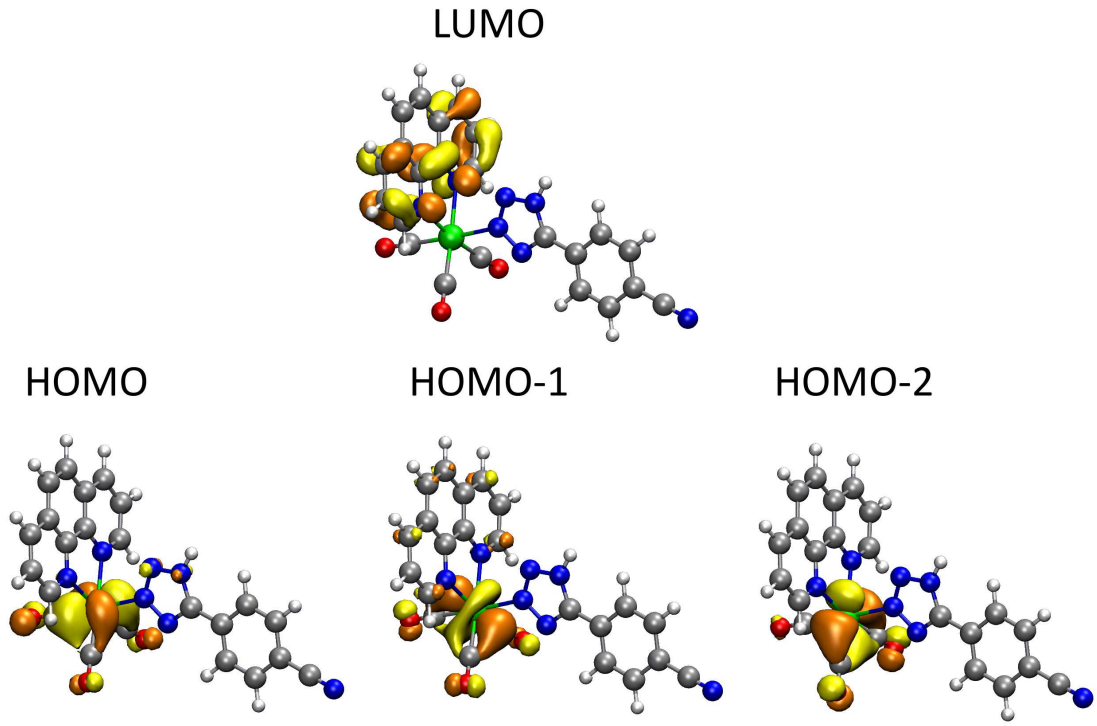


Figure A2.5: Localisation of the HOMO and LUMO for *fac*-[Re(**phen**)$(CO)_3$(**TcyaH**)]$^+$ (**25**).

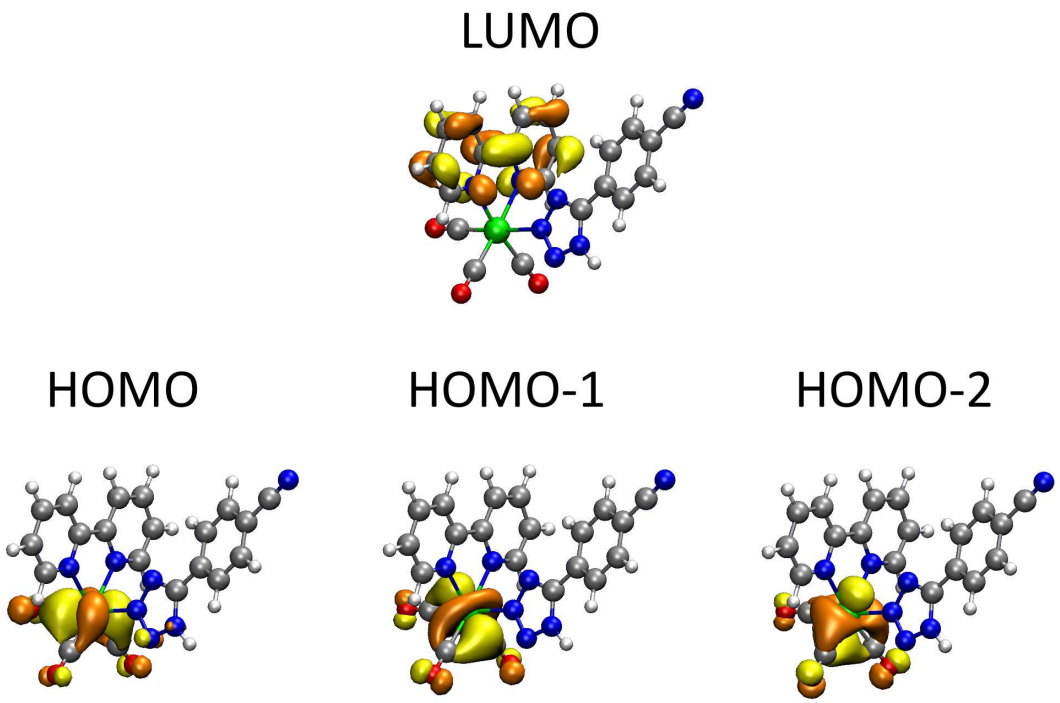


Figure A2.6: Localisation of the HOMO and LUMO for *fac*-[Re(**bipy**)$(CO)_3$(**TcyaH**)]$^+$(**26**).

## A3.3 Appendix: Chapter Four

Table A3.1: Crystallographic data for *fac*-[Re(**phen**)$(CO)_3$(**TphCH$_3$**)]$^+$ (**31**) and *fac*-[Re(**bipy**)$(CO)_3$(**TphCH$_3$**)]$^+$(**32**).

| Identification code | **31** | **32** |
|---|---|---|
| Empirical formula | $C_{23}H_{16}F_6N_6O_3PRe$ | $C_{23}H_{18}Cl_2F_3N_6O_6ReS$ |
| Formula weight | 755.59 | 820.59 |
| Temperature | 298(2) K | 100(2)K |
| Wavelength | 0.71073 Å | 1.54178 Å |
| Crystal system | Monoclinic | Monoclinic |
| Space group | $P2_{1/c}$ | $P2_{1/n}$ |
| Unit cell dimensions | a = 12.1607(13) Å | a = 9.2488(13) Å |
| | b = 14.9974(17) Å | b = 22.212(3) Å |
| | c = 14.0496(16) Å | c = 14.293(2) Å |
| | $\alpha$=90.00 | $\alpha$=90.00 |
| | $\beta$= 90.0710(10)° | $\beta$= 90.906(2)° |
| | $\gamma$=90.00 | $\gamma$=90.00 |
| Volume | 2562.3(5) Å$^3$ | 2934.8(7) Å$^3$ |
| Z | 4 | 4 |
| Density (calculated) | 1.959 Mg/m$^3$ | 2.991 Mg/m$^3$ |
| F(000) | 1456 | 1592 |
| $\mu$ | 4.887 mm$^{-1}$ | 4.461 mm$^{-1}$ |
| Crystal size | 0.16 x 0.13 x 0.11 mm$^3$ | 0.223 x 0.14 x 0.12 mm$^3$ |
| $\theta$ range for data collection | 1.36 to 26.00° | 1.83 to 25.02 ° |
| Index ranges | -15<=h<=15, -18<=k<=18, | -11<=h<=11, -26<=k<=26, |
| | -17<=l<=17 | -17<=l<=17 |
| Reflections collected | 5037 | 5166 |
| Independent reflections | 4189 [*R*(int) = 0.0519] | 4353 [*R*(int) = 0.0508] |
| Completeness to $\theta$ max | 99.9 % | 99.8 % |
| Absorption correction | Empirical | Empirical |
| Max. and min. transmission | 0.5085 and 0.6154 | 0.4403 and 0.6166 |
| Refinement method | Full-matrix least-squares on $F^2$ | Full-matrix least-squares on $F^2$ |
| Data / restraints / parameters | - | - |
| Goodness-of-fit on F2 | 1.1021 | 1.100 |
| Final R indices [I>2$\sigma$(I)] | *R*1 = 0.0519, *wR2* = 0.0539 | *R*1 = 0.0582, *wR2* = 0.1246 |
| R indices (all data) | *R*1 = 0.0369, *wR2* = 0.0493 | *R*1 = 0.0469, *wR2* = 0.1183 |
| Largest diff. peak and hole | | |

Table A3.2: Crystallographic data for *fac*-[Re(**phen**)$(CO)_3$(**TbzCH$_3$**)]$^+$(**33**) and *fac*-[Re(**bipy**)$(CO)_3$(**TbzCH$_3$**)]$^+$(**34**).

| Identification code | **33** | **34** |
|---|---|---|
| Empirical formula | $C_{24}H_{16}F_6N_6O_4PRe \cdot CDCl_3$ | $C_{22}H_{16}F_6N_6O_4PRe \cdot CHCl_3$ |
| Formula weight | 902.97 | 878.95 |
| Temperature | 100(2) K | 100(2)K |
| Wavelength | 0.71073 Å | 1.54178 Å |
| Crystal system | Monoclinic | Monoclinic |
| Space group | C2/*c* | C2/*c* |
| Unit cell dimensions | a = 20.7999(12) Å | a = 23.0576(9) Å |
| | b = 11.1806(5) Å | b = 16.6963(5) Å |
| | c = 26.1866(14) Å | c = 15.9749(6) Å |
| | $\beta$= 99.901(5)° | $\beta$= 97.077(4)° |
| Volume | 5999.1(5) Å$^3$ | 6103.1(4) Å$^3$ |
| Z | 8 | 8 |
| Density (calculated) | 2.000 Mg/m$^3$ | 1.913 Mg/m$^3$ |
| F(000) | 1512 | 3392 |
| $\mu$ | 4.454 mm$^{-1}$ | 3.375 mm$^{-1}$ |
| Crystal size | 0.22 x 0.12 x 0.03 mm$^3$ | 0.4321 x 0.1910 x 0.0878mm$^3$ |
| $\theta$ range for data collection | 3.36 to 28.43° | 2.88 to 30.00 ° |
| Index ranges | -23<=h<=26, -14<=k<=14, | -28<=h<=32, -23<=k<=23, |
| | -34<=l<=2 | -22<=l<=19 |
| Reflections collected | 17010 | 38648 |
| Independent reflections | 6501 [*R*(int) = 0.0965] | 8891 [*R*(int) = 0.0763] |
| Completeness to $\theta$ max | 98.8 % | 99.9 % |
| Absorption correction | Analytical | Analytical |
| Max. and min. transmission | 0.884 and 0.623 | 0.688 and 0.277 |
| Refinement method | Full-matrix least-squares on F$^2$ | Full-matrix least-squares on F$^2$ |
| Data / restraints / parameters | 6501/ 84/ 479 | 8891 / 19 / 459 |
| Goodness-of-fit on F2 | 0.937 | 1.197 |
| Final R indices [I>2$\sigma$(I)] | *R*1 = 0.0548, *wR*2 = 0.0876 | *R*1 = 0.0598, *wR*2 = 0.1206 |
| R indices (all data) | *R*1 = 0.1115, *wR*2 = 0.0969 | *R*1 = 0.0771, *wR*2 = 0.1263 |
| Largest diff. peak and hole | 3.124 and -1.739 e.Å$^{-3}$ | 2.474 and -0.960 e.Å$^{-3}$ |

Table A3.3: Crystallographic data for *fac*-[Re(**phen**)$(CO)_3$(**TmeCH$_3$**)]$^+$(**35**) and *fac*-[Re(**bpiy**)$(CO)_3$(**TmeCH$_3$**)]$^+$(**36**).

| Identification code | **35** | **36** |
|---|---|---|
| Empirical formula | $C_{25}H_{18}F_6N_6O_5PRe$ | $C_{23}H_{18}F_6N_6O_5PRe$ |
| Formula weight | 813.62 | 789.60 |
| Temperature | 100(2) K | 100(2)K |
| Wavelength | 0.71073 Å | 0.71073Å |
| Crystal system | Monoclinic | Monoclinic |
| Space group | $P2_1/c$ | $P2_1/c$ |
| Unit cell dimensions | a = 18.0672(6) Å | a =10.6468(1) Å |
| | b =9.8480(2) Å | b = 13.1055(1) Å |
| | c = 16.8781(6) Å | c = 19.4480(1) Å |
| | $\beta$= 114.201(4)° | $\beta$= 91.955(1)° |
| Volume | 2739.12(17)Å$^3$ | 2712.03(4) Å$^3$ |
| Z | 4 | 4 |
| Density (calculated) | 1.973 Mg/m$^3$ | 1.934 Mg/m$^3$ |
| F(000) | 1576 | 1528 |
| $\mu$ | 4.585 mm$^{-1}$ | 4.628 mm$^{-1}$ |
| Crystal size | 0.27 x 0.23 x 0.20mm$^3$ | 0.28 x 0.24 x 0.16 mm$^3$ |
| $\theta$ range for data collection | 3.85 to 36.45° | 2.88 to 30.00 ° |
| Index ranges | -29<=h<=29, -16<=k<=15, | -28<=h<=32, -23<=k<=23, |
| | -27<=l<=27 | -22<=l<=19 |
| Reflections collected | 81206 | 181307 |
| Independent reflections | 12974 [*R*(int) = 0.0403]] | 23179 [*R*(int) = 0.0401] |
| Completeness to $\theta$ max | 99.0 % | 99.8 % |
| Absorption correction | Analytical | Analytical |
| Max. and min. transmission | 0.483 and 0.405 | 0.535 and 0.398 |
| Refinement method | Full-matrix least-squares on $F^2$ | Full-matrix least-squares on $F^2$ |
| Data / restraints / parameters | 12974 / 0 / 400 | 23179 / 0 / 381 |
| Goodness-of-fit on F2 | 0.967 | 0.874 |
| Final R indices [I>2$\sigma$(I)] | *R*1 = 0.0360, *wR*2 = 0.0914 | *R*1 = 0.0197, *wR*2 = 0.0392 |
| R indices (all data) | *R*1 = 0.0599, *wR*2 = 0.0960 | *R*1 = 0.0340, *wR*2 = 0.0400 |
| Largest diff. peak and hole | 2.000 and -1.326 e.Å$^{-3}$ | 1.390 and -0.646 e.Å$^{-3}$ |

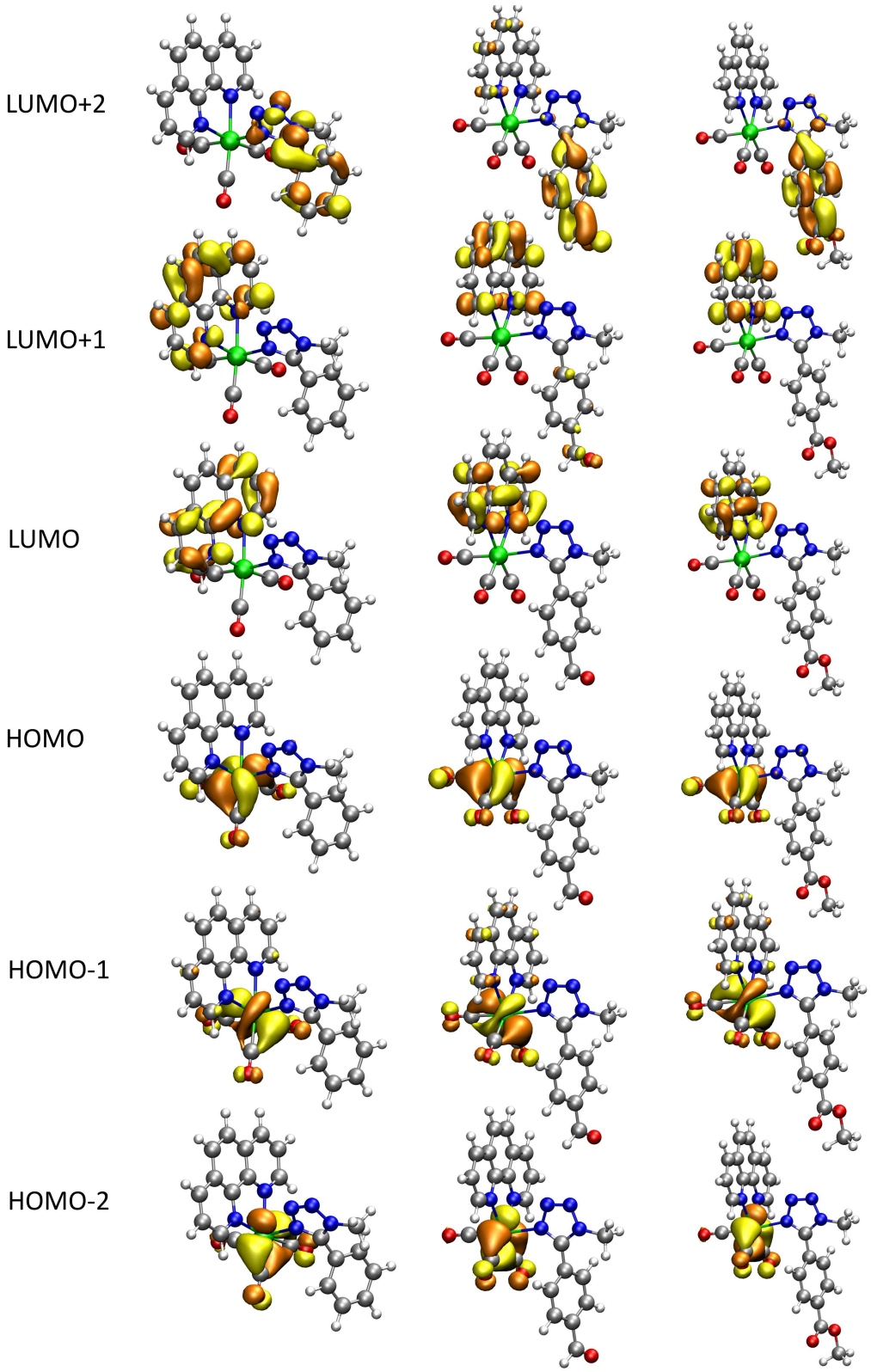


Figure A3.1: Localisation of the HOMO-*n* and and LUMO+*m* orbitals, where *n* and *m* = 0-2, for the methylated Re(I) **phen** complexes (left to right); *fac*-[Re(**phen**)$(CO)_3$(**TphCH$_3$**)]$^+$ **31**, *fac*-[Re(**phen**)$(CO)_3$(**TbzCH$_3$**)]$^+$(**33**) and *fac*-[Re(**phen**)$(CO)_3$(**TmeCH$_3$**)]$^+$(**35**).

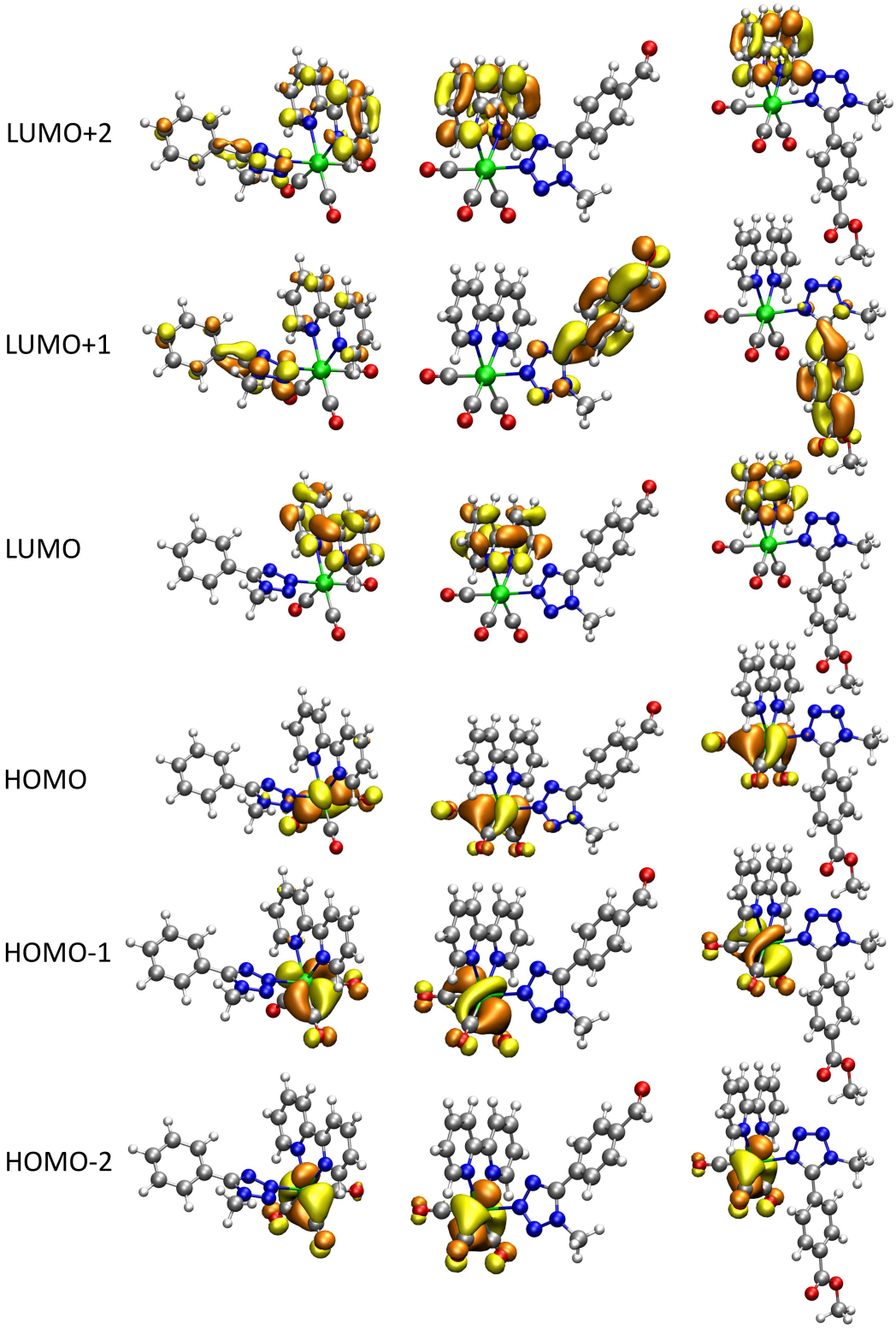


Figure A3.2: Localisation of the HOMO-*n* and and LUMO+*m* orbitals, where *n* and *m* = 0-2, for the methylated Re(I) **bipy** complexes (left to right); *fac*-[Re(**bipy**)$(CO)_3$(**TphCH$_3$**)]$^+$ **32**, *fac*-[Re(**bipy**)$(CO)_3$(**TbzCH$_3$**)]$^+$(**34**) and *fac*-[Re(**bipy**)$(CO)_3$(**TmeCH$_3$**)]$^+$(**36**).

Table A3.4: Calculated low energy transitions for *fac*-[Re(**phen**)$(CO)_3$(**TphCH$_3$**)]$^+$ (**31**).

| Wavelength | Intensity | Levels | Character |
|---|---|---|---|
| 423.94 nm | 0.0014 | HOMO -> LUMO | 98.70% |
| 398.67 nm | 0.0219 | HOMO-2 -> LUMO | 33.30% |
| | | HOMO-1 -> LUMO | 60.90% |
| | | HOMO -> LUMO+1 | 4.70% |
| 388.06 nm | 0.0203 | HOMO-2 -> LUMO | 54.20% |
| | | HOMO-1 -> LUMO | 15.40% |
| | | HOMO -> LUMO+1 | 29.50% |
| 373.51 nm | 0.0787 | HOMO-2 -> LUMO | 11.40% |
| | | HOMO-1 -> LUMO | 22.00% |
| | | HOMO -> LUMO+1 | 64.80% |
| 362.16 nm | 0.0124 | HOMO-2 -> LUMO+1 | 5.10% |
| | | HOMO-1 -> LUMO+1 | 91.40% |
| 351.35 nm | 0.0055 | HOMO-2 -> LUMO+1 | 93.70% |
| | | HOMO-1 -> LUMO+1 | 4.20% |
| 315.15 nm | 0.0023 | HOMO-6 -> LUMO+1 | 7.80% |
| | | HOMO-4 -> LUMO | 26.70% |
| | | HOMO-3 -> LUMO | 62.20% |

Table A3.5: Calculated low energy transitions for *fac*-[Re(**bipy**)$(CO)_3$(**TphCH$_3$**)]$^+$(**32**).

| Wavelength | Intensity | Levels | Character |
|---|---|---|---|
| 395.25 nm | 0.0098 | HOMO -1 -> LUMO | 38.50% |
| | | HOMO -> LUMO | 60.50% |
| 386.82 nm | 0.0836 | HOMO-2 -> LUMO | 12.00% |
| | | HOMO-1 -> LUMO | 54.40% |
| | | HOMO -> LUMO | 32.60% |
| 375.88 nm | 0.0487 | HOMO-2 -> LUMO | 86.80% |
| | | HOMO-1 -> LUMO | 6.10% |

| | | | |
|---|---|---|---|
| | | HOMO -> LUMO | 6.00% |
| 304.65 nm | 0.1357 | HOMO-5 -> LUMO | 44.80% |
| | | HOMO-1 -> LUMO+1 | 23.30% |
| | | HOMO-1 -> LUMO+2 | 3.00% |
| | | HOMO -> LUMO+1 | 14.80% |
| | | HOMO -> LUMO+2 | 6.80% |
| 300.66 nm | 0.0767 | HOMO-5 -> LUMO | 17.40% |
| | | HOMO-1 -> LUMO+1 | 38.00% |
| | | HOMO-1 -> LUMO+2 | 9.40% |
| | | HOMO-1 -> LUMO+3 | 4.30% |
| | | HOMO-1 -> LUMO+4 | 14.40% |
| | | HOMO -> LUMO+1 | 4.30% |
| | | HOMO -> LUMO+2 | 6.20% |
| | | HOMO -> LUMO+4 | 2.60% |

Table A3.6: Calculated low energy transitions for *fac*-[Re(**phen**)$(CO)_3$(**TbzCH$_3$**)]$^+$(**33**).

| Wavelength | Intensity | Levels | Character |
|---|---|---|---|
| 390.60 nm | 0.0035 | HOMO -> LUMO | 98.20% |
| 372.04 nm | 0.1107 | HOMO-2 -> LUMO | 10.80% |
| | | HOMO-1 -> LUMO | 83.80% |
| | | HOMO -> LUMO+1 | 3.40% |
| 362.27 nm | 0.0392 | HOMO-2 -> LUMO | 85.20% |
| | | HOMO-1 -> LUMO | 7.80% |
| | | HOMO -> LUMO+1 | 4.90% |
| 348.32 nm | 0.0884 | HOMO-2 -> LUMO | 2.50% |
| | | HOMO-1 -> LUMO | 6.40% |
| | | HOMO -> LUMO+1 | 75.60% |
| | | HOMO -> LUMO+2 | 13.10% |
| 343.92 nm | 0.0000 | HOMO-4 -> LUMO | 2.10% |
| | | HOMO-4 -> LUMO+1 | 18.20% |
| | | HOMO-4 -> LUMO+2 | 73.10% |

| | | | |
|---|---|---|---|
| 336.98 nm | 0.019 | HOMO -> LUMO+1 | 14.30% |
| | | HOMO -> LUMO+2 | 81.30% |
| 336.48 nm | 0.0423 | HOMO-5 -> LUMO | 2.70% |
| | | HOMO-2 -> LUMO+1 | 2.30% |
| | | HOMO-1 -> LUMO+1 | 82.30% |
| | | HOMO-1 -> LUMO+2 | 7.80% |
| | | HOMO -> LUMO+2 | 2.60% |
| 327.25 nm | 0.0044 | HOMO-2 -> LUMO+1 | 3.20% |
| | | HOMO-1 -> LUMO+1 | 7.80% |
| | | HOMO-1 -> LUMO+2 | 84.40% |
| 325.88 nm | 0.011 | HOMO-2 -> LUMO+1 | 84.60% |
| | | HOMO-2 -> LUMO+2 | 9.90% |
| | | HOMO-1 -> LUMO+1 | 2.90% |
| 316.09 nm | 0.0016 | HOMO-2 -> LUMO+1 | 8.40% |
| | | HOMO-2 -> LUMO+2 | 85.90% |
| | | HOMO-1 -> LUMO+2 | 2.80% |
| 314.29 nm | 0.0009 | HOMO-5 -> LUMO+1 | 4.90% |
| | | HOMO-3 -> LUMO | 88.90% |
| 297.06 nm | 0.0004 | HOMO-5 -> LUMO | 34.60% |
| | | HOMO-3 -> LUMO+1 | 53.20% |
| | | HOMO-3 -> LUMO+2 | 10.70% |

Table A3.7: Calculated low energy transitions for *fac*-[Re(**bipy**)$(CO)_3$(**TbzCH$_3$**)]$^+$(**34**).

| Wavelength | Intensity | Levels | Character |
|---|---|---|---|
| 401.02 nm | 0.0057 | HOMO -> LUMO | 99.00% |
| 378.20 nm | 0.0288 | HOMO-2 -> LUMO | 29.50% |
| | | HOMO-1 -> LUMO | 69.40% |
| 366.84 nm | 0.111 | HOMO-2 -> LUMO | 69.40% |
| | | HOMO-1 -> LUMO | 29.40% |
| 348.16 nm | 0.0002 | HOMO-3 -> LUMO+1 | 90.60% |
| | | HOMO-3 -> LUMO+8 | 4.00% |

| | | | |
|---|---|---|---|
| 343.20 nm | 0.0215 | HOMO -> LUMO+1 | 98.30% |
| 328.61 nm | 0.0004 | HOMO-1 -> LUMO+1 | 97.20% |
| | | HOMO-1 -> LUMO+3 | 2.10% |
| 320.17 nm | 0.0011 | HOMO-2 -> LUMO+1 | 97.10% |
| | | HOMO-2 -> LUMO+3 | 2.30% |
| 305.75 nm | 0.093 | HOMO-4 -> LUMO | 36.30% |
| | | HOMO -> LUMO+2 | 57.50% |
| 304.65 nm | 0.2815 | HOMO -> LUMO+3 | 83.90% |
| | | HOMO -> LUMO+4 | 4.30% |
| | | HOMO -> LUMO+6 | 3.80% |
| 303.16 nm | 0.0086 | HOMO-4 -> LUMO | 4.20% |
| | | HOMO-2 -> LUMO+3 | 4.00% |
| | | HOMO-1 -> LUMO+3 | 78.30% |
| | | HOMO-1 -> LUMO+4 | 3.20% |
| | | HOMO-1 -> LUMO+6 | 4.50% |
| 295.86 nm | 0.281 | HOMO-4 -> LUMO | 44.10% |
| | | HOMO-2 -> LUMO+3 | 18.60% |
| | | HOMO-2 -> LUMO+4 | 2.50% |
| | | HOMO-1 -> LUMO+4 | 3.30% |
| | | HOMO -> LUMO+2 | 26.90% |

Table A3.8: Calculated low energy transitions for *fac*-[Re(**phen**)$(CO)_3$(**TmeCH$_3$**)]$^+$(**35**).

| Wavelength | Intensity | Levels | Character |
|---|---|---|---|
| 391.89 nm | 0.0033 | HOMO -> LUMO | 98.50% |
| 373.05 nm | 0.1043 | HOMO-2 -> LUMO | 11.80% |
| | | HOMO-1 -> LUMO | 83.20% |
| | | HOMO -> LUMO+1 | 3.60% |
| 363.19 nm | 0.0418 | HOMO-2 -> LUMO | 84.10% |
| | | HOMO-1 -> LUMO | 8.50% |
| | | HOMO -> LUMO+1 | 6.20% |
| 349.56 nm | 0.0899 | HOMO-2 -> LUMO | 2.90% |

| | | | |
|---|---|---|---|
| | | HOMO-1 -> LUMO | 6.60% |
| | | HOMO -> LUMO+1 | 88.40% |
| 337.46 nm | 0.0442 | HOMO-4 -> LUMO | 2.60% |
| | | HOMO-2 -> LUMO+1 | 2.80% |
| | | HOMO-1 -> LUMO+1 | 92.60% |
| 326.88 nm | 0.0123 | HOMO-2 -> LUMO+1 | 95.90% |
| | | HOMO-1 -> LUMO+1 | 2.00% |
| 314.48 nm | 0.0009 | HOMO-4 -> LUMO+1 | 5.80% |
| | | HOMO-3 -> LUMO | 81.50% |
| | | HOMO -> LUMO+2 | 8.90% |
| 313.09 nm | 0.0247 | HOMO-3 -> LUMO | 8.40% |
| | | HOMO -> LUMO+2 | 87.50% |
| 305.15 nm | 0.0098 | HOMO-2 -> LUMO+2 | 2.90% |
| | | HOMO-1 -> LUMO+2 | 89.80% |
| | | HOMO-1 -> LUMO+3 | 2.20% |
| 297.18 nm | 0.0005 | HOMO-4 -> LUMO | 33.90% |
| | | HOMO-3 -> LUMO+1 | 62.70% |

Table A3.9: Calculated low energy transitions for *fac*-[Re(**bpiy**)$(CO)_3$(**TmeCH$_3$**)]$^+$(**36**).

| Wavelength | Intensity | Levels | Character |
|---|---|---|---|
| 396.42 nm | 0.0054 | HOMO -> LUMO | 99.10% |
| 374.97 nm | 0.0557 | HOMO-2 -> LUMO | 19.10% |
| | | HOMO-1 -> LUMO | 79.80% |
| 362.84 nm | 0.1065 | HOMO-2 -> LUMO | 79.80% |
| | | HOMO-1 -> LUMO | 19.10% |
| 312.33 nm | 0.0222 | HOMO -> LUMO+1 | 95.30% |
| 304.29 nm | 0.1595 | HOMO-3 -> LUMO | 52.70% |
| | | HOMO -> LUMO+2 | 42.00% |
| 302.80 nm | 0.0131 | HOMO-1 -> LUMO+1 | 90.30% |
| | | HOMO-1 -> LUMO+4 | 3.40% |
| 294.68 nm | 0.2847 | HOMO-3 -> LUMO | 36.80% |

| | |
|---|---|
| HOMO-2 -> LUMO+1 | 4.90% |
| HOMO-1 -> LUMO+3 | 3.20% |
| HOMO -> LUMO+2 | 47.10% |

# A4.4 Appendix: Chapter Five

Table A4.1: Crystallographic data for *fac*-[Re(**mercaptophen**)$(CO)_3$(**Cl**)] (**39**) and *fac*-[Re(**mercaptophenPEG**)$(CO)_3$(**Cl**)] (**40**).

| Identification code | **39** | **40** |
|---|---|---|
| Empirical formula | $C_{17}H_{12}Cl\ N_2O_4SRe{\cdot}CH_2Cl_2$ | $C_{22}H_{20}Cl\ N_2O_7SRe$ |
| Formula weight | 616.92 | 678.11 |
| Temperature | 100(2) K | 100(2)K |
| Wavelength | 0.71073 Å | 1.54178 Å |
| Crystal system | Monoclinic | Triclinic |
| Space group | $P2_{1/c}$ | $P\bar{1}$ |
| Unit cell dimensions | a = 10.1763(5) Å | a = 11.5291(11) Å |
| | b = 20.8369(4) Å | b = 13.1863(12) Å |
| | c = 10.3782(3) Å | c = 16.323(2) Å |
| | $\beta$= 110.147(4)° | $\alpha$= 90.450(8) |
| | | $\beta$=92.944(8)° |
| | | $\gamma$=110.770(9)° |
| Volume | 2065.97(12) $Å^3$ | 2316.3(4) $Å^3$ |
| Z | 4 | 4 |
| Density (calculated) | 2.080 $Mg/m^3$ | 1.945 $Mg/m^3$ |
| $\mu$ | 6.399 $mm^{-1}$ | 12.585 $mm^{-1}$ |
| Crystal size | 0.15 x 0.06 x 0.05 $mm^3$ | 0.25 x 0.05 x 0.015 $mm^3$ |
| $\theta$ range for data collection | 2.86 to 33.00° | 3.59 to 67.36° |
| Index ranges | -15<=h<=15, -31<=k<=31, | -13<=h<=13, -10<=k<=15, |
| | -15<=l<=15 | -19<=l<=19 |
| Reflections collected | 56790 | 23868 |
| Independent reflections | 7775 [*R*(int) = 0.0525] | 8213 [*R*(int) = 0.0464] |
| Completeness to $\theta$ max | 99.9 % | 98.6 % |
| Absorption correction | Analytical | Analytical |
| Max. and min. transmission | 0.775 and 0.538 | 0.808 and 0.188 |
| Refinement method | Full-matrix least-squares on $F^2$ | Full-matrix least-squares on $F^2$ |
| Data / restraints / parameters | 7775 / 3 / 279 | 8213 / 0 / 615 |
| Goodness-of-fit on F2 | 1.110 | 1.044 |
| Final R indices [I>2$\sigma$(I)] | *R*1 = 0.0383, *wR2* = 0.0679 | *R*1 = 0.0466, *wR2* = 0.1131 |
| R indices (all data) | *R*1 = 0.0497, *wR2* = 0.0710 | *R*1 = 0.0569, *wR2* = 0.1229 |
| Largest diff. peak and hole | 1.743 and -1.625 $e.Å^{-3}$ | 3.640 and -0.944$e.Å^{-3}$ |

# A4.5 Appendix: Chapter Six

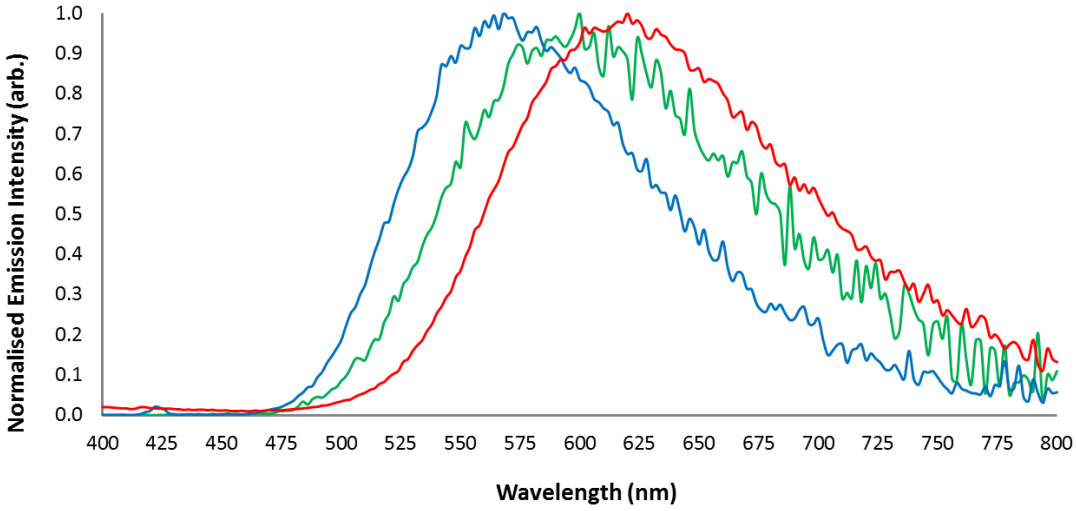


Figure A5.1: Normalised emission spectra of *fac*-[Re(**phen**)$(CO)_3$(**Tbz**)] (**13**) in DCM (red), DMSO (green) and 1% (v/v) DMSO in water (blue).

# References


[1] Bradley, W. G. *P. Am. Philos. Soc.* **2008**, *152*, 349–361.

[2] Ruggi, A.; Reinhoudt, D.; Velders, A. In *Bioinorganic Medicinal Chemistry*; Alessio, E., Ed.; Wiley-VCH: Weinheim, 2011; Chapter Biomedical, p 406.

[3] Unknown, Pregnancy Ultrasounds. 2011.

[4] Higgins, M. Shannon Higgins, MRI Films. 2010.

[5] Unknown, Capital Health: Diagnostic X-Ray. 2014.

[6] Kobayashi, H.; Ogawa, M.; Alford, R.; Choyke, P. L.; Urano, Y. *Chem. Rev.* **2010**, *110*, 2620–40.

[7] Choi, J.; Raghavan, M. *Cancer Control* **2012**, *19*, 102–112.

[8] Zhou, S.-A.; Brahme, A. *Physi Medica* **2008**, *24*, 129–48.

[9] Fenster, A.; Downey, D. *IEEE Eng. Med. Biol. Mag.* **1996**, *15*, 41–51.

[10] Blomqvist, L.; Torkzad, M. R. *JAMA-J. Am. Med. Assoc.* **2003**, *290*, 3248–3249.

[11] Macdonald, G. a.; Peduto, a. J. *J Gastroen. Hepatol.* **2000**, *15*, 980–91.

[12] Henderson, R. G. *J. R. Soc. Med.* **1983**, *76*, 206–212.

[13] Lepage, M.; Gore, J. C. *J. Phys.* **2004**, *3*, 78–86.

[14] Terreno, E.; Castelli, D. D.; Viale, A.; Aime, S. *Chem. Rev.* **2010**, *110*, 3019–42.

[15] Narouze, S. N., Ed. *Atlas of Ultrasound-Guided Procedures in Interventional Pain Management*, 1st ed.; Springer: New York, 2011.

[16] Brooks, D. J. *Neurotherapeutics* **2005**, *2*, 226–36.

[17] Holland, J. P.; Williamson, M. J.; Lewis, J. S. *Mol. Imaging* **2010**, *9*, 1–20.

[18] Cherry, S. *Semin. Nucl. Med.* **2009**, *39*, 348–353.

[19] Kim, J.; Piao, Y.; Hyeon, T. *Chem. Soc. Rev.* **2009**, *38*, 372–90.

[20] Martí-Bonmatí, L.; Sopena, R.; Bartumeus, P.; Sopena, P. *Contrast Media Mol. Imaging* **2010**, *5*, 180–9.

[21] Leblond, F.; Davis, S. C.; Valdés, P. a.; Pogue, B. W. *J. Photochem. Photobiol. B* **2010**, *98*, 77–94.

[22] Huett, A. HeLa Cell Infected with EPEC. 2012.

[23] Hadjipanayis, C.; Jian, H.; Roberts, D.; Yang, L. *Semin. Oncol.* **2011**, *38*, 109–18.

[24] Gompels, L. L.; Lim, N. H.; Vincent, T.; Paleolog, E. M. *Rheumatology (Oxford, England)* **2010**, *49*, 1436–46.

[25] Baggaley, E.; Weinstein, J.; Williams, J. *Coord. Chem. Rev.* **2012**, *256*, 1762–1785.

[26] Gibbs, S. L. *Quant. Imaging .Med. Surg.* **2012**, *2*, 177–87.

[27] Klein, K.; Gigler, A. M.; Aschenbrenner, T.; Monetti, R.; Bunk, W.; Jamitzky, F.; Morfill, G.; Stark, R. W.; Schlegel, J. *Biophys. J.* **2012**, *102*, 360–8.

[28] Michael, N.; Bischof, H.-J.; Löwel, S. *PloS one* **2014**, *9*, e85225.

[29] Berlier, J. E.; Rothe, A.; Buller, G.; Bradford, J.; Gray, D. R.; Filanoski, B. J.; Telford, W. G.; Yue, S.; Liu, J.; Cheung, C.-Y.; Chang, W.; Hirsch, J. D.; Beechem Rosaria P. Haugland, J. M.; Haugland, R. P. *J. Histochem. Cytochem.* **2003**, *51*, 1699–1712.

[30] Panchuk-Voloshina, N.; Haugland, R. P.; Bishop-Stewart, J.; Bhalgat, M. K.; Millard, P. J.; Mao, F.; Leung, W.-Y. *J. Histochem. Cytochem.* **1999**, *47*, 1179–1188.

[31] Tsien, R. Y. *Angew. Chem. Int. Ed. Engl.* **2009**, *48*, 5612–26.

[32] Yang, M.; Baranov, E.; Jiang, P.; Sun, F. X.; Li, X. M.; Li, L.; Hasegawa, S.; Bouvet, M.; Al-Tuwaijri, M.; Chishima, T.; Shimada, H.; Moossa, a. R.; Penman, S.; Hoffman, R. M. *Proc. Natl. Acad. Sci. U.S.A.* **2000**, *97*, 1206–11.

[33] Chishima, T.; Miyagi, Y.; Wang, X.; Yamaoka, H.; Shimada, H.; Moossa, A. R.; Hoffman, M. *Cancer Res.* **1997**, *57*, 2042–2047.

[34] Jablonski, A. *Z. Phys.* **1935**, *94*, 38–46.

[35] Birks, J. *J. Res. Natl. Stand. Sec. A* **1976**, *80A*, 389.

[36] Jaffe, H. H.; Miller, A. L. *J. Chem. Educ.* **1966**, *43*, 469.

[37] Sauer, M.; Hofkens, J.; Enderlein, J. *Handbook of Fluorescence Spectroscopy and Imaging : From Ensemble to Single Molecules*; 2011; Chapter One, pp 1–30.

[38] Stokes, G. G. *Phil. Trans. R. Soc. Lond.* **1852**, *142*, 463–562.

[39] Lakowicz, J. R. *Principles of Fluorescence Spectroscopy*, 3rd ed.; Springer: New York, 2006; Chapter Introducti, pp 1–25.

[40] Lakowicz, J. R. In *Principles of Fluorescence Spectroscopy*, 3rd ed.; Lakowicz, J. R., Ed.; Springer: New York, 2006; Chapter Two, pp 27–60.

[41] Aebischer, A.; Salley, G. M.; Gudel, H. U. *J. Chem. Phys.* **2002**, *117*, 8515.

[42] Berezin, M. Y.; Akers, W. J.; Guo, K.; Fischer, G. M.; Daltrozzo, E.; Zumbusch, A.; Achilefu, S. *Biophys. J.* **2009**, *97*, L22–4.

[43] Lakowicz, J. R.; Terpetschnig, E.; Murtaza, Z.; Szmaeinskp, H. *J. Fluoresc.* **1997**, *7*, 17–25.

[44] Billinton, N.; Knight, a. W. *Anal. Biochem.* **2001**, *291*, 175–97.

[45] Lakowicz, J. R. *Principles of Fluorescence Spectroscopy*, 3rd ed.; Springer: New York, 2006; Chapter Fluorophor, pp 63–94.

[46] Peters, R.; Brunger, A.; Schulten, K. *Proc. NatL Acad. Sci. USA* **1981**, *78*, 962–966.

[47] Caspar, J. V.; Kober, E. M.; Sullivan, B. P.; Meyer, T. J. *J. Am. Chem. Soc.* **1982**, 630–632.

[48] Caspar, J. V.; Meyer, T. J. *J. Phys. Chem.* **1983**, *87*, 952–957.

[49] Sacksteder, L.; Zipp, A. P.; Brown, E. A.; Streich, J.; Demas, J. N.; Degraff, B. A. *Inorg. Chem.* **1990**, *29*, 4335–4340.

[50] Beljonne, D.; Shuai, Z.; Pourtois, G.; Bredas, J. L. *J. Phys. Chem. A* **2001**, *105*, 3899–3907.

[51] Lamansky, S.; Djurovich, P.; Murphy, D.; Abdel-Razzaq, F.; Lee, H. E.; Adachi, C.; Burrows, P. E.; Forrest, S. R.; Thompson, M. E. *J. Am. Chem. Soc.* **2001**, *123*, 4304–12.

[52] Abdel-Shafi, A. a.; Worrall, D. R. *J. Photochem. Photobiol. A* **2005**, *172*, 170–179.

[53] Abdel-shafi, A. A.; Beer, P. D.; Mortimer, R. J.; Wilkinson, F. *Journal of Physical chemistry Chemistry A* **2000**, *104*, 192–202.

[54] Schweitzer, C.; Schmidt, R. *Chem. Rev.* **2003**, *103*, 1685–757.

[55] Leonidova, A.; Pierroz, V.; Rubbiani, R.; Heier, J.; Ferrari, S.; Gasser, G. *Dalton. Trans.* **2014**, *43*, 4287–94.

[56] Bünzli, J.-C. G. *Chem. Rev.* **2010**, *110*, 2729–55.

[57] Lakowicz, J. R.; Castellano, F. N.; Gryczynski, I.; Gryczynski, Z.; Dattelbaum, J. D. *J. Photochem. Photobiol. A.* **1999**, *122*, 95–101.

[58] Sekiguchi, Y.; Yamashita, T.; Vacha, M. *J. Lumin.* **2008**, *128*, 848–850.

[59] Ho, M.-L.; Lin, M.-H.; Chen, Y.-T.; Sheu, H.-S. *Chem. Phys. Lett.* **2011**, *509*, 162–168.

[60] Diaspro, A.; Bianchini, P.; Vicidomini, G.; Faretta, M.; Ramoino, P.; Usai, C. *Biomed. Eng. Online* **2006**, *5*, 36.

[61] Thorp-Greenwood, F. L.; Balasingham, R. G.; Coogan, M. P. *J. Organomet. Chem.* **2012**, *714*, 12–21.

[62] Coogan, M. P.; Fernández-Moreira, V. *Chem. Comm.* **2013**, *50*, 384–99.

[63] Svoboda, K.; Block, S. M. *Annu. Rev. Biophys. Biomol. Struct.* **1994**, *23*, 247–85.

[64] Kovar, J. L.; Simpson, M. a.; Schutz-Geschwender, A.; Olive, D. M. *Anal. Biochem.* **2007**, *367*, 1–12.

[65] Youn, H.-Y.; McCanna, D. J.; Sivak, J. G.; Jones, L. W. *Mol. Vis.* **2011**, *17*, 237–46.

[66] Gentile, M.; Latonen, L.; Laiho, M. *Nucleic Acids Res.* **2003**, *31*, 4779–4790.

[67] Zhao, Q.; Huang, C.; Li, F. *Chem. Soc. Rev.* **2011**, *40*, 2508–24.

[68] Fernández-Moreira, V.; Thorp-Greenwood, F. L.; Coogan, M. P. *Chem. Comm.* **2010**, *46*, 186–202.

[69] New, E. J.; Parker, D. *Org. Biomol. Chem.* **2009**, *7*, 851–5.

[70] Thibon, A.; Pierre, V. C. *Anal. Bioanal. Chem.* **2009**, *394*, 107–20.

[71] Montgomery, C. P.; Murray, B. S.; New, E. J.; Pal, R.; Parker, D. *Acc. Chem. Res.* **2009**, *42*, 925–37.

[72] Smith, D. G.; McMahon, B. K.; Pal, R.; Parker, D. *Chem. Comm.* **2012**, *48*, 8520–2.

[73] Edkins, R. M.; Sykes, D.; Beeby, A.; Ward, M. D. *Chem. Comm.* **2012**, *48*, 9977–9.

[74] Thorp-greenwood, F. L.; Coogan, M. P. *Dalton. Trans.* **2011**,

[75] Lichtman, J. W.; Conchello, J.-a. *Nat. Methods.* **2005**, *2*, 910–9.

[76] Yu, M.; Zhao, Q.; Shi, L.; Li, F.; Zhou, Z.; Yang, H.; Yi, T.; Huang, C. *Chem. Comm.* **2008**, *44*, 2115–7.

[77] Zhou, Y.; Jia, J.; Li, W.; Fei, H.; Zhou, M. *Chem. Comm.* **2013**, *49*, 3230–3232.

[78] Murphy, L.; Congreve, A.; På lsson, L.-O.; Williams, J. a. G. *Chem. Comm.* **2010**, *46*, 8743–5.

[79] Zhang, G.; Zhang, H.; Gao, Y.; Tao, R.; Xin, L.; Yi, J.; Li, F.; Liu, W.; Qiao, J. *Organometallics* **2014**, *33*, 61–68.

[80] You, Y.; Cho, S.; Nam, W. *Inorg. Chem.* **2013**,

[81] Gerritsen, H. C.; Sanders, R.; Draaijer, A.; Ince, C.; Levine, Y. K. *J. Fluoresc.* **1997**, *7*, 11–15.

[82] Ji, J.; Rosenzweig, N.; Jones, I.; Rosenzweig, Z. *J. Biomed. Opt.* **2002**, *7*, 404–9.

[83] Morales, A. F.; Accorsi, G.; Armaroli, N.; Barigelletti, F.; Pope, S. J. a.; Ward, M. D. *Inorg. Chem.* **2002**, *41*, 6711–9.

[84] Klimant, I.; Wolfbeis, O. S. *Anal. Chem.* **1995**, *67*, 3160–3166.

[85] Zhong, W.; Urayama, P.; Mycek, M.-A. *J. Phys. D: Appl. Phys.* **2003**, *36*, 1689–1695.

[86] Puckett, C. a.; Ernst, R. J.; Barton, J. K. *Dalton. Trans.* **2010**, *39*, 1159–70.

[87] Hartshorn, R. M.; Barton, J. K. *J. Am. Chem. Soc.* **1992**, *114*, 5919–5925.

[88] Freidman, A.; Chmbron, J.-C.; Sauvage, J.-p.; Turro, N. J.; Barton, J. *J. Am. Chem. Soc.* **1990**, *112*, 4960–4962.

[89] Zhao, X.-L.; Li, Z.-S.; Zheng, Z.-B.; Zhang, A.-G.; Wang, K.-Z. *Dalton. Trans.* **2013**, *42*, 5764–77.

[90] General, I. J.; Dragomirova, R.; Meirovitch, H. *J. Phys. Chem. B* **2012**, *116*, 6628–36.

[91] Lo, K. K.-W.; Lee, T. K.-M. *Inorg. Chem.* **2004**, *43*, 5275–82.

[92] Lo, K. K.-W.; Lee, T. K.-M. *Inorg. Chim. Acta.* **2007**, *360*, 293–302.

[93] Lo, K. K.-W.; Hui, W.-K.; Chung, C.-K.; Tsang, K. H.-K.; Lee, T. K.-M.; Li, C.-K.; Lau, J. S.-Y.; Ng, D. C.-M. *Coord. Chem. Rev.* **2006**, *250*, 1724–1736.

[94] Slim, M.; Sleiman, H. F. *Bioconjugate Chem.* **2004**, *15*, 949–53.

[95] Stephenson, K. a.; Banerjee, S. R.; Besanger, T.; Sogbein, O. O.; Levadala, M. K.; McFarlane, N.; Lemon, J. a.; Boreham, D. R.; Maresca, K. P.; Brennan, J. D.; Babich, J. W.; Zubieta, J.; Valliant, J. F. *J. Am. Chem. Soc.* **2004**, *126*, 8598–9.

[96] Amoroso, A. J.; Coogan, M. P.; Dunne, J. E.; Fernández-Moreira, V.; Hess, J. B.; Hayes, A. J.; Lloyd, D.; Millet, C.; Pope, S. J. A.; Williams, C. *Chem. Comm.* **2007**, 3066–8.

[97] Amoroso, A. J.; Arthur, R. J.; Coogan, M. P.; Court, J. B.; Fernández-Moreira, V.; Hayes, A. J.; Lloyd, D.; Millet, C.; Pope, S. J. a. *New J. Chem.* **2008**, *32*, 1097.

[98] Lo, K. K.-W.; Louie, M.-W.; Sze, K.-S.; Lau, J. S.-Y. *Inorg. Chem.* **2008**, *47*, 602–11.

[99] Louie, M.-W.; Liu, H.-W.; Lam, M. H.-C.; Lau, T.-C.; Lo, K. K.-W. *Organometallics* **2009**, *28*, 4297–4307.

[100] Levina, A.; Mitra, A.; Lay, P. a. *Metallomics* **2009**, *1*, 458–70.

[101] Alessio, E.; Mestroni, G.; Bergamo, A.; Sava, G. *Curr. Top. Med. Chem.* **2004**, *4*, 1525–35.

[102] Page, S. *Educ. Chem.* **2012**, 26–29.

[103] Fernández-Moreira, V.; Thorp-Greenwood, F. L.; Amoroso, A. J.; Cable, J.; Court, J. B.; Gray, V.; Hayes, A. J.; Jenkins, R. L.; Kariuki, B. M.; Lloyd, D.; Millet, C. O.; Williams, C. F.; Coogan, M. P. *Org. Biomol. Chem.* **2010**, *8*, 3888–901.

[104] Yin Zhang, K.; Ka-Shun Tso, K.; Louie, M.-W.; Liu, H.-W.; Kam-Wing Lo, K. *Organometallics* **2013**, *32*, 5098–5102.

[105] Balasingham, R. G.; Coogan, M. P.; Thorp-Greenwood, F. L. *Dalton. Trans.* **2011**, *40*, 11663–74.

[106] Sharghi, H.; Ebrahimpourmoghaddam, S.; Doroodmand, M. M. *J. Organomet. Chem.* **2013**, *738*, 41–48.

[107] Singh, H.; Chawla, A. S.; Kapoor, V. K.; Paul, D.; Ravinder K. Malhotra, *Prog. Med. Chem.* **1980**, *17*, 151–183.

[108] Palazzi, a. *J. Organomet. Chem.* **2003**, *669*, 135–140.

[109] Koguro, K.; Oga, T.; Mitsui, S.; Orita, R. *Synthesis* **1998**, 910–914.

[110] Szczepura, L. F.; Oh, M. K.; Knott, S. a. *Chem. Comm.* **2007**, *8*, 4617–9.

[111] Palazzi, A.; Stagni, S.; Bordoni, S.; Monari, M.; Selva, S. *Organometallics* **2002**, *21*, 3774–3781.

[112] Palazzi, A.; Stagni, S. *J. Organomet. Chem.* **2005**, *690*, 2052–2061.

[113] Stagni, S.; Colella, S.; Palazzi, A.; Valenti, G.; Zacchini, S.; Paolucci, F.; Marcaccio, M.; Albuquerque, R. Q.; De Cola, L. *Inorg. Chem.* **2008**, *47*, 10509–21.

[114] Stagni, S.; Palazzi, A.; Zacchini, S.; Ballarin, B.; Bruno, C.; Marcaccio, M.; Paolucci, F.; Monari, M.; Carano, M.; Bard, A. J. *Inorg. Chem.* **2006**, *45*, 695–709.

[115] Bader, C. a. *et al. R. Soc. Chem. Adv.* **2014**, *4*, 16345–16351.

[116] Bélanger, S.; Gilbertson, M.; Yoon, D. I.; Stern, C. L.; Dang, X.; Hupp, J. T. *Dalton. Trans.* **1999**, 3407–3411.

[117] Li, M.-J.; Liu, X.; Nie, M.-J.; Wu, Z.-Z.; Yi, C.-Q.; Chen, G.-N.; Yam, V. W.-W. *Organometallics* **2012**, *31*, 4459–4466.

[118] Mullice, L. a.; Pope, S. J. a. *Dalton. Trans.* **2010**, *39*, 5908–17.

[119] Cattaneo, M.; Fagalde, F.; Borsarelli, C. D.; Katz, N. E. *Inorg. Chem.* **2009**, *48*, 3012–7.

[120] Uppadine, L. H.; Redman, J. E.; Dent, S. W.; Drew, M. G.; Beer, P. D. *Inorg. Chem.* **2001**, *40*, 2860–9.

[121] Slater, J. *Phys. Rev.* **1951**, *81*, 385–390.

[122] Kohn, W.; Sham, L. *Phys. Rev.* **1965**, *140*, 1133–1138.

[123] Marques, M. a. L.; Gross, E. K. U. *Annu. Rev. Phys. Chem.* **2004**, *55*, 427–55.

[124] Wrighton, M.; Morse, D. L. *J. Am. Chem. Soc.* **1974**, *96*, 998–1003.

[125] Yam, V. W.-W.; Wong, K. M.-C. *Chem. Comm.* **2011**, *47*, 11579–92.

[126] Qin, J.; Hu, L.; Li, G.-N.; Wang, X.-S.; Xu, Y.; Zuo, J.-L.; You, X.-Z. *Organometallics* **2011**, *30*, 2173–2179.

[127] Itokazu, M. K.; Polo, A. S.; Iha, N. Y. M. *J. Photochem. Photobiol. A* **2003**, *160*, 27–32.

[128] Anderson, C. B.; Elliott, A. B. S.; McAdam, C. J.; Gordon, K. C.; Crowley, J. D. *Organometallics* **2013**, *32*, 788–797.

[129] Baková, R.; Chergui, M.; Daniel, C.; Vlček Jr., A.; Záliš, S. *Coord. Chem. Rev.* **2011**, *255*, 975–989.

[130] Yi, X.; Zhao, J.; Wu, W.; Huang, D.; Ji, S.; Sun, J. *Dalton. Trans.* **2012**, *41*, 8931–40.

[131] Yi, X.; Zhao, J.; Sun, J.; Guo, S.; Zhang, H. *Dalton. Trans.* **2013**, *42*, 2062–74.

[132] Wolff, M.; Munoz, L.; François, A.; Carrayon, C.; Seridi, A.; Saffon, N.; Picard, C.; Machura, B.; Benoist, E. *Dalton. Trans.* **2013**, 7019–7031.

[133] Elliott, P. I. P. *Inorg. Chem.* **2010**, *106*, 526.

[134] Ko, C.-C.; Cheung, A. W.-Y.; Lo, L. T.-L.; Siu, J. W.-K.; Ng, C.-O.; Yiu, S.-M. *Coord. Chem. Rev.* **2012**, *256*, 1546–1555.

[135] Ko, C.-c.; Ng, C.-o.; Yiu, S.-m. *Organometallics* **2012**, *31*, 7074–7084.

[136] Si, Z.; Li, X.; Li, X.; Zhang, H. *J. Organomet. Chem.* **2009**, *694*, 3742–3748.

[137] Wenger, O. S. *Acc. Chem. Res.* **2013**, *46*, 1517–26.

[138] Striplin, D.; Crosby, G. *Chem. Phys. Lett.* **1994**, *221*, 426–430.

[139] Koike, K.; Okoshi, N.; Hori, H.; Takeuchi, K.; Ishitani, O.; Tsubaki, H.; Clark, I. P.; George, M. W.; Johnson, F. P. A.; Turner, J. J. *J. Am. Chem. Soc.* **2002**, *124*, 11448–11455.

[140] Stufkens, D. *Coord. Chem. Rev.* **1998**, *177*, 127–179.

[141] Giordano, P. J.; Wrighton, M. S. *J. Am. Chem. Soc.* **1979**, *3*, 2888–2897.

[142] Yarnell, J. E.; Deaton, J. C.; Mccusker, C. E.; Castellano, F. N. *Inorg. Chem.* **2011**, *50*, 7820–7830.

[143] Wang, J.-X.; Xia, H.-Y.; Liu, W.-Q.; Zhao, F.; Wang, Y.-b. *Inorg. Chim. Acta.* **2013**, *394*, 92–97.

[144] Wang, D.; Xu, Q.-L.; Zhang, S.; Li, H.-Y.; Wang, C.-C.; Li, T.-Y.; Jing, Y.-M.; Huang, W.; Zheng, Y.-X.; Accorsi, G. *Dalton. Trans.* **2012**, 2716–2723.

[145] Vlček Jr., A. *Top. Organomet. Chem.* **2010**, 73–114.

[146] Coogan, M. P.; Fernández-Moreira, V.; Hess, J. B.; Pope, S. J. a.; Williams, C. *New J. Chem.* **2009**, *33*, 1094.

[147] Henry, K. E.; Balasingham, R. G.; Vortherms, A. R.; Platts, J. A. *Chem. Sci.* **2013**,

[148] Liu, C.; Li, J.; Li, B.; Hong, Z.; Zhao, F.; Liu, S.; Li, W. *Chem. Phys. Lett.* **2007**, *435*, 54–58.

[149] Lundin, N. J.; Blackman, A. G.; Gordon, K. C.; Officer, D. L. *Angew. Chem. Int. Ed. Engl.* **2006**, *45*, 2582–4.

[150] Mauro, M.; Procopio, E. Q.; Sun, Y.; Chien, C.-H.; Donghi, D.; Panigati, M.; Mercandelli, P.; Mussini, P.; D'Alfonso, G.; De Cola, L. *Adv. Funct. Mater.* **2009**, *19*, 2607–2614.

[151] Kurz, P.; Probst, B.; Spingler, B.; Alberto, R. *Inorg. Chem.* **2006**, *2006*, 2966–2974.

[152] Takeda, H.; Ohashi, M.; Tani, T.; Ishitani, O.; Inagaki, S. *Inorg. Chem.* **2010**, *49*, 4554–9.

[153] Takeda, H.; Ishitani, O. *Coord. Chem. Rev.* **2010**, *254*, 346–354.

[154] Amoroso, A. J.; Coogan, M. P.; Dunne, J. E.; Fernández-Moreira, V.; Hess, J. B.; Hayes, A. J.; Lloyd, D.; Millet, C.; Pope, S. J. a.; Williams, C. *Chem. Comm.* **2007**, 3066–8.

[155] Balasingham, R. G.; Thorp-Greenwood, F. L.; Williams, C. F.; Coogan, M. P.; Pope, S. J. A. *Inorg. Chem.* **2012**, *51*, 1419–26.

[156] Coogan, M. P.; Doyle, R. P.; Valliant, J. F.; Babich, J. W.; Zubieta, J. *J. Labelled Comp. Radiopharm.* **2014**,

[157] Fernández-Moreira, V.; Ortego, M. L.; Williams, C. F.; Coogan, M. P.; Villacampa, M. D.; Gimeno, M. C. *Organometallics* **2012**, *31*, 5950–5957.

[158] Zheng, Z.-B.; Wu, Y.-Q.; Wang, K.-Z.; Li, F. *Dalton. Trans.* **2013**, 3273–3284.

[159] Leonidova, A.; Pierroz, V.; Adams, L. a.; Barlow, N.; Ferrari, S.; Graham, B.; Gasser, G. *ACS Med. Chem. Lett.* **2014**, *5*, 809–814.

[160] Kluba, C. a.; Mindt, T. L. *Molecules* **2013**, *18*, 3206–26.

[161] Mindt, T. L.; Struthers, H.; Spingler, B.; Brans, L.; Tourwé, D.; García-Garayoa, E.; Schibli, R. *ChemMedChem* **2010**, *5*, 2026–38.

[162] Baiano, J. A.; Kessler, R. J.; Lumpkin, R. S.; Munley, M. J.; Murphy, W. R. *J. Phys. Chem.* **1995**, *99*, 17680–17690.

[163] Demko, Z. P.; Sharpless, K. B. *J. Org. Chem* **2001**, *66*, 7945–50.

[164] Himo, F.; Demko, Z. P.; Noodleman, L.; Sharpless, K. B. *J. Am. Chem. Soc.* **2002**, *124*, 12210–6.

[165] Butler, R.; McEvoy, T. *J. Chem. Soc., Perkin Trans. 2* **1978**, 1087–1090.

[166] Butler, R. N.; Garvin, V. C. *J. Chem. Soc., Perkin Trans. 1* **1981**, 390–393.

[167] Butler, R. N.; Garvin, V. C.; Lumbroso, H.; Liegeois, C. *J. Chem. Soc., Perkin Trans. 2* **1984**, 721–725.

[168] Albertino, A.; Garino, C.; Ghiani, S.; Gobetto, R.; Nervi, C.; Salassa, L.; Rosenberg, E.; Sharmin, A.; Viscardi, G.; Buscaino, R.; Croce, G.; Milanesio, M. *J. Organomet. Chem.* **2007**, *692*, 1377–1391.

[169] Kalyanasundaram, K. *J. Chem. Soc., Faraday Trans. 2* **1986**, *82*, 2401.

[170] Werrett, M. V.; Chartrand, D.; Gale, J. D.; Hanan, G. S.; MacLellan, J. G.; Massi, M.; Muzzioli, S.; Raiteri, P.; Skelton, B. W.; Silberstein, M.; Stagni, S. *Inorg. Chem.* **2011**, *50*, 1229–41.

[171] Hevia, E.; Pérez, J.; Riera, V.; Miguel, D.; Kassel, S.; Rheingold, A. *Inorg. Chem.* **2002**, *41*, 4673–9.

[172] Álvarez, C. M.; García-Escudero, L. a.; García-Rodríguez, R.; Miguel, D. *Chem. Comm.* **2012**, *48*, 7209–11.

[173] Cuesta, L.; Huertos, M. a.; Morales, D.; Pérez, J.; Riera, L.; Riera, V.; Miguel, D.; Menéndez-Velazquez, A.; García-Granda, S. *Inorg. Chem.* **2007**, *46*, 2836–45.

[174] Wright, P. J.; Muzzioli, S.; Werrett, M. V.; Raiteri, P.; Skelton, B. W.; Silvester, D. S.; Stagni, S.; Massi, M. *Organometallics* **2012**, *31*, 7566–7578.

[175] Coe, B. *Coord. Chem. Rev.* **2000**, *203*, 5–80.

[176] Miessler, G.; Tarr, D. *Inorganic Chemistry*, 3rd ed.; Pearson Prentice Hall: Minnesota, 2004; pp 467–469.

[177] Orgel, L. E. *Inorg. Chem.* **1962**, *1*, 25–29.

[178] Bullock, J. P.; Carter, E.; Johnson, R.; Kennedy, A. T.; Key, S. E.; Kraft, B. J.; Saxon, D.; Underwood, P. *Inorg. Chem.* **2008**, *47*, 7880–7.

[179] Gamelin, D. R.; George, M. W.; Grevels, P. G. F.-w.; Johnson, F. P. A.; Klotzbucher, W.; Morrison, S. L.; Russell, G.; Schaffner, K.; Turner, J. J. *Inorg. Chem.* **1994**, 3246–3250.

[180] Janiak, C. *Dalton. Trans.* **2000**, 3885–3896.

[181] Frisch, M. J. *et al.* Gaussian09 Revision B.01. 2009.

[182] Villegas, J. M.; Stoyanov, S. R.; Huang, W.; Rillema, D. P. *Inorg. Chem.* **2005**, *44*, 2297–309.

[183] Villegas, J. M.; Stoyanov, S. R.; Huang, W.; Rillema, D. P. *Dalton. Trans.* **2005**, 1042–51.

[184] Gabrielsson, A.; Busby, M.; Matousek, P.; Towrie, M.; Hevia, E.; Cuesta, L.; Perez, J.; Zális, S.; Vlcek, A. *Inorg. Chem.* **2006**, *45*, 9789–97.

[185] Vlček, A.; Záliš, S. *Coord. Chem. Rev.* **2007**, *251*, 258–287.

[186] Kumar, A.; Sun, S.-s.; Lees, A. J. *Top. Organomet. Chem.* **2010**, *29*, 1–35.

[187] Atkins, P.; Overton, T.; Rourke, J.; Weller, M.; Armstrong, F. In *Shriver and Atkins Inorganic Chemistry*, 4th ed.; Atkins, P., Shriver, D., Eds.; Oxford University Press: Oxford, 2006; pp 459–490.

[188] Liptayf, W. *Angew. Chem. Int. Ed. Engl.* **1969**, *8*, 177–188.

[189] Solntsev, K. M.; Huppert, D.; Agmon, N. *J. Phys. Chem. A* **1998**, *102*, 9599–9606.

[190] Vogler, a. *Coord. Chem. Rev.* **2000**, *200-202*, 991–1008.

[191] Lees, A. *Chem. Rev.* **1987**, *87*, 711–743.

[192] Lees, A. J. *Inorg. Chem.* **1995**, *17*, 319–346.

[193] Sousa, S. F.; Sampaio, R. N.; Barbosa Neto, N. M.; Machado, a. E. H.; Patrocinio, a. O. T. *Photochem. Photobiol. Sci.* **2014**, *13*, 1213–24.

[194] Makal, A.; Benedict, J.; Trzop, E.; Sokolow, J.; Fournier, B.; Chen, Y.; Kalinowski, J. A.; Graber, T.; Henning, R.; Coppens, P. *J. Phys. Chem. A* **2012**, *116*, 3359–65.

[195] Juris, A.; Balzani, V.; Barigelletti, F.; Campagna, S.; Belser, P.; Zelewsky, A. *Science* **1988**, *84*, 85–277.

[196] Demas, J.; Crosy, G. *J. Phys. Chem.* **1971**, *75*, 991–1024.

[197] Bold, G. *et al. J. Med. Chem.* **1998**, *41*, 3387–401.

[198] Tang, H.; Zhang, Z.; Cong, C.; Zhang, K. *J. Org. Chem* **2009**, *45*, 559–563.

[199] Bonnamour, J.; Bolm, C. *Chem. Eur. J* **2009**, *15*, 4543–5.

[200] Rostamizadeh, S.; Ghaieni, H.; Aryan, R.; Amani, A. *Chin. Chem. Lett.* **2009**, *20*, 1311–1314.

[201] Werrett, M. V.; Muzzioli, S.; Wright, P. J.; Palazzi, A.; Raiteri, P.; Zacchini, S.; Massi, M.; Stagni, S. *Inorg. Chem.* **2014**, *53*, 229–43.

[202] Sheldrick, G. M. *Acta Crystallogr. Sect. A* **2008**, *64*, 112–22.

[203] Xiao, L.; Chen, Z.; Qu, B.; Luo, J.; Kong, S.; Gong, Q.; Kido, J. *Adv. Mater.* **2011**, *23*, 926–52.

[204] Holder, E.; Langeveld, B. M. W.; Schubert, U. S. *Adv. Mater.* **2005**, *17*, 1109–1121.

[205] Fantacci, S.; De Angelis, F. *Coord. Chem. Rev.* **2011**, *255*, 2704–2726.

[206] Vougioukalakis, G. C.; Philippopoulos, A. I.; Stergiopoulos, T.; Falaras, P. *Coord. Chem. Rev.* **2011**, *255*, 2602–2621.

[207] Chandrasekharam, M.; Suresh, T.; Singh, S. P.; Priyanka, B.; Bhanuprakash, K.; Islam, a.; Han, L.; Lakshmi Kantam, M. *Dalton. Trans.* **2012**, *119*, 8770–8772.

[208] Grätzel, M. *Inorg. Chem.* **2005**, *44*, 6841–51.

[209] Bignozzi, C.; Argazzi, R.; Boaretto, R.; Busatto, E.; Carli, S.; Ronconi, F.; Caramori, S. *Coord. Chem. Rev.* **2013**, *257*, 1472–1492.

[210] Thorp-Greenwood, F. L. *Organometallics* **2012**, *31*, 5686–5692.

[211] Liu, Z.; He, W.; Guo, Z. *Chem. Soc. Rev.* **2013**, *42*, 1568–600.

[212] Ma, D.-L.; Ma, V. P.-Y.; Chan, D. S.-H.; Leung, K.-H.; He, H.-Z.; Leung, C.-H. *Coord. Chem. Rev.* **2012**, *256*, 3087–3113.

[213] Stork, C. J.; Li, Y. V. *J. Neurosci.* **2006**, *26*, 10430–7.

[214] Poteet, S. a.; Macdonnell, F. M. *Dalton. Trans.* **2013**, 13305–13307.

[215] Zhang, R.; Ye, Z.; Song, B.; Dai, Z.; An, X.; Yuan, J. *Inorg. Chem.* **2013**,

[216] Durham, J. L.; Tirado, J. N.; Knott, S. a.; Oh, M. K.; McDonald, R.; Szczepura, L. F. *Inorg. Chem.* **2012**, *51*, 7825–36.

[217] Yeh, S.-J.; Wu, M.-F.; Chen, C.-T.; Song, Y.-H.; Chi, Y.; Ho, M.-H.; Hsu, S.-F.; Chen, C. H. *Adv. Mater.* **2005**, *17*, 285–289.

[218] Chou, P.-T.; Chi, Y.; Chung, M.-W.; Lin, C.-C. *Coord. Chem. Rev.* **2011**, *255*, 2653–2665.

[219] Stagni, S.; Orselli, E.; Palazzi, A.; De Cola, L.; Zacchini, S.; Femoni, C.; Marcaccio, M.; Paolucci, F.; Zanarini, S. *Inorg. Chem.* **2007**, *46*, 9126–38.

[220] Duati, M.; Tasca, S.; Lynch, F. C.; Bohlen, H.; Vos, J. G.; Stagni, S.; Ward, M. D. *Inorg. Chem.* **2003**, *42*, 8377–84.

[221] Becke, A. D. *J. Chem. Phys.* **1993**, *98*, 5648.

[222] Andrae, D.; HauBerman, U.; Dolg, M.; Stoll, H.; Preub, H. *Theor. Chim. Acta.* **1990**, *77*, 123–141.

[223] Tomasi, J.; Mennucci, B.; Cammi, R. *Chem. Rev.* **2005**, *105*, 2999–3093.

[224] Magee, K. D. M.; Wright, P. J.; Muzzioli, S.; Siedlovskas, C. M.; Raiteri, P.; Baker, M. V.; Brown, D. H.; Stagni, S.; Massi, M. *Dalton. Trans.* **2013**, *42*, 4233–6.

[225] Wright, P. J.; Muzzioli, S.; Skelton, B. W.; Raiteri, P.; Lee, J.; Koutsantonis, G.; Silvester, D. S.; Stagni, S.; Massi, M. *Dalton. Trans.* **2013**, *42*, 8188–91.

[226] Wright, P. J.; Affleck, M. G.; Muzzioli, S.; Skelton, B. W.; Raiteri, P.; Silvester, D. S.; Stagni, S.; Massi, M. *Organometallics* **2013**, *32*, 3728–3737.

[227] Zanarini, S.; Bard, A. J.; Marcaccio, M.; Palazzi, A.; Paolucci, F.; Stagni, S. *J. Phys. Chem. B* **2006**, *110*, 22551–6.

[228] Takach, N. E.; Holt, E. M.; Aicock, N. W.; Henry, R. A.; Ia, J. H. N. *J. Am. Chem. Soc.* **1980**, *102*, 2968–2979.

[229] Stagni, S.; Palazzi, A.; Zacchini, S.; Ballarin, B.; Bruno, C.; Marcaccio, M.; Paolucci, F.; Monari, M.; Carano, M.; Bard, A. J. *Inorg. Chem.* **2006**, *45*, 695–709.

[230] Hall, J. H.; Purcell, W. L. *Inorg. Chem.* **1990**, *29*, 3806–3811.

[231] Butler, M. *Animal Cell Culture and Technology*, 2nd ed.; BIOS Scientific: Oxford, 2004; pp 1–26.

[232] Clarke, S.; Dillon, J. In *Animal Cell Culture:Essential Methods*, 1st ed.; Davis, J. M., Ed.; John Wiley & Sons: West Sussex, 2011; Chapter One, pp 1–31.

[233] Stacey, G. N.; Hawkins, R.; Fleck, R. A. In *Animal Cell Culture: Essential Methods*, 1st ed.; Davis, J. M., Ed.; John Wiley & Sons: West Sussex, 2011; Chapter Six, pp 185–203.

[234] Hayflick, L.; Moorhead, P. S. *Exp. Cell. Res.* **1961**, *25*, 585–621.

[235] Shay, J. W.; Wright, W. E. *Nat. Rev. Mol. Cell Biol.* **2000**, *1*, 72–6.

[236] Masters, J. R. *Nat. Rev. Cancer* **2002**, *2*, 315–319.

[237] Evennett, P. J.; Hammond, C. In *Reference Module in Chemistry, Molecular Sciences and Chemical Engineering*, 2nd ed.; Reedijk, J., Ed.; Elsevier: Leeds, 2005; pp 32–41.

[238] Gray, C.; Zicha, D. In *Animal Cell Culture:Essential Methods*, 1st ed.; Davis, J. M., Ed.; John Wiley & Sons: West Sussex, 2011; Chapter Three, pp 61–90.

[239] Conchello, J.-a.; Lichtman, J. W. *Nat. Methods.* **2005**, *2*, 920–931.

[240] Wright, S.; Wright, D. In *Cell Biological Applications of Confocal Microscopy*, 2nd ed.; Matsumoto, B., Ed.; Elsevier Science (ESA): California, 2002; pp 1–16.

[241] Zeviani, M. Basis of Confocal Microscopy. 2014; `http://www.mrc-mbu.cam.ac.uk/node/207`.

[242] Inoue, S. In *Handbook of Biological Confocal Microscopy*, 3rd ed.; Pawley, J., Ed.; Springer: Wisconsin, 2006; pp 1–6.

[243] Dan, D.; Lei, M.; Yao, B.; Wang, W.; Winterhalder, M.; Zumbusch, A.; Qi, Y.; Xia, L.; Yan, S.; Yang, Y.; Gao, P.; Ye, T.; Zhao, W. *Sci. Rep.* **2013**, *3*, 1116.

[244] Ko, K. *J. Microsc.* **2000**, *200*, 83–104.

[245] Zimmermann, T.; Rietdorf, J.; Pepperkok, R. *FEBS Lett.* **2003**, *546*, 87–92.

[246] Law, W. H.-T.; Lee, L. C.-C.; Louie, M.-W.; Liu, H.-W.; Ang, T. W.-H.; Lo, K. K.-W. *Inorg. Chem.* **2013**,

[247] Louie, M.-W.; Liu, H.-W.; Lam, M. H.-C.; Lam, Y.-W.; Lo, K. K.-W. *Chem. Eur. J* **2011**, 8304 – 8308.

[248] Gores, G.; Herman, B.; Lemasters, J. *Hepatology* **1990**, *11*, 690–698.

[249] Zhang, Y.; Gao, F.; Popov, V. L.; Wen, J. W.; Hamill, O. P. *J. Physiol.* **2000**, *523 Pt 1*, 117–30.

[250] Cao, R.; Jia, J.; Ma, X.; Zhou, M.; Fei, H. *J. Med. Chem.* **2013**, *56*, 3636–44.

[251] Josefsen, L. B.; Boyle, R. W. *Met.-Based Drugs* **2008**, *2008*, 276109.

[252] Zhao, S.; Liao, H.; Ao, M.; Wu, L.; Zhang, X.; Chen, Y. *FEBS Open Bio.* **2014**, *4*, 190–9.

[253] Kong, X.; Mohanty, S. K.; Stephens, J.; Heale, J. T.; Gomez-Godinez, V.; Shi, L. Z.; Kim, J.-S.; Yokomori, K.; Berns, M. W. *Nucleic Acids Res.* **2009**, *37*, e68.

[254] Skovsen, E.; Snyder, J. W.; Lambert, J. D. C.; Ogilby, P. R. *J. Phys. Chem. B* **2005**, *109*, 8570–3.

[255] Moan, J. *J. Photochem. Photobiol. B.* **1990**, *6*, 343–347.

[256] Merkel, P. B.; Kearns, D. R. *J. Am. Chem. Soc.* **1972**, *94*, 7244–7253.

[257] Niedre, M.; Patterson, M. S.; Wilson, B. C. *Photochem. Photobiol.* **2002**, *75*, 382–91.

[258] Sousa, C.; Botelho do Rego, A.; Sá e Melo, T. *Química Nova* **2008**, *31*, 1392–1399.

[259] Felsher, D. W. *Nat rev. Cancer* **2003**, *3*, 375–80.

[260] Agostinis, P. *et al. CA Cancer J. Clin.* **2011**, *61*, 250–81.

[261] Dougherty, T. J.; Gomer, C. J.; Henderson, B. W.; Jori, G.; Kessel, D.; Korbelik, M.; Moan, J.; Peng, Q. *J. Natl. Cancer Inst.* **1998**, *90*, 889–905.

[262] Madani, F.; Lindberg, S.; Langel, U.; Futaki, S.; Gräslund, A. *J. Biophys.* **2011**, *2011*, 414729.

[263] Brown, D. H.; Skelton, B. W. *Dalton Trans.* **2011**, *40*, 8849–58.

[264] Evanko, D. *Nat. Methods* **2013**, *10*, 1135–1135.

[265] Kovar, J. L.; Simpson, M. a.; Schutz-Geschwender, A.; Olive, D. M. *Anal. Biochem.* **2007**, *367*, 1–12.